THE INTERACTION BETWEEN LIQUID ALUMINIUM AND ~~SiC~~ silicone carbide IN METAL MATRIX COMPOSITES

Thesis submitted for the
degree of Doctor of Philosophy
of the University of London

by

Peter Kenneth Johnson

September 1990

Department of Materials
Royal School of Mines
Imperial College
London, SW7

TO MY PARENTS

ABSTRACT

Commercial purity (CP) Al + 10.5-12.5vol%SiC; Al-12wt%Si-14vol%SiC; LM13 + 18-20vol%SiC; and Al-19Si-14vol%SiC, composites were manufactured commercially by a spray co-deposition process. The SiC was Acheson process produced grit, with an average particle size of ~13microns.

The study centres on the following reaction between liquid CP aluminium and particulate SiC:

$$4Al(l) + 3SiC(s) \longrightarrow Al_4C_3(s) + 3Si(l).$$

Microstructural changes during the reaction have been characterised, and correlated with kinetic data to provide a basis for the understanding of the mechanisms involved. Kinetic data were collected from quantitative metallography, quantitative energy dispersive X-ray spectroscopy, matrix liquidus temperature determinations and direct residual SiC mass fraction measurements. The temperature range was from ~670^{o}C to 1000^{o}C for times up to 10^4 minutes. Time-temperature-transformation diagrams were constructed. Microstructural data were collected using light microscopy, and both scanning and transmission electron microscopy (SEM and TEM) techniques. The reaction was found to proceed in three stages. Stage 1 was SiC dissolution controlled (activation energy 260+/-40kJ/mol) and was characterised by epitaxial nucleation and the initial growth of hexagonal Al_4C_3 platelets at the SiC-liquid interface resulting in the early coverage of the sites of preferred dissolution. Stage 2 follows nucleation site saturation: the rate decreases as the activation energy rises. Solid state processes and less favourable direct dissolution sites contribute significantly to the reaction, and Al_4C_3 grows laterally to cover the remaining SiC-liquid interface. Stage 3 occurs as SiC is isolated from the melt (if saturation of the liquid with Si does not intervene).

With Al-Si matrices the Al_4C_3 morphology resulting from stage 1 processes is different: this was postulated to be due to a decrease in the Al_4C_3 nucleation rate with increasing temperature. Solidification phenomena are discussed in relation to preliminary observations with emphasis on SiC behaving as a nucleation site, and on the wetting of SiC by aluminium. The results of a brief fractographic study are presented.

Index

Abstract 3

Index 4

Text 4

List of Figures 8

List of Tables 12

Chapter I

Introduction 13

Chapter II

Literature Survey 15

2.1 Silicon-Carbon 15

2.1.1 *The C-Si phase diagram* 15

2.1.2 *SiC structure* 15

2.1.3 *SiC transformations* 17

2.1.4 *SiC manufacture* 18

2.1.5 *SiC properties* 19

2.2 The Al-Si system 19

2.2.1 *Al-Si phase diagram* 19

2.2.2 *Aspects of Al-Si solidification* 20

2.3 The Al-C system 20

2.3.1 *Al-C phase equilibria* 20

2.3.2 *Al_4C_3 : structure and properties* 22

2.3.3 *Al_4C_3 chemistry and its role in composite degradation* 22

2.4 The Al-C-Si system 23

2.4.1 *Al-C-Si phase equilibria* 23

2.4.2 *Reactions at low temperatures at normal pressures* 25

2.4.3 *The effect of pressure on reactions at low temperatures* 26

2.4.4 *Reaction kinetics* 26

2.5 Interfaces and wetting 28

2.5.1 *SiC surfaces* 28

2.5.2 *Solid Al -SiC interfaces* 29

2.5.3 *Wetting of ceramics by Al alloys* 30

2.6 Composite processing involving a liquid metal alloy melt 31

2.6.1 *Discontinuously reinforced composites* 31

2.6.2 *Particles in liquid alloys* 31

2.6.3 *Spray co-deposition* 32

Chapter III

Experimental Procedures 33
3.1 Introduction 33
3.2. Starting Materials 33
3.3 Heat treatments 34
3.3.1 *Initial heat treatments* 34
3.3.2 *Synthesis of the spray-cast microstructure* 34
3.3.3 *Arc-melting* 37
3.4 Microstructural characterisation 37
3.4.1 *Metallographic preparation* 37
3.4.2 *Deep etching* 38
3.4.3 *Thin foil preparation* 38
3.4.4 *Powder for XRD (X-ray diffraction) examination* 39
3.4.5 *EPMA (electron probe microanalysis)* 39
3.5 Quantitative kinetic evaluation 39
3.5.1 *Area fraction of primary aluminium in AC samples* 40
3.5.2 *Area fraction of primary aluminium in WQ samples* 40
3.5.3 *Area fraction of impurity intermetallic phases in AC samples* 40
3.5.4 *Mass fraction of SiC in preform materials* 41
3.5.5 *Mass fraction of SiC following re-melting* 41
3.5.6 *Quantitative energy dispersive X-ray spectroscopy (EDS) of MMC matrix following re-melting and WQ* 43
3.5.7 *Calibration alloys for EDS* 44
3.5.8 *Thermal analysis methods: general remarks* 44
3.5.9 *Differential thermal analysis (DTA) of the initial set of heat treated samples* 45
3.5.10 *Differential thermal analysis (DTA) of rapidly heated re-melted samples* 45
3.5.11 *Thermal analysis of bulk samples* 48
3.6 Fractographic study of tensile specimens 49

Chapter IV

The reaction between SIC and liquid aluminium 50
4.1 Introduction 50
4.2 Starting materials 50
4.2.1 *MH87-S* 50
4.2.2 *MH85-S* 51
4.2.3 *Silicon carbide in the composites* 51
4.2.4 *SiC surface morphology* 52
4.3 Remelting 53
4.3.1 *Re-melting: initial results* 53
4.3.2 *Impurity phases* 54

4.3.3 *Arc-melting* 55
4.3.4 *Prediction of the ultimate extent of reaction* 55
4.4 Microstructural results: nucleation 57
4.4.1 *Deep etching experiment* 57
4.4.2 *Nucleation sites at the SiC -liquid Al interface* 57
4.4.3 *Orientation relationships between Al_4C_3 and SiC* 59
4.4.3.1 *'Simple' orientation relationship* 59
4.4.3.2 *Minor misorientations* 59
4.4.3.3 *Alternative orientation relationships* 60
4.5 Microstructural results: Al_4C_3 growth 61
4.5.1 *Al_4C_3 morphology as an interface product* 61
4.5.2 *Al_4C_3 twins* 63
4.5.3 *Al_4C_3 - free SiC - liquid Al interfaces* 63
4.6 SiC surface post reaction 64
4.7 Summary: 'reaction zone' microstructure in the liquid CP.Al + 10.5-12.5vol% SiC particulate system 64
4.8 Quantitative kinetics 64
4.8.1 *Introduction* 64
4.8.2 *Initial volume fraction of SiC* 65
4.8.3 *Volume fraction of primary Al in AC samples* 66
4.8.4 *Area fraction of primary Al in WQ samples* 67
4.8.5 *Mass fraction of SiC following re-melting* 68
4.8.6 *Quantitative EDS of the MMC matrix following re-melting and WQ* 68
4.8.7 *Differential thermal analysis (DTA) of the initial set of heat treated samples (table 3.3)* 69
4.8.7.1 *Impurities* 70
4.8.7.2 *Heating rate* 71
4.8.7.3 *Total sample mass* 71
4.8.7.4 *Actual amount of sample undergoing transformation* 72
4.8.7.5 *Methods of DTA peak evaluation* 72
4.8.7.6 *Final remarks on the processing of the DTA results* 73
4.8.8 *Comparison of the quantitative methods* 74
4.9 Kinetic data collected for the deduction of mechanisms 74
4.9.1 *Measured temperatures* 75
4.9.2 *Comparison of thermal analysis data* 75
4.9.3 *Rapidly heated re-melted samples* 76
4.9.4 *'Stage1' activation energies* 77
4.9.5 *Summary* 78
4.10 TTT diagrams 78
4.10.1 *Introduction* 78
4.10.2 *TTT curves: discussion* 79

4.11 Activation energies 80
4.12 Correlation of the quantitative results with the microstructural analysis 81
4.13 Further work 82

Chapter V

Al-Si-SiC Composites 155
5.1 Introduction 155
5.2 Al-19Si-SiC composite 155
5.2.1 *Al-19Si-SiC as-sprayed microstructure* 155
5.2.2 *Synthesis of the as-sprayed microstructure* 156
5.2.3 *Primary silicon in re-melted Al-Si-SiC composites* 157
5.3 Al-12Si-SiC composite 158
5.3.1 *As-sprayed Al-12Si-SiC* 158
5.3.2 *Re-melted Al-12Si-SiC* 158
5.3.3 *Al_4C_3 formation in Al-Si-SiC melts* 159
5.3.4 *Suggested mechanism for the nucleation and growth of Al_4C_3 in Al-Si-SiC composites* 160
5.3.5 *Anomalous structures* 162
5.4 LM13+ 18-20vol%SiC composite 162
5.4.1 *As-sprayed LM13+ 18-20vol%SiC* 162
5.4.2 *Re-melted LM13 + 18-20vol%SiC* 163
5.4.3 *Intermetallics in re-melted LM13 + 18-20vol%SiC and in LM13* 164
5.5 Orientation relationships 167
5.6 Summary : Chapter V 167
5.7 Further work 168

Chapter VI

Fractography 199
6.1 Introduction 199
6.2 General remarks on the tensile results 199
6.2.1 *Test A* 199
6.2.1.1 *Test A : summary* 200
6.2.2 *Test B* 200
6.2.2.1 *Test B: summary* 202
6.2.3 *Test C* 202
6.2.3.1 *Test C: summary* 203
6.2.4 *Test D* 204
6.2.5 *Corrosion induced cracking* 204
6.3 Discussion 205
6.3.1 *General* 205
6.3.1.1 *Fracture mechanism transition from test A to test B* 205
6.3.1.2 *Lack of Al-Al_4C_3 debonding in test C when present in test B* 206
6.3.1.3 *Apparent absence of Al_4C_3- Si/β(FeSi) debonding in test C* 206

6.3.2 *Al_4C_3 on fracture paths* 207

6.3.3 *Comparison with the literature* 208

6.3.4 *Summary* 208

6.4 Further work 208

Chapter VII

Conclusions & references 225

7.1 Conclusions 225

7.2 References 230

Acknowledgements 238

List of Figures

Figure 2. 1 The C-Si phase diagram, with selected data, according to [46] 16

Figure 2. 2 Stacking of C and Si atoms in {11.0} planes of the common polytypes 16

Figure 2.3 The Al-Si phase diagram with selected liquidus data according to [60] 21

Figure 2.4 The Al-C phase diagram 21

Figure 2.5 The Al-C-Si phase diagram 24

Figure 2.6 Experimental Al-C-Si phase diagram results from Viala et al 24

Figure 2.7 The kinetics of SiC wetting by Al and Al alloys from Choh and Oki [109] 27

Figure 2.8 Osprey composite manufacturing plant [145] 27

Figure 3.1 Use of a protective atmosphere during composite re-melts for samples of mass ~1.5g 36

Figure 3.2 Route for SiC particle extraction from free-Si containing Al matrix alloys: after Kujur et al [151]. 42

Figure 3.3 Diagram showing the simple method employed for rapidly heating Al-SiC MMC 'hat' samples 47

Figure 4.1 Light micrographs of MH87-S (CP. Al + SiC) both as-produced and following arc-melting 84

Figure 4.2 Micrographs of starting material MH85-S (CP.Al + SiC) 86

Figure 4.3 SiC surface morphology 88

Figure 4.4 SiC particle morphology: schematic 90

Figure 4.5 Micrographs of re-melted CP.Al +SiC 91

Figure 4.6 Si content of the Al-Si-C liquid in metastable equilibrium with SiC and Al_4C_3 93

Figure 4.7 Miscellaneous micrographs 94

Figure 4.8a Volume fraction of impurity transition element containing phases in re-melted CP.Al-SiC composite (MH87-S) castings (air-cooled). 96

Figure 4.8b Model of a SiC 'asperity' 96

Figure 4.9 Deep-etching 97

Figure4.10 TEM micrographs of a CP.Al - SiC composite (MH87-S) re-melted for a nominal time of 10minutes at 672^{o}C 99

Figure 4.11 TEM micrographs of a CP.Al - SiC composite re-melted at 672^{o}C 101

Figure 4.12 Suggested sites (lettered) at which coherency could exist between groups of atoms in the 'simple' epitaxial SiC-Al_4C_3 relationship 103

Figure 4.13 TEM micrographs of CP.Al - SiC (MH85-S) following re-melting for10s at 800^{o}C 104

Figure 4.14 TEM micrographs of CP.Al - SiC (MH87-S) re-melted at 800^{o}C for 1000minutes and WQ 106

Figure 4.15 TEM micrographs of CP.Al - SiC (MH87-S) re-melted at 1000^{o}C for 1000minutes and WQ 108

Figure 4.16 TEM micrographs of CP.Al - SiC (MH87-S) re-melted at 1000^{o}C for 1000minutes and WQ 110

Figure 4.17 Electron diffraction patterns 112

Figure 4.17 : KEY 114

Figure 4.18 Experimental isothermal kinetics: the volume fraction of primary Al in re-melted CP.Al-SiC (MH87-S) samples, which were air cooled, as a function of the re-melt time. 115

Figure 4.19 The volume fraction of eutectic in samples of CP.Al+SiC (MH87-S) re-melted at 800^{o}C and water quenched as a function of the re-melt time. 116

Figure 4.20 Experimentally determined wt%SiC in CP.Al+SiC (MH85-S) as a function of the re-melt time. 117

Figure 4.21 Calibration curve for the EDS analysis of cast Al-Si alloys. 118

Figure 4.22 EDS (energy dispersive X-ray spectroscopy) results. 119

Figure 4.23 Analysis of DTA traces 120

Figure 4.24 Comparison of liquid composition results derived from DTA trace temperatures. 121

Figure 4.25 Comparison of liquid composition results derived from the change in the estimated liquidus temperature with the EDS results 122

Figure 4.26 Curves illustrating the increase in the 'eutectic' DTA peak temperature as the liquidus peak temperature decreases. 123

Figure 4.27 CP.Al-SiC composite DTA peak temperatures found upon heating versus DTA sample mass 124

Figure 4.28 Comparison of liquid composition results derived from the corrected change in the DTA 'primary' peak temperature ΔT(corr) with the EDS results 125

Figure 4.29 Comparison of data produced by various techniques and converted to volume fractions of Al_4C_3 for Al-SiC composite reacted at 672^{o}C 126

Figure 4.30 Comparison of data produced by various techniques and converted to volume fractions of Al_4C_3 for Al-SiC composite reacted at 800^{o}C 127

Figure 4.31 Comparison of data produced by various techniques and converted to volume fractions of Al_4C_3 for Al-SiC composite reacted at 1000^{o}C 128

Figure 4.32 Averaged results for MH87-S using DTA, EDS and the volume fraction of primary Al in air-cooled samples data 129

Figure 4.33 Plots of DTA peak temperatures and thermal arrest temperatures recorded on heating versus the re-melt time for samples of MH85-S re-melted at 672^{o}C 130

Figure 4.34 Plots of DTA peak temperatures and thermal arrest temperatures recorded on heating versus the re-melt time for samples of MH85-S re-melted at 715^{o}C 131

Figure 4.35 Plots of DTA peak temperatures and thermal arrest temperatures recorded on heating versus the re-melt time for samples of MH85-S re-melted at 760^{o}C 132

Figure 4.36 Plots of DTA peak temperatures and thermal arrest temperatures recorded on heating versus the re-melt time for samples of MH85-S re-melted at 800^{o}C 133

Figure 4.37 Plots of DTA peak temperatures and thermal arrest temperatures recorded on heating versus the re-melt time for samples of MH85-S re-melted at 850^{o}C 134

Figure 4.38 Comparison of the thermal analysis data obtained for the different isothermal treatments 135

Figure 4.39 Decrease in the DTA peak temperature associated with the liquidus recorded on heating ΔTp for MH85-S 'rapidly heated re-melted samples' as a function of the re-melt time. 136

Figure 4.40 Kinetic curves derived from the thermal analysis and DTA based methods for reaction (4.1) at 672^{o}C 137

Figure 4.41 Kinetic curves derived from the thermal analysis and DTA based methods for reaction (4.1) at 715^{o}C 138

Figure 4.42 Kinetic curves derived from the thermal analysis and DTA based methods for reaction (4.1) at 760^{o}C 139

Figure 4.43 Kinetic curves derived from the thermal analysis and DTA based methods for reaction (4.1) at 800^{o}C 140

Figure 4.44 Linear extrapolations of the kinetic data presented in figures 4.40-4.43. 141

Figure 4.45 Decrease in the DTA peak temperature versus the re-melt time. 142

Figure 4.46 Arrhenius plots. 143

Figure 4.47 CP.Al-SiC liquid (matrix) composition as a function of time and temperature. 144

Figure 4.48 The volume fraction of Al_4C_3 produced in CP.Al-SiC composites as a function of the re-melting time and temperature 145

Figure 4.49 TTT diagram for the reaction between CP.Al and 10.5vol%SiC and 12.5vol%SiC of F600 grit grade particulate. 146

Figure 4.50 TTT diagrams for the two composites in which the 100% transformation has been taken as being the same so that a comparison can be made between the extents of reaction. 147

Figure 4.51 TTT diagram for the CP.Al+10.5vol%SiC composite alone. 148

Figure 4.52 Schematic of the interface reaction in 2 dimensions 149

Figure 4.53 Summary of the three stages in the kinetics of the reaction $4Al(l) + 3SiC(s) \longrightarrow Al_4C_3(s) + 3Si(l)$ and the rate controlling mechanisms operating at each stage 150

Figure 5.1 As-sprayed Al-19Si-SiC 170

Figure 5.2 As-sprayed Al-19Si-SiC 172

Figure 5.3 Synthesis of the as-sprayed Al-19Si-SiC microstructure 174

Figure 5.4 Primary Si - SiC interactions and as-sprayed Al-12Si-SiC 176

Figure 5.5 Re-melted Al-12Si-SiC 178

Figure 5.6 Re-melted Al-12Si-SiC 180

Figure 5.7 Re-melted Al-12Si-SiC 182

Figure 5.8 As- sprayed LM13+18-20vol%SiC 184

Figure 5.9 Re-melted LM13+18-20vol%SiC 186

Figure 5.10 Re-melted LM13+18-20vol%SiC 188

Figure 5.11 Phases in LM13 190

Figure 5.12 Orientation relationships between SiC and matrix phases 192

Figure 5.13 Proposed temperature dependence of rate phenomena early in the reaction: $4Al(l) + 3SiC(s) \longrightarrow Al_4C_3(s) + 3Si(l)$ 194

Figure 6.1 Tensile test results 211

Figure 6.2 Fractography via light microscopy 212

Figure 6.3 Fractography via light microscopy: transverse sections 214

Figure 6.4 SEM of fracture surfaces 216

Figure 6.5 SEM of fracture surfaces 218

Figure 6.6 SEM of fracture surfaces 220

Figure 6.7 Potential and observed failure mechanisms 222

Figure 6.8 Shear crack growth 223

List of Tables

Table 2.1	Properties of beta-SiC [53]	19
Table 2.2	C solubilities in liquid Al [74]	22
Table 3.1	Matrix alloy compositions	35
Table 3.2	Composite details	35
Table 3.3	Initial set of 'isothermal' re-melts	35
Table 3.4	Thermal analysis of bulk samples	36
Table 4.1	Initial results of the re-melting of the composites	151
Table 4.2	Estimate of the transformation temperature at which L-SiC equilibrium (metastable) is replaced by L-SiC-Al_4C_3	151
Table 4.3	Intermetallic phases in CP.Al+SiC composites MH85-S, and MH87-S, following re-melting	152
Table 4.4	Mole fraction of Si in liquid Al when L-SiC-Al_4C_3 equilibrium is established	153
Table 4.5	Misorientations	153
Table 4.6	Initial volume fraction of SiC	153
Table 4.7	Al-Si liquidus slope	154
Table 4.8	Empirical activation energies	154
Table 5.1	Intermetallic phases in LM13+18-20vol%SiC (MH35-L) composite following re-melting, and in conventional LM13	195
Table 5.1	cont.	196
Table 5.1	cont.	197
Table 5.2	Identification of intermetallics in LM13+18-20vol%SiC (MH35-L) composite following re-melting	198
Table 6.1	Fractography results summary and proposed dominant mechanisms	224

Chapter I

Introduction

Metal matrix composites (MMCs) are material systems in which ceramic fibres (continuous reinforcement) or ceramic whiskers, particulates, or platelets (discontinuous reinforcements) are mechanically mixed with, and bonded together by, a metal alloy. MMCs are currently the subject of an intense research effort [1]: materials of this type are destined to find major markets in aerospace structures and aeroengines [1-9], automotive applications [1,10,11,12,13], and in consumer leisure goods [1].

The recent increase in the availability of cheap sources of SiC whiskers prompted an expansion of interest in the discontinuously reinforced aluminium-silicon carbide MMCs [4,5]. Although the increases in specific properties possible with the discontinuous forms of reinforcement are lower than for the equivalent level of reinforcement in a continuously reinforced MMC, the economic advantages of discontinuously reinforced MMCs include the low cost of the ceramic, and the general capability of the materials to be processed using largely conventional processing technology [8] as a consequence of the near-isotropic properties acheivable in these materials: design constraints on components incorporating the near-isotropic discontinuously reinforced composites are also reduced which in turn will lead to the wider application of this type of MMC material.

Discontinuously reinforced MMCs show enhanced specific stiffness and specific strength [3,5], improved wear resistance [11,13,14,15], and beneficial changes in the elevated temperature properties eg. creep rupture [5,15,16] with respect to the properties of the unreinforced base alloy. The fatigue resistance of the discontinuously reinforced MMCs has been found to be generally no better than the matrix [17], and toughness needs improvement [3,5,18,19]. MMCs offer the possibility of tailoring physical properties eg. thermal, and electrical conductivities, coefficients of thermal expansion and magnetic properties [1] to the needs of the engineer.

The low stiffness of aluminium and its poor high temperature properties, combined with the ease of processing, and relative cheapness, have made aluminium alloys the major matrix materials: further improvements in specific properties are produced using Al-Li alloys [3,16,5,9,20] as matrices. Alloys ranging from Mg and Be [15] to steel [13] and titanium alloys [21] have had particulate fillers added principally to reduce wear and improve creep resistance (with the added advantage of a reduction in density).

The improved strength due to discontinuous forms of reinforcement had been the source of debate between supporters of continuum mechanics models [22] and incomplete microstructural strengthening models [23-31]. The failure of the continuum mechanics models (except for the prediction of stiffness) is apparent as they fail to predict the increased strength

of the MMCs as the aspect ratio of the reinforcements approach unity [32]. For microstructural models to be capable of predicting the strength improvements of discontinuous MMCs accurately requires a better understanding of the interactions between the basic metal alloy strengthening mechanisms, which have been reviewed in the context of discontinuous MMCs [32]. Matrix to reinforcement load transfer takes place via an Orowan mechanism, with further significant strengthening contributions from subgrain structures, and refined grain sizes developed in the matrix during processing [32]. Precipitation in MMC matrices is found to differ from that in the matrix alloys alone [33,34,35].

Discontinuous SiC reinforced Al MMCs fabricated by a low cost, melt based route, may represent the earliest type of MMCs to be produced in large-scale commercial plants [36]: production of such MMCs is now expected to expand, from hundreds to tens of thousands of tonnes per annum within the next few years [2], in order to supply MMC ingots with both wrought and casting alloy matrices to product manufacturers. The casting of MMCs offers the capability to bulk produce near net shape components: only by producing MMC components as economically as possible have in-roads into the automotive market been made: a market in which the enhancement of properties at zero extra cost is needed for acceptance [1]. Reciprocating parts in engines [10] are considered as candidate components for replacement: the higher damping capacity of MMCs [37] compared to the matrix alloy is a further advantage in such applications.

The major disadvantage of the melt based routes to manufacture, and process MMCs is the increased possibility of the occurrence of detrimental ceramic reinforcement-melt interactions which limits the number of MMC systems that can be processed in this way. The higher temperature melting matrices tend to be fabricated more by powder metallurgy methods at temperatures below the solidus. A composite system formed from the mixing of phases intended to be present during the materials application needs each phase to remain unaltered, except for the formation of an 'adequate' matrix-ceramic bond which is most important if the improvements envisaged in creating the composite system are to be realised. The problems are related to the thermodynamics of the composite system, and the kinetics of phase transformations that can potentially take place during both processing and MMC application. In the Al-SiC MMC system a widely recognised reaction takes place during liquid route processing which produces both an undesirable interface product and alters the chemistry of the matrix [38]: although the large scale production of such materials is imminent, basic phase transformation studies are necessary if current MMCs of this type are to be optimised, and for future MMC systems to be improved.

Chapter II

Literature Survey

2.1 Silicon-Carbon

2.1.1 *The C-Si phase diagram*

A single, stable compound SiC, which has 90% covalent bonding [39], forms in the C-Si system. SiC decomposes at 2545+/-40^{o}C according to the recently published C-Si phase diagram reproduced as in figure 2.1 [40]. It is suggested that the cubic form of SiC, commonly referred to as beta-SiC is the stable crystal type [40]. However, SiC structural transformations are very sensitive to temperature, and traces of impurities. The following paragraphs only serve to illustrate the complex nature of SiC, a material that continues to be extensively studied owing to its growing importance as a raw material for advanced 'technical' ceramics, and semi-conductor devices [39,41,42], and more recently as the most popular reinforcement for inclusion in MMCs.

2.1.2 *SiC structure*

SiC can exist in two basic allotropic forms: the hexagonal 'alpha' SiC form, and the cubic 'beta' SiC form based on the wurtzite and cubic ZnS structures respectively [39]. The alpha-SiC exists in 'inumerable' crystalline modifications called polytypes [40,43,44]. Each alpha-SiC polytype unit cell has the same 'a' and 'b' parameters but different 'c' parameters: this arises due to the different periodic stacking sequences of identical, puckered Si-C layers perpendicular to the 'c' axis.

The Acheson SiC production route, as described below, mainly yields the common alpha-polytypes [45,46] with Ramsdell notations 6H, 15R and 4H, as illustrated in figure 2.2, with some beta-SiC. The 'Ramsdell notation' is used to indicate the number of layers in a unit cell, plus the type of symmetry exhibited: hexagonal (H), rhombohedral (R), cubic (C) and trigonal (T) [47] symmetries are distinguished. Polytypes with Ramsdell notations rangeing from 2H to 1200R were reported by 1978 [48], and more continue to be discovered. 'Long period' polytypes are often conveniently described in terms of sequences of short period polytypes [44,48], and Zhdanov notation provides a simple means of expressing complicated SiC structures [44,47,48]. The origins of polytypism, and its nature, remains unclear, with the apparent stable coexistence of polytypes [43]. As the temperature of SiC formation increases (in an Acheson resistance furnace) so does the abundance of longer period stacking sequences, in order of increasing 'c' spacing from 2H, 3C, 4H, 15R, 6H, 21R, 8H.....[43]. Various theories have been proposed to account for the formation of polytypes [43], though screw dislocation mechanisms do not appear to be relevant to the long-range polytype phenomenon in which long range, periodic, strain fields apparently play a role, the strain fields created during the formation and processing of polycrystalline SiC [48]. The SiC polytypes, consisting of stacks of the the same basic layer structure, are closely related energetically

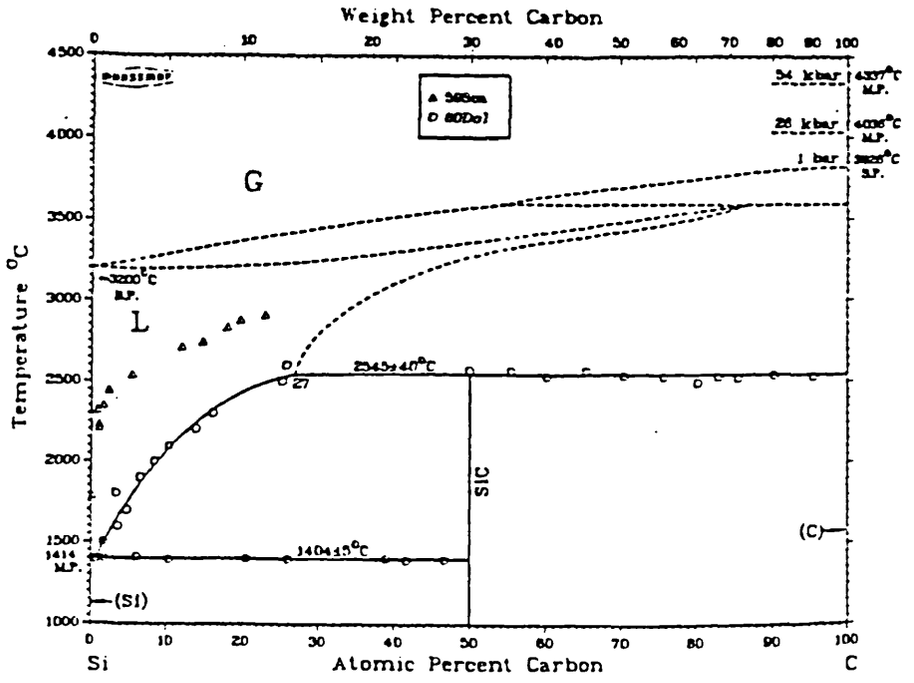


Figure 2.1 The C-Si phase diagram, with selected data, according to [46].

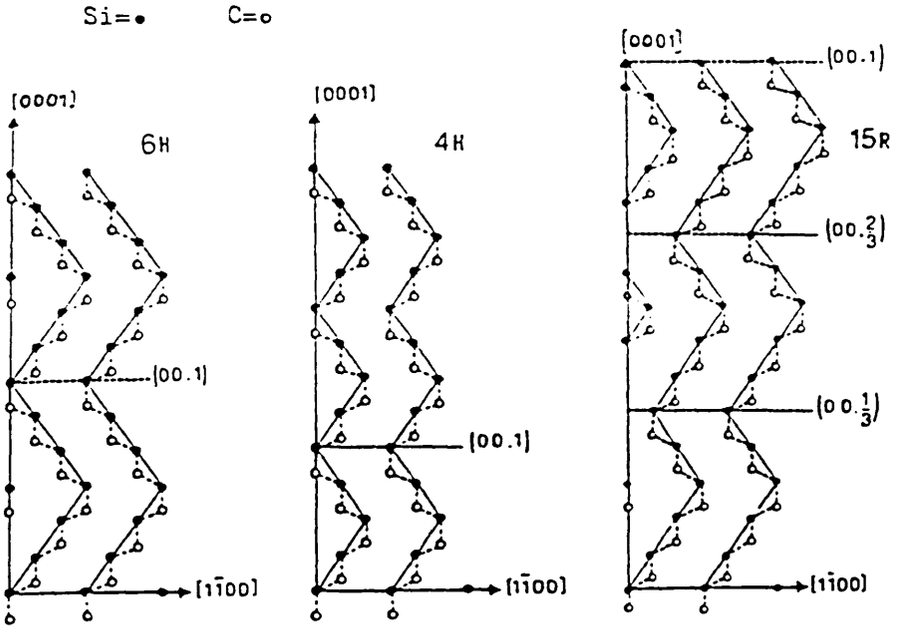


Figure 2.2 Stacking of Si and C atoms in 11.0 planes of the common polytypes. The smallest spacing between C-Si layers is 0.251nm. The unit cell parameters are 'a'=0.395nm and 'c'=1.5nm (6H), 'c'=1nm (4H) and 'c'=3.77nm (15R) [40].

[48,49]. Stacking-faults are common throughout these materials; where high densities of stacking-faults appear the SiC is described as 'disordered', and the long-period polytypes are a related phenomenon [48,49].

2.1.3 *SiC transformations*

Transformations from one polytype to another are reported to occur during the processing of SiC over a wide range of temperatures: annealing CVD (chemically vapour deposited) SiC fibres [48]; sintering [50]; hot-pressing [51,52] and in SiC fibre production [53]. A number of transformations in the literature are listed below with the proposed mechanism. Where additives have been made to the SiC these are also included.

1). Ground-up 2H SiC flakes transform to 3C at low temperatures:

2H -----> 3C at 400^{o}C;

a screw dislocation mechanism was proposed to account for this observation by the investigators [54].

2). The annealing of 2H single crystals leads to a sequence of transformations :

2H -------> 3C at 1400^{o}C -1600^{o}C ;

with subsequent annealing +1600^{o}C 3C ---------->6H.

When annealing is undertaken at an initially higher temperature:

2H -------> 'disordered' --------->6H at 1600^{o}C -2000^{o}C;

and apparently direct transformation occurs at +2000^{o}C:

2H --------> 6H at +2000^{o}C.

The investigators suggest that a mechanism involving stacking faults is operative [54].

3). During heating the following sequence of polytype changes were found [54]:

2H --- 1600^{o}C ---> 3C -----1900^{o}C---> 4H----2000^{o}C---->6H.

4). Annealing at +1500^{o}C leads to 2H-------->3C apparently via surface diffusion, and annealing at +2000^{o}C a mixture of polytypes 4H/15R ---------> 6H via surface diffusion [54].

5). Both hot pressed and pressureless sintered B, and C doped 3C SiC transformed via 'feather formation' (twinning) [51]:

3C---------> 6H + increasing amounts of 15R at 2060^{o}C - 2200^{o}C .

6). The pressureless sintering of 3C SiC with B and C additions leads to the retention of 3C to 2000^{o}C, followed by its transformation [52]:

3C ---------> 6H at +2000^{o}C.

7). Sintering 3C SiC with C and a little Al and B can allow 3C SiC to exist at 2100^{o}C with little transformation. Increasing the additions of Al and B leads [50] to:

3C ---------> 4H + a little 6H at 2100^{o}C.

8). The pressureless sintering of 3C SiC with less than 0.5wt%Al was reported to lead to no change at 2200^{o}C. With an Al content >1.5wt%:

3C---------->4H at 2200^{o}C according to [55].

9). Hot pressing 3C SiC with Al and Al_2O_3 additions results [52] in :

3C-------->4H with a little 6H at +1900^oC.

10). With 'high' Al_2O_3 + C additions :

3C--------> 4H with little 6H and 15R at 1950^oC-2000^oC;

and with 'low' Al_2O_3 and C levels the 3C SiC is reported [52] to be little transformed in the same temperature range.

11). During the production of "Nicalon^{TM}" fibres 3C SiC is formed from a mixture of SiC, C and amorphous SiO_2 at >1000^oC [53].

12). During the hot pressing of Al_4C_3 and Si powders (1800MPa) beta-SiC is reported to be produced in the temperature range 547^oC-572^oC along with Al or an Al-Si alloy [56].

13). During the reaction below, in which the solid phases are in a melt saturated in C and Si:

$Al_4C_3(s) + 3Si$ --------> $3SiC\ (s) + 4Al$ at 730^oC;

where the authors claim that both alpha- and beta-SiC are produced [57].

The transformations show that the polytypes generally transform in a sequence of increasing 'c' parameter, as in the sequence for the formation of the polytypes. It has been proposed that the nucleation of stacking faults in SiC leads to the wide temperature variations for the same reported transformations [54]. Layer displacement mechanisms have been suggested to account for the structural changes [54]. Beta-SiC appears to be produced in the low temperature reactions between non-SiC reactants. The beta-SiC cubic structure has been calculated to be the most stable thermodynamically below the decomposition temperature [40], and the literature suggests that this is at least the stable form at low temperatures [40] although the above transformations show some 3C to alpha changes below 2000^oC: the sensitivity of these transformations to impurities is also evident, and may complicate any attempts to generalise where information on impurities is lacking. 4H SiC stabilisation results from the Al, Al_2O_3 and C additions, possibly as a result of Al_2OC formation [52]. The 6H polytype has also been proposed as 'the' stable form of SiC [54]. The melting point of beta-SiC has been given as 2830^oC at 35 atmospheres [53] since the beta to alpha transformation is suppressed under an external pressure [43].

2.1.4 *SiC manufacture*

SiC is a synthetic product used industrially as an abrasive, and is produced in bulk by the carbothermic reduction of silica in the 'Acheson' resistance furnace [41,42]:

			2400-2500^oC	
SiO_2	+	C	---------->	SiC + CO(g)
99.5% pure silica sand		low sulphur petroleum coke	electric current	products

The above reaction is thermodynamically possible above 1000^oC [53]. The crude SiC produced for grit production undergoes a selection, and grading procedure: the highest purity grit is formed at the reactor core and is light green in colour which represents ~99.8%purity

[41]. As the purity declines the colour of the SiC alters, changing through dark-green at ~99.5%, to black at ~99.0% and grey at 90%: uncombined material is removed prior to purity selection, crushing and grading [41]. Other methods of bulk manufacture are currently at an experimental stage, for example the production of SiC powders by laser synthesis via gas phase reactions [58], producing high purity and ultra-fine powders for the manufacture of engineering ceramics [41]. The main methods of SiC fibre, and SiC whisker production have been reviewed and the structure and composition of these items are very sensitive to process variables [53]: the chemistry and properties are subject to rapid changes as the current commercially available product ranges are developed and expanded [1]; it is important to note that in general the description 'SiC' is often loosely used, and covers material that contains as little as 50wt%SiC [53]: the impurities and additives vary according to the product form and manufacturer, and can drastically affect chemical durability [42].

2.1.5 *SiC properties*

The following table of SiC properties is reproduced from [53]. The values correspond to fully dense polycrystalline beta-SiC, and were taken from several sources.

Table 2.1 Properties of beta-SiC [53]

Property	Value
Crystallography	Cubic (FCC), a=0.4360nm
Melting point	2830^{o}C (at 3.55MPa (35 atmospheres), decomposes at 101kPa (atmospheric pressure))
Density	3.21gcm^{-3}
Hardness	3100-3500 Knoop
Coefficient of thermal expansion	3.8 x 10^{-6} ^{o}C^{-1} (200^{o}C)
	5.8 x 10^{-6} ^{o}C^{-1} (1000^{o}C)
Thermal conductivity	0.25 W/cm^{o}C (200^{o}C)
	0.15 W/cm^{o}C (1000^{o}C)
Young's Modulus	450GPa (RT), 420GPa(1000^{o}C)
Poissons Ratio	0.17 (RT) , 0.18 (1000^{o}C)
Fracture toughness, K_{1C}	3 - 4.5MNm$^{-3/2}$

A more recent determination of the coefficient of thermal expansion of beta-SiC is given by [59].

2.2 The Al-Si system

2.2.1 *Al-Si phase diagram*

No compound forms in this simple eutectic system, figure 2.3, which is the basis of a technologically important class of Al casting alloys [60]. Up to 1.5at%Si dissolves in Al at the eutectic temperature 577+/-1^{o}C, and Si solubility decreases to 0.05at% Si at 300^{o}C [60]. Silicon takes up to 0.016 +/-0.003 at%Al into solution at the Si solidus retrograde point at

1190°C [60]. Splat-quenching can increase the solubility of Si in Al to 11+/-1at%Si [60]. The eutectic composition value 11.3at%Si is now considered to be obsolete, and has been replaced by 12.2at%Si (12.64wt%Si) [60].

2.2.2 *Aspects of Al-Si solidification*

The Al-Si eutectic has been the subject of recent TEM studies and some aspects of the variety of structures observed have been clarified [61]. The Al-Si eutectic is generally classified as irregular [62] and is an example of a faceting-non-faceting eutectic system. Several modes of eutectic growth in this system have been described [63,64]. During the growth of a 'flake' eutectic, single Si eutectic colonies are nucleated to form eutectic grains, in which the Al is polycrystalline: the Si leads the Al at the liquid melt interface (principally due to the assymetry of the phase diagram, and the subsequent difference in the equilibrium distribution coefficients for Al and Si [62]) and Al continuously re-nucleates on the Si. The Si grows by a TPRE (twin plane re-entrant edge) mechanism, and coupled eutectic growth is maintained by the continued branching of the Si flakes via various twinning mechanisms [61]. When rapidly cooled the Si is refined in accordance with the generally observed eutectic-spacing versus undercooling relationship: the constraints on Si growth imposed by its habit are reduced by a significant increase in the Si twin density [61].

Al-Si alloys are often 'modified' using additions of Na or Sr, which lead to the refinement of the Al-Si eutectic without the necessity for rapid cooling [61,62,65,66,67,68]. The modified eutectic appears optically to be the same as the quench modified structure, but the twin density is very much greater than in quench modification (at similar undercoolings), and the Si growth directions possible covers a wide range allowing almost co-planar Al-Si growth, and no necessity for Al re-nucleation [61].

Some discussion of primary Si is found in [65,67]. Primary Si can be observed in hypoeutectic, and eutectic alloys due to Si segregation to surfaces in a melt [11,69], and due to Si nucleation on primary AlP at a lower undercooling than for primary Al [70]: the P content of all commercial Al-Si alloys is greater than the eutectic Al-P composition [70].

2.3 The Al-C system

2.3.1 *Al-C phase equilibria*

The generally accepted form of the Al-C phase diagram is as shown in the computer calculated phase diagram in figure 2.4a [71], with the results of recent experimental determinations for comparison in figure 2.4b [72]. A eutectic occurs at ~655°C at a composition of approximately 0.02at%C according to [73] though the source of this data is not given. Experimental values of C solubilities in liquid Al are given in table 2.2 on the following page [74], though this data needs to be compared with that presented in figure 2.4b.

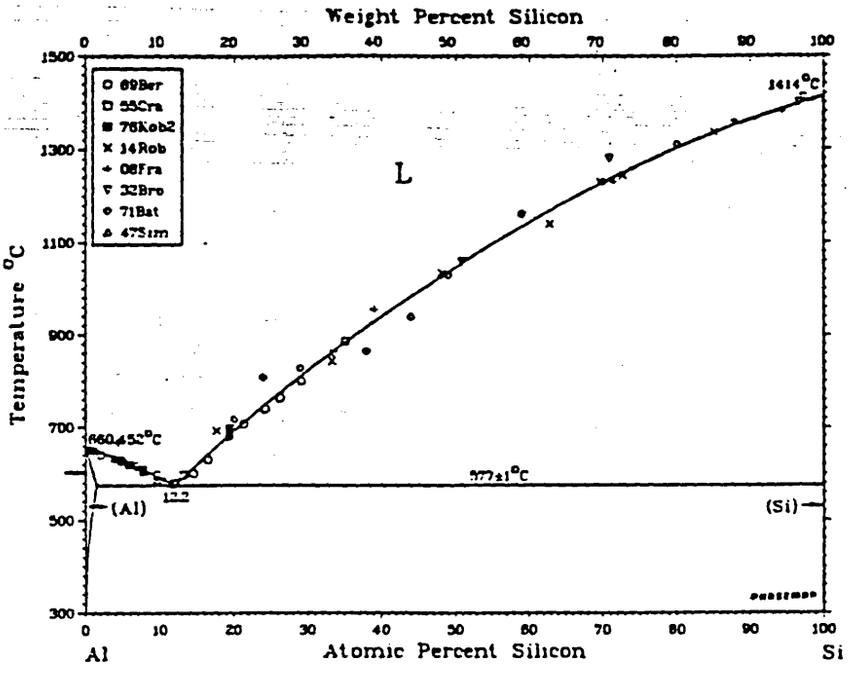
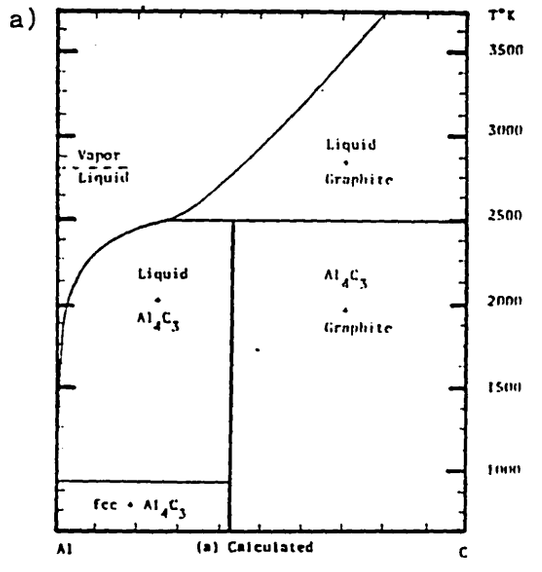


Figure 2.3 The Al-Si phase diagram, with selected liquidus data, according to |60|



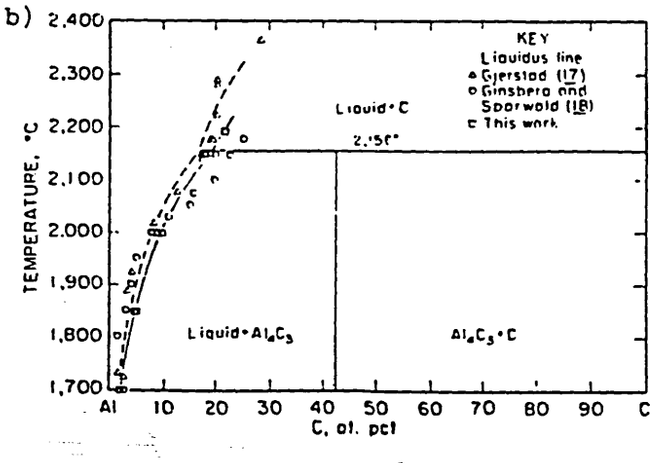


Figure 2.4 Al-C phase diagram:
a) computed |71|;
b) experimental data |72|.

Table 2.2 C solubilities in liquid Al [74]

T/ °C	C/wt%	T/°C	C/wt%
800	0.10	1800	0.9
1000	0.14	1850	1.7
1100	0.16	1900	2.2
1200	0.32	2000	4.2
		2050	7.4
		2100	9.4
		2180	12.9

A peritectic at 2050°C had been speculated to produce Al_2C_2 which decomposes peritectically to give Al_4C_3 at about 1700°C [74]. AlC was an alternative formula given for this compound [71]. Maximum C solubilities in solid Al variously determined as 0.015wt%C, and 0.02 - 0.04wt%C are considered to be too high [74]. Al can be expected to be nearly saturated in C from production: Al_4C_3 forms on the graphite anodes in the Hall-Heroult process through reaction with liquid Al [75]: Al_2O_3 at the anode-melt interface in the cryolite appears to inhibit this reaction [76].

2.3.2 *Al_4C_3 : structure and properties*

In accordance with the computed phase diagram and more recent experimental work, the Al_4C_3 phase is considered to be the only stable binary Al-C compound, although Al_2C_6 is reported to be formed by passing acetylene over Al at 450°C-500°C [77]. The structure of Al_4C_3 was determined in 1934 [78] showing that rhombohedral symmetry is exhibited by the phase ($R\bar{3}m$). Al_4C_3 is ionic and forms pale-yellow, non-conducting crystals which are reported to melt at 2200°C (sublime at 1800°C in a vacuo) [77]; melt at 2977K [79]; and decompose at 2223°C [71]. Bending tests on an Al_4C_3 sintered body gave bend-strengths of 152 MN/m^2 and 165MN/m^2 at RT and 1000°C respectively [79].

2.3.3 *Al_4C_3 chemistry and its role in composite degradation*

Discrete C^{4-} ions in the compound give rise to CH_4 (g) with less than 10%H_2 (g) on hydrolysis [77,80], and the action of dilute acids is similar [80]. According to [81] the reaction can be represented as;

$$Al_4C_3 + 12H_2O \text{ ----------> } 4Al(OH)_3 + 3CH_4 ;$$

and the hydroxide of Al is sparingly soluble in hot or cold water, but dissolves in acids and alkalis. A weight loss from a piece of hot-pressed Al_4C_3 immersed in cold water of only 2.8% after 100hours was recorded [79]. Pfeifer reports [82] that weight changes are a poor method for monitoring the corrosion of Al-graphite bonded in the solid-state at 500°C, but it was also found that Al_4C_3 was not the main corrosion path and that poor metal-metal consolidation and galvanic corrosion were dominant. Otani et al [83] do not mention Al_4C_3 in their corrosion study of SiC fibre reinforced CP Al produced by melt infiltration, and concentrate on the galvanic effects of intermetallics in the composite matrix in other matrix alloys studied. Bhagat et al [84] found that the corrosion behaviour of Ni coated graphite fibre-Al composites was superior to Al-graphite. Al_4C_3 dispersion hardened Al considered as an aerospace material

[85] shows good property retention at elevated temperatures, and good corrosion resistance is claimed [86] for similar materials produced by milling Al powders with carbon-black followed by hot-extrusion.

Al_4C_3 is recognised as an embrittling interfacial product in Al-graphite composites in which it forms above 400°C [87,88], and in Al-SiC composite systems above 500°C [89], though it is noted here that 'SiC' in commercial fibres often contains free carbon. Carbon diffuses from graphite into Al to form Al_4C_3 [87] at as low a temperature as 400°C [88]. In Al-graphite composites annealed for 100hours above 475°C (for HT graphite), and above 550°C (for HM graphite fibres) the carbide formed at the fibre-matrix interface was reported to lead to mechanical degradation: either the carbide itself was cracked with the subsequent propagation of the crack into the fibre, or notches were produced in the fibre surface due to dissolution [88]. Fibre composite systems with a brittle interface product have been modelled [90,91]. Alternative reports suggest that Al_4C_3 can be debonded from graphite fibres following the examination of pulled-out fibres [92]. The morphology of the Al_4C_3 as an interface reaction product has been described following SEM [69] and TEM [93] examinations of Al-graphite and Al-'SCS-coated' SiC fibre composites respectively (an SCS coating is largely composed of C).

2.4 The Al-C-Si system

2.4.1 *Al-C-Si phase equilibria*

The system has been given some recent attention due to its importance for composites [72,89,94], and has been the focus of some experimental investigations with respect to the carbothermic reduction of alumina [72]. The stable phase diagram is presented in figure 2.5 after [72]. Samples were prepared from high purity elements, which were partially reacted prior to the experiments.Isothermal sections at 2150°C and 2000°C were established [72]. Thermal analysis was used to locate the transformation temperatures on the Al_4C_3-SiC isopleth over the temperature range 1900°C-2300°C, and combined with the chemical and structural analysis of heat-treated and quenched samples [72] the isopleth was constructed: carbon was available in excess. Three ternary compounds Al_4SiC_4 [95,96,97], $2Al_4C_3.SiC$ [97] and $2SiC.Al_4C_3$ [98] in the system had been reported previously, but some uncertainty remains as to the existance of the $2SiC.Al_4C_3$ phase in the ternary system: some workers had reported it in the Al-B-C-Si system, but not in the Al-C-Si system [72]. However, $2SiC.Al_4C_3$ was reported to be stable above 1900°C, and decomposed to Al_4SiC_4 + SiC [98] on cooling. Synthesis of the $2Al_4C_3.SiC$ phase was achieved above 1600°C [72,97]. The solubility of C in Si, and C in Al was found in the temperature range 1700°C-2150°C for the binary equilibria [72]. DTA (differential thermal analysis) experiments performed to establish the four low temperature ternary reactions in the system which would occur below the Al-C eutectic (~660°C) were unsucessful: only high purity elements were used [72]. From the division of the base triangle [72] (figure 5.2b) Al-Si-SiC composites are seen to be stable at all temperatures below 577°C. The solubility range of C in solid Al has been predicted to be reduced by Si alloying (Mg, Mn

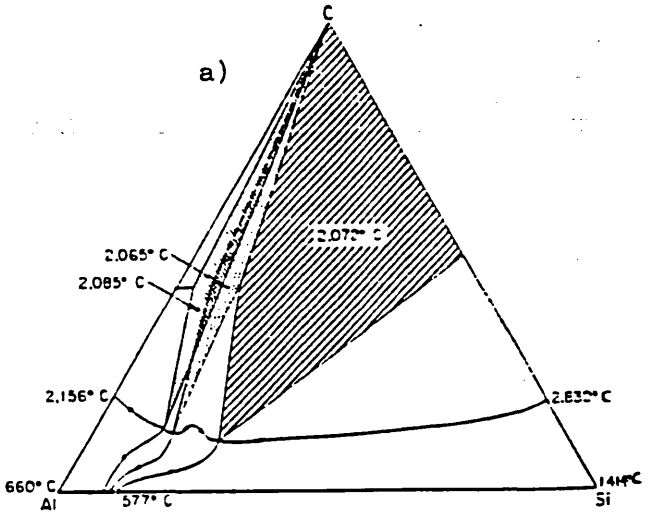
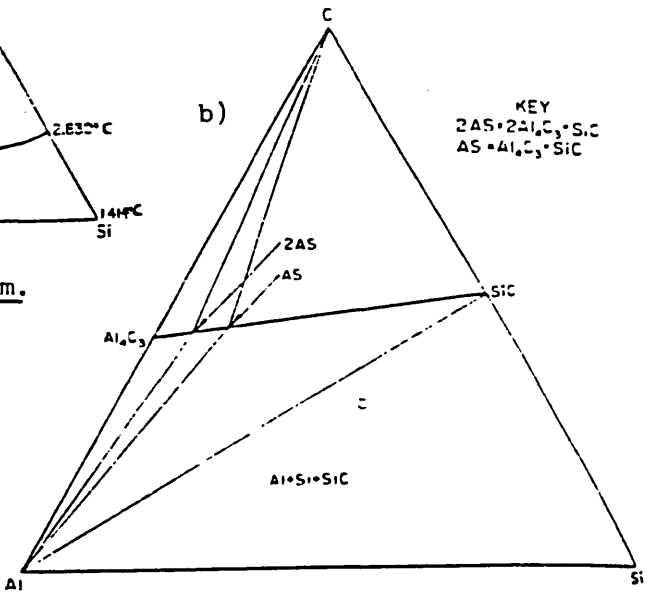


Figure 2.5 Al-C-Si phase diagram.

a) Liquidus projection with 3 ternary invariant reactions shown |72|

Figure 2.5

b) Division of the base triangle at low temperatures |72|.



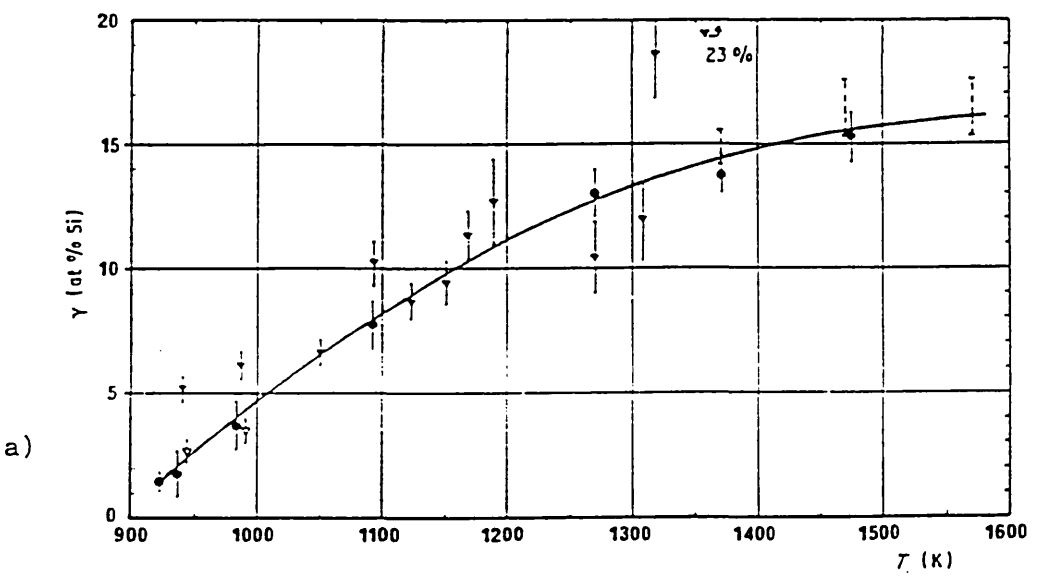
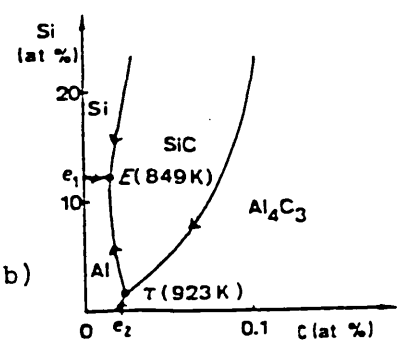


Figure 2.6
Experimental Al-C-Si phase diagram results from Viala et al.:

a) variation of the Si content of the liquid phase, in equilibrium with SiC and Al_4C_3, with temperature |94|;

b) liquidus projection |73|.



have the same effect, and Cr the reverse), following the use of pseudopotential models to calculate the heat of mixing [99]. Carbon activities were also calculated as a function of increasing Si content, and were found to increase [100]. Al solubility in SiC at 2200^{o}C has been found to be 1.0wt% by Al substituting for Si, dropping to 0.26wt% at 1800^{o}C , and the heat of solution of Al in SiC has been given as 147kJ/mole [55]. The heat of solution of neutral gaseous Al atoms in SiC has been determined as 57.4kcal/mole [101]. The activation energy for diffusion of Al in SiC has been given as 471kJ/mole, and the diffusion coefficient D_0 as 1.8cm^2/s, though two original sources were used for these figures [102]. A diffusivity for Al in SiC at 2200^{o}C of 5.6x10^{-14}cm^2/s has been reported [103].

Al_4SiC_4 thermodynamic data has been reported by [96] following the thermal decomposition of the phase studied in the temperature range 1150^{o}C-1500^{o}C. The compound was synthesised from the elements at 1620^{o}C by Barczak, as reported in [72]. The formation of Al_4SiC_4 from SiC and Al_4C_3 is reported above 1550^{o}C and the reaction gives Al_4SiC_4 alone above 1800^{o}C [95]. According to [73] Al_4SiC_4 can be produced by reacting either Al and SiC, or Al_4C_3 and SiC mixtures at temperatures above 1377^{o}C.

2.4.2 *Reactions at low temperatures at normal pressures*

The temperatures of concern to Al-SiC and Al-Si-C MMC producers are below normal Al-alloy melt superheat temperatures eg.<850^{o}C. According to [89,73] neither the ternary phase Al_4SiC_4 forms, or the other ternary phases reported in the Al-C-Si system form, until high temperatures are reached [72,94] ie. well above 850^{o}C. The system at low temperatures is discussed in terms of metastable equilibria [94]. The reaction generally observed between some liquid Al alloys and SiC is:

$4Al(l) + 3SiC(s) <====> Al_4C_3(s) + 3Si(l)$ ----------(2.1);

which goes to the right above the melting point of Al as the reaction product Si dissolves in the liquid Al [104]. Several studies have reported calculations to predict the extent of the reaction as a function of temperature [104,73,105,106], and experimental determinations of the Si content of the Al-C-Si liquid in equilibrium with SiC and Al_4C_3 have been presented, and the data is shown in figure 2.6a [94]. Prevention of the reaction (2.1) by pre-alloying the Al with Si has been widely reported, and a similar effect is predicted for Al-graphite though there appears to be little data on the reaction [69], except for the predictions on the C activity in solid Al-Si alloys made by Portnoi et al [69,100]. SiC formation has been reported in Al-Si-graphite composites in which Al_4C_3 has also formed [69]. It is claimed [73,57,94] that the reaction L + Al_4C_3 ------> Al + SiC is 'observed' in a DTA experiment ~10^{o}C (at ~650^{o}C) below the melting point of Al in the Al-Si-C system, and the interpretation of the DTA results infers that the reaction would have an infinite rate below the melting point of Al. It is also claimed that a reaction corresponding to L---> Al + Si + Al_4C_3 is observed at 576^{o}C [73,57,94] during the heating of powder mixtures in the DTA, the Al being of commercial purity in both instances: the attempts by [72] to detect the low temperature reactions was unsucessful: neither of the

temperatures on figure 2.6b have been shown to correspond to reactions in the ternary Al-Si-C system and no metallographic support for the claims of [73,57,94] was given. The corresponding liquidus has been presented by these authors [73] and is shown in figure 2.6b. The reported composition of the liquid which is apparently involved in the reaction at ~650^{o}C appears to be subject to larger errors than are cited [94]. The reports on the reaction (2.1) being reversible are with respect to the reaction between 'Nicalon' fibres and Al or Al-Si melts at 1000K , the fibres contain C, SiC, silicon oxy-carbides and silica [57]. It is claimed by [57] that the observations of [69] for SiC formation in the Al-Si-graphite system containing Al_4C_3 support their results.

2.4.3 *The effect of pressure on reactions at low temperatures*

Viala et al [56] studied the effect of temperature and pressure on the low temperature reaction (2.1) above and found that the reverse reaction occurs when powders of Si and Al_4C_3 are hot-pressed at 1800MPa producing solid Al and beta-SiC at 547^{o}C and 557^{o}C, and Al-Si liquid with beta-SiC at 572^{o}C: there was an unquantified uncertainty in the actual temperatures of the samples due to the experimental arrangement. Also it was found by these workers that the forward reaction did not occur at 552^{o}C when Al and SiC powders were hot-pressed at 2000MPa, but was observed at 572^{o}C [56]. On the basis of these results a high-pressure liquidus was proposed for temperatures between 800 and 1000K, with essentially the same features as in figure 2.6b [56]. Al-SiC whisker, and Al-Li-SiC whisker composites produced by pouring the melt at 800^{o}C onto a whisker preform at 550^{o}C and squeezing for 3 minutes, apparently showed increasing amounts of Al_4C_3 , Al_4SiC_4 and Al-Si as the pressure was increased from 32MPa to 132MPa according to [20].

2.4.4 *Reaction kinetics*

Still little data on the kinetics of reaction (2.1) exists. Iseki et al [104] reported that the reaction is faster for the smaller grain size powders (0.9 and 0.27microns compared with 7.9microns). Viala et al had presented limited kinetic results at two temperatures [73]. Lloyd et al [107,108] have also examined the reaction kinetics using a method by which the amount of Si evolved in the reaction is quantified by taking DTA liquidus temperature determinations, and converting them to the amount of Si evolved in the reaction (2.1) by reference to the appropriate alloy Al-Si-X equilibrium liquidus surface.

Choh and Oki [109] performed wetting experiments using the extent of Al and Al alloys coverage on polycrystalline beta-SiC discs as a function of time and temperature. The incubation times were recorded. A function was fitted to the wetting data based on an expression for the nucleation rate of the wetting reaction, and that the SiC coverage rate was

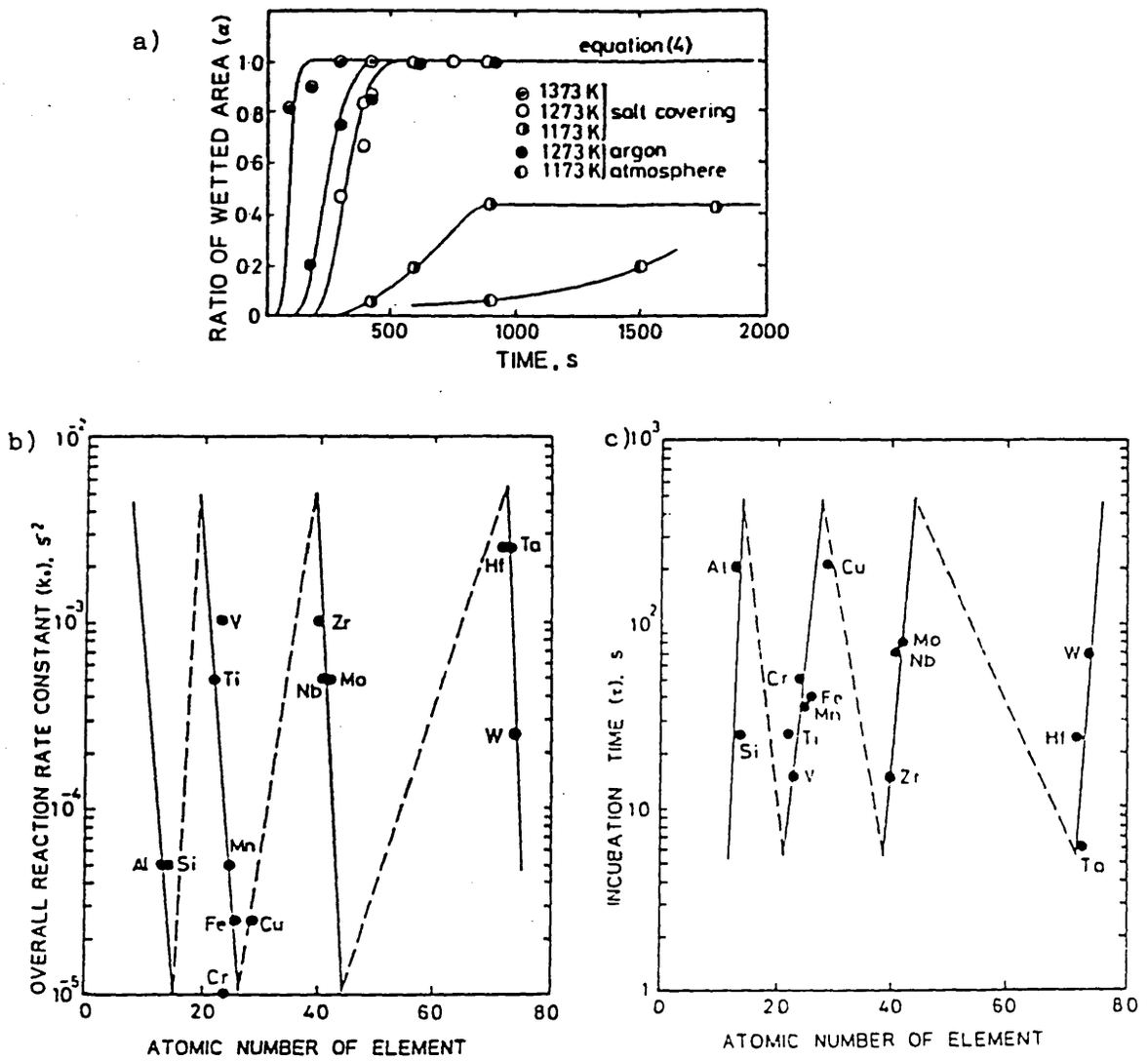


Figure 2.7 The kinetics of SiC wetting by Al, and Al alloys, from Choh and Oki |109|: a)time dependence of wettability of pure Al;b)overall reaction rate constant versus Z of alloying element at 1273K;c)incubation time versus Z at 1273K.

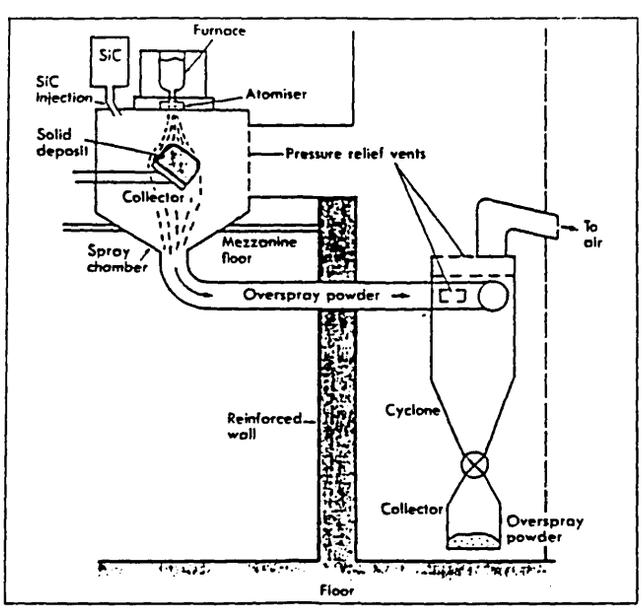


Figure 2.8
Osprey composite manufacturing plant |145|.

proportional to the area of uncovered SiC (1-*a*) which was expressed in the form:

$\ln [1/(1-a)] = ko.(t - t)^2$

where *a* is the extent of area covered; *t* is the incubation time/s; and ko the overall rate constant with units $time^{-2}$. The value of the exponent was determined from the wetting of SiC by Al over a range of temperatures as shown in figure 2.7a, from which the authors deduced that the nucleation rate is constant. Values of the rate constants and incubation times for a series of binary Al alloys are shown in figures 2.7b and 2.7c. The activation energy for the process was the same for Al, Al-Ti, Al-Zr and Al-V, and its value 327-335kJ/mol was correlated with the dissociation of SiC.

2.5 Interfaces and wetting

2.5.1 *SiC surfaces*

A general review of the type of surface presented by SiC and its impact on the production of SiC reinforced MMCs is given in [89]. SiC is well known for its oxidation resistance, and above a critical partial pressure of oxygen a passive oxide layer forms. In Al-SiC composite systems the SiO_2-Al interface is considered to be important if steps have not been taken to remove the oxide [89]. The passive oxidation of SiC concerns the reaction:-

$$SiC + 3O_2 \text{ --------> } SiO_2 + CO$$

which drastically reduces the oxidation rate [42,89], allowing the use of SiC to 1650^{o}C in oxidising atmospheres [42]. In reducing atmospheres the oxidation is active, and the kinetic barrier is not formed: the volatile oxide SiO is produced:-

$$SiC + O_2 \text{ ----------> } SiO(g) + CO(g).$$

There are a number of complex oxidation mechanisms which depend on the precise atmospheric conditions, and minor concentrations of H_2O, and H_2 play important roles [89,110]. Heating SiC in H_2 and H_2/argon mixtures has been reported as being effective in reducing the silica layer, and to remove free C and hydrocarbons from the SiC surface [111]. Impurities in SiC may lower the viscosity of the oxide, and enhance oxidation [89] above 1000^{o}C, as is the case with thermal-cycling via a spalling mechanism [42].

A 3 - 5 nm layer of amorphous silicon oxide, with characteristics very similar to SiO_2, exists on the Acheson process produced SiC powder surface as analysed in [111] forming the native oxide: the total oxygen content of such powders can be above 0.5wt% [111]. A model of the surface of polycrystalline SiC exposed to the atmosphere for one week included a 1.2nm layer of SiO_2-like oxide, with a 0.3nm layer of adsorbed hydrocarbons [112].

Pure SiC is attacked/etched appreciably by fused alkali carbonates, and alkali hydroxides eg. Na_2CO_3, NaOH and KOH [42]. The combustion products of fuels including Na salts and vanadium compounds are reported to attack SiC [42]. SiC is attacked by concentrated H_3PO_4 (+250^{o}C), but it is resistant to concentrated HF, although HF will remove the surface oxide at RT [42]. The corrosion data on SiC is often confused by the range of 'SiC' products in which

free C, Si and other impurities exist: otherwise 'pure' SiC exhibits excellent chemical durability [42]. Molten metals, including Al, are handled in a range of carbide, and carbon products due to the poor wettability of these materials [42,113]. Often the poor wetting of carbides or carbon is due to adsorbed gases, or oxides at the interface: wetting is a necessary prerequisite for liquid-metal/ceramic reaction [42].

2.5.2 *Solid Al -SiC interfaces*

Al-B composites fabricated at 800K incorporated SiC coated B fibres ('BORSIC') to sucessfully prevent the B fibres being attacked by the Al [114]. Bermudez [115,116] performed experiments using surface techniques (XPS =X-ray photoelectron spectroscopy, LEED =low energy electron diffraction, ELS= energy loss spectroscopy, and AES =Auger electron spectroscopy) on characterised single crystal alpha-SiC. Si and C terminated basal planes were examined. Al was evaporated onto the surfaces to different thicknesses and the samples were very briefly annealed between 350^{o}C and 1050^{o}C. During Al deposition, initially the Al is adsorbed as continuous monolayers, and only after a few layers have been deposited does the Al begin to coarsen locally which indicates that the Al-SiC bonding is strong: it is further suggested that XPS data shows that Al-Si interactions at the interface are strong enough to weaken Si-C bonds. Al_4C_3 was not found to form on the well ordered 0001 Si terminated surface with the thin Al films used, unless the surface was enriched in C or disordered by Ar^+ bombardment in which case the carbide was found to form at ~600^{o}C [115,116]. A study on the reaction between amorphous SiC and pure Al in the solid state was made [117], and the reaction kinetics followed by resistivity measurements were correlated with the dissolution of SiC: the results however tend to suggest that both free Si and free C were present in the deposited SiC which allowed Si to be precipitated at 400^{o}C, and Al_4C_3 at 480^{o}C. Li et al [118] have attempted to determine Al-SiC interface energies by by initially assuming actual Al-SiC bonding, and epitaxial relationships to simplify the calculations.

TEM studies of interfaces have revealed differences between the interfaces depending on the type of SiC and the production route. A 2124 Al alloy- SiC whisker powder product had 'amorphous' layers at the interface [19]; with a T6 treated 6061 Al alloy matix a polycrystalline layer of MgO was found, often as a 3nm continuous layer, or as individual MgO particles with Mg segregating to the interface generally [19,119] though much of the oxide was assumed to have formed following a consolidation process step above the liquidus. Gamma-Al_2O_3 has been found at Al-SiC interfaces [120]. The reduction of SiO_2 in solid Al above 400^{o}C forms alpha- and theta-alumina [89,121] and Si. Excessive oxide in PM alloys may enhance this effect, by forming $Me^{2+}O^{2-}$ complexes in the liquid (during a possible consolidation step) which can segregate to charged surfaces [113]. TEM studies on melt route produced Al-SiC composites show reaction products [38,122] ie. Al_4C_3, and features due to the use of coatings on the reinforcement phase [38]: apart from the various matrix phases at the interface as a result of segregation of alloying elements in the melt and the association of the reinforcement

phase with the last liquid to solidify, the Al-SiC interfaces appear to be very clean [38,122]: imaging of interface oxides on un-treated SiC in these materials has so far not been reported: attempts to observe diffraction effects from the narrow interface region which could be due to an interface phase have so far been unsucessful [122]. Iseki et al [104] found that Al and Al_4C_3 were oriented with respect to each other in samples taken from a SiC-Al couple heated to 1100°C:

(111)Al // (0001) Al_4C_3 with

[110]Al // [10$\bar{1}$0] Al_4C_3.

Reactions in model composites produced by the controlled deposition layers of Al or Si oxides on a substrate ie. SiC, representing the reinforcement, followed by matrix alloy deposition ie. Al, have been studied by TEM [123].

2.5.3 *Wetting of ceramics by Al alloys*

The formation of MMC interfaces is reviewed in [113], and more specifically for Al-SiC composites by [89]. Oxide present on the surface of the Al (unless the partial pressure of oxygen is less than 7.6×10^{-37} torr !) initially contacting the material to be wetted is also generally identified as a factor which will lead to poor wettability [124]. Al oxide is reported to dissolve into liquid Al at ~950°C [89,113,125], where non-wetting to wetting transitions are reported. Under high vacuum conditions the transition is reported to occur at a much lower temperature ~730°C [125]. Due to the silica, or silica-like oxide layer, on SiC surfaces [89,111,112] it is generally suggested that the wetting of SiC in composites would correspond to Al-SiO_2 wetting [89,113]. The reduction of SiO_2 in solid Al above 400°C forms alpha- and theta-alumina [89,113] and Si. Bulk SiO_2 is reduced by liquid Al in a series of redox reactions at the interface [121]: such reactions will be influenced by the external oxygen partial pressure and any oxygen in the melt [121,126,113] and include the formation of unstable sub-oxides which decompose on cooling, though extended layers of such reaction products would be unlikely to form from the narrow oxide layers at composite interfaces. Oxidized SiC is less readily wetted by liquid Al [125,127] than cleaner polished [125], or HF treated SiC surfaces [127], though oxides at the interface are recognised as acting as diffusion barriers on graphite and reduce the extent of Al_4C_3 formation [113]. That SiO_2 is wetted by Al at all is due to the net decrease in free energy as the Al spreads, reducing the fresh SiO_2 encountered [113,121]. In the absence of a reaction a sub-oxide monolayer can be expected to be formed eg. Al-O which provides electronic continuity between both the metal and oxide substrate [126].

Alloying elements which lower the surface energy segregate to the surfaces [113,124,128], in accordance with the Gibbs Adsorption Isotherm : these are Li, Mg, Si and Zn in Al. The alloying elements may promote bonding by allowing wetting due to a reduction in the liquid alloy surface energy, and/or by taking active part in chemical reactions at the interface. Such processes may involve the disruption of interface oxides eg. 'the Mg weakening of Al_2O_3' [113], or the formation of compounds by enhanced reaction of the liquid alloy with the reinforcement

phase itself. Li is reported as the most effective wetting agent, forming strong bonds between SiC and Al alloys [16,113]. Mg is often reported to be segregated to interfaces, where it can form MgO or spinel $MgAl_2O_4$, especially on Al_2O_3 fibres [113]. Several wetting studies on Al alloy-SiC have been carried out [109,125,129], and the wetting kinetics are controlled overall by the interface reaction [109,129] between Al and SiC.

The wetting behaviour of covalent carbides and graphite are similar [113]; the wettability of the carbides decreases as their heat of formation increases [124]. Strong carbide (Ti,V) and oxide formers (Cr) [109,124,130] can promote the wetting of SiC and graphite by Al. Often the poor wetting of carbides or carbon is due to adsorbed gases, or oxides at the interface. Si, Fe, Mn and groups 4a, 5a and 6a elements added to Al improved the wetting of SiC by Al [109]. Groups 1b to 6b elements, periods 4 to 6 show little wetting themselves with carbon; B, Al and Si wet carbon [113].

2.6 Composite processing involving a liquid metal alloy melt

2.6.1 *Discontinuously reinforced composites*

A recent review of the manufacture and processing of discontinuously reinforced MMCs has been made [131] in which the three main process routes begin with either molten metal, powder or deposition processing. The molten metal route, in which the ceramic particles are mixed into the melt by various methods [131,132], and then the composite slurry is solidified in a mould, is potentially very economic when near net-shape, bulk produced components are required. Some applications of cast metal matrix composites are given in [10,11]. The problems of initial wetting, unwanted melt-ceramic reactions, creating a homogeneous dispersion and controlling segregation can be largely overcome in the Al alloy-SiC systems by appropriate selection of the melt alloy, surface treatment of the ceramic filler and the use of 'good foundry practice' [133]. Processing with the matrix alloy in a semi-solid state has also been considered by a number of workers: either as a manufacturing route [134,135] or as a post-manufacturing forming process in which the ease of shaping and the novel microstructures produced are promising [136].

2.6.2 *Particles in liquid alloys*

The physical problems involved in incorporating particles into liquid metals have been discussed [124,11,12]: a chemical treatment of SiC particle surfaces to improve wetting has been developed [137]. The thermodynamics and the kinetics of the reaction between SiC and some molten Al alloys has been discussed in terms of melt superheats and melt holding times [36,38,107,108,133]. The gravity induced settlement of particles has also been examined [11,133], and improved particle dispersions created under conditions of microgravity have been reported [11]. Casting fluidity and the experimentally determined response of the microstructure to various cooling rates have had some coverage in the literature [11,38,133,138,139]. Problems encountered upon solidification of the melt-particulate systems

include the 'particle pushing' phenomena: this is readily explained on thermodynamic grounds by the reduction of the interfacial free-energy of the system [124] when insoluble particles in the melt are transferred into the solid. However, the necessary interface energy values are not readily available, and since solidification is usually carried out under non-equilibrium conditions a number of theoretical kinetic models have been formulated [124,139,140] along with some empirical kinetic models [11,12] which have been discussed critically in [124]: the empirical models are based on very little evidence [11,12,139]. No data had been presented to support the model presented by [140]. It is reported that both primary Si, and primary $NiAl_3$ capture graphite particles [11]. A Zn rich phase in Al-Zn alloys was found to reject SiC [141]. There appears to be no evidence that SiC particles are captured by Al under any conditions of solidification used in the literature. McCoy et al [138] suggest that B_4C particles are not pushed by Al, but no phase characterisation was done, and reactions do not seem to have been considered. The solidification of hypereutectic Al-Si alloys with dispersed graphite particles, and additions of Na and P have been examined [142].

2.6.3 *Spray co-deposition*

One MMC deposition route is based on the Osprey^{TM} Preform Process [143] in which a dense, segregation-free metal deposit is rapidly built-up from an atomised melt stream. The process overcomes many of the draw-backs in both the foundry based methods (the liquid-particle/whisker contact times are very short, and good dispersions are ach ved), and the powder route which is typically an expensive batch process with a large number of steps. The apparatus in figure 2.8 represents a modification of the Osprey process for the spray co-deposition of MMCs, a method which is now reaching commercial maturity with 100kg composite ingot production in 1988 [144], and 250kg ingots in 1990 [2]: the technology allows composites to be produced with alloy matrices ranging from Al-Li [9] and steel [13]. Early work by A.R.E Singer and co-workers included the addition of insoluble particles into the sprayed melt stream from the equipment developed for spray rolling [14] to produce composite strip. The Osprey process itself evolved from spray rolling [144], and some stastistical modelling of the process is being undertaken [145,146] in order that the heat content of the spray cone and the deposit be known under any set of operating conditions. In the Osprey process a stream of molten metal impinges on a moveable substrate [143]. By controlling the of the amount of heat in the spray, when molten droplets reach the substrate the heat content in the spray is such that only a thin layer of liquid/semi-solid alloy exists on the surface of the solidified deposit which therefore requires no containment, both leading to a reduction in macroscopic segregation and grain refinement as a consequence of the impingement of droplets onto the partially solidified liquid layer to produce nuclei (broken dendrites); rapid solidification takes place at the surface principally due to the gas stream, but the bulk of the preform can remain at high temperatures until the deposition is complete [143,146] by which stage some coarsening of the microstructure will have occurred.

Chapter III

Experimental Procedures

3.1 Introduction

In order to elucidate the mechanisms of the reaction between liquid aluminium alloys and silicon carbide various experimental techniques were employed.

Experimental work was focussed on the commercial purity aluminium particulate SiC system. These composites, and others which were less extensively studied, are described in section 3.2.

Both the starting materials, and the composite material heat treated to promote reaction (section 3.3) were subjected to the microstructural characterisation techniques generally employed, as described in section 3.4. Quantitative characterisation methods performed to measure the constitutional changes that occur following re-melting of the composite matrix are described in section 3.5.

Finally, a brief fractographic study is detailed in section 3.6. This study was undertaken to look at one aspect of the consequences of the formation of the interface product in the Al-SiC composite system.

3.2. Starting Materials

Composite material consisting of aluminium alloy matrices with dispersed SiC particulate filler were manufactured using modified Osprey^{TM} Preform Process equipment by ALCAN International Ltd.

The SiC particulate contained in these composites was a commmercially produced SiC grit product. The particulate of 13micron average particle size would have been the result of the crushing and grading of a SiC polycrystalline mass produced by the carbothermic reduction of silica. Details of the particle size distribution in these composites is given elsewhere [150].

Four matrix alloys were examined ,though the work was concentrated on a commercial purity (CP.) aluminium (ALCAN 2S) matrix composite which was supplied both as-sprayed (MH87-S) and hot-extruded (MH85-S). The other matrix alloys were CP.Al-12wt%Si ,CP.Al-19wt%Si ,and LM13. These three casting alloys were supplied combined with SiC particles, as slices of as-sprayed composite preform. Further details are given in tables 3.1, and 3.2.

LM13, which was apparently from the same batch of ingots used to produce the composite, was also supplied for comparison with the LM13 + SiC composite matrix.

3.3 Heat treatments

Heat treatments of the MMCs were generally carried out above the matrix alloy liquidus at various superheats to temperatures from 670°C to 1100°C ,in order to promote reaction between the matrix alloy and the SiC filler.

3.3.1 *Initial heat treatments*

An initial set of heat treatments was carried out to provide samples for the first attempt at an evaluation of the kinetics of the liquid aluminium-silicon carbide interaction as outlined in sections 3.5.1 to 3.5.9. These heat treatments, performed on MH87-S, are tabulated in table 3.3.

Samples, typically 1.5 - 3g, were surface cleaned by filing followed by degreasing in methanol, and heat treated in air in the hot zone of a tube furnace. Samples were either cooled in their container (alumina boat or crucible) on the bench (AC) or dropped into a water bath at RT (WQ). If the conditions of the heat treatment led to unacceptable oxidation (determined by metallography), samples were held in alumina boats which were encapsulated within argon filled silica ampules. Figure 3.1 illustrates two time - temperature regimes representing the conditions under which air or argon atmospheres were used. LM13 based composite (Mg containing) was treated more cautiously than the Al or Al-Si alloys. With some borderline cases, as far as the selection of an atmosphere was concerned, a larger sample was simply employed to offset oxidation effects.

In order to estimate the heat-up time (see table 3.3) ie. the time to reach the heat treatment temperature following sample insertion into the hot -zone of the pre-heated furnace (typically of the horizontal tube type) a thermocouple was inserted into samples of Al-SiC composite. A 1mm diameter hole was drilled into the composite , the hole was filled with an alumina slurry and the junction of a K-type (chromel-alumel) thermocouple was inserted. This enabled the sample temperature to be closely monitored.

3.3.2 *Synthesis of the spray-cast microstructure*

Samples of approximately 1g of 202-19 composite material were re-melted at 750°C. The samples were removed from their containers and directly dropped onto a cast iron plate (~6mm thick) from a height of about 1m. Splat material was cut into approximately 1cm^2 pieces and fixed to the end of a thermocouple, and inserted into a pre-heated tube furnace at 550°C or set to a temperature a few degrees Celsius above the Al-Si equilibrium eutectic temperature of 577°C eg. at 578+/-3°C and 580+/-3°C . The attached thermocouple allowed the heat treatment to be closely monitored.

Table 3.1 Matrix alloy compositions

Element	ALCAN 2S wt% element [147]	Element	LM13 wt% element [148]	MH35-L matrix /wt% [149]
Al	99.0min	Cu	0.7 - 1.5	0.98
Si	0.5max	Mg	0.8 - 1.5	1.00
Fe	0.7max	Si	10 - 13	10.80
Mn	0.1max	Fe	1.0max	0.57
Cu	0.1max	Mn	0.5max	0.32
Zn	0.1max	Ni	1.5max	0.92
Others	1.0max	Zn	0.5max	0.19
		Pb	0.1max	0.02
		Sn	0.1max	0.02
		Ti	0.2max	0.02
		Al	Remainder	85.16

Table 3.2 Composite details

Cast Designation	Matrix alloy	Experimental estimate of vol%SiC +/- σ_{n-1} (see table 4.6)	Number of estimates n
MH87-S	2S	10.5 +/- 0.3	4
MH85-S	2S	12.6 +/- 0.2	2
MH35-L	LM13	18 - 20*	-
200-12	CP. Al-12wt%Si	14.1 +/- 0.8	2
202-19	CP.Al-19wt%Si	13.9 +/- 3.17	2

*Supplier's communicated estimate.

Table 3.3 Initial set of 'isothermal' re-melts

	Temperature /°C		
	672+/-3	800+/-3	1000+/-5
Nominal 'isothermal' re-melt time/ minutes	10 30 100 1000 10 000	10 - 100 1000 10 000	10 - 100 1000 10 000
Representative time to reach temperature /minutes	~14	~6.7	Not evaluated

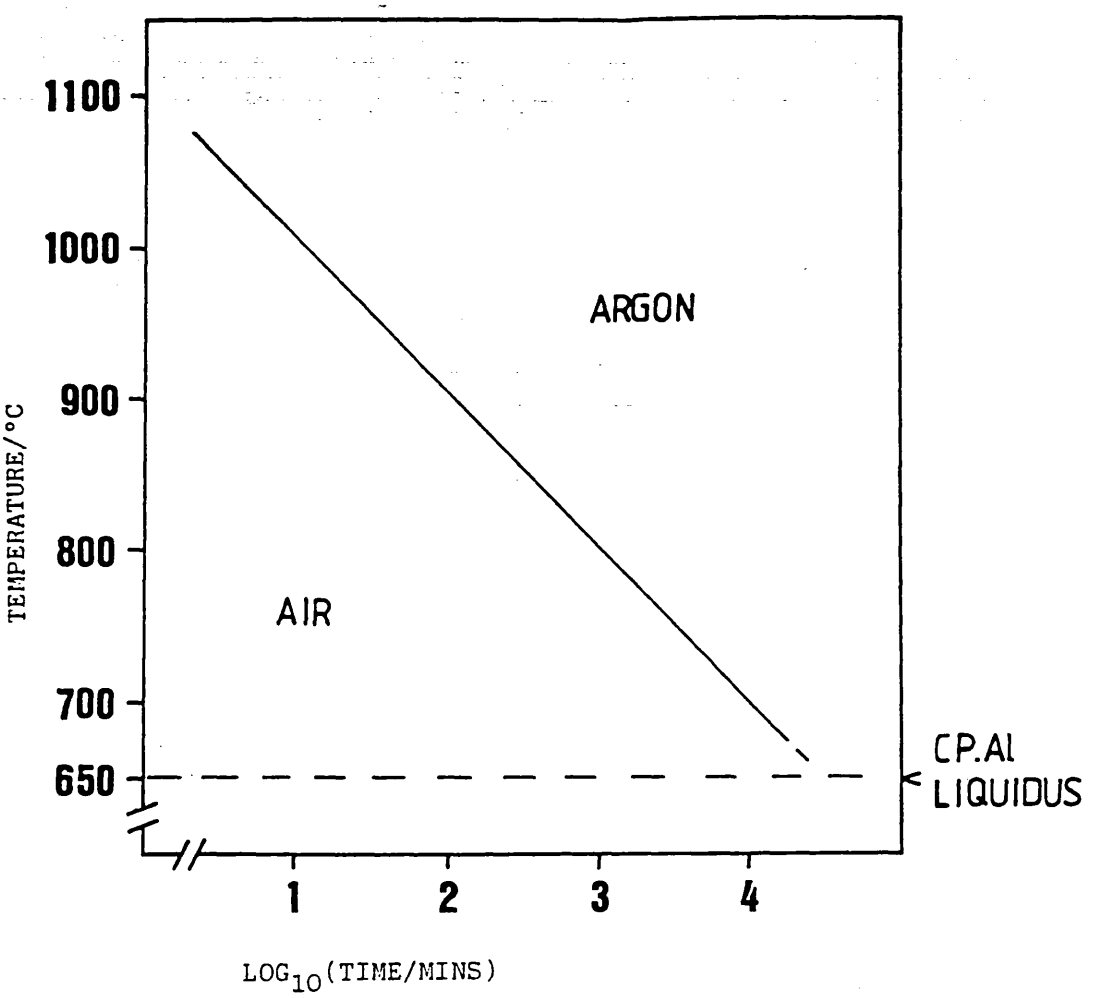


FIGURE 3.1 Use of a protective atmosphere during composite re-melts for samples of mass ≅ 1.5g

Table 3.4 Thermal analysis of bulk samples

Temperature Tiso/ °C (+/-3)	Sample	Heating range/ method	Heating rate on approach to initial melting/ °C/min	Initial melting arrest Tm/ °C	Time to cover (Tiso-1) -Tm/ min	Average eutectic arrest / °C +/-σ_{n-1}
672	#4	RT-(Tiso-1)	~30	652.5	2.8	582.0+/-4.3
	#5	/Natural	~30	653.0	"	585.6+/-1.9
715		500-(Tiso-1)	15+/-1	667.3*	2.25	582.4+/-1.6
760		/Heated	15.5+/-1	657.1	4.33	580.8+/-0.6
800		with	19+/-1	658.6	6.25	580.4+/-1.3
850	#1	furnace	19.5+/-1	659.3	9.0	583.7+/-0.6
850	#2		20+/-1	655.8	8.96	581.2+/-0.4

*Thermocouple repositioned prior to 3rd heating.

Samples of both the splat, and heat treated splat material were examined optically following polishing as described in section 3.4.1. These were compared with the as-sprayed Al-19Si-SiC (202-19) composite microstructure.

Note: molten material was also splat quenched when a water quench was inappropriate. Non-composite, or low viscosity MMC material (eg. re-melted 200-12, 202-19) tended to expand as a result of bubble formation, yielding a very porous sample upon water quenching which made specimen preparation difficult.

3.3.3 *Arc-melting*

In an attempt to establish in which phase field primary separation occured for the composite composition, all the SiC was to be taken into solution in the liquid state and the solidification products characterised by X-ray diffraction, optical microscopy, SEM (scanning electron microscopy), and EDS (energy dispersive X-ray spectroscopy).

A sample of CP Al-SiC (MH87-S) was cleaned in NaOH(aq), weighed, and and placed in the hearth of an electric arc melter made by the Materials Research Corporation, Orangeburg ,New York. The sample was melted under argon (1/3 atm.) by an arc struck from a W electrode. A Ti "O_2 getter" was employed. The arc current was taken to 180A on the sample. A total melting time of ~5.5 minutes was followed by quenching onto the water cooled Cu hearth of the melter.

3.4 Microstructural characterisation

3.4.1 *Metallographic preparation*

Samples were sectioned with a hacksaw, rough ground on SiC papers and hot mounted in Bakelite. Samples were then ground through 240,400 and 800 grade SiC papers with water lubrication.

The first polishing stage involved a 6 micron diamond polish on a low relief, napless cloth (TEXMET). This was performed under the maximum load obtainable from a Metaserv Auto-Pol polishing unit (carrying only two samples at a time). This stage took typically 2 - 3 minutes to remove SiC picked-up from the grinding papers, but the time was varied depending on the matrix hardness, increasing polishing times for the softer matrix conditions.

An ultrasonic bath was used to clean-out porosity prior to the final polishing stage, which involved the lapping of the sample by hand on a napped cloth (MICROCLOTH or METCLOTH) carrying colloidal SiO_2 made-up with distilled water. The lapping duration depended on the required results: longer lapping gives some SiC relief but removes 6 micron diamond damage and eliminates SiO_2 particle "pick-up" which tends to occur at SiC- soft matrix interfaces. However, the prolonged lapping of the softer matrices leads to the gradual incorporation of

SiO_2 particles into the matrix surface. Prolonged exposure to the colloid also tends to have a mild etching effect on some of the intermetallics phases in the alloys studied.

It was necessary to vacuum desiccate polished samples to preserve Al_4C_3, where present, from hydrolysis. The hydrolysis of the carbide was useful as a recognition-identification aid when allowed to procede to a controlled extent ,except that some confusion with hygroscopic oxides may occur. Samples were generally examined by optical microscopy using a Vickers Photoplan microscope coupled to a 35mm camera and an automatic exposure unit. Samples were examined unetched. Etching in 0.5HF(aq) was performed to aid matrix intermetallic identification, and to enhance the contrast in secondary electron images of the Al-Si phases where appropriate.

3.4.2 *Deep etching*

In order to extract further information on the morphology of the aluminium carbide as an interface product, deep etching was performed, involving the prolonged electropolishing of samples of re-melted and as-sprayed CP Al-SiC composite.

Two sets of heat treated samples were examined: the initial set of 672^{o}C heat treated samples in an AC condition, and a series of samples given short heat treatments in an attempt to produce small amounts of reaction product which might be characterised more easily, the aluminium carbide then being in a less cluttered environment.

Samples were sectioned and mechanically polished (3.4.1). These samples were then electropolished in methanol plus 30vol% of bench dilute (70vol%) nitric acid, with an applied potential of 20V and a dissolution current of ~0.5A (the exposed sample area was ~0.5cm^2) at -20^{o}C or less: an effectively non-aqueous electrolyte was used to preserve the aluminium carbide [69]. A high electrolyte stirring rate was employed. After several minutes had elapsed, and the samples were visibly well over-etched, the samples were washed in methanol and then baked at ~80^{o}C prior to gold coating, and insertion into a JEOL JSM T200 or JSM T220A SEM. Atmospheric exposure of the samples was kept to a minimum.

3.4.3 *Thin foil preparation*

Thin foils were prepared in order to provide detailed microstructural data on reaction product nucleation sites, product phase continuity, morphology and crystallographic information eg. SiC-Al_4C_3 orientation relationships. This information could be correlated with the kinetic data collected (section 3.5).

Slices of material for thin foils were ground on SiC papers on a water cooled grinding wheel to 0.2 - 0.3mm thickness from which 3mm diameter discs were electrodischarge machined. The discs were further ground to ~150 micron thick on 1200 grade SiC paper cooled with water.

Discs were then reduced to 80 - 100 micron from one side on a DIMPLER^{TM} Model D500 built by VCR Group, San Francisco, CA. Samples were then dimpled from the opposite side to leave a 10 - 20 micron thickness of material at the centre. A 3 micron diamond slurry alone was used; no polishing stages were incorporated.

The dimpled discs were thinned in a Gatan Duel Ion Mill Model 600. Argon fed gun pairs were operated at 6kV and with a 0.5mA total gun current: each gun was used with an incidence angle of 8^{o} to the horizontal.

Foils were examined in a Philips EM301 TEM and a JEOL 120CX Temscan, both operated at 100kV. One sample was examined in an AEI EM7 operated at 500kV. Multiple ion thinning was used to extend the total area examined. Prior to examination foils kept vacuum desiccated were briefly ion milled to remove oxide, and possible hydrolysis products in aluminium carbide containing foils in cases where any hydrolysis had only affected the aluminium carbide surface.

3.4.4 *Powder for XRD (X-ray diffraction) examination*

X-ray diffraction was used to identify phases in powder samples. An Elliot X-Ray Diffractometer was used operated with a Cu anode excited by a 40kV, 30mA electron beam.

Dissolution of the bulk aluminium matrix was performed electrolytically as in 3.4.2 to concentrate the insoluble constituents, and to simplify the diffractometer output. Reference was made to the ASTM Powder Diffraction File to identify phases where possible.

3.4.5 *EPMA (electron probe microanalysis)*

Electron probe microanalysis was used to provide chemical data to aid the identification of intermetallics in the alloys, especially where polishing and etching (typically with 0.5HF(aq)) and optical examination was inadequate.

A 20kV probe was used on plane polished samples in a JEOL JSM-35 SEM with a LINKS SYSTEMS EDS (energy dispersive spectroscopy) detector, and energy spectrum analysis computer software by which means ZAF corrections were applied. A cobalt standard was employed together with stored, elemental peak profiles.

3.5 Quantitative kinetic evaluation

In an attempt to quantify the extent of the reaction :

$$4\,Al(l) + 3SiC(s) \text{ --------> } Al_4C_3(s) + 3Si(l)$$

following composite matrix melting several methods were tried. In each case, to estimate the volume fraction of Al_4C_3 at room temperature, conversions needed to be made from the

measured quantities based on assumptions outlined in the description of the results given in sub-section 4.8.3.

3.5.1 *Area fraction of primary aluminium in AC samples*

Plane polished samples of heat treated material (see table 3.3 for the conditions) in an AC condition were photomicrographed at x50 on 35mm black and white negative film. Typically ten regions were selected for each sample to both cover a representative sample area across the cast, and to avoid excessive porosity.Enlargements x9 linear were made to provide prints 10"x8". Tracings were made of the Al dendrites, and porosity; both regions of the tracing were then cut-out; the porosity being discarded.

For each print both the dendrite cut-outs, and the rest of the tracing paper were weighed. Then the area fraction of the dendrites is given by:-

$$\text{Area fraction of aluminium dendrites} = \frac{\text{Area of dendrites}}{\text{Total area examined}} = \frac{\{\text{Mass of dendrite cut-outs / MOPPUA}\}}{\{\text{Total mass of tracing / MOPPUA}\}}$$

where the MOPPUA is the mass of the tracing paper per unit area. Approximately 2.35mm^2 of each real cast section was analysed in this way ie. typically 5% or less of the sectioned area examined.

3.5.2 *Area fraction of primary aluminium in WQ samples*

Samples of MH87-S which were re-melted and held at 800^{o}C for nominally 10, 100, 1000 and 10 000 minutes (as in table 3.3) and AC were then re-melted at a low superheat ~670^{o}C for ten minutes, and WQ into a water bath at RT. Typically five areas of the quenched matrix, avoiding both porosity and particles, were photomicrographed at x100. Prints were made at 10"x8" , and dendrites were cut-out directly from the prints. Any particles or pores were discarded. The dendrites and the interdendritic phases were weighed separately. The weighings yield area fractions of dendrites and eutectic as for 3.5.1.

3.5.3 *Area fraction of impurity intermetallic phases in AC samples*

Samples that were re-melted and held at 672^{o}C for nominally 10, 30 and 100 minutes ,and air cooled were prepared for metallographic examination in the SEM. Five areas of each sample section were photomicrographed at x500 in both SEI (secondary electron image) and BEI (backscattered electron image) modes in the JEOL JSM T200 SEM. These image pairs were used to eliminate the porosity highlighted in the SEI images, and to provide contrasty images of the high atomic number element containing constituents in the BEI mode. Each pair of images were individually projected with a darkroom enlarger onto an A4 tracing paper sheet, and sketched, with the porosity and intermetallics being differentiated. The pores and the

intermetallics were then cut-out; the porosity being discarded. The intermetallics and matrix (including Al-Si-SiC and Al_4C_3 combined) were each weighed as before, and the area fractions calculated as in 3.5.1.

3.5.4 *Mass fraction of SiC in preform materials*

It was necessary to find the mass fractions of SiC in the MMCs in order to characterise the initial state of the composites: the mass fractions being converted into volume fractions.

Two general approaches were taken depending on the matrix composition.

Accurately weighed (+/- 0.0002g) 1 -1.5g bulk samples of MMC with a CP Al matrix could be readily and rapidly dissolved in excess hot 2M NaOH(aq). The residue was washed with distilled water and treated with bench HCl (35vol%) to remove Fe based impurities. This was followed by further washing until the liquor was neutral.

The earliest assessments on MH87-S were made without the HCl treatment. The washing process was either carried out in a beaker with numerous decantings/syphonings, or during gravity filtration. Whatman 54 filter papers were used which were dried in the same manner before and after use for weighing purposes. All necessary weighings were carried out for mass fraction determination.

Matrix alloys with free-silicon present were treated with a mixture of acids in a process outlined in figure 3.2.The chemical process was that determined by B.Kujur *et al* [151]. The Al-12Si-SiC and Al-19Si-SiC MMCs were made into turnings from radially selected rods (radial with respect to the preform which was cylindrical and showed gross radial SiC segregation with concentric bands of alternating high, and low SiC volume fraction occurring on a scale of 3 - 5mm) to provide material for an averaged SiC volume fraction in these early experimental spray-casts. The residue was collected by filtration.

3.5.5 *Mass fraction of SiC following re-melting*

A brief attempt was made to follow the reaction kinetics via the direct measurement of the mass fraction of the residual SiC.

Rectangular rods ~6mm x 6mm x 40mm of CP.Al + SiC (MH85-S)were re-melted in air at 800^{o}C for 15, 100, and 1000 minutes, and at 672^{o}C for 1000 minutes. Following heat treatment the oxide scale was filed away, and clean turnings taken from each sample, and from MH85-S itself. The turnings were immediately vacuum desiccated following collection since aluminium carbide would be expected to be present , and some of its hydrolysis products might not readily dissolve.

Figure 3.2 Route for SiC particle extraction from free-Si containing Al matrix alloys: after Kujur et al [151].

Apparatus	*Route*	*Notes*
Principle Reaction Vessel	Acid mixture in vessel	12.6vol%H_2SO_4 of 98%conc. +20vol%HCl of 35%conc. +20vol%HNO_3 of 70% conc. +47.4vol% H_2O distilled.
	Add known mass of turnings	
	Add acid mixture to excess	Warm to initiate if necessary
	Dissolve turnings overnight	Exothermic reaction. Effervescence.
	Add excess 30wt%NaOH(aq) whilst stirring	Heavy ppt thrown and dissolved.
	Add excess fresh mixture 2vols HCl:1volHNO_3 whilst stirring	Bench conc. reagents as above. Heavy ppt thrown and dissolved.
Vacuum Filtration or Gravity Filtration	Filter reaction vessel contents	
	Wash filtrate in excess water	Distilled water throughout procedure.
	5wt%NaOH(aq) wash	
	Wash filtrate in excess water	
	5vol%HCl(aq) wash	
	Wash filtrate in excess water to neutrality	
	Wash filtrate in absolute alcohol	Drying aid
	Dry filtrate and filter	

Following the dissolution process the washed residue was collected on a filter of a known dry mass, dried, and weighed (see figure 3.2). The result of a vacuum filtration was a fairly solid mat. Whatman GF/F glass microfibre filters were used which had a claimed 98% retention for 0.7micron particles.

Samples of residue were examined in the SEM in the SEI mode following the completion of weighings. The residue of the sample heat treated 1000 minutes at 800^{o}C was separated ultrasonically into distilled water and dried - unfortunately filter fibre debris appears to have been included with the SiC upon examination. The powder was glued to a conducting block, dried and Au coated.

3.5.6 *Quantitative energy dispersive X-ray spectroscopy (EDS) of the MMC matrix following re-melting and WQ*

During the course of the principal reaction studied the amount of silicon in the matrix will increase.

Water quenched samples corresponding to the initial set of heat treatments (refer to Table 3.3) were plane polished and carbon coated: care was taken to ensure that the samples could be mounted for analysis with the electron beam normal to the polished section. A JEOL JSM-35 SEM, operated at 25kV, with a LINKS SYSTEMS EDS, was utilised.

The largest areas of the quenched matrix, devoid of all particles, were scanned to produce X-rays from areas large enough to be representative of the matrix composition for a total live time of 100s. The best 10 - 14 analysis results (those results taken from the largest areas, and with weight totals of within 100+/-2wt%) for each condition, from different areas were selected. The scatter in the results suggests that there is little scatter in the apparent Si content across the quenched samples: the scatter in the analysis being of the order of that inherent in the EDS technique (2% relative).

These results were, however, obtained following a ZAF (atomic number-absorption-fluorescence) correction, which is inappropriate for a two phase structure like the Al-Si eutectic in which the Si K_{α} X-rays excited by the electron beam are assumed to strongly fluoresce the aluminium. However, since both elements are present as almost pure elements, many characteristic Si X-rays escape the sample without fluorescing aluminium. The major error will result from Si X-rays generated in, and escaping directly from the silicon exposed at the sample surface. As the silicon particle size is reduced relative to the size of the excitation volume then the estimate of the silicon content following ZAF correction becomes closer to the actual value. Generally the result is an overestimate of the silicon content.

3.5.7 *Calibration alloys for EDS*

To provide a correction for the above Si content overestimate, a series of calibration alloys were prepared of known compositions of 2wt%Si, 5.5wt%Si, 8.5wt%Si and 12wt%Si with aluminium, and with similar silicon particle sizes to those of the water quenched re-melted MMC material. Chill casts provided a range of microstructural scales, so the standards were splat quenched which provided relatively large regions of uniform microstructure that could be characterised. Such material was characterised crudely by optical and SEM techniques eg. secondary dendrite arm spacings were estimated. The eutectic was typically unresolved optically.

Samples of the splat alloys were mounted, plane polished and areas were analysed as described above. A curve of nominally known alloy composition *versus* apparent as-analysed ZAF corrected composition was thereby produced. Although it would have been desireable, the pieces of sample analysed were not subjected to an independent check on the compositions ("wet" chemical analysis for example).

3.5.8 *Thermal analysis methods: general remarks*

D.J.Lloyd and I.Jin [109] used differential scanning calorimetry (DSC) to monitor the liquidus temperature change for samples of re-melted 6061 + 20vol%SiC; the liquidus temperature determined being directly converted into the new matrix composition via the equilibrium phase diagram of the matrix alloy. In this manner kinetic data could be accrued.

In this study differential thermal analysis (DTA) was used to determine the liquidus temperature change of the CP.Al + SiC matrix following re-melting. The DTA method involves heating or cooling an enclosure (DTA cell), often with a controlled atmosphere, in which the sample under study and an inert reference material are held and experience equivalent conditions [153]. The temperature of the sample, and the temperature difference between the sample and the reference, are recorded as a function of temperature and/or time. The DTA cell is heated/cooled at a predetermined rate. When an exothermic or an endothermic reaction occurs in the sample a temperature difference between it, and the reference is recorded leading to a deviation from the baseline of the temperature difference *versus* sample temperature curve (the baseline being the hypothetical DTA response without the transformation induced DTA peaks). The precise shape, and position of the peaks about the equilibrium transformation temperature depends on the nature of the sample (egs. powder, solid, geometry, mass), and the selected experimental conditions (egs. heating/cooling rate, atmosphere).

In this study a Stanton Redcroft STA-780 Series machine was used. The time, sample temperature, and DTA ie. the temperature difference in mV (which is amplified) are recorded, whilst a sample is being heated/cooled in the DTA apparatus, on magnetic tape via a data

aquisition unit (IEEE-DAU) which acts as an interface with the computer storage/processing system. The data is then transferred to the user's magnetic computer disc for analysis using a commercial software package.

Generally, heating curves alone were recorded when it was found that the samples would need to be heated to ~780^{o}C to record a cooling curve. Samples re-melted at temperatures <780^{o}C or for very short times generally would undergo further reaction during the course of the DTA experiment making the heating and cooling peaks incomparable.

3.5.9 *Differential thermal analysis (DTA) of the initial set of heat treated samples*

Portions of MMC samples which had been re-melted (see Table 3.3) were ground to produce ~3mm diameter coupons with a finely ground base (1200 grit SiC paper) to contact the flat bottom of an alumina DTA crucible. The samples, typically 20 - 55mg each, were heated in a crucible at 20^{o}Cmin^{-1} from 450^{o}C to 750^{o}C in the DTA cell with a calcined alumina powder reference of the same mass. A flowing argon atmosphere, or static air, were used during the DTA runs causing no apparent difference to the recorded peaks.

During the course of this study a series of MH85-S (CP.Al + SiC) samples of various masses were run and the DTA peak temperatures plotted as a function of mass at heating rates of 20^{o}Cmin^{-1} and 3^{o}Cmin^{-1}. The liquidus peak temperatures of the re-melted samples were compared with the estimates of the original matrix liquidus recorded under similar dynamic conditions.

Initially, large samples 20mg - 55mg were used to provide repesentative samples of the original casts. However the peak temperatures were not always obtainable. An alternative method to obtain a temperature was to take the point at which the thermal effect starts to decay linearly back to the baseline. This point is at approximately the "end of the thermal effect in the sample". This point was taken to correspond with the peak maximum when sharp peaks were obtained eg. for a reaction taking place over a narrow temperature range and/or for small sample masses <15mg.

The conflicting requirements - a large sample mass for a single representative result for a sample condition, and a reduced sample mass which provided sharper, separated peaks, led to the adoption of sample sizes of 9mg - 15mg (also largely as a consequence of the small mass of the parent sample) as in the experiments outlined below .

3.5.10 *Differential thermal analysis (DTA) of rapidly heated re-melted samples*

By reducing the sample size of the heat treated material the samples could be heated to the required temperatures in short times (from the melting point) eg. from ~7s to 13s to superheats

at 672^{o}C and 800^{o}C respectively. The kinetics of the principle reaction studied could be followed over the first few minutes following careful control of the heat treatments.

Samples of MH85-S (CP.Al + SiC), of the approximate shape and dimensions as indicated in figure 3.3, were manufactured. The plane of the sample disc was that perpendicular to the extrusion direction. The masses of the samples were normalised (ie. 48 samples of mass 23.14 +/- 0.4mg) at this stage. These samples shall be referred to as "hats". Prior to this developement an alternative shape was tried and tested (referred to as "spades") which were more massive and slower to respond to heating than the hat samples. The samples were designed to provide material for either a DTA specimen or a TEM foil and to accomodate a thermocouple junction internally to monitor the sample temperature. The lower centre of gravity of the hat samples meant that they could be more successfully manipulated when held on the end of a thermocouple, as described below, compared with the spades. The method exploits the high viscosity of the re-melted composite, making containment unnecessary.

The heat treatment was as follows, with reference to figure 3.3. A tube furnace with an open end was pre-heated to the required temperature plus 4 - 5^{o}C at the hot zone. A sample was filled with an alumina powder - water slurry and placed onto the junction of a 0.418gm^{-1} K-type thermocouple: the slurry dries and provides a barrier between the thermocouple and the liquid aluminium alloy during re-melting. A digital thermometer (+/- 0.5^{o}C) was employed as was a stopwatch (times to the nearest second). After insertion of the thermocouple plus sample assembly into the furnace hot zone the following events occurred:-

a) thermal arrest ~100^{o}C as water was driven-off,

b) thermal arrest as the MH85-S matrix melted - at the end of melting the time was recorded,

c) when the heat treatment temperature minus 1^{o}C was reached the time was again noted.At this point the sample is rapidly withdrawn from the hot zone to maintain the sample temperature at the required temperature +/-1^{o}C throughout the heat treatment. The point in the furnace actually at the required temperature can be found rapidly with experience. The +4 to +5^{o}C excess hot zone temperature allowed the required temperature minus 1^{o}C to be reached quickly, but not so fast as to prevent controlled manipulation of the sample, and for the required temperature to be situated within a furnace region with a shallow temperature gradient. The heat treatment was completed with the withdrawal of the sample from the furnace where the sample experiences a rapid air cool.

For each sample a heat-up time, the time taken for the sample to heat-up from the end of the matrix melting point to the isothermal temperature minus 1^{o}C, was estimated to check that the heating transient was consistent for each sample heated to a given superheat, and to provide a maximum time by which the isothermal heat treatment time need be extended to account for reaction occurring during the heating transient. The initial heating arrest period is considered as insignificant in this respect: the arrest lasts several seconds only, and results show that

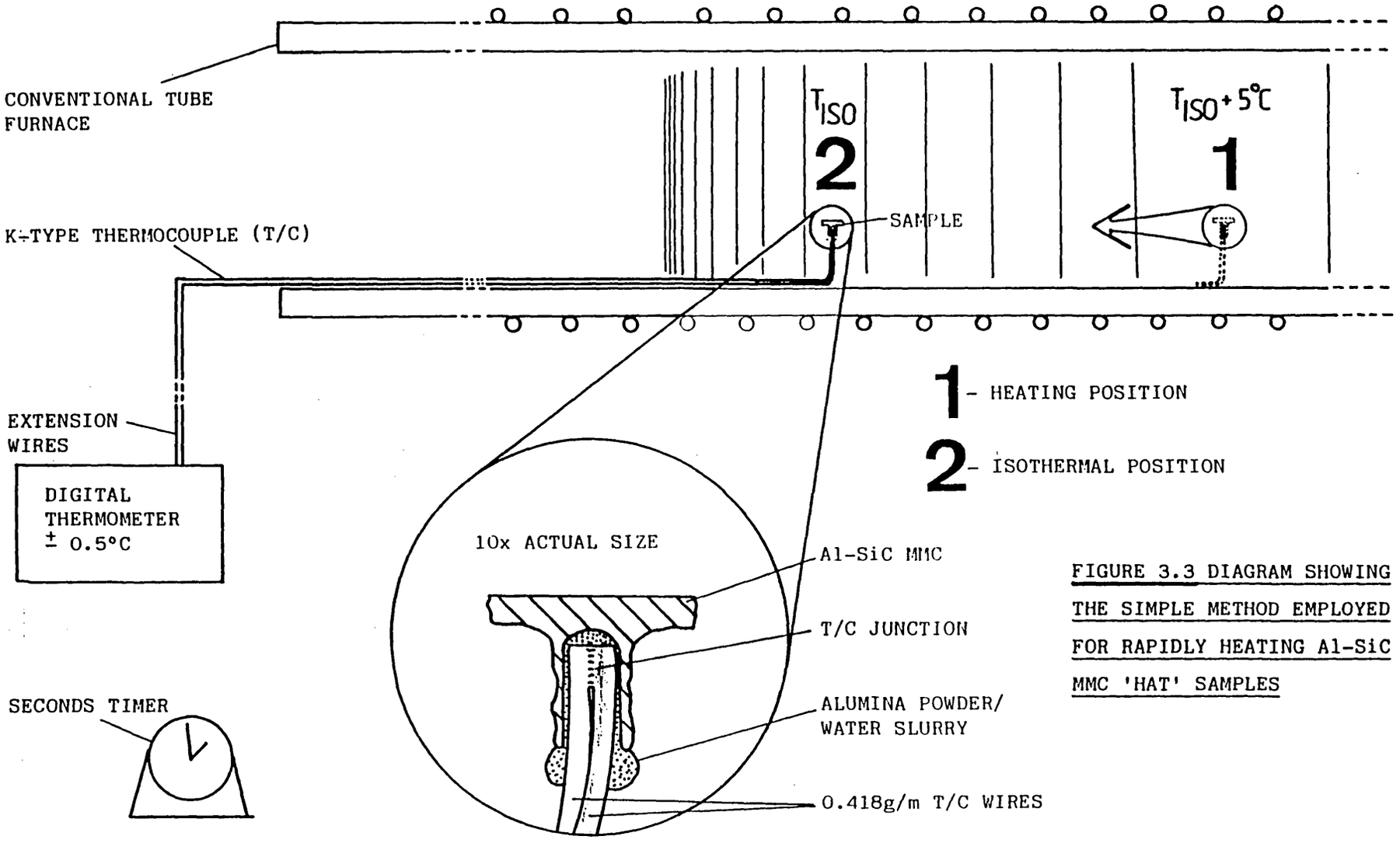


FIGURE 3.3 DIAGRAM SHOWING THE SIMPLE METHOD EMPLOYED FOR RAPIDLY HEATING Al-SiC MMC 'HAT' SAMPLES

several minutes at the melting temperature produces limited reaction compared with any degree of superheating.

A series of heat treatments to one superheat were performed in a few hours with high success rates. Heat treatment times from 0s to 6000s were attempted at 672^{o}C, the range was reduced to 0s to 600s at 800^{o}C since an inert atmosphere was not employed. A series of samples heat treated at one temperature were ground, finishing on 1200 grit SiC paper, to provide equal mass discs (+/- 0.05mg). An MH85-S sample was also prepared with the same mass. All samples of one series could be run in a day in the DTA on heating ramps of 20^{o}Cmin^{-1}. All endothermic peak temperatures were found on melting.

3.5.11 *Thermal analysis of bulk samples*

A crude thermal analysis method was used to monitor the change in the matrix melting point temperature of a large sample of MH85-S as a function of time at temperatures of 672, 715, 760, 800 and 850^{o}C. The semi-continuous method was intended to provide data over intermediate times limited by the oxidation of the sample and/or thermocouple.

A K-type thermocouple was inserted into a 1.2mm diameter hole drilled into typically 1.5g of MH85-S. The hole was carefully filled with an alumina powder - water slurry and the thermocouple junction inserted. The assembly was thoroughly dried in an oven (at ~70^{o}C). Details of each experiment are given in Table 3.4.

A sample - thermocouple assembly was inserted into the pre-heated tube furnace at 672^{o}C, or more usually (see Table 3.4), the temperature was reduced to 500^{o}C at which temperature the sample assembly was equilibrated prior to being heated to the heat treatment temperature. The sample was held rigidly with respect to the thermocouple in an alumina boat throughout the experiments. The furnace was heated at a constant power input. During heating the temperature was recorded manually every ten seconds, or every five seconds whilst a thermal event was occurring to +/- 0.5^{o}C. In this way arrests were recorded. After plotting, the end of the arrest temperature was found via extrapolation. Times were measured after reaching the required temperature minus 1^{o}C. Initially the sample was manipulated in the furnace so that overheating did not occur. The samples were cooled in air on removal from the furnace. The furnace temperature would then be reduced to 500^{o}C and the sequence repeated, except for the 672^{o}C samples which were cooled to room temperature and then re-inserted into the furnace. The heat treatment times were the cumulative times: it was assumed that the initial transient incurred the most significant errors on the hypothetically perfect isothermal heat treatment.

3.6 Fractographic study of tensile specimens

A brief study of the tensile fracture of composite containing aluminium carbide as a matrix - SiC interface product was undertaken in an attempt to qualitatively assess the reaction products' influence on the fracture mechanism. Tensile failures at a low strain rate were essentially produced for microstructural examination.

Three rods ~6mm x 6mm x 40mm were cut from MH85-S (CP.Al + SiC) and one from 200-12 (Al - 12wt%Si -SiC). The rods were re-melted to provide distinctly different conditions and AC, the rod shape being maintained. From this material Hounsfield tensile specimens were machined, which were pulled at RT on an Instron machine.

Fracture surfaces were examined in the SEI mode in the SEM, and sections perpendicular to the fracture surface were polished and examined by light metallography.

Chapter IV

The reaction between SIC and liquid aluminium

4.1 Introduction

In general the results in this chapter will be concentrated on the reaction between SiC and liquid CP.Al over the range of temperatures studied from ~650°C to 1100°C. The reaction is as follows:

$$4Al(l) + 3SiC(s) \longrightarrow Al_4C_3\,(s) + 3Si(l) \quad \text{----------(4.1);}$$

the 'liquid Si' product being miscible in the liquid Al.

Some results concerning the Al-Si matrix alloys (200-12, 202-19 and MH85-S) are included here, although more detailed consideration of the microstructural aspects of these composites are treated in chapter 5.

The SiC used was common to all the composites and is characterised in this chapter. Results related to the thermodynamics of the Al-C-Si system are discussed in this chapter, followed by the presentation and treatment of the microstructural and kinetic results concerned with the reaction (4.1).

A mechanism for the reaction is proposed following the correlation of kinetic and microstructural data.

4.2 Starting materials

4.2.1 *MH87-S*

The experimental CP.Al -SiC composite material MH87-S was supplied in the as-sprayed condition from ALCAN International Ltd. The microstructure of this early spray-cast composite consisted of ~10.5vol% SiC (as determined empirically) particulate dispersed throughout a porous aluminium matrix as in figure 4.1a. Features within the microstructure characteristic of the spray deposition process (Osprey Preform Process) are evident eg. the occurrence of presolidified Al droplets free from SiC particles, and the layered matrix porosity. Typical particle sections are evident in figure 4.1b. Closer examination reveals the occurrence of impurity phases typically at the matrix particle interface as indicated in figure 4.1c. Such impurity phases would be expected in the CP.Al. The association of the impurity phases with the SiC particles would be due to the particle pushing phenomenon: the SiC particles are pushed into the solute rich liquid by the growing primary Al grains. The spray-casting production route results in a fine equiaxed Al grain structure as in figure 4.1d, with a grain size ~30 - 50microns, and with the SiC and impurity eutectic phases at the grain boundaries.

4.2.2 MH85-S

The second CP.Al - SiC composite , designated MH85-S, had been manufactured by spray-deposition, and then hot extruded. The composite was found to contain ~12.5vol% SiC. The general microstructure was as shown in figure 4.2a in which SiC banding in the extrusion direction is clearly evident, as were larger clusters of SiC particles~50 - 100microns across. The impurity phase distribution was similar to the as-sprayed composite, the impurity phases residing at SiC interfaces and on grain boundaries (figure 4.2b and c). The extrusion step caused some SiC particles to separate into smaller pieces as in figure 4.2c, and some open porosity remained. A suprisingly large number of fractured SiC particles could be observed in a single thin foil. Heavily damaged SiC particles, as shown in figure 4.2d, were most probably the result of the SiC particulate manufacture process and not the extrusion step.

4.2.3 *Silicon carbide in the composites*

The SiC particulate used in all the composites was a product of the carbothermic reduction of silica, and was added to the composites in the form of a 13micron grade (F600) grinding grit.

The silicon carbide was generally extracted from the composites using 10 - 30% NaOH(aq) for the CP.Al - SiC composites, 30%HNO_3 in methanol for the composites both as-produced and following reaction, and also with the acid mixture (section 3.5.5). None of these reagents was expected to appreciably attack the SiC [42], and SEM examination of the extracted particles showed a similar range of surface morphologies independent of the extraction medium used. During the initial characterisation of the SiC, bulk powder X-Ray diffraction of extracted SiC, or SiC-Si mixtures depending on the matrix alloy, showed that the common alpha polytypes were present in abundance ie. 4H, 15R and 6H were identified. A few peaks were correlated with 2H. The XRD did not indicate the presence of the beta polytype since the cubic reflections tend to overlap with alpha polytype reflections. Subtraction of peaks, made possible by using peak intensity ratios from standard polytype mixtures, might allow beta SiC to be identified [46].

The non-aqueous based reagent (30%HNO_3 in methanol) used to dissolve the matrix and concentrate the insoluble SiC and Si, and any Al_4C_3, showed that Al_4C_3 was not present in the as-produced composites in a great enough quantity so as to produce diffraction peaks above the background noise on the XRD trace. The total absence of Al_4C_3 from the SiC-matrix interface, in the as-produced composites, was confirmed by TEM.

During thin foil analysis in the TEM SiC particles of 4H, 15R and 6H were often found, and the <11.0> zone patterns by which they can be readily identified are shown in figures 4.2e, f and g. Other longer range polytypes were found, for example 87R (Zhadanov $(33)_4 32$). Some SiC particles showed what was apparently continuous streaking in the diffraction patterns in the <00.1> directions suggesting disorder or partial disorder. Each SiC grit particle was generally composed of a single polytype. However some particles did show syntactically coalesced

ordered and disordered (or complex stacking) regions. Stacking faults and twins were also common features.

Few large subgrains were observed, where part of a particle was misoriented from the rest (eg. figure 4.14a). Regions of the SiC, typically at the surface, show what can be described as high concentrations of faults, where parts of the SiC have slipped past others, referred to here as 'crushing damage' to differentiate the feature from the pure fractures. The crushing damage most likely arises during the pulverising stage of grit production where extremely high particle contact pressures may generate heat and allow limited dislocation movement in the otherwise purely brittle SiC: one author attributes similar features to foil preparation [122]. Figure 4.2d shows a SiC particle where crushing damage has resulted in the formation of crystallographic shear cracks (on {11.0} planes), and evidence of extended dislocations. Extended dislocations were otherwise a rarely imaged feature in the SiC, in one case appearing around an inclusion.

4.2.4 *SiC surface morphology*

The surface structure of the SiC was examined and showed features due to the pulverising stage of the SiC powder production. The surfaces were composed of fracture surfaces, free-surfaces (associated with voids in the polycrystalline SiC prior to crushing) with a high proportion of grain boundary surfaces deduced from the general absence of polycrystalline SiC (except with the rare occurrence of fine grained SiC aggregates as in figure 4.7 g).

Close examination of the interface shows the generally rough nature of the surface in the as-produced composite (figure 4.3a). Fracture through non-cleavage surfaces tends to leave rough surfaces with faceting produced on a scale of a few nanometres to make the surface indistinguishable from an intergranular fracture surface, except for the frequent deviations to produce significant portions of cleavage surface. Basal SiC cleavage was the dominant type of cleavage found. Some exceptionally perfect cleavage fractures had resulted in crystallographically defined surfaces extending over as large an area as a particle can accomodate.

An important feature of the fracture surfaces are the deep, sharp ridges or 'asperities' which cover local areas of many of the particle surfaces as in figures 4.3b and c. The importance of these features in the early stages of the reaction with liquid aluminium will become clear as this chapter progresses. These ridges appear to be generated largely due to the fracture paths through individual SiC crystals being diverted onto cleavage planes, the {00.1} and {11.0} planes for example (as evident from figure 4.2d). Some asperities are associated with crushing damage, as also shown by figure 4.2d.

Extracted particles also exhibited regions of complex surface morphology, figures 4.3d and e, which are considered to be consistent with porosity in the polycrystalline SiC prior to

pulverisation. The small recesses in the surface of the particle in 4.3d suggests that gas-filled pores remain at the SiC formation temperatures, further SiC being deposited epitaxially upon cooling in a platelet morphology, or other morphologies that reflect the substrate SiC defect structure. The particle surface features in figure 4.3e were also seen on particles extracted from as-produced composite. The topographical features on the SiC surface made subsequent interpretation of the surface structure of reacted- extracted SiC particles, by morphological means and correlation with the other microstructural techniques, less conclusive than was anticipated. General SiC particulate features are summarised in figure 4.4.

4.3 Remelting

4.3.1 *Re-melting: initial results*

Initial identification of the phases in the re-melted composites in general was made by the use of powder X-ray diffractometry. The results of the diffractometry are summarised in table 4.1 for samples extracted electrolytically using essentially non-aqueous 30% HNO_3 in methanol: the aluminium is therefore absent. The results show that reaction (4.1) takes place. Metallographic examination of the CP.Al - SiC composite following reaction at temperatures above the initial matrix liquidus showed a striking change in the solidified microstructure. The matrix appears as an hypoeutectic Al-Si alloy with the unreacted SiC and the Al_4C_3 incorporated into the eutectic, figures 4.5a and b , as a result of 'particle pushing' of SiC, and Al_4C_3 coated SiC, by primary Al under the solidification conditions indicated which alter the original particle distribution. The faceted Al_4C_3 product resides at the SiC - matrix interface as in figures 4.5c and d. Particles close together in the melt can become linked by continuous reaction product as suggested by figure 4.5d, and demonstrated by [154].

Quenching the composite into water was generally found not to result in long-range particle pushing due to Al dendrite refinement. Regions of the melt devoid of particles were common in the water quenched material following re-melting, which in the low volume fraction particulate composite provided extensive areas of matrix of average 'liquid phase' composition for areal EDS analysis, as shown in figure 4.5e.

Some details of the interface reaction are readily apparent in the initial metallographic results, as for example the extreme thickness differences in the reaction product around the SiC particles which persist even following heavy reaction eg. 1000 minutes at 800^{o}C, figure 4.5f.

The Al_4C_3 reaction product was not found in the LM13 in large enough quantities for confirmation by XRD at temperatures below 1000^{o}C. The product was undetected by any method used at 848^{o}C. By examining re-melted and quenched LM13 + SiC, Al-12Si + SiC and Al-19Si + SiC composites the temperature at which Al_4C_3 is first produced could be identified, and the temperature at which the L - SiC 'equilibrium' becomes L - SiC - Al_4C_3 could

be estimated: the results are in table 4.2. The corresponding compositional points are plotted on the diagram in figure 4.6 for comparison with the extensive data of Viala *et al* [94]. Interpretation of the results in table 4.2 was complicated by a very low volume fraction of 'rogue' particles which appeared to dissolve prematurely. Light microscopy, figure 4.7b, suggested that the nature of the 'rogue' particles was different from the SiC in general, tending to be of dark brown colouration, and softer. Clusters of reaction product appeared in the vicinity of these particles prior to general SiC dissolution in the Al-Si alloy melts, the product was similar in colour and morphology to Al_4C_3 and readily hydrolysed.

4.3.2 *Impurity phases*

The use of CP.Al matrix alloys presented minor problems with respect to the impurity phases present and their effect on the attempted quantification of kinetic results.

In as-sprayed CP.Al - SiC the cubic compound $Al_{15}(FeMn)_3Si_2$ [155,156] was identified by electron diffraction, figure 4.7d. Other phases may have been present but were not characterised. Following reaction the matrix eutectic showed the commonly observed script - like phase (figure 4.7f) identified with the above compound, and the common needle - like phase beta(FeSi) [157] figure 4.7e. Both phases were readily chemically analysed in the as-cast state following a sufficiently slow cool, and the results are in table 4.3 which are consistent with the literature.

Fe is a minor impurity in the silica which is used to produce SiC commercially. A brief study was made to assess whether a significant increase in the volume fraction of matrix impurity phases could be detected due to the reaction. The initial results in figure 4.8 show no change above the variations in the matrix constitution. Dissolution of a high volume fraction of SiC could lead to a measureable effect, more readily monitored in an initially superpure Al matrix.

Very little Fe is needed to produce large volumes of ternary eutectic products eg. Al - Si-beta(FeSi), or various binary products as the result of non-equilibrium cooling which will affect the estimates of the liquid composition using volume fraction measurements in which the 'eutectic' is assumed to be the Al-Si binary. The commonly occurring Al - Si - beta(FeSi) ternary in these alloys does have a composition very close to the Al-Si binary [157]. Other errors encountered in the quantitative use of results are discussed in section 4.8.

The increase in the ratio of transition elements to free-aluminium concentration, coupled with increasing Si could account for the absence of ternary beta(FeSi) phase observed in a heavily reacted MH87-S sample following a DTA run to 1320^{o}C, in which otherwise rarer script-like phases alone were found, some containing relatively high concentrations of Cu.

A more serious consequence of the impurities is in the interpretation of DTA results, and the attempted use of DTA results to obtain quantitative chemical data via reference to established phase diagrams as in section 4.8.7.

The Fe, Mn, Cu and the initial Si content of the CP.Al would swamp any effect of the extremely low concentrations of C in the liquid phase on the Al - Si phase equilibrium diagram, such that the solidification of the Al matrix alloys are almost independent of the additional component C except for the appearance of minute quantities of Al-Al_4C_3 and associated eutectics: the pseudo-peritectic described by Viala *et al* [73] fits the phase constitution produced upon heating, but does not occur at any practical cooling rate, and the experimental evidence for the metastable Al-C-Si liquidus projection at low temperatures <660^oC presented by these authors is unconvincing, partly due to the use of CP.Al powders in the experiments.

4.3.3 *Arc-melting*

The arc-melting of the CP.Al - SiC composite MH87-S which was estimated to contain 10.5vol%SiC resulted in the production of Al_4C_3 crystals in the form of thin, hexagonal plates, in a quench modified Al-Si alloy matrix as in figure 4.1e. A small, very localised amount of SiC remained undissolved due to poor heat transfer during melting, though the microstructure was generally consistent with the composite having been taken above the Al-Si-C liquidus, the Al_4C_3 having precipitated out upon cooling producing crystal diameters ranging from 300microns (at the top of the cast), to 3microns at the base. The result places the composite composition (84at%Al, 8at%C, 8at%Si) in the primary Al_4C_3 phase field, consistent with the equilibrium phase diagram due to Oden and M^{c}Cune [72]. The sample mass was checked after melting, and the Al losses were considered negligible compared with the uncertainty in the composite composition. On cooling none of the product Al_8SiC_7 was formed, nor was there any evidence for the peritectic transformation L+Al_4C_3 --> SiC+L under the solidification conditions.

XRD of the extracted Al_4C_3 from the arc-melted button revealed {00.3}, {00.6}, and {00.12} Al_4C_3 reflections only along with the Si peaks. The absence of other Al_4C_3 peaks was attributed to the habit of the platelets: the extracted Al_4C_3 plates would settle onto the glass substrate in the diffractometer with the large pinacoidal facets parallel with the plane of the substrate, resulting in the observed texture, which suggests that such pinacoids would be {00.1} planes ie. basal. The excessively large basal facets are the result of the inherently low growth rates in the c-axis direction in the Al_4C_3.

4.3.4 *Prediction of the ultimate extent of reaction*

From the analysis of kinetic results following the initial set of re-melt experiments it was apparent that the reaction between CP.Al and SiC was not producing as much Si in the liquid as in the LM13 alloy when heat treated above 950^oC for a week ie. 10 000minutes at 1000^oC.

The matrix compositions following reaction for 10 000minutes are plotted on figure 4.6 from the results given in figures 4.29-4.31. From the experimental equilibrium results and the calculation of the curve for the composition of the liquid phase following reaction in equilibrium with SiC and Al_4C_3 , which is outlined below, it is apparent that the reaction is not saturating at 1000°C, but possibly has progressed further towards equilibrium at the lower temperatures. These points will be discussed further in section 4.10 with respect to the TTT curves constructed following the analysis of kinetic data.

In order to calculate the composition of the liquid phase in the three phase L-SiC-Al_4C_3 equilibrium it is necessary to consider the reaction (4.1) involving pure Al and an excess of SiC. Over the temperature range considered the solubility of C in the Al melt is very low, and Si additions are considered to increase the C activity so reducing its solubility. On this basis the liquid phase was approximated as an Al-Si alloy for the calculation. The method follows the suggestion of Lloyd and Dewing [106] in the use of the optimised Al-Si liquid free energy function given by Murray and McAlister [60] since intelligible results are obtained.

Above the melting point of Al at a fixed temperature 933<T /K<1685 the free energy change for the reaction :

$$4Al(l) + 3SiC(s) \text{ -------> } Al_4C_3(s) + 3Si(s) \qquad \Delta G_1$$

can be readily calculated from the free energy of formation of SiC [40], and Al_4C_3 [158] since here the phases are in their normal states. However, the 3Si are actually in solution in the liquid Al. To take this into account the heat of fusion of the Si is needed:

$$3Si(s) \text{ --------> } 3Si(l) \qquad \Delta G_2$$

calculated from tabulated heat capacity data given in [40] and checked from:

$$\Delta G_{fusion} = \Delta H_m \cdot (T_m - T) / T_m$$

where ΔH_m the heat of fusion, and T_m = 1685K are given in [159]. At equilibrium

$$\Delta G + RT \ln K = 0 \qquad \text{----- (4.2)}$$

where K is the equilibrium constant [160], $\Delta G = \Delta G_1 + \Delta G_2$ for reaction (4.1), and R is the universal gas constant. K expands for reaction (4.1) as:

$$K = \{a(Al_4C_3).a(Si)^3\}/\{a(SiC).a(Al)^4\} = a(Si)^3/a(Al)^4$$

where the activities a(x) are the final activities at equilibrium when (4.2) is satisfied. Using the free energy function for the mixing of liquid Al-Si alloys [60] in terms of T and mole fractions, the activities of Si and Al at any liquid composition can be found using the tangent and intercept (by Newton-Raphson) method simply carried out on a microcomputer upon the free energy function [161]. The K value to satisfy equation (4.2) could be searched for and hence the corresponding mole fractions of Al and Si found. The results are tabulated in table 4.4 and plotted on figure 4.6.

The calculated curve is almost linear upto 1200K, and then begins to deviate from linearity in the manner of the most recent version of the experimental results of Viala *et al* [94]. The curve lies parallel to, but significantly below, that published by Lloyd and Dewing [106].

It is suggested that by translating the calculated curve 'A' in figure 4.6 to pass through the experimental points a and b, a better estimate of the equilibrium composition of the liquid can be made. This concept, and the raw calculated curve, have been used as the basis for the construction of TTT diagrams in section 4.10.

4.4 Microstructural results: nucleation

4.4.1 *Deep etching experiment*

Some of the results of a survey of the microstructures present on the surface of deep etched samples of both CP.Al - SiC and the same composite after re-melting are shown in figure 4.9. Prior to remelting the SiC particles appear as in figure 4.9a. Following a limited amount of reaction the SiC surface microstructure changes as is evident by comparing figures 4.9a and b. Some of the new structures on the SiC surface are considered to be Al_4C_3 crystals. Only by limiting the reaction via short re-melt times can the surface reaction product be observed without excessive product eutectic Si interferring.

As was suggested in section 4.2.4 that what are presumably SiC platelets, already present as in figure 4.9c, could be confused with Al_4C_3 crystals at an early stage of growth. In further descriptions an Al_4C_3 platelet means a single crystal of Al_4C_3 . The narrow, overlapping platelets shown in figure 4.9d are likely to be Al_4C_3 , and a comparison with the Al_4C_3 platelets sectioned in 4.10a supports this interpretation. The irregular leading edges on the Al_4C_3 plates in figure 4.9d suggests that each plate can be composed of a parallel row of similarly oriented platelets, the fairly regular spacing being due to regularity in the spacing of nucleation sites on the SiC surface, and the growing platelets have already grown enough in one dimension to impinge and overlap: where the platelets overlap the aggregate plate-like crystal appears thicker. In figure 4.9e three sets of parallel Al_4C_3 platelets are seen, presumably due to three different Al_4C_3 - SiC orientation relationships. Figure 4.9f illustrates a stack of Al_4C_3 plates, presumably with a SiC particle beneath: the plates are both thicker than in the above examples, following heating to 800^{o}C, and show misorientations from each other: it is not clear, in this case, whether each plate is due to a single nucleation event or several localised events. Identifiable structures were rarer on the sample heated to 800^{o}C due to dense colonies of eutectic Si covering the reacted SiC particles.

4.4.2 *Nucleation sites at the SiC -liquid Al interface*

A TEM survey of re-melted CP.Al - SiC samples allowed nucleation sites to be identified. Al_4C_3 crystals were found to be associated with some well defined features at the SiC - liquid Al interface.

Sharp ridges, or asperities, which are a common feature of the SiC particle surface , were the major influence on the distribution of the interfacial reaction product in the CP. Al based composites at the early stages of the reaction. Examples of Al_4C_3 platelets and plates nucleated on asperities are seen in figures 4.10a,d, 4.11a,d,e, 4.13c,d,e, and 4.14b.

A second type of nucleation site is identified with the regions of SiC described as 'crushing damage' in section 4.2.3. These regions exhibit relatively high densities of SiC surface steps between adjacent portions of displaced/rotated SiC. Figures 4.11b,c and 4.13a show such damage regions with associated reaction product. The regions of 'crushing damage' were more rarely observed than the asperites produced by the purer fracture events.

It was also evident during the survey that Al_4C_3 crystals would nucleate on each other, giving rise to simple orientation relationships between adjacent Al_4C_3 crystals.

Nucleation of Al_4C_3 on SiC surfaces in general cannot be ruled out, however a certain type of surface structure provides exceptionally good sites for nucleation events to occur: the combination of a high C supersaturation in the melt adjacent to the surface and a high average surface energy. The important difference between the interface at the tip of an asperity and a large proportion of the rest of the interface is that the tip surface must lie away from any cleavage planes. In this way the fracture path which produces the asperity runs on and off cleavage surfaces, and in doing so creates a high surface density of microscopic ridges ie. edges between microscopically defined facets: it is the density of the microscopic ridges which reaches a maximum at the tip which makes it important. If it is assumed that the cleavage surfaces have a lower surface energy than SiC surfaces on average, (and would lie at cusps in the alpha-SiC gamma-plot) then the surface at the tip, which is increasingly composed of non-cleavage surfaces, as in figure 4.8b, will have a higher than average surface energy. The surface energy at the tip of an asperity will be higher than the sum of the areas multiplied by the surface energy of each facet from which the tip region is composed by the addition of the 'edge energies' where the microscopic facets meet. The same 'asperity tip effect' appears on extensive areas of interface which have therefore presumably been created by a similar fracture process (for example the surface in 4.3a possibly will be able to support nucleation due to a high density of microscopic interface ridges, a consequence of the fracture path deviating onto cleavage surfaces on the nanometre scale).

Many macroscopic asperities represent the junction between a cleavage surface and a microfaceted surface. The reaction product Al_4C_3 usually forms on the microfaceted side, presumably having nucleated at the tip representing the junction, and either does not encroach on the cleavage surface, or partially covers the whole tip of the asperity. The partial coverage of the cleavage surface could simply be the effect of another Al_4C_3 platelet growing

to encroach on the cleavage surface during the platelet's initial growth stage from outside the plane of the thin foil . The growth of the reaction product with respect to the asperities gives an important clue to the interfacial Al_4C_3 growth mechanism.

4.4.3 *Orientation relationships between Al_4C_3 and SiC*

During the course of the TEM survey of the re-melted composite, SADPs (selected area diffraction patterns) were taken from regions of the interface containing adjacent SiC and Al_4C_3 crystals. A high degree of selectivity was exercised at the microscope, with respect to the recording of results. One crystal would be oriented on a simple zone, and if an adjacent crystal also exhibited a simple diffraction pattern, or near coincidence of some diffracted spots, then the mixed zones were recorded, supplemented with the individual SADPs from each crystal where necessary. The survey was not exhaustive, and quantification of the frequency of occurrence of any particular orientation relationship could not be made.

4.4.3.1 *'Simple' orientation relationship*

Al_4C_3 platelets were often found to exhibit the following orientation relationship with the parent silicon carbide:

(00.1) Al_4C_3 // (00.1) alpha SiC

(10.0) Al_4C_3 // (10.0) alpha SiC

(11.0) Al_4C_3 // (11.0) alpha SiC

The above relationship is illustrated in figures 4.10a, 4.10c, 4.17c and k. Imaging of the {00.1} 6H SiC planes and {00.3} Al_4C_3 planes in figure 4.11a also clearly shows the above relationship. Enlargement of the interface region arrowed suggests that the SiC {00.1} planes match closely with the {00.3} Al_4C_3 planes alternately every 9 and 11 Al_4C_3 {00.3} planes such that the dark fringe runs continuously across the interface, and that the interface is semicoherent. With reference to figure 4.12 it is suggested that the close coincidence of the groups of atoms indicated by letters are responsible for the coherent regions of the {100} type plane interface: the illustration shows the type of matching that is possible and is not meant to be a complete analysis.

As also indicated in figure 4.11a part of the Al_4C_3 is slightly misoriented, and the {00.3} fringes show less contrast: many examples of such minor misorientations away from the 'simple' orientation relationship were observed.

4.4.3.2 *Minor misorientations*

The rotation between mixed SiC and Al_4C_3 $[1\bar{2}.0]$ zones was measured on enlarged projections of the SADPs on which the rotations were observed. The angles were measured between pairs of {00./ }, {10./ } and {$\bar{1}$0./ } orders of reflections corresponding to both alpha SiC and Al_4C_3. The measured angles are in table 4.5.

Variations in the angles between the different orders of reflections suggests that the misorientations are not simply represented by rotations about a <1$\bar{2}$.0> direction. However as a first approximation in the rationalisation of the observed variations, the rotations predicted for the tabulated orientation relationships are presented for comparison. The ~2^{o} rotation between the [11.0] directions in the [10.$\bar{1}$] 6H SiC and [20.$\bar{1}$] Al_4C_3 zones in figure 4.23a further shows that the simple rotation suggested above is only an approximation. The SiC adjacent to the Al_4C_3 in the figure 4.13a is highly defective and constitutes a region of 'crushing damage': the Al_4C_3 could be simply oriented to a small portion of SiC, but because the SiC is heavily faulted the mixed SADP shows a minor misorientation with the SiC bulk. That a set of reflections are not present could be due either to the nucleation site lying outside the plane of the foil, or to a low diffracted intensity. It is possible that some minor misorientations are in fact alternative orientation relationships, and some appear to be misorientations due to minor SiC substrate misorientations. Epitaxial relationships are often reported to show small variations [162].

4.4.3.3 *Alternative orientation relationships*

As was evident from the deep etching experiment, some Al_4C_3 crystals, presumably of the same habit which was generally confirmed by the TEM survey, showed different orientation relationships with the same parent SiC crystal. The TEM micrographs 4.10b, and 4.10d show Al_4C_3 crystals with alternative orientation relationships to the simple one. The relationship between the crystals imaged in figure 4.10b was found to be approximately:

[00.1] Al_4C_3 // [1$\underline{\bar{1}}$4.3] 6H SiC

(10.0) Al_4C_3 // (01.9) 6H SiC

(11.0) Al_4C_3 // (11.1) 6H SiC.

The near coincidence of the (2$\bar{2}$.0) Al_4C_3 and (01.9) 6H SiC reflections strongly confirms that the above relationship is real. However, the appearance of both (2$\bar{1}$.$\bar{1}$) and (2$\bar{1}$.0) 6H SiC reflections on the [1$\underline{\bar{1}}$4.3] 6H SiC zone suggests that a simpler zonal relationship may exist, namely between the [00.$\bar{1}$] Al_4C_3 zone and an [0$\bar{9}$.2] 6H SiC zone. The minor misorientation onto the [1$\underline{\bar{1}}$4.3] may be due to reasons as discussed in section 4.4.3.2 above. The indexing is clarified for this orientation relationship by reference to figures 4.17i and j.

The oriented particle of Al_4C_3 in figure 4.10d, with the SiC on the same zone as in the above case, shows that the Al_4C_3 crystals are rotated by ~90^{o} relative to each other. The Al_4C_3 {00.1} planes in 4.10d would be parallel to {1$\bar{2}$.0} planes of the Al_4C_3 in figure 4.17j. The two Al_4C_3 crystals were several microns apart on the foil, but it appears that the Al_4C_3 crystal in 4.10d shows a more convincing orientation relationship with the second Al_4C_3 crystal from which it is apparently detached, than with the substrate SiC. That the crystal has grown along the asperity in figure 4.10d is not a coincidence. These features illustrate the immediate complicating effects of the Al_4C_3 nucleation (distribution), and growth of further Al_4C_3 crystals, with very low volume fractions of Al_4C_3 interface product. Nucleation of Al_4C_3 on Al_4C_3 can

produce some simple symmetrical structures. However, in general, at the earliest stages of the reaction, the reaction product has some epitaxial relationship with the parent SiC substrate.

A further convincingly precise orientation relationship is illustrated in figure 4.17f:
[$\bar{6}$2.1] Al_4C_3 // [1$\bar{2}$.0] 6H SiC
(11.$\underline{12}$) Al_4C_3 // (10.0) 6H SiC
(10.$\underline{10}$) Al_4C_3 // (00.1) 6H SiC
in which the (10.$\underline{10}$) Al_4C_3 reflection is nearly coincident with (00.8) 6H SiC. Some of the reflections in figure 4.17f are due to the partial Al_4C_3 zone shown in figure 4.17h : there was initially suspected to be some relationship between the zone illustrated in 4.17h and the [1$\bar{2}$.0] 6H SiC zone in figure 4.17f. The sequence of {10.*l* } Al_4C_3 reflections in figure 4.17f and 4.17h suggests that the Al_4C_3 giving giving rise to the SADP in 4.17h was oriented with the crystal responsible for the [$\bar{6}$2.1] zone in 4.17f.

A further orientation relationship is suggested by the mixed SADPs in figure 4.17g in which the following parallel planes and directions are suggested:
[5$\bar{1}$.$\bar{2}$] Al_4C_3 // [1$\bar{2}$.0] 6H SiC
(11.6) Al_4C_3 // (20.1) 6H SiC
A minor misorientation of the prominent planes from a simpler orientation relationship is again suggested.

4.5 Microstructural results: Al_4C_3 growth

4.5.1 *Al_4C_3 morphology as an interface product*

At the early stages of the reaction it has been seen that the Al_4C_3 product crystals tend to be discrete platelets with large, pinacoidal, basal facets. Often these crystals will be faulted as is generally observed eg. crystal 2 in figure 4.10a. The high defect content of the platelets probably results from the condition of the SiC substrate. Some apparently single crystal Al_4C_3 particles contain low angle boundaries, possibly due to the result of substrate misorientations described as crushing damage. A simple Al_4C_3 platelet will develop low index {10.0} type facets as in figure 4.10b. If the reaction is extensive enough the Al_4C_3 crystals coarsen, involving layer-by -layer crystal growth on some facets projected out into the liquid, and a ledge mechanism by which Al_4C_3 growth can occur quite rapidly by the repeated nucleation of basal-layers of atoms at the ledge formed at an Al_4C_3 basal facet-SiC substrate-liquid Al junction (as in figure 4.52 'lateral growth mechanism'). Where such ledges do not exist the Al_4C_3 platelets can reach quasi-stable dimensions, with low index facets, the basal layer nucleation rate being extremely slow. This partly explains why some Al_4C_3 crystals are constrained to grow only in one direction away from an asperity, or not advance over a cleavage surface, especially a cleavage surface that is almost parallel with a low index Al_4C_3 plane (a situation which arises frequently due to the 'simple' orientation relationship).

Al_4C_3 platelets can impinge very early in the reaction, as several platelets nucleate in close proximity, especially due to rapid <10.0> growth. However, once the nucleation rate has dropped towards zero, then the growth of the Al_4C_3 crystals to cover the SiC surfaces will be mainly by growth in the 'c' direction, either as ideally sketched in figure 4.52 in two dimensions, or involving Al_4C_3-Al_4C_3 ledges as well.

As Al_4C_3 coarsening occurs generally the Al_4C_3 crystals impinge. If the nucleation is predominantly of the simple orientation relationship with minor misorientations then large textured interface product regions develop as in figure 4.15 in which the foil plane presumably cuts through the interface product hence leaving part of the parent SiC particle outside the plane of the foil. Due to Al_4C_3 growth anisotropy, when crystallites impingement occurs regions of liquid may be isolated within the Al_4C_3 aggregate. Either this liquid is consumed by the reaction, or else the contraction of the liquid upon cooling from the reaction temperature produces large numbers of voids. Such voids were evident on many Al_4C_3 - SiC and Al_4C_3 - Al_4C_3 interfaces as in figure 4.15b.

Potential sites for void formation at an earlier stage of reaction than in figure 4.15b are shown by the regions marked M in figure 4.14c. The 'liquid' in the micrograph is seen to penetrate the interface product at the sites marked M, which are are characterised by ending in a SiC cleavage surface. Such features are discussed in more detail in 4.5.3.

Some of the Al_4C_3 - Al_4C_3 sub-boundaries are apparent in figures 4.16d and e. Such features would be the result of Al_4C_3 crystals with a minor misorientation from each other impingeing. The dislocation structures developed in the Al_4C_3 in figures 4.16b, d and e add a possible additional factor to the growth kinetics of the interface product: these dislocations were apparent only following extensive reaction eg. 1000minutes at 1000^{o}C when complex polycrystalline aggregates were common.

When minor misorientations are neglible or non-existent between nucleated Al_4C_3 platelets, upon coarsening single crystals can develop which are impenetrable. Figure 4.14d shows an apparent example of 'an Al_4C_3 crystal' exhibiting various facets, the variety of facets presented by 'the crystal' are presumably the result of the polycrystalline origin of 'the crystal'. Micrographs 4.16a and c also show that continuous reaction product layers can develop after sufficient time at a high liquid superheat. It was noted that some interface regions, not shown, exhibited Al_4C_3 - Al_4C_3 boundaries which finished within the Al_4C_3 suggesting that some uncharacterised low angle boundaries can be 'grown out'.

The 'blocky' Al_4C_3 morphology shown in figure 4.7a appeared in the sample as an inhomogeneity. The concentration of this type of feature locally in one sample could not be adequately explained, for example in terms of carbon segregation during solidification.

4.5.2 *Al_4C_3 twins*

Twin related Al_4C_3 crystals were common in the reaction product. One twinned Al_4C_3 aggregate was examined, figure 4.17a, and the SADP indicates that the twins are of a simple rotation type. The structure can be explained either by the nucleation of several discrete Al_4C_3 plates with the simple orientation relationship with respect to the SiC substrate, or else the twin relationship occurs randomly as a result of the individual 'lateral nucleation' events responsible for interfacial Al_4C_3 thickening. Due to the low symmetry electron diffraction can separate the crystals depending on their relative orientation ie. a +/- 60^o or 180^o rotation of one crystal about the c-axis of an initially identically oriented pair of Al_4C_3 crystals results in a twin relationship beween the crystals.

4.5.3 *Al_4C_3 - free SiC - liquid Al interfaces*

In contrast to the nucleation sites, various SiC surfaces remained reaction product free even following extensive reaction. Variation in reactivity could be observed around any single SiC particle, as is clear in figure 4.13e.

Extensive regions of basal SiC cleavage surfaces remained reaction product - free after 1000minutes at 800^oC. An extensive basal surface, unattacked, is shown in figure 4.13b at an earlier stage of reaction (the disappearance of the nucleation site at the Al_4C_3 - SiC - L junction when the Al_4C_3 reaches the cleavage surface prevents the Al_4C_3 crystals extending further, as suggested in section 4.5.1)

An example of extensive {11.0} type SiC surface, free of reaction product, was found in a sample reacted 10minutes at 800^oC.

Figure 4.14a shows a $\{1\bar{1}.l\}$ surface, with $l = \bar{}10$ -13, free from reaction product following 1000minutes at 800^oC. The cleavage surfaces, and many less extensive ones do not generally support nucleation. Growth of the interface reaction product either eventually isolates these surfaces away from the melt or overgrows them, though it is apparent that due to a low dissolution rate from the cleavage surfaces overgrowth by Al_4C_3 must be controlled by long range diffusion through the liquid, or across the substrate surface supplied from readily dissolving SiC in contact with the liquid: it is plausible that only ledges on the microfaceted SiC surfaces will support nucleation due to an sufficient C supersaturation immediately available ie. good lateral growth nucleation site = direct C source + ledge. Low C supersaturation at poor sources of dissolution products, C and Si, would severely reduce the local Al_4C_3 growth rate.

4.6 SiC surface post reaction

When the Al_4C_3 is removed from the SiC surface which has been heavily reacted eg. 1000minutes at 800^oC the SiC revealed beneath the product exhibits more faceting than observed prior to reaction. An example of such faceting is shown in figure 4.7c.

4.7 Summary: 'reaction zone' microstructure in the liquid CP.Al + 10.5-12.5vol% SiC particulate system

As the CP.Al matrix melts on heating the composite nucleation of Al_4C_3 occurs epitaxially at the SiC - liquid aluminium interface at SiC surface asperities. The most common epitaxial relationship is:

{10.0} Al_4C_3 // {10.0} alpha SiC

{00.1} Al_4C_3 // {00.1} alpha SiC

{11.0} Al_4C_3 // {11.0} alpha SiC.

Plate - like Al_4C_3 crystals, exhibiting large basal facets, initially extend into the melt due to crystal growth anisotropy when oriented with the above relationship to the parent SiC, until low index facets are established generally. The nucleated Al_4C_3 platelets coarsen by a simple lateral growth mechanism involving repeated nucleation at the Al_4C_3 - SiC - liquid Al ledge and rapid spreading of basal Al_4C_3 layers from the nucleation site at the ledge until adjacent Al_4C_3 crystals impinge. Some further nucleation of differently oriented Al_4C_3 crystals occurs on the established interface Al_4C_3 crystals. Pure cleavage surfaces on the SiC do not support Al_4C_3 nucleation and resist coverage by the growing Al_4C_3. The reaction tends to ultimately create SiC facets at the SiC-Al_4C_3 interface.

The nucleation and growth of the Al_4C_3 interface product are summarised schematically in figure 4.52. In figure 4.52 the following assumptions have been made:

i. the reaction is two dimensional so that no Al_4C_3 nucleated outside the plane of the page can cross into it;

ii. the Al-SiC interface remains fixed (for reference);

iii. the plane of the page is a {11.0} plane of the alpha-SiC substrate.

4.8 Quantitative kinetics

4.8.1 *Introduction*

In this section quantitative data showing the extent of reaction (4.1) as a function of time and temperature in terms of the volume fraction of Al_4C_3 produced are presented for the CP.Al based composites MH87-S and MH85-S. The difference in the initial volume fraction of SiC between the two composites studied ~2vol% was found to produce a significant difference in the reaction kinetics.

The kinetics of the reaction in the MH87-S composite was followed using three main techniques which could then be compared. Thermal analysis techniques alone were adopted to follow the reaction in the MH85-S composite. The data collected is analysed to provide activation energies to be correlated with the microstructural analysis of the preceding section. Time , temperature, transformation diagrams were finally constructed, two of which propose to display the kinetics of the reaction in practical terms.

4.8.2 *Initial volume fraction of SiC*

In order to define the initial state of the system in which the reaction is to be followed the volume fraction of SiC needs to be determined. The results are tabulated below in table 4.6. The results suggest that the NaOH(aq) treatment alone of the CP.Al is inadequate: a yellow - brown residue was left with the SiC. The addition of dilute HCl(aq) following washing of the residue removes the colouration -suspected to be due to Fe based impurities- suggests that a single step dilute HCl(aq) treatment would suffice for the CP.Al matrix dissolution.

The decanting process was suspected of underestimating the result due to the formation of an unidentified liquor surface product which was lost with the washing liquor. The filtration method using paper filters required the paper to be dried completely in an oven prior to and after use: this made the paper very suseptible to water absorption from the atmosphere, requiring prompt weighings. The glass fibre filters once dried appeared to be less suseptible to water pick-up during weighing. The difference between the 202-19 composite results (the Al-Si alloy matrix composite results are included here for completion) could reflect the variation in the actual SiC content of the preform. However, the large sample size and the attempt to obtain an averaged estimate for the 202-19 and 200-12 composites SiC contents to compensate for the observed SiC variations suggests that errors are a significant contribution to the difference in the individual results obtained.

For the purposes of calculation a 12.5vol% SiC estimate was adopted for both MH87-S and MH85-S for the initial sets of processed kinetic data. Over the range of Al_4C_3 volume fractions calculated as being produced by the reaction under the conditions studied use of an initial volume fraction of 10.5vol% SiC or 12.5vol% SiC makes little difference, figure 4.32, in the numerical results ie. the difference is neglible compared to experimental errors and actual scatter in the measured values. However if the reaction was to completely dissolve the SiC then the error introduced by the above assumption would become as great as the experimental scatter. Complete SiC dissolution would provide material with which the initial SiC content could be checked independently by matrix Si concentration measurements.

For the purposes of the TTT diagram construction MH87-S and MH85-S derived data were processed using initial SiC volume fractions of 10.5% and 12.5% SiC respectively, as suggested by the figures in table 4.6.

The ~2vol% difference estimated to exist between the SiC contents of the composites with CP.Al matrices, does lead to a significant difference in the kinetics. For example, compare the few MH85-S results with the main MH87-S data in figures 4.24 , 4.25, 2.28 - 4.30 where the MH85-S points are consistently at a more advanced stage of the reaction. The difference between the composites appear to be outside the scatter shown by the MH87-S data, though the scatter can only be estimated from the few repeated 1000^{o}C data shown ie. 3 pairs of data points, σ_{n-1} = 1.5^{o}C (the error bars on the DTA data only show uncertainty in the initial matrix Si content).

It would appear, as discussed later that the excess extent of reaction shown by the initial MH85-S results is incurred principally during the initial rapid stage of the reaction. The effect of the initial SiC content on the reaction kinetics is returned to during the discussion of the TTT diagrams.

4.8.3 *Volume fraction of primary Al in AC samples*

Assuming that the area fraction of primary Al can be converted directly into volume fractions, the results are plotted in figure 4.18. The scatter indicates real variations in the cast structure. Errors due to 'cutting out' appear to be less than 2.5% of the value determined, though there remains the uncertainty in the judgement of the primary Al dendrite boundaries, especially with the coarser appearing Al-Si eutectic. Scatter bars are plotted at σ_{n-1}. Uncertainties in the isothermal times were plotted. The data points lie at the nominal re-melt times, the start of each time bar marks the time at temperature as determined by subtracting the time to reach the temperature from the nominal re-melt times (refer to table 3.3). Taking the initial heating transient into account the true isothermal re-melt time can be judged to lie at some point on the time error bar.

As the reaction proceeds the volume fraction of primary Al in the casting decreases both as Al is converted into Al_4C_3 and as Al is incorporated into the eutectic upon solidification. In order to calculate the vol%Al_4C_3 the following assumptions were made:

i) the air cooled matrix microstructure contains Al and Al - Si as equilibrated at the eutectic temperature ie. 1.5 at%Si in the primary Al and 12.2 at%Si at the eutectic point [60];

ii) the proportions of the matrix constituents vary in accordance with the lever rule;

iii) the reaction products are produced according to the stoichiometry of reaction (4.1);

iv) the composite matrix was initially 99.67wt%Al and 0.33wt%Si (the ALCAN 2S CP.Al composition expressed as a binary);

v) the initial volume fraction of SiC was 12.5%;

vi) the densities in g/cc of Al = 2.70; Si = 2.33; SiC = 3.21; and Al_4C_3= 2.99.

As displayed in figure 4.18 the volume fraction of Al_4C_3 is seen to increase at all temperatures until towards 1000minutes at 800^{o}C, and 100minutes at 1000^{o}C, where the volume fraction

attains an apparently constant value. Such behaviour can indicate that either the reaction has saturated or else a kinetic barrier has intervened in the course of the reaction.

An estimate of the maximum error due to the assumption of equilibrium cooling can be made by application of the Scheil equation [163] which, with an estimated equilibrium partition coefficient k=0.11 from the Al-Si liquidus, suggests that up to 5vol% eutectic can be produced due to coring. The estimate would lead to typically a 0.5-0.6at%Si maximum overestimate from this source (when greater than 1.5at%Si is present in the matrix), though the figure is potentially greater still for the least reacted material: the appearence of any amount of eutectic, with an actual matrix Si content <1.5at%Si, automatically leads to the assumption of a minimum of 1.5at%Si in the matrix. An additional factor that would tend to lead to an overestimate is the neglect of impurities: the existence of volumes of ternary Al-Si-beta(FeSi) would reduce the actual Si content of the matrix microstructure assumed to be binary Al-Si only. A degree of underestimation would be introduced to counter the above effects by way of the partial chill modification of portions of the eutectic as a result of the relatively high air-cooling (>150^{o}C/min through the solidification range) rate for the small samples used, which would tend to shift the eutectic composition to higher Si contents.

4.8.4 *Area fraction of primary Al in WQ samples*

The area fraction of eutectic (ie. 1 minus the area fraction of primary aluminium) in the matrix of water quenched CP.Al -SiC (MH87-S) samples re-melted at 800^{o}C are directly expressed as volume fractions and are presented in figure 4.19. The determination of the matrix composition following reaction with the liquid Al was simplified except that the composition of the eutectic was now less certain than for the air-cooled samples treated above. The eutectic was completely fibrous following quench modification. In unidirectional solidification experiments Steen and Helawell [64] determined that a coupled Al-Si eutectic becomes completely fibrous with a composition of approximately 14.5wt%Si, which increases further as the freezing rate increases. At a constant interface velocity the coupled eutectic composition can be between ~14.5wt%Si to 16wt%Si; therefore if the eutectic was just completely fibrous under the experimental cooling conditions, the uncertainty in the lowest Si composition is represented by these limits. Estimates of the matrix composition were therefore made assuming eutectic compositions of 14.5wt%Si and 16wt%Si with a primary Al composition of 1.56wt%Si (from the equilibrium diagram). The average primary Al composition was likely to be closer to 1wt%Si.

With the calculated matrix composition, and the initial MH87-S matrix composition and SiC content as in 4.8.3., the volume fraction of Al_4C_3 could be found. However considering the uncertainty in the eutectic composition little weight was given to these results. The trend in the results is similar to that in 4.18 at 800^{o}C, though the pronounced plateau in the curve in figure 4.18 is not as apparent in figure 4.19. However, the general agreement between the results suggests that the above assumptions are not unreasonable.

NB It would be a simple step to take to anneal the WQ structure to produce constituents whose compositions can be better estimated eg. anneal at 550^{o}C and refer to the Al-Fe-Si isothermal section [164] or check the Al solid solution composition roughly with EDS. Referring to the spheroidised structures produced in the synthesis experiment, shown in chapter 5, the shape and size of the Si precipitates following initial coarsening at ~570^{o}C would make volume fraction determinations a relatively simple task, and only the volume fraction of Si need be found by selecting large areas of SiC particle free matrix. Such evaluations of the matrix composition would produce by far the most reliable estimates.

4.8.5 *Mass fraction of SiC following re-melting*

The mass fraction of SiC measurements, made on MH85-S samples re-melted at 800^{o}C, and 670^{o}C , are given in figure 4.20. The SiC mass fraction was found to decrease, and the calculated volume fraction of Al_4C_3 increase as the re-melt time increases. The initial composite composition was assumed to be as given in 4.8.3. Mass fractions of all the constituents could be found, then the matrix composition corresponding to the SiC mass fraction could be determined and hence all the relavent volume fractions found. Owing to the scarcity of results of this type the scatter could not be determined.

4.8.6 *Quantitative EDS of the MMC matrix following re-melting and WQ*

The results of the calibration experiment are given in figure 4.21. The as-analysed results have already been ZAF corrected. The results are seen to overestimate the actual Si content of the alloys. The samples used were characterised by the cooling rate, estimated from dendrite secondary arm spacings (DAS) using the following relationship:

$DAS = 50.K^{-1/3}$

where K is the cooling rate in ^{o}C/s and the constant 50 is that applicable to Al 7-11wt%Si alloys [165], and the DAS is in microns.

The air cooled eutectic gives an average result of 18wt%Si (31 analyses) which is a great overestimate of the accepted composition, which would be expected to be nearer the equilibrium eutectic composition 12.56wt%Si (12.2at%Si). The eutectic Si refinement produced by increasing the cooling rate by 4 orders of magnitude is seen to be inadequate for reducing the fluorescence error to a neglible value, though a large reduction in the overestimate is made. Details of the method used were mentioned in chapter 3, section 3.5.7: further reference to figures 6.5e, and f will give an impression of the scale of the microstructure, though the limitation on the area the calibration alloys scanned for analysis was made to mimic that of the reacted, and quenched, MMC matrix material. Increasing the cooling rate has the disadvantage of decreasing the amount of Si in solution, though this effect is more than offset by the separation of Si fibres by the Al on a sub-micron scale, which increases the applicability of the fluorescence correction in the ZAF procedure.

Due to variations in the contact made by the splatted liquid on the substrate, and transient substrate heating during the splat, a range of dendrite arm spacings was found either occurring over a long range, or locally due to coarsening during growth. Areas of approximately constant microstructure could be found. At the fastest cooling rates the eutectic was optically unresolved, and comparable to much of the water quenched re-melted composite material. In general it would be appreciated that identical microstructures could not be produced. In order that sets of curves be generated to provide corrections expressed as a function of dendrite spacing or eutectic flake/ fibre spacing would require extensive and detailed characterisation of the matrix microstructure, defining precisely which microstructural parameters are measured.

Errors were therefore due to microstructural scale variations in the calibration alloys, and due to the EDS technique itself. The analysis of superpurity Al indicated 0.5- 1.0at% Si from several analyses. This effect was partly due to the poor condition of the EDS detector at the time and the subsequent reduction in energy resolution. A broad Al peak can result in in residual counts in the Si position following subtraction of the standard Al peak during the quantification procedure. A substantial amount of Si can be suggested to be present as the ZAF correction increases the apparent Si peak by a factor of ~3.

The analysis results of the re-melted and WQ matrices are given in figure 4.22 both before and after correction. The uncorrected results provide a useful known overestimate of the matrix Si contents. The original errors reflect variations both due to minor macrosegregation effects and cooling rate changes across a sample. No adjustment of the error in the results had been made following correction. The analysis values used were those from normalised Al-Si binary results (Al, Si and Fe were analysed) for which the weight totals given were 100+/-2wt% for the total sample analysis.

The resulting curves in figure 4.22 vary in a manner similar to the previously presented data, except that the 800^{o}C and 1000^{o}C results are separated more than in the volume fraction results. The EDS analysis results are useful since they depend on very different assumptions to those used in the previous methods discussed: they provide a useful set of comparative data indedendent of assumptions about the nature of the phase diagram. The volume fractions of Al_4C_3 are calculated for the same assumptions about the matrix microstructure and initial composite constitution as in 4.8.3 so that they are directly comparable with the preceding results. The volume fraction of Al_4C_3 results are given in figures 4.29 to 4.31.

4.8.7 *Differential thermal analysis (DTA) of the initial set of heat treated samples (table 3.3)*

When attempting to use the DTA traces to provide liquidus temperature data for quantitative

purposes, several factors need to be considered:

i) impurities in the matrix;

ii) the heating rate;

iii) the sample mass;

iv) the actual amount of material melting to produce a DTA peak;

v) the method of DTA trace evaluation.

4.8.7.1 *Impurities*

According to Lloyd and Jin [107,108] and Lloyd *et al* [38] an alloy's equilibrium liquidus can be used to convert DSC trace peak liquidus temperatures for 15-20mg samples heated at 20^{o}C/min into liquid compositions. The alloy necessarily needs to be approximated to a well established binary or ternary liquidus if a complete calibration is to be avoided.

For CP.Al-SiC with the subsequent change in the Si content of the matrix, and neglible effect of dissolved carbon, the Al-Fe-Si liquidus projection [156] would appear to be appropriate. By inspection the Al-Si liquidus [60] would provide a good approximation to Al-Si alloys containing up to 0.7wt%Fe with Si contents up to the eutectic composition, even considering that the Al-Si eutectic point given in [156] at a composition of 11.3wt%Si is now an obsolete value.

The CP.Al matrix would, with a working assumed maximum Si content of 0.33wt%Si, provide an initial liquidus depression of 1.9^{o}C, which which becomes 3-4^{o}C with an added 0.5-0.7wt%Fe. However, as pointed out in [156] minor impurities in Al-Si alloys can have significant effects on the measured liquidus temperature, and liquidus depressions of up to 15^{o}C are cited. In this study the initial CP.Al liquidus is most probably 649+/-1^{o}C, estimated following the construction of symmetrical peaks on the DTA traces for samples of CP.Al-SiC with a range of masses, heated at 3^{o}C/min. The peak construction, as in figure 4.23a and b allows a better estimate of the equilibrium liquidus temperature to be made, compared with the peak temperature.

According to [152] the transformation temperature should be nearest to the start of the thermal event, ie. from the point at which the DTA trace deviates from the base-line. However, in cases where the point required is preceded immediately by other thermal events the point cannot be determined. Hence, the method of peak construction as in figure 4.23a and b was adopted.

Cooling curves yield a temperature T_L (figure 4.23a) which closely corresponds to the actual liquidus temperature. Figure 4.23 a suggests that T_L, taken from a cooling curve, and the apparent equivalent point produced by constructing a symmetrical heating liquidus peak are in good agreement. When cooling curves were not available, as for the initial composite melting liquidus, as mentioned above the derived T_L value can be substituted with some confidence. It

is suggested that the DTA apparatus used is very sensitive, and that the temperature indicated as T_{EQ} in figure 4.23a would be a very good estimate of the equilibrium liquidus temperature. The 649+/-2^{o}C liquidus estimate would add an unpredicted 8.5^{o}C depression to the liquidus ie. the additional traces of Mn and Cu (<0.2wt% total) are significant when combined with the other impurities. The melting liquidus depression would translate into an initial apparent ~2at%Si content when estimated from the Al-Si binary diagram [60].

To reduce the impurity problem the Al-Si binary liquidus was retained as a calibration, but absolute temperatures would not be referred to the liquidus, only temperature changes ie. the equilibrium liquidus was assumed to be uniformly depressed. Table 4.7 shows a conversion chart derived from the Al-Si binary liquidus [60] used to convert temperature changes to at%Si in this study which is alternatively referred to as a 'floating liquidus'.

4.8.7.2 *Heating rate*

The melting peak temperatures (Tp in figure 4.23d and b) will increase as the heating rate increases, and the cooling peak temperature will be similarly depressed [152]. The peak temperature Tp comes closer to the equilibrium transformation temperature as the rate decreases. The effect of the heating rate upon Tp of CP.Al - SiC, which are referred to as Tmp values, can be seen in figure 4.27 at 3^{o}C/min and 20^{o}C/min. Much of the scatter in the 20^{o}C/min case was due to the data being collected over a period of several months.

4.8.7.3 *Total sample mass*

With reference to figure 4.27 variation in the sample mass can be corrected for. At 3^{o}C/min the peak temperatures are almost independent of mass. At 20^{o}C/min an approximately simple Al, single peak producing CP.Al - SiC sample will peak at temperatures indicated by the curve. Such peaks are 'sharp', even when large samples are used as shown in figure 4.23b. The Tmp at 20^{o}C/min can be compared to an estimated zero mass Tmp value, estimated by extrapolation of the 3^{o}C/min data in figure 4.27 to be 652^{o}C. The inability of the extrapolation to predict the 649^{o}C value suggests that the curve drops more sharply at <3mg than is indicated in figure 4.27. The value 652^{o}C was adopted as an effective minimum heating peak temperature for CP.Al-SiC and is referred to as Top.

Lloyd and Jin [107,108] suggest that small samples may suffer from casting induced inhomgeneities. The composite material used in this study was re-melted as relatively large samples ~1.5g either air cooled or water quenched. AC and WQ pairs of samples re-melted at 1000^{o}C showed scatter in the DTA peak temperature of 1.5^{o}C, based on the standard error of the differences between each pair of values. The DTA sample size taken from the initial set of re-melted samples was typically large (20-55mg) to ensure a representative result from the minimum number of DTA samples.

4.8.7.4 *Actual amount of sample undergoing transformation*

As the reaction (4.1) proceeds and increases the silicon content of the MMC matrix, the Tp liquidus will move to lower temperatures both due to thermodynamic effects and due to heat transfer effects. As the fraction of the sample absorbing heat during the primary Al melting range decreases, then at a constant finite heating rate the DTA peak maximum (characterised by Tp) due to primary Al melting shall be reached in a shorter time and therefore at a lower temperature. The mass correction suggested by figure 4.27 ie. at a given sample mass the starting liquidus to which temperature changes be referred (for reacted samples of the same mass) on the appropriate heating rate curve, would only apply to a single peak producing composite ie. 100% Al matrix or 100% eutectic matrix, assuming the thermal properties of the Al and eutectic to be the same. The effect is seen as the eutectic peak temperature increases as the liquidus peak temperature decreases, as in figure 4.26, and is most noticeable for the large samples. The eutectic peak temperature increase is initially rapid due to the impurity ternary eutectics being replaced by Al-Si eutectic and Al-Si- beta(FeSi) reactions at 577^{o}C and 576^{o}C. For the primary Al peak it is suggested that for conditions between the two limiting cases of 100% Al and 100% eutectic an ideal, linear correction could be applied to account for the changing proportions of constituents.

From the above arguments the reduction in the liquidus peak temperature can be as great as ΔTp=Tmp - Tp and as small as ΔTo=Top - Tp where Top =652^{o}C as defined above. The Tp temperature can take values over the Al - Al-Si eutectic temperature interval, which is 83.5^{o}C. The proportion of the correction Tmp - Top, found from figure 4.27, which is required to be added to ΔTo would be:

(1 - ΔTp/83.5).

Defining:

$$\Delta T(corr) = \Delta To + (Tmp - Top) .(1 - \Delta Tp/83.5) \quad \text{—(4.3)}$$

where Tp is the liquidus peak temperature on heating at 20^{o}C /min; Tmp is the peak temperature of a CP.Al - SiC sample of the same mass as the Tp sample; ΔTp=Tmp-Tp ie. the maximum peak temperature change; ΔTo=Top-Tp ie. the minimum peak temperature change. It is suggested that (ΔTp +ΔTo)/2 may provide a better first approximation to the temperature change to be substituted for ΔTp. However, expression (4.3) was used to provide corrected liquidus temperature changes ΔT(corr) for conversion to at%Si via table 4.7.

4.8.7.5 *Methods of DTA peak evaluation*

From the preceding practical considerations four treatments have been applied to the DTA data.

I) The peak temperatures can be directly converted via the Al-Si equilibrium diagram into at%Si, after Lloyd and Jin [107,108]. Similarly 'end-points' (T_{EP} in figure 4.23c for large, heavily reacted samples as approximated peak temperatures), constructed heating liquidii T_{EQ}, or cooling liquidii T_L can all be similarly used to estimate the silicon content of the matrix. The

results of this approach are plotted in figure 4.24. The heating peak temperatures Tp (and 'end-points') appear to provide values in good agreement with the EDS data. However the preceding discussion suggests that this is purely coincidental. The more logical use of the temperatures closer to the equilibrium values, T_{EQ} and T_L , suggest excessive extents of reaction, even beyond the uncorrected EDS data, as is also shown by the slower heating rate (3^oC/min) 672^oC data. No 672^oC 20^oC/min heating Tp data was available for MH87-S, but it is interesting to note that the MH85-S data is out of step with the MH87-S data suggesting the previously mentioned (section 4.8.2) effect of the ~2vol% SiC difference between the composites.

ii) The estimated equilibrium temperatures T_L and T_{EQ} can be compared with the estimated CP.Al equilibrium liquidus of 649^oC, and the difference converted to at%Si via table 4.7. (strictly the initial CP.Al Si content would be added prior to conversion). The results in figure 4.25 are in better agreement than when compared directly with the equilibrium diagram. The results do suggest that adove ~5at%Si the values tend to overestimate the matrix Si contents as determined by EDS.

iii) The corrected heating peak temperature changes $\Delta T(corr)$ can be converted to at%Si via table 4.7. A very similar result , figure 4.28, is achieved as in the case of the raw Tp type values treated in **i)** above above in relation to the EDS data. This method was adopted for data processing. Strictly a mixture of the results of the approach given in **ii)** above, and the results of this approach would have been a more objective choice.

iv) The 3^oC/min data, that is, the 672^oC curve in figure 4.28 has been found from the ΔTp estimates which were converted to at%Si via table 4.7. A very minor correction for heavily reacted 672^oC material could be made as in **iii)** above but has been neglected. The good agreement between the 672^oC curve and the EDS results suggests that the use of the Al-Si liquidus slope is valid for values <5at%Si.

4.8.7.6 *Final remarks on the processing of the DTA results*

It is suggested that the simplest use of the DTA method for the CP.Al - SiC system is to run one large sample (35mg) at $<3^oC$/min per datum point, at a fixed sample mass, and refer the peak temperature to the initial composite peak temperature found under the same conditions.

Use of the DTA at 20^oC/min was adopted to enable a high through put of samples to be achieved, given limited use of the DTA apparatus. Initially it was hoped that both heating and cooling curves could be taken, but as mentioned in 3.5.8 this was not always possible.

It is suggested that the Al-Si liquidus slope can be used effectively provided primary separation of the Al does not occur in the region of other reaction in an Al-Si-X or higher system. It will be

seen that minor impurity reactions do occur over the temperature range of the primary Al separation, and these undoubtedly lead to errors in the resulting estimated Si contents of the liquid.

4.8.8 *Comparison of the quantitative methods*

Isothermal curves showing the data collected for the MH87-S composite are shown in figures 4.29 to 4.31, assuming an initial SiC content of 12.5vol% with 0.32at%Si in the matrix.

At 672^{o}C the data lie within 1.5vol%Al_4C_3 as in figure 4.29; at 800^{o}C the points are within 0.75vol%Al_4C_3 in figure 4.30, and at 1000^{o}C 0.8vol%Al_4C_3 as in figure 4.31. The volume fraction of Al_4C_3 produced during re-melting the composite, and holding at 672^{o}C, rises rapidly initially, and the rate of change decreases after 10^4s. At 800^{o}C the volume fraction of Al_4C_3 already appears to have undergone a rapid change prior to the results measured. The Al_4C_3 content of the composite increases approximately linearly on the log scale, and reaches an apparently constant value after 1000minutes. The volume fraction of primary Al data from the WQ samples has been added to the 800^{o}C results, following the averaging of the Si content values obtained assuming the 14.5 and 16wt%Si eutectic compositions: the dotted error bars indicate the extent of the scatter with these assumptions. The amount of Al_4C_3 produced at 1000^{o}C shows a similar trend to the 800^{o}C data, except that the first portion of the data probably exhibits a slightly shallower gradient, since the addition of time error bars, for example to the 10minute datum point, would tend to reduce the gradient of the curve.

The few MH85-S data points eg. mass fraction data at 800^{o}C , and a few DTA points suggest that these two methods tend to be in disagreement: the DTA values look realistic, but the mass fraction data changes over too great a range although the trend is as expected. It is feasible that very fine SiC residue due to the reaction could be lost during filtration to give the high gradient on the mass fraction data, though microstructural observations suggest that the proportion of sub-0.7micron SiC particles produced following even heavy reaction will be very small: the method still requires further assessment.

A results summary has been given in figure 4.32, where the results of the three principal methods have been averaged with equal weighting. The initial SiC content of the MH87-S has been assumed to be either 10.5 or 12.5vol% to examine the variation introduced into the results: the scatter is small over the range of the reaction studied. The maximum Al_4C_3 volume fractions would be 13.26 and 15.73vol% for 10.5 and 12.5vol%SiC respectively, by which stage errors in the initial SiC content would become more important.

4.9 Kinetic data collected for the deduction of mechanisms

A thermal analysis method was utilised to provide semi-continuous monitoring of the reaction isothermally in MH85-S as a single bulk sample via the change in the matrix liquidus. The

earliest stages of the reaction, not accessible by the above method, was investigated by rapidly heating small samples of composite to the isothermal re-melting temperature, and performing DTA on the sample after the re-melting treatment

The results are analysed to provide activation energy values using the 'time to a given fraction of transformation' method [166]. Since the reaction was found to consist of at least three stages, neither the fitting of a simple kinetic function nor mathematical modelling were attempted, though a possible model is outlined in the suggestions for further work.

4.9.1 *Measured temperatures*

The actual recorded thermal analysis arrest temperatures and all DTA sample peak temperatures are shown in figures 4.33 to 4.37. The results in table 4.3 show that the re-melted CP.Al - SiC matrix contains $(FeSi)_2Al_5$, $(FeMn)_3(SiCu)_2Al_{15}$ and Si. The reactions in which these constituents are involved, according to [167], which could correspond to some of the peaks recorded are:

$L + Fe_2SiAl_8 \text{ ----> } FeSiAl_5$ at 612°C;

$L + Fe_2SiAl_8 \text{ ----> } Al + FeSiAl_5 + (FeMn)_3Si_2Al_{15}$ at ~600°C;

$L \text{ ----> } Al + Si$ at 577°C;

$L \text{ ----> } Al + Si + FeSiAl_5$ at 576°C;

$L + FeSiAl_5 \text{ -----> } Al + Si + (FeMn)_3Si_2Al_{15}$ at 565°C.

All the DTA data collected shows similar trends, independent of the isothermal temperature of the re-melt, except that the minor thermal events at short times on the diagrams 4.33 to 4.37 are lost as the reaction temperature, and the kinetics of the reaction, increase. After extensive reaction only two peaks are apparent, though these can be considered as the sum of several peaks: the impurity peaks likely to affect the position of the assumed primary Al peak will exert small but measurable changes on 'the peak' position. It is apparent that the 'eutectic peak' temperature moves to higher values, problably commencing at ~570°C due to the 565°C reaction indicated above. The addition of further Si takes the 'eutectic' to ~576°C and potentially beyond as the amount of eutectic in the DTA sample increases, however due to the small DTA sample size used the latter effect will be initially neglible.

The 715°C thermal analysis data is unreliable beyond 10^5s (figure 4.34) probably due to either excessive oxidation of the sample, eventual partial dissolution of the thermocouple or both; the first two results obtained with a partially inserted thermocouple were neglected in further analysis.

4.9.2 *Comparison of thermal analysis data*

Average eutectic temperatures were calculated for the thermal analysis results, and were assumed to be constant and the result of the same set of invariant reactions for each set of isothermal data. Plotting the difference between the primary arrest temperature and the

appropriate eutectic arrest temperature, for each set of isothermal data, against time, figure 4.38 was produced. Due to the different method used to collect data for the 672^{o}C thermal analysis result this has not been incorporated: the eutectic is shifted further to higher temperatures compared to the amount the primary arrest is altered during the natural heating compared to when the heating rate is more constant over the melting range of the matrix alloy as in the case of the furnace heating.

From the estimates of the initial furnace heating rates (table 3.4), and the general agreement after sufficient reaction between the DTA and thermal analysis eutectic temperature estimates, it is suggested that the 715, 760, 800 and 850^{o}C data could be compared. Time errors have been added to the data in figure 4.38 due to the combined time spent at the primary arrest temperature and that time spent heating the liquid matrix to the isothermal temperature.

Best fit lines were placed through the open symbols in figure 4.38, neglecting those points for which the time errors were substantial. Two lines were placed through the 850^{o}C data: the first through the larger data set from the first sample, and the second line incorporates data both from the first sample and a second sample. The second line was judged to be more reliable, since the second set of data compensates for anomalous behaviour in the last points in the first data set, probably the result of unwanted reactions eg. excessive oxidation, or thermocouple dissolution.

The activation energies, given in table 4.8 under 'stage2' , are derived from Arrhenius plots, three of which are shown in figure 4.46. Since these values tend to be based on extrapolations of the kinetic data large uncertainties are introduced into the results ie. as a result of the assumption that the same kinetic mechanisms are operating to the extrapolated times.

4.9.3 *Rapidly heated re-melted samples*

The change in the liquidus peak temperature for the DTA samples was plotted as in figure 4.39. Apart from the overlap in some 800^{o}C and 760^{o}C data, and the excessive scatter in one set of 715^{o}C data, four well defined isothermal curves were produced. Time errors, ie. the time between the end of the melting and reaching the isothermal temperature, were added.

Zero isothermal time results have been placed at 1s, which is justified on the basis of the 'time errors'. A curve fitted to the 672^{o}C data, in figure 4.39, and simply translated to fit approximately with the other isothermal sets of data has been included to produce a set of isokinetic curves. Generally a reasonable fit for the isokinetic curves is achieved, as judged by eye, however it is clear that following the more extensive reaction at 760^{o}C and 800^{o}C the isokinetic hypothesis fails, suggesting that the kinetic mechanism changes for the range of times and temperatures in figure 4.39, although this simple analysis places too much weight on the last of the 672^{o}C data points. The activation energy derived from the isokinetic curves will

be a constant 258+/-30kJ/mol. The uncertainty in the activation energy being that due to the non-calibration of the thermocouples used. The error was estimated as +/-0.75% of the indicated temperature, as suggested for K-type thermocouples [168]. This treatment of the error appears to be reasonable: a selection of thermocouples as used to measure the melting arrest temperature of the MH85-S in the thermal analysis experiment gave less scatter than suggested above even when compounded with the added variations in the experimental conditions (which would tend to increase the scatter).

When the peak liquidus temperature change data, as in figure 4.39, is plotted with the same data derived from the DTA of bulk re-melted samples (eg. see figures 4.29 and 4.30) and with the thermal analysis liquidus arrest temperature change results, two distinct regions of the kinetic curves emerge, with a change in the kinetics at ΔTp values ~24 - 28^{o}C (as in figures 4.40 - 4.43). The first region denoted 'stage 1' corresponds almost directly with the data range in figure 4.39, and the isokinetic test suggests that the same mechanism is controlling 'stage1'. In the second stage, 'stage2' , the reaction occurs at a lower rate, and the kinetics are approximated by a linear curve when plotted on a log time scale. The previously discussed MH87-S data shows similar trends, as shown by the 672^{o}C data in figure 4.32; at higher temperatures data for stage 1 is absent owing to the limitations of the methods originally employed.

Plots of ΔT(corr) have been included in figures 4.40 - 4.43. All the curves are fitted by eye, as opposed to the use of a single curve as in figure 4.39. The placing of the thermal analysis data in figure 4.41 was made assuming that the heating conditions to 715^{o}C were the same as to 760^{o}C, such that the the 760^{o}C initial melting arrest temperature could be used to estimate the changes in the 715^{o}C arrest temperatures: this approach being necessary since the initial 715^{o}C data was corrupted as previously noted.

The second stage of the curves in figures 4.40 - 4.43 were extrapolated and reproduced on figure 4.44. The end of stage 2 was judged to be ~1000minutes at 800^{o}C as suggested in the MH87-S results. Two maximum activation energies for stage 2 are found: 853kJ/mol and 571kJ/mol for the ΔT(corr) and ΔTp results respectively. The extrapolation would inevitably be erroneous. Exclusion of the 672^{o}C data for stage 2 reduces the activation energies to 631kJ/mol and 566kJ/mol for ΔT(corr) and ΔTp results respectively.

4.9.4'*Stage1' activation energies*

As a function of time the ΔTp curves for the rapidly heated re-melted MH85-S samples show a rapid increase followed by a very gradual increase, as in figure 4.45. Times (to a given extent of reaction) were taken at fixed ΔTp values, and activation energies calculated. The required times were found using figure 4.45, and the ΔTp curves in figures 4.40 - 4.43 (where necessary to find the times corresponding to a given extent of reaction when the times extend beyond

those covered in figure 4.45). The resulting activation energies are given in table 4.8, and the Arrhenius plots in figure 4.46. The correlation for the series of Arrhenius plots was >+0.99, though the errors in the activation energies due to the temperature measurement were +/-20 to +/-30 kJ/mol.

4.9.5 *Summary*

In the reaction (4.1) of the CP.Al -SiC composites containing 10.5 - 12.5vol%SiC particulate, there are at least three stages in the temperature range 672^{o}C to 800^{o}C :

i) an initially rapid stage with an activation energy of 260+/- 42kJ/mol;

ii) a slower stage where the activation energy increases from 270kJ/mol up to ~570 - 900kJ/mol;

iii) a very slow stage where either the reaction has saturated or the activation energy is>=570 - 900kJ/mol.

4.10 TTT diagrams

4.10.1 *Introduction*

Time-temperature-transformation diagrams were constructed using data for both the MH87-S (CP.Al + 10.5vol%SiC) and MH85-S (CP.Al + 12.5vol%SiC) composites. For MH87-S two sets of data were used separately in the construction of the TTT diagrams: the averaged DTA, EDS and volume fraction of primary Al results given in figure 4.32, and the ΔT(corr) data given in 4.28. For the MH85-S the ΔT(corr) data in figures 4.40 - 4.43 were utilised ie. curve 2 in each figure. Then either the Si content of the liquid after a given time was found (figure 4.47) or the times to reach a predetermined '% of transformation' or vol%Al_4C_3 were found (figures 4.48 - 4.51) from the data selected above, using conversions where necessary.

The '% transformation' under isothermal conditions was defined as:

$$\% = 100.\ \Delta T(corr)(t) / \Delta T(corr)(f);$$

or:

$$\% = 100.\ \{XSi(t) - XSi(0)\} / \{XSi(f) - XSi(0)\} \text{ approximated to } 100.XSi(t) / XSi(f);$$

where ΔT(corr)(t) is the value of ΔT(corr) at time t ; ΔT(corr)(f) is the predicted maximum ΔT(corr) value at the end of the reaction; and XSi(0) is the initial composite Si content; XSi(t) is the Si content of the matrix liquid following reaction for time t ; and XSi(f) is the predicted Si content of the matrix liquid at the end of the reaction.

The end of the reaction was predicted by calculation as in section 4.3.4. The composites studied would, based on the calculation completely dissolve above some temperature in the range studied forming a two phase equilibrium. The appropriate curves for the XSi(f) values are plotted in figure 4.47. An alternative, semi- empirical, estimate of the end of the transformation

was also used, based on the translation of the calculated equilibrium curve, referred to as curve 'C' in figure 4.47, to pass through points 'a' and 'b' previously given in table 4.2. The semi-empirical curve 'C' was judged to increase linearly from 5.9at%Si at 672^{o}C to 12.0at%Si at 1000^{o}C.

4.10.2 *TTT curves: discussion*

The diagrams constucted shown in figure 4.47 and 4.48 are for practical purposes ie. to act as a source of information. The changes in matrix chemistry are potentially useful for predicting the change in the matrix Si content during the arbitary re-melting of similar composites. The Al-Si binary phase diagram is included in figure 4.47 to show approximately how the matrix microstructure will evolve on solidification. The amount of C in precipitated as Al_4C_3 on cooling would be neglible over the temperature range studied and under practical cooling conditions the chemistry of the liquid can be expected to remain approximately constant during cooling until the separation of Al dendrites occurs.

Data was reprocessed to produce figure 4.48 in which the time to reach a given volume fraction of Al_4C_3 is presented. The MH85-S composite leads the MH87-S composite by ~1vol%Al_4C_3 . At 1000^{o}C an effective kinetic barrier is seen to require 7 - 8vol%Al_4C_3 which corresponds to the loss of about 60% of the SiC in an initially 10.5vol%SiC based composite. Figure 4.49 shows the '% transformation' for the MH85-S and MH87-S data using the calculated transformation end-points and the end-points appropriate to each composite.The diagram suggests that the transformation in each composite is at a similar extent of completion after 40 - 50% transformation. The early MH87-S data at 10 - 20% transformation is not very reliable due to time errors. By using the same set of transformation end-points for both the MH87-S and MH85-S data as in figure 4.50 the reaction in the 12.5vol%SiC composite MH85-S increases to ~9% of the transformation ahead of the 10.5vol%SiC composite MH87-S. Assuming the initial volume fractions of SiC to be as given, the difference in the extent of the reaction is not as great as would be predicted if the reaction kinetics increased proportionately with the amount of SiC, or more specifically the surface area, ie. 20%. At a high initial SiC powder content of a similar or smaller particle size than used in this study the reaction could be completed via stage 1 processes alone, allowing the single mechanism to be described more analytically.

Finally, figure 4.51 uses the MH87-S data and the semi-empirical end-points for the transformation. This treatment suggests that the reaction has only reached a maximum of about three quarters completion. It is interesting to note that the overall reaction rates are highest in the mid-temperature range. This is a consequence of the changes in the reaction mechanisms. The reaction, after a very rapid start at 1000^{o}C, lags behind the reaction at 800^{o}C after ~55% completion. The reaction at 800^{o}C remains just ahead of that at 672^{o}C until 10^{6}s. It is not clear whether the reaction at 672^{o}C has become very sluggish, or else is approaching saturation, the end-point predictions being erroneous. Comparison with Viala *et al*

's [94] data in figure 4.6 suggests that the 800^{o}C reaction is effectively saturating, but the maximum 672^{o}C matrix Si content measured in this study is approximately twice that suggested by [94].

4.11 Activation energies

The activation energies in table 4.8 can be attributed to two processes, taking the microstructural results into consideration.

According to [169] the C-Si bond energy is 250 - 335kJ/mol. The experimental activation energy of 260+/-42kJ/mol for stage1 of the reaction can be correlated with this result, as suggested by Choh and Oki [109]. Choh and Oki [109] determined the activation for the wetting of SiC by various Al alloys and obtained activation energies of 327, 330, and 335 kJ/mol which they compared with a SiC bond strength in the literature of 327kJ/mol: their analysis of the kinetic data provided rate constants with the units (time)$^{-2}$ and so a direct comparison of the activation energy presented here cannot be made. However it is the opinion of the current author that the activation energy can be expected to lie below estimates of the bulk SiC bond strength due to a degree of bond formation with the adjacent liquid Al atoms, especially involving the surface C atoms, and likely to involve the Si atoms as suggested for solid Al-SiC interfaces [116]: C and Si atoms will leave the SiC surface at different rates but the overall reaction SiC ---->Si + C will produce products in a 1 to 1 ratio if it is assumed that C diffusion to the SiC surface from the bulk SiC will be negligible. In stage 1 of the reaction studied here much of the SiC surface remained reaction product free. A SiC surface atom will be able to escape into the melt in a stepwise fashion eg. an atom at a kink site will diffuse onto a ledge site, and then onto an adatom site from which, perhaps following some surface diffusion, complete escape into the melt results: the activation energy to move from one type of site to the next will be of the order of 'a bond energy' but would correspond more closely to the vaporisation energy, and larger jumps will be much less probable.

Activation energies for substitutional self-diffusion in carbides can be estimated from:

$Q/(R.Tm) = 22 - 26$;

where Q is the activation energy for diffusion in kJ/mol; Tm is the carbide's melting point /K; and R is the universal gas constant in K /kJ/mol [170]. Using Al_4C_3 decomposition temperatures given in the literature of 2156 - 2223^{o}C gives a Q value ~440 - 540kJ/mol : these results are only to illustrate the order of magnitude expected for solid-state diffusion processes. The experimental activation energy for stage 2 rises from 270kJ/mol to 570 - 900kJ/mol prior to the onset of stage 3. The evidence therefore that the reaction becomes diffusion controlled is that the activation energy is of the right order, and that the interface product is seen to become continuous from the microstructural observations.

The discrepency of ~200kJ/mol between the activation energies at the end of stage 1, and that at the begining of stage 2 as estimated from the data in figure 4.38, leaves little confidence in the method by which the data has been necessarily extrapolated to obtain the time values for the 'time to a given fraction of transformation' analysis of the kinetic data.

4.12 Correlation of the quantitative results with the microstructural analysis

The quantitative kinetic analysis suggests that the reaction exhibits three distinct stages, as in figure 4.53. The initial rapid stage 1 is characterised by an activation energy for the initial rate controlling process of 260kJ/mol suggesting that the Si-C dissolution step is unimpeded. Micrographs showing details from this stage were presented in figures 4.10, 4.11, and 4.13. It is evident that the nucleation and initial growth of the Al_4C_3 crystals at the interface is the dominant feature of the first stage of the reaction. For the nucleation to occur at the interface a high supersaturation of C needs to be produced in the melt. The sites where nucleation is dominant are those sites where the supersaturation of C necessary for nucleation of Al_4C_3 is reached first. Such areas of the SiC surface are the asperities, for example, and a proportion of the transgranular SiC fracture surface, characterised by a higher than average density of surface steps, and ledges etc. Once nucleation and the initial platelet coarsening has occurred the areas where dissolution takes place at the highest rate per unit area are covered, and the reaction rate reduces dramatically as stage 2 is approached. Further nucleation does not take place due to the population of growing Al_4C_3 crystals, which can grow at a lower supersaturation than is needed for nucleation, preventing the level of C in the melt attaining a high enough level of supersaturation of C for further nucleation as supplied by the dissolution process.

Stage 2 of the reaction in which the activation energy rises to ~570 - 900kJ/mol, is dominated by the remaining lateral growth of the Al_4C_3 product. This process leads to the gradual separation of the dissolving SiC from the liquid Al alloys, blocking the remaining effective dissolution sites. The activation energy increases as a significantly increasing proportion of the reaction product is produced following the inclusion of a solid state diffusion process, with a decreasing proportion of the reaction product forming following the dissolution of SiC in direct contact with the melt.

The final stage of the reaction, shown by the material reacted at 1000^{o}C in figures 4.15, and 4.16, and perhaps, but not so convincingly so, by the 1000minutes at 800^{o}C sample in figure 4.14, is the stage where the SiC is completely separated from the melt by the polycrystalline Al_4C_3 interface product. 'Stable' L-SiC facets can remain, the activation energy for dissolution from these sites being of the same order as for the solid state diffusion processes, if not higher. SiC facets will tend to continue to form at the SiC - Al_4C_3 interface as existing surface ledges are removed by solid-state diffusion: the reaction kinetics could become controlled by a still more difficult process than the diffusion through the interface product if the amount of SiC

faceting becomes extensive. Diffusion from the SiC surface will probably occur preferentially across the SiC -Al_4C_3 surface, and through short circuit paths in the Al_4C_3 .

The SiC reacted at 672^{o}C for 10 000minutes produces ~6vol%Al_4C_3 which is sufficient to significantly reduce the reaction kinetics at 1000^{o}C. Micrographs show that the SiC at this stage at 672^{o}C still exhibits some SiC - L interfaces other than cleavage facets. It remains unresolved, therefore, whether the reaction at 672^{o}C is in fact reaching saturation, or being subject to a combination of the low temperature, and the beginning of the kinetic barrier effect experienced at 1000^{o}C.

4.13 Further work

1). An analytical model for the reaction could be produced to generate the correct form of the experimental kinetic curves produced in this study and to predict the behaviour of different Al-SiC composite systems in which the following parameters are involved:

i. the total area of SiC surface per unit volume of composite A;

ii. define areas of interface characterised by their rate of dissolution per unit area eg. area type 1, 2 and 3 as A1, A2 and A3 where A1 + A2 + A3 =A;

iii. assign dissolution rates per unit area D / kg of C per square metre for each type of interface in i. eg. D1,D2 ,D3;

iv. define the rate of SiC surface area coverage by Al_4C_3 of each type of interface ie. model the Al_4C_3 growth rate, which follows the dissolution rate, assuming that the growth rate is a function of the local dissolution rate K1=f(D1) etc;

v. define the rate of dissolution via solid state processes D4 /kg of C per square metre where D4 is of the same order as D3;

vi. then generate curves of $\sum_{i=0}^{n}$volume fraction of Al_4C_3 formed in time $\delta t'_i = Z\sum_{i=0}^{n}\{$ D1.(A1 -δt.K1) + D2.(A2 -δt.K2) + D3.(A3 -δt.K3) + D4δt.(K1 + K2 + K3)$\}_i$ against time t^*, where Z is a constant and where at time t=0 the the volume fraction of Al_4C_3 =0, and K is initially assumed to be time independent.*(t=$i.\delta t$).

From an appropriate choice of the above parameters a series of curves can be generated, and the experimental results could be fitted, where for example D1>>D2> D3 ~D4 and A1=A3 <<A2 ie. a permutation based on the experimental evidence. Many of the necessary parameters could be determined experimentally eg. further work suggestion 2 below. A feedback of the reducing surface area will need to be included especially if the initial amount of SiC is small or the extent of the reaction is large. A temperature dependence can be readily added.

2) The relative dissolution rates for the different types of SiC surface could be determined from Al-SiC couples produced by sputtering Al onto prepared and characterised surfaces on single

crystal SiC. An area of cleavage surface {00.1}, and a surface created by fracturing the crystal (by fatigue) in an attempt to create a {10.0} type surface could be compared to test whether a significant difference in dissolution rates exists by melting the Al for a short period and performing a quantitative analysis of the alloy layer produced. Other surface types could also be tested. The 'areas' would need to be measured macroscopically and characterised by BET.

3) The reaction could be monitored in the temperature range 1000^{o}C to 1400^{o}C in order to provide more data on the process giving rise to the kinetic barrier effect.

4) Composite produced from Al with the SiC being of the platelet type morphology which is commercially available could be considered. Two composites: one with a conventional grit and the other made with the platelet SiC could be compared, with respect to the reaction rates above the matrix liquidus, where the particle sizes and volume fractions of the SiC are initially similar.

6) The precipitation kinetics of Al_4C_3 from a carbon saturated Al melt could be examined. An Al-graphite couple could be equilibrated at 700^{o}C-1400^{o}C, quenched to various liquid temperatures, and held for various lengths of time, followed by quenching to RT. The aspect ratio of the plates formed freely in the melt could be measured as a function of temperature, time, and C supersaturation.

Figure 4.1

Light micrographs of MH87-S (CP. Al + SIC) both as-produced and following arc-melting

a. As-sprayed CP.Al + SiC (MH87-S) : unetched. Features visible include voids (black), SiC particles (mid-grey), and Al (white)

b. As in **a** above.

c. As in **a** above except that the features seen are SiC particles (dark grey), impurity phases (pale grey as indicated by arrows), and the Al matrix (white).

d. As-sprayed CP.Al+ SiC (MH87-S) following anodising with Barkers' reagent. The micrograph was produced with a polarising microscope. The SiC particles are as arrowed, residing at the grain boundaries.

e. CP.Al + SiC (MH87-S) following arc-melting. The features present include Al_4C_3 (dark grey / faceted), quench modified Al-Si eutectic (speckled mid-grey), and Al dendrites (white). The sample was unetched.

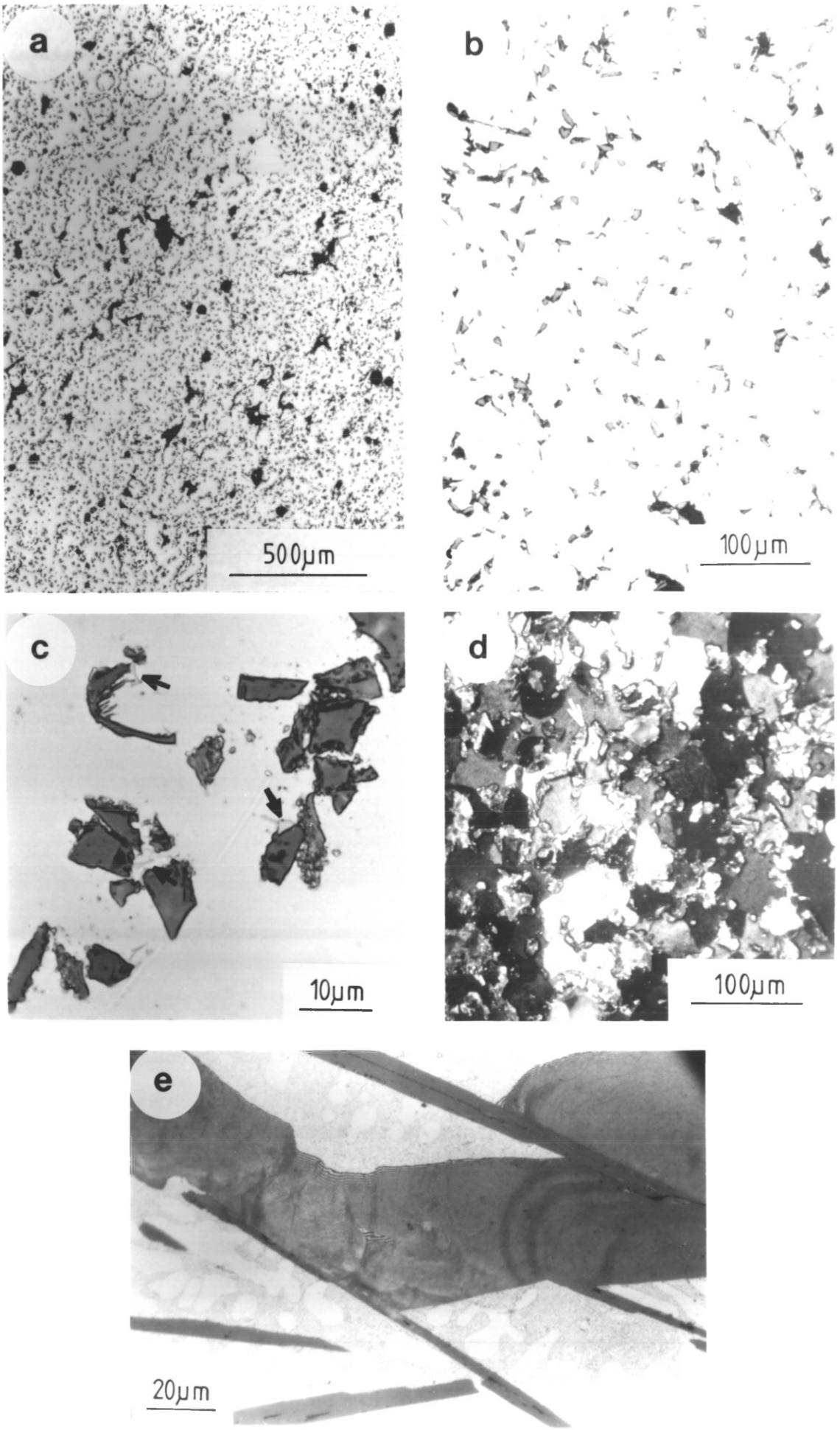

a
500µm
b
100µm
c
10µm
d
100µm
e
20µm

Figure 4.2

Micrographs of starting material MH85-S (CP.Al + SiC)

a SEM SEI micrograph of deep electrolytically etched CP.Al + SiC (MH85-S) as hot-extruded. Banding of the SiC along the extrusion direction is evident. SiC particles are bright, the matrix is dark. Clusters of particles are evident eg. as arrowed.

b. TEM micrograph at 100kV. Bright field (BF) of CP.Al + SiC (MH85-S). Grain boundary intermetallic indicated by the arrow. SiC particles are labelled 'S'.

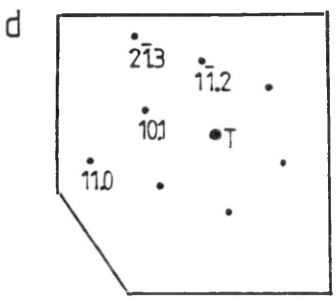
c TEM micrograph at 100kV. BF of MH85-S showing fractured SiC particle 'S' and interfacial impurity phase(s) eg.'F', and void above 'V'.

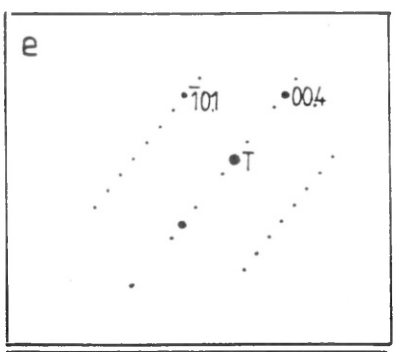
d. TEM micrograph at 100kV. BF of intense crushing damage on 6H SiC particle eg. at 'D'. Sheared portions of crystal displaced parallel to <11.0> directions. Note dislocations in regions arrowed. The BF was taken with the particle tilted off the [00.$\bar{1}$] zone axis and onto the [1$\bar{1}$.$\bar{1}$] SADP as in the inset (λl=2.68nm.mm).

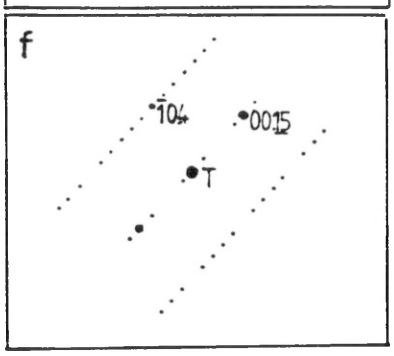
e. TEM SADP of 4H SiC [1$\bar{2}$.0] zone (λl=2.73nm.mm).

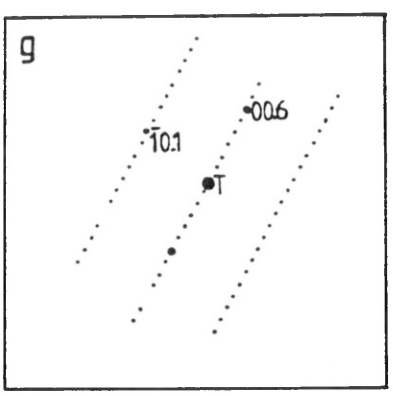
f. TEM SADP of 15R SiC [1$\bar{2}$.0] zone (λl=2.53nm.mm).

g. TEM SADP of 6H SiC [1$\bar{2}$.0] zone (λl=2.66nm.mm).









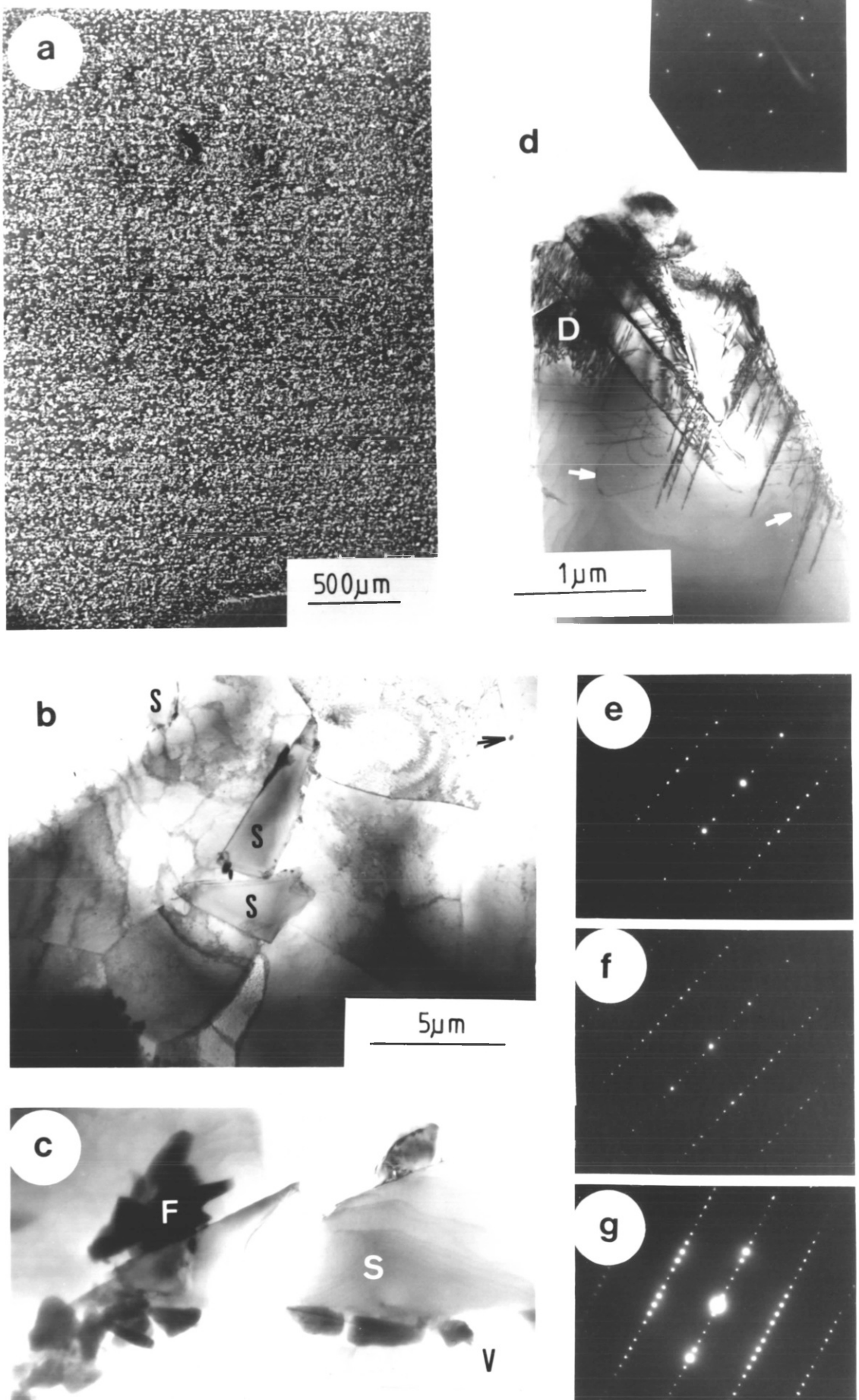

a
500µm
d
D
1µm
b
S
S
S
5µm
e
f
g
c
F
S
V
1µm

Figure 4.3

SiC surface morphology

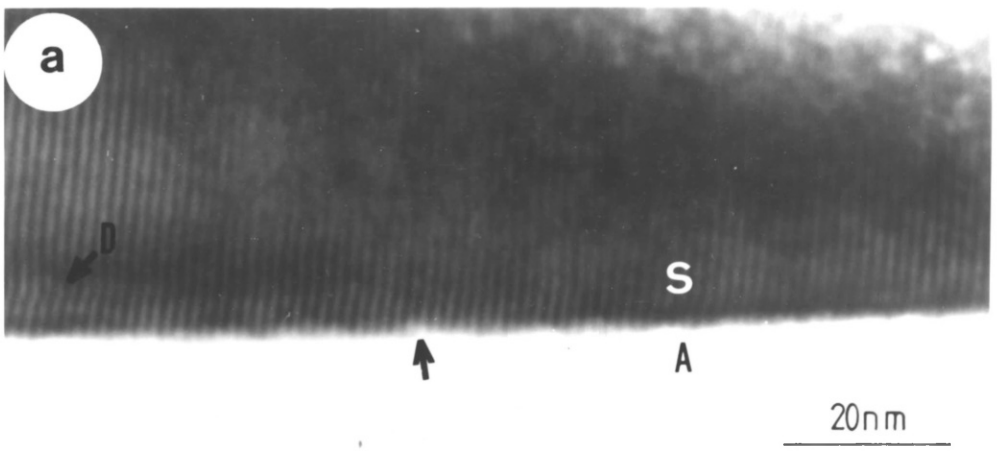
a. TEM micrograph at 100kV. BF of as-supplied MH85-S Al-SiC interface with the SiC at 'S' and the Al at 'A' showing {00.6} 6H SiC fringes (1.5nm spacing). Note interface roughness eg. arrowed. Fringes deviate at 'D' possibly due to underlying Al or as a result of thickness changes in the SiC [153].

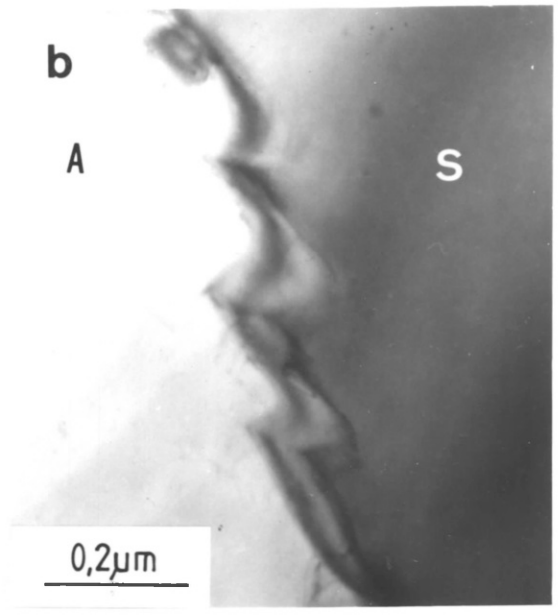
b. TEM micrograph at 100kV. BF of as-supplied MH85-S showing a section through asperities in the SiC at 'S' with the Al at 'A'.

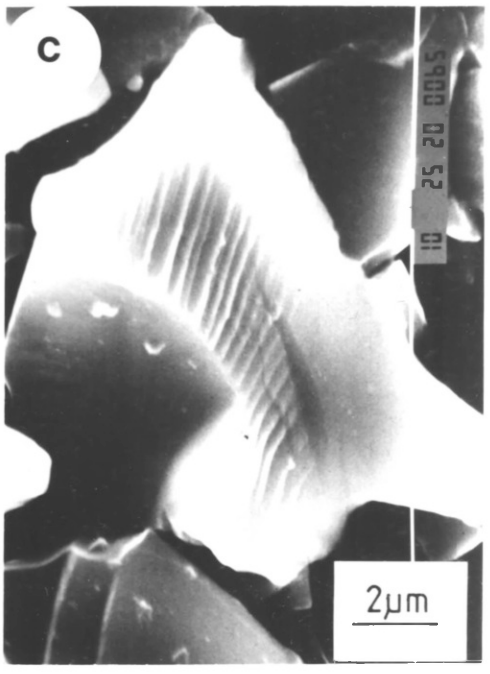
c. SEM SEI micrograph of extracted SiC particle from as-sprayed Al-19Si-SiC (202-19) prepared with the acid mixture treatment. Surface ridges (asperities) are evident.

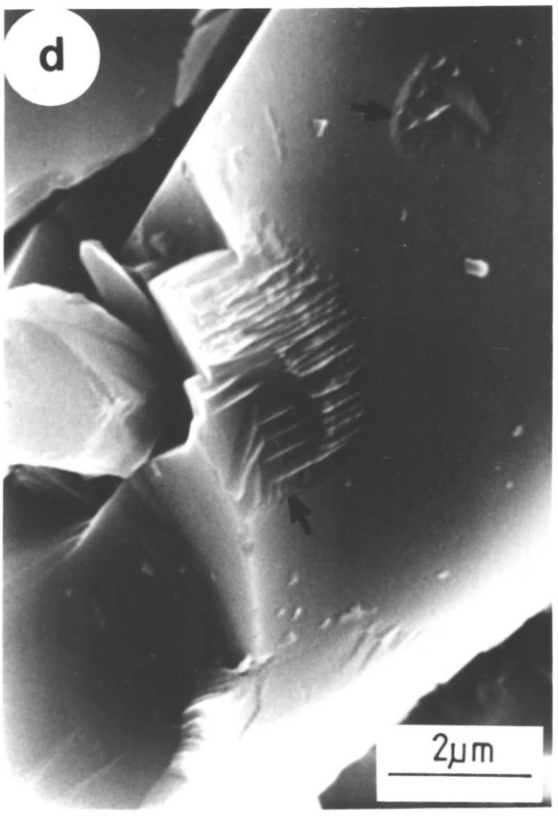
d. SEM SEI micrograph of deep electrolytically etched MH85-S material showing a detail on a SiC particle surface. Note surface structure within what appear to be 'exposed voids', the edges of which are arrowed.

e. SEM SEI micrograph of deep electrolytically etched MH85-S material following rapid heating to715^{O}C and a prompt air-cool. The particle exhibits a complex surface structure: compare with the 'void' features in **d.** above.


a
D
S
A
20nm


b
A
S
0,2µm


c
2µm


d
2µm

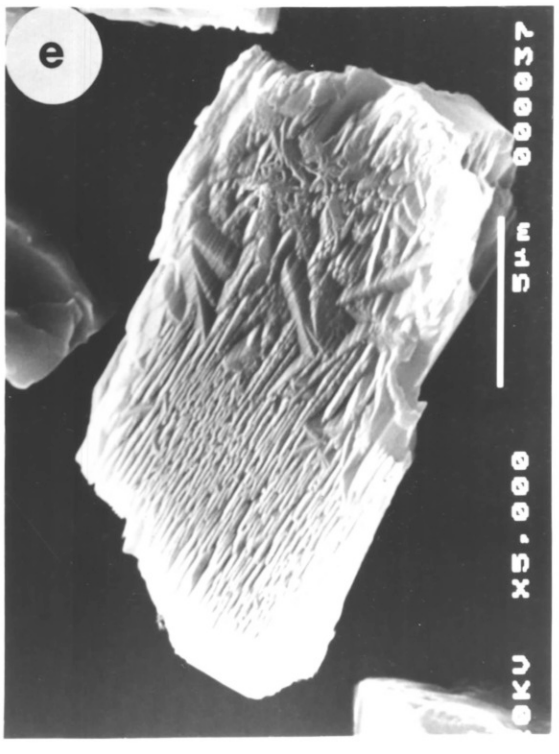
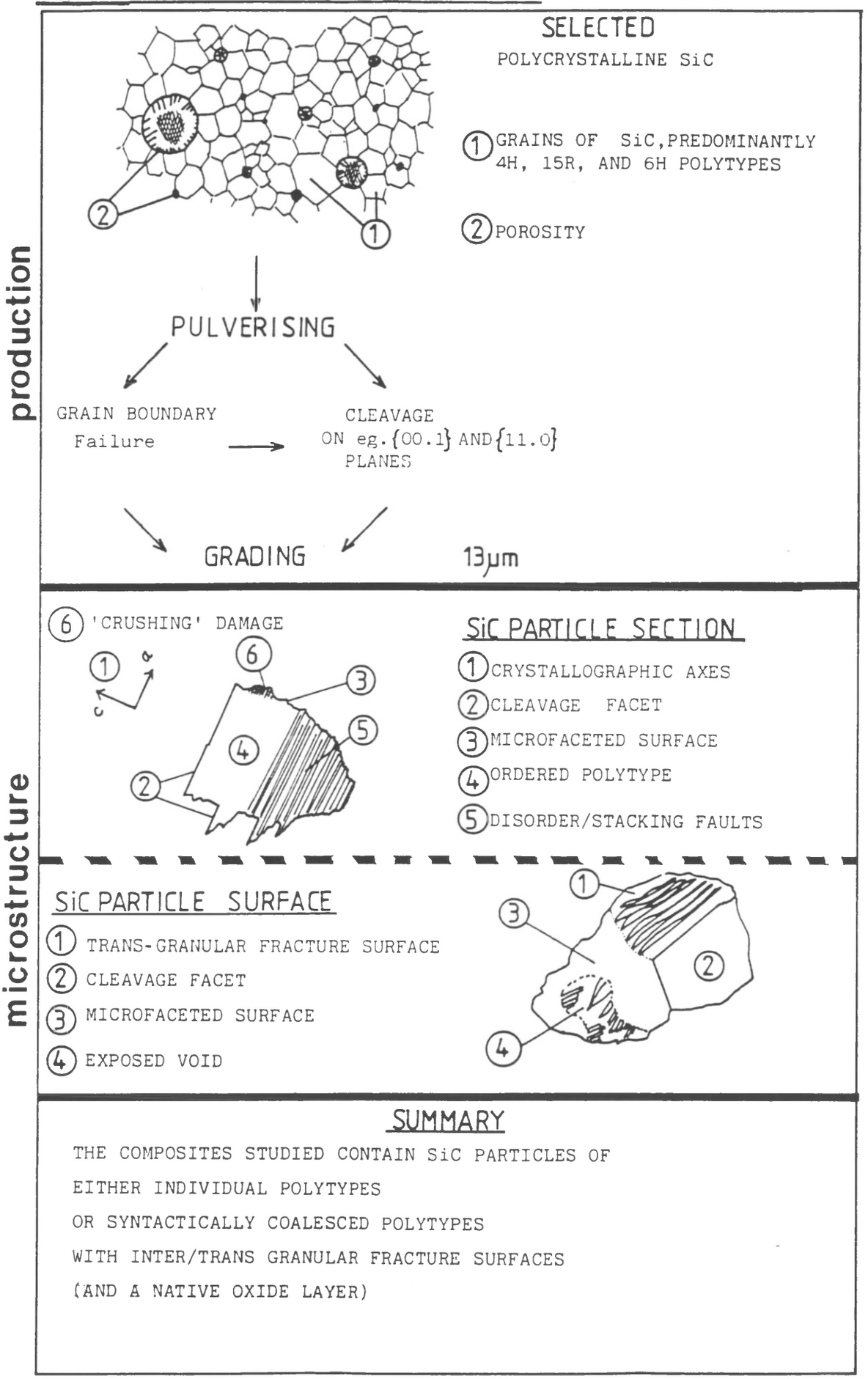

e
5µm 000037
XS,000

Fig.4.4 SiC Particle Morphology: schematic



SUMMARY

THE COMPOSITES STUDIED CONTAIN SiC PARTICLES OF
EITHER INDIVIDUAL POLYTYPES
OR SYNTACTICALLY COALESCED POLYTYPES
WITH INTER/TRANS GRANULAR FRACTURE SURFACES
(AND A NATIVE OXIDE LAYER)

Figure 4.5

Micrographs of re-melted CP.Al +SiC

a. Light micrograph of MH85-S re-melted at 800^{o}C for 100mins and cooled at 20^{o}C/min following a DTA run. The features are: 'A' Al dendrites; 'E' the Al-Si eutectic ; and the dispersed black particles in the eutectic are the reacted SiC particles.

b. SEM SEI micrograph of MH85-S re-melted 30minutes at 800^{o}C and cooled at 1^{o}C/min. The sample was lightly etched in 0.5%HF(aq). The features are: 'A' Al dendrites; 'E' the Al-Si eutectic ; and the dispersed black particles in the eutectic are the reacted SiC particles. A bright impurity phase crystal is arrowed. The white bar length is 100microns.

c. Light micrograph of MH87-S re-melted at 972^{o}C for 100minutes and AC (air-cooled). The sample was as-polished. The phases shown are as in **d**. below.

d. Light micrograph of MH87-S re-melted at 972^{o}C for 100minutes and AC (air-cooled). The sample was as-polished. Phases present are: 1 - Al matrix; 2 - SiC ; 3 - Al_4C_3 ; and 4 - flake Si.

e. SEM SEI micrograph of MH87-S re-melted at 800^{o}C for 1000minutes and WQ (water-quenched). The sample was lightly etched in 0.5%HF(aq). The reacted particle distribution is evident,the SiC appearing bright, the Al-Si eutectic grey and the Al dendrites black (Al_4C_3 is not readily discernable). Note the large particle-free areas eg. at 'X'. The bar indicates 100microns.

f. As in **e**. above. Detail revealing faceted Al_4C_3 interface phase. The Al matrix is labelled as 1; the SiC as 2; the Al_4C_3 as 3; and the quench modified eutectic as 4. The bar indicates 10microns.

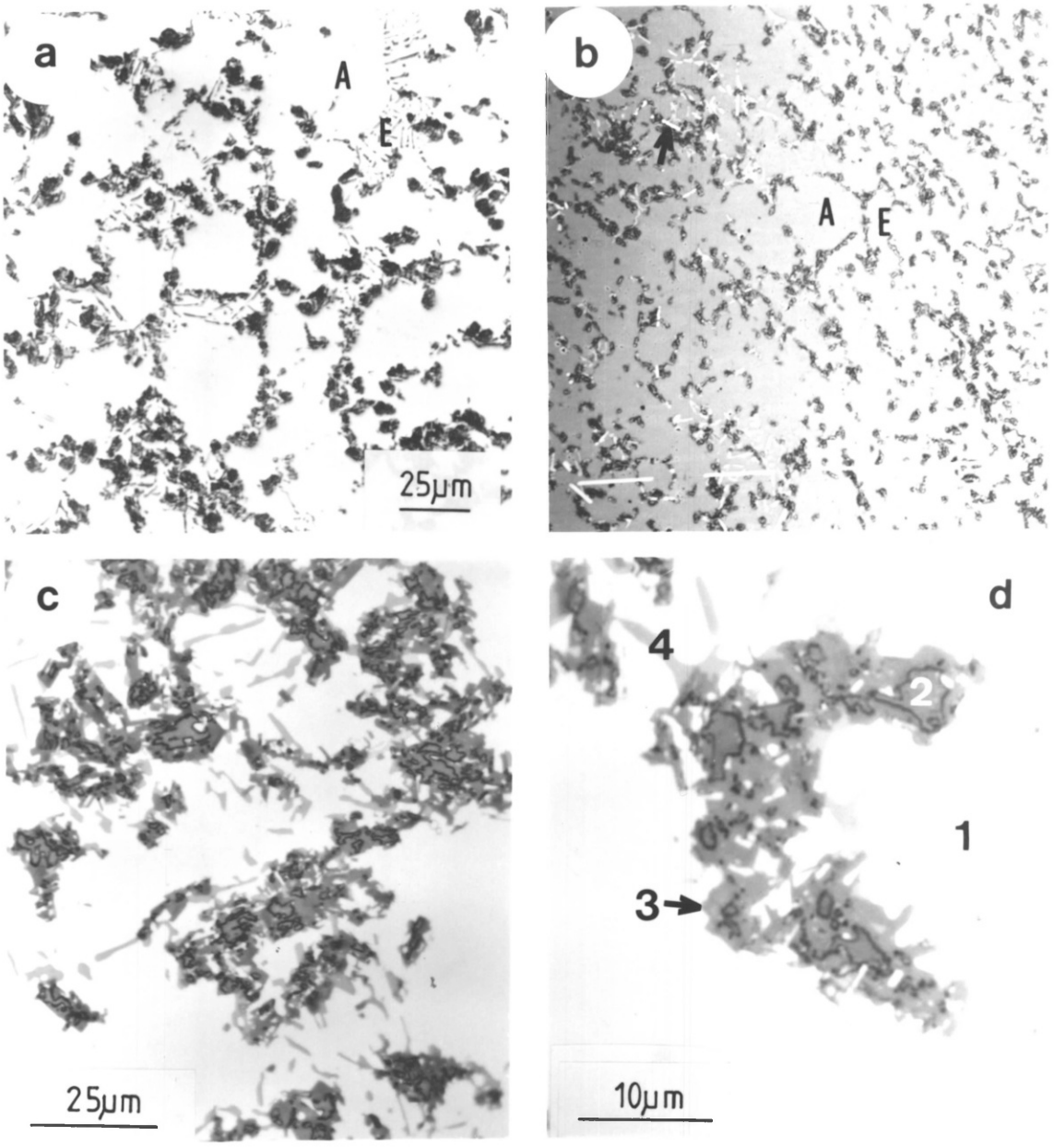

a
A
E
25µm
b
A
E
c
25µm
d
4
2
1
3
10µm
e
X
f
2
3
1
4

Figure 4.6 Si content of the Al-Si-C liquid in metastable equilibrium with SiC and Al_4C_3

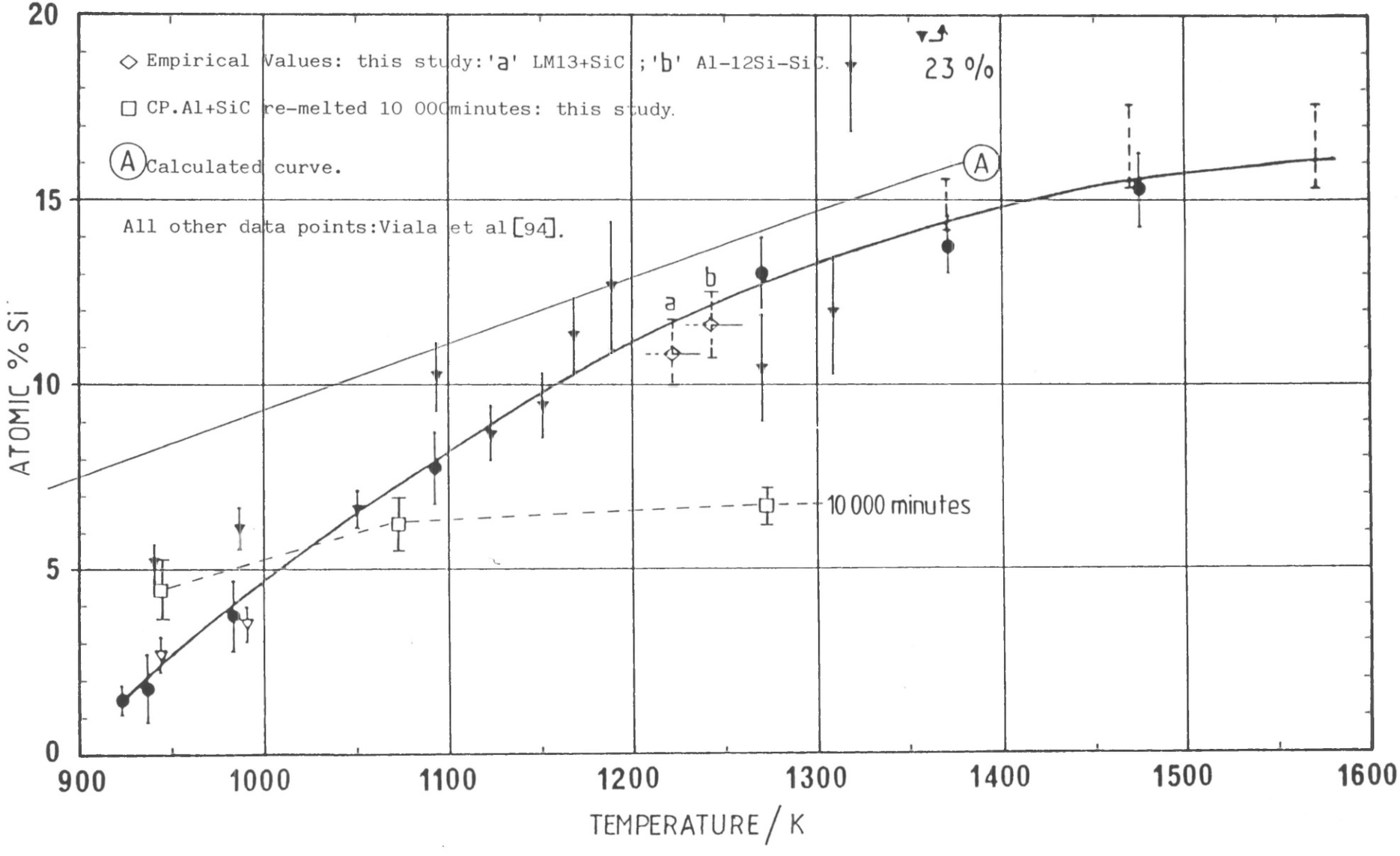


Figure 4.7

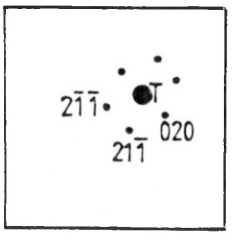
Miscellaneous micrographs

a. Light micrograph of MH87-S following re-melting at 800 ^{o}C for 1000minutes and AC. The sample was unetched. Blocky, faceted Al_4C_3 ,eg. at 'X', segregated within the cast.

b. Light micrograph of MH87-S following re-melting at 800 ^{o}C for 1000minutes and AC. The sample was unetched. 'Rogue' particle labelled as 1, and its interface product labelled as 2.

c. SEM SEI micrograph. A sample of MH87-S was re-melted 1000minutes at 800^{o}C and AC. The particle shown was in the residue collected following treatment of the sample with the acid mixture. Facets on the SiC surface are labelled 1 - 5.

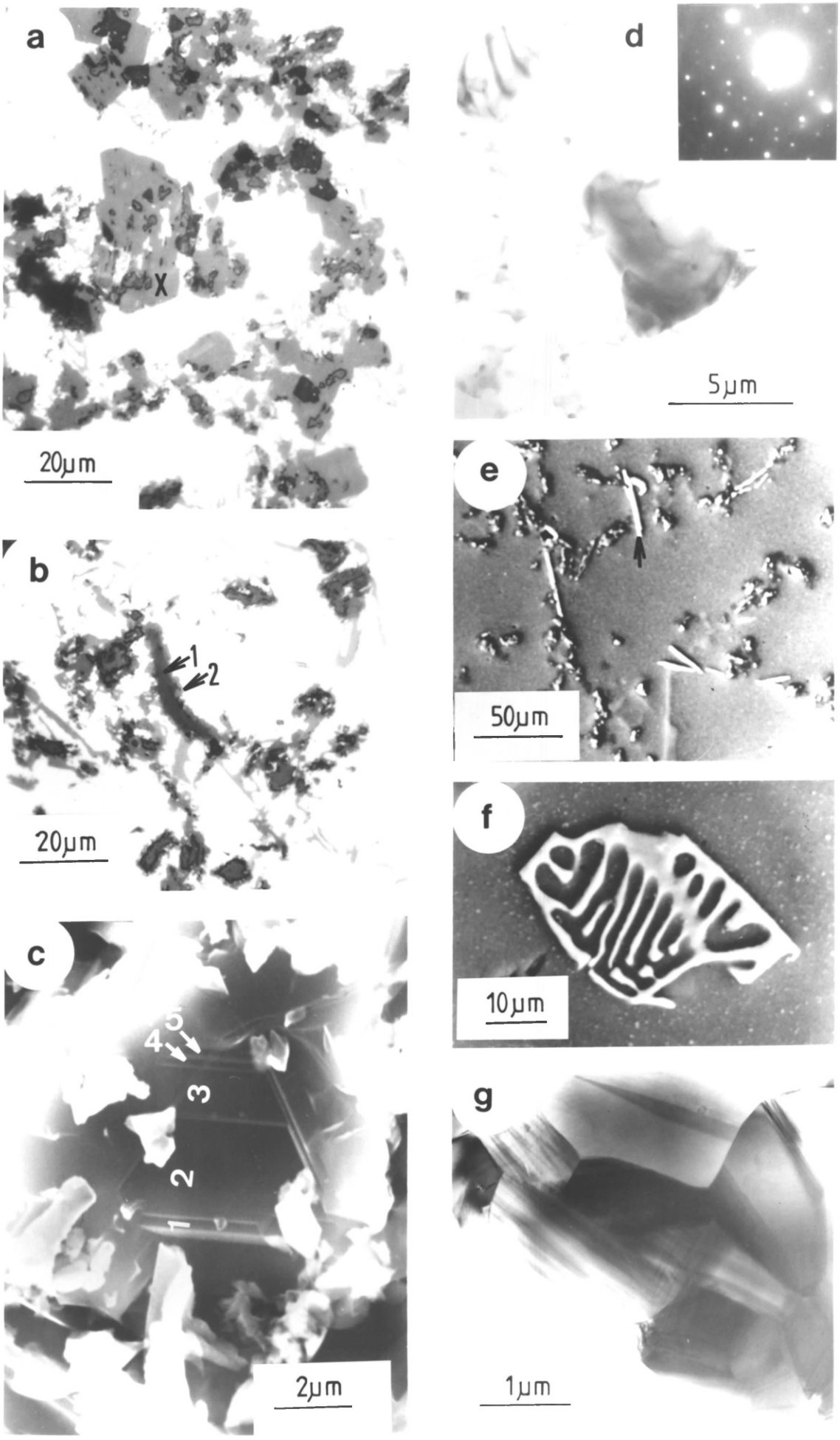
d. TEM micrograph at 100kV. BF of an intermetallic particle in as-sprayed MH87-S. The SADP suggests that the particle is $Al_{15}(FeMn)_3Si_2$. Indexing the SADP as a cubic <102> zone gives the 'a' parameter as 1.27nm given that the camera constant λ l= 2.54nm.mm. (Compare with literature values: 'a'=1.256nm [155] and 'a'=1.25 - 1.265nm [156].)



e. SEM SEI micrograph. MH85-S re-melted 30minutes at 800^{o}C and cooled at 1^{o}C/min. Needle-like impurity phase (arrowed) analysed as $Al_4(FeSi)_2$ (see table 4.1) and identified with Al_5FeSi.

f. As in **e.** above except that the micrograph shows a script-like impurity phase identified with $Al_{15}(FeMn)_3Si_2$ (see table 4.1).

g. TEM micrograph at 100kV. BF of a fine grained, polycrystalline aggregate found in Al-12Si-SiC (200-12) re-melted material.


a
X
20µm
b
1
2
20µm
c
4
5
3
2
1
2µm
d
5µm
e
50µm
f
10µm
g
1µm

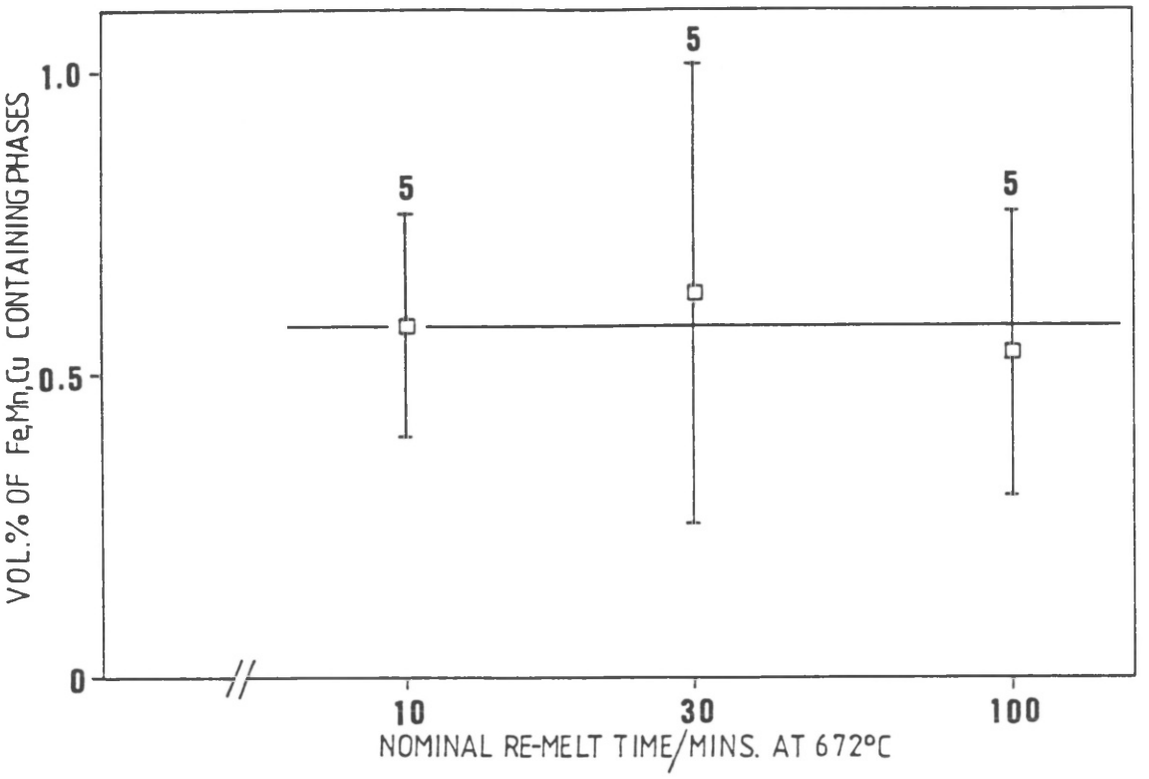
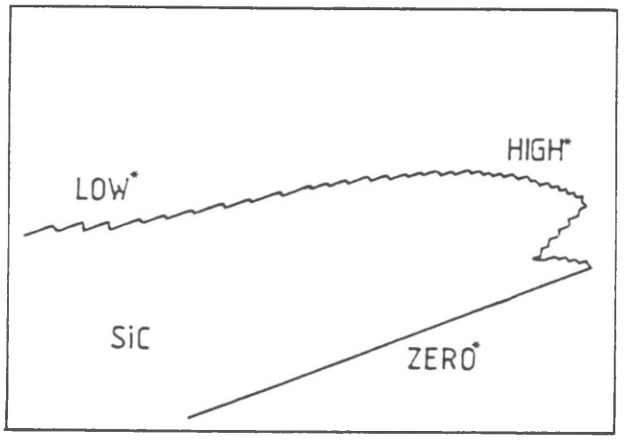


FIGURE 4·8a Volume fraction of impurity transition element containing phases in re-melted CP.Al-SiC composite (MH87-S) castings (air-cooled)



*Density of cleavage-non-cleavage plane intersections per unit area of SiC surface.

FIGURE 4.8b Model of a SiC 'asperity'

Figure 4.9

Deep-etching

The samples were prepared by electropolishing in a 30%HNO_3 solution in methanol. All micrographs are taken on a SEM operated at 20kV in the SEI mode.

a. As-supplied MH85-S: the matrix is black, and the SiC particles are grey. The scale is the same as in **b**. below.

b. As-supplied MH85-S following re-melting (~8minutes at 650^{O}C with ~2minutes at 670^{O}C and WQ). Particles labelled 1 - 4 are considered to be carrying Al_4C_3 plates. Particles labelled 4 - 6 have alternative surface morphologies. The eutectic Si product of the reaction is as arrowed. The bar on the right indicates 10microns.

c. MH85-S sample as in **b**. above. The platelets arrowed on the SiC surface are considered to be SiC platelets, and not the Al_4C_3 interface reaction product.

d. MH85-S following re-melting at 650^{O}C for ~10minutes and AC. The micrograph shows what are considered to be parallel Al_4C_3 platelets covering a SiC particle.

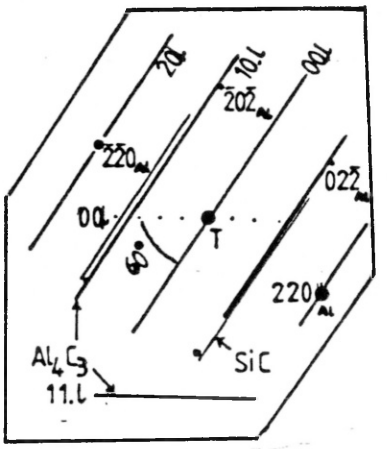
e. MH85-S following re-melting at 650^{O}C for ~10minutes and AC. The particle arrowed is considered to be covered in discrete Al_4C_3 crystals. Note that the platelets are in distinct parallel sets.

f. MH85-S heated to 800^{O}C and WQ. The arrow indicates what are considered to be Al_4C_3 platelets. The 'white' contrasted feature in the micrograph is eutectic Si.

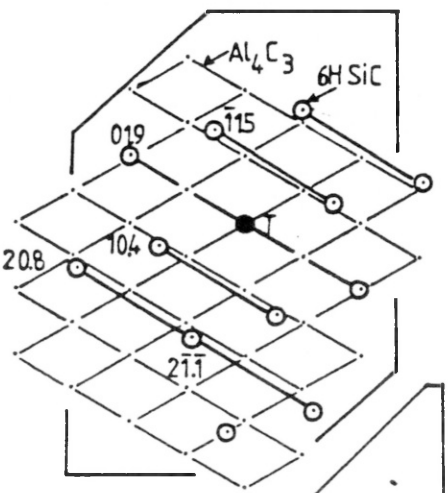
a
b
5
3
4
2
1
20KU
c
20KU X5,000 5µm 000051
d
2µm
e
10µm
f
5µm

Figure4.10

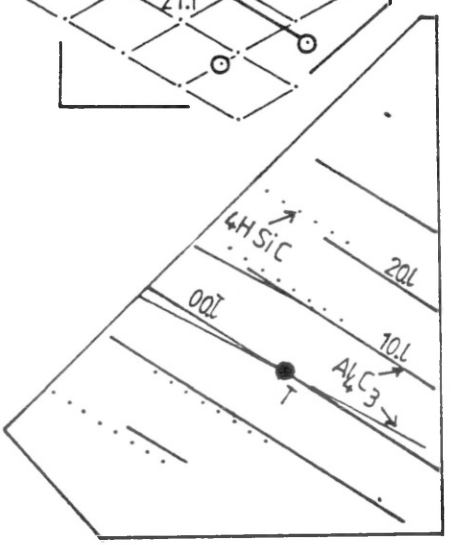
TEM micrographs of a CP.Al - SIC composite (MH87-S) re-melted for a nominal time of 10minutes at 672°C



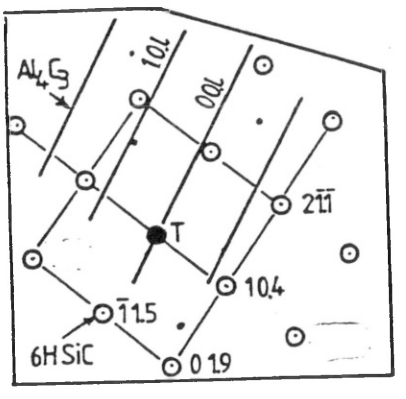
a. 15R SiC with Al_4C_3 platelets numbered 1,2 and 3 nucleated at the interface.
The SADP (λl= 2.33nm.mm) shows
<1$\bar{2}$.0> SiC // <1$\bar{2}$.0> Al_4C_3 platelets 1 and 2;
<01.0> SiC // <01.0> Al_4C_3 platelets 1 and 2;
<00.1> SiC // <00.1> Al_4C_3 platelets 1 and 2.
The rows of reflections at 60° to the <1$\bar{2}$.0> type zones arise from platelet 3 which is close to a <01.0> zone. Matrix reflections are indexed as a [111] Al zone.



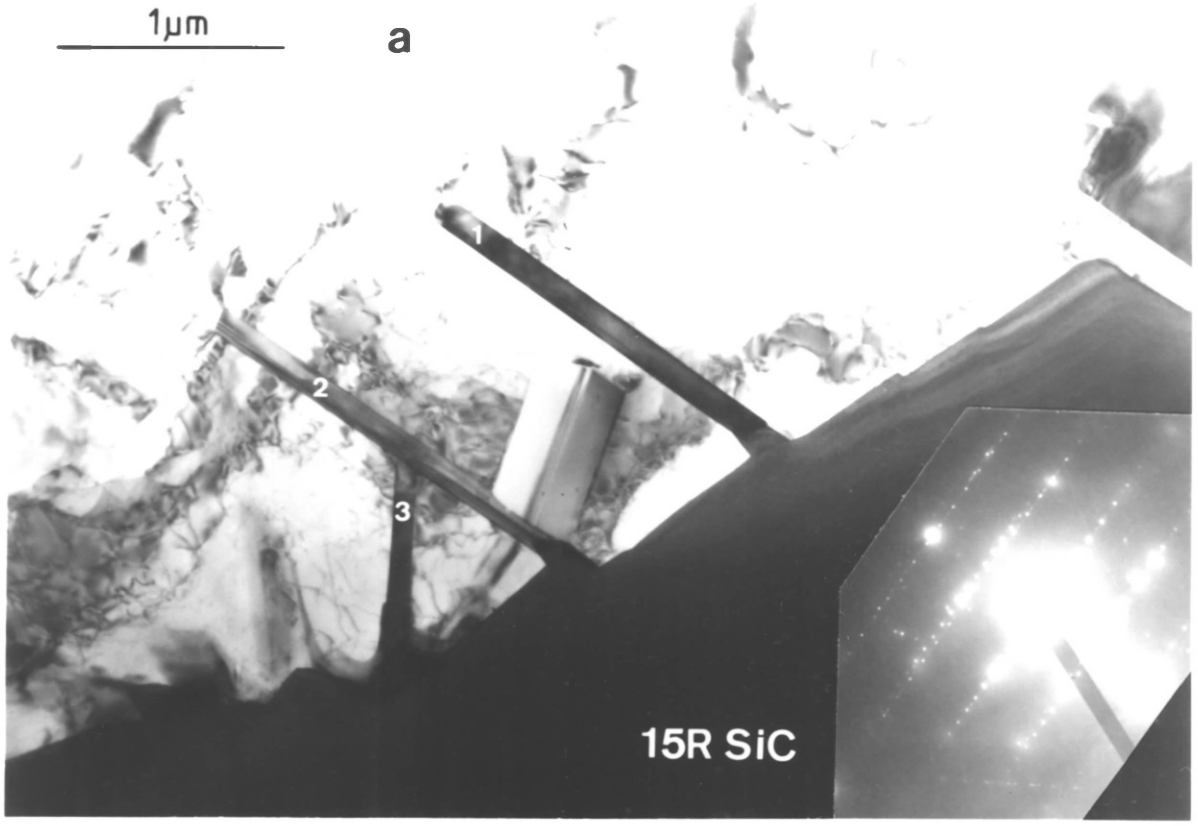
b. Al_4C_3 platelet 'A' on a [00.$\bar{1}$] zone, with the 6H SiC 'S' on a [1$\bar{1}\bar{4}$ .3] zone with λl= 2.34nm.mm. (refer to figures **4.17i** and **4.17j** for the separate indexing of the zones in the inset SADP and its key. The arrows on the micrograph indicate <01.0> Al_4C_3 directions.

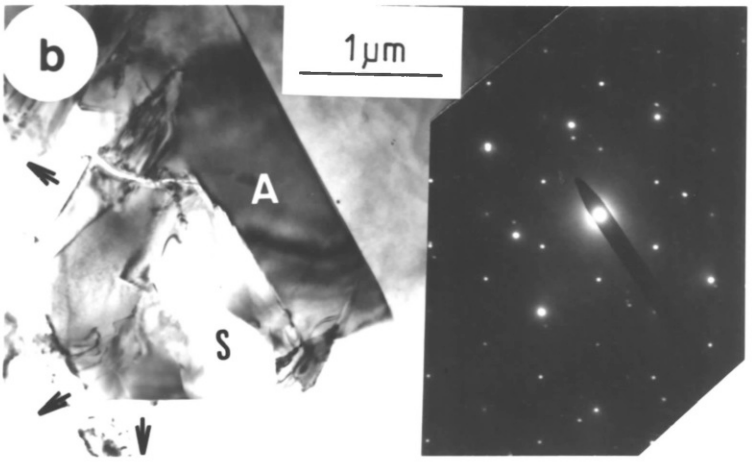


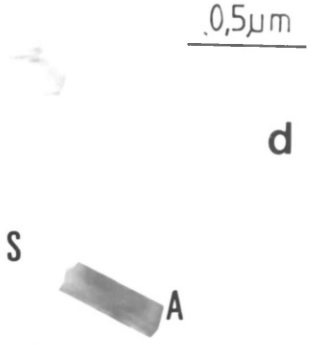
c. 4H SiC 'S' with Al_4C_3 crystals 1 - 6 showing a simple orientation relationship and some minor variations eg. platelet 4 is not parallel with the other platelets.The crystals 2 and 3 are composed of platelets that have impinged at a very early stage in the reaction. The SADP (λl=2.31nm.mm) shows the 4H SiC on a <1$\bar{2}$.0> zone along with the Al_4C_3 on similar zones.

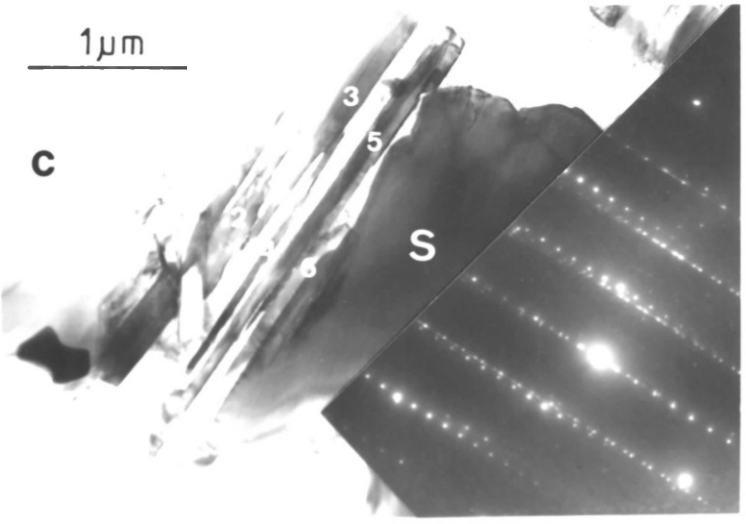


d. 6H SiC 'S' in the BF image oriented as in **b** above ie. refer to figure **4.17i** for indexing. The Al_4C_3 'A' is on a <1$\bar{2}$.0> zone indicated in the SADP (λl=2.51nm.mm). Al_4C_3 'B' is not oriented on a simple zone axis.The crystal 'A' is twinned.


1µm
a
1
2
3
15R SiC


b
1µm
A
S


0,5µm
d
S
A


1µm
c
3
5
S

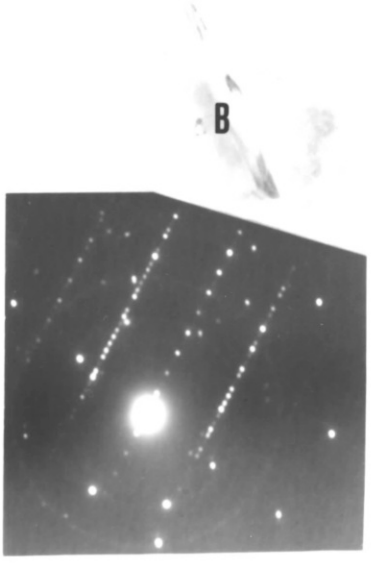

B

Figure 4.11

TEM micrographs of a CP.Al - SiC composite re-melted at 672°C

Re-melt times were for a nominal 30minutes in **a - d** inclusive, and 10 000minutes in **e**.

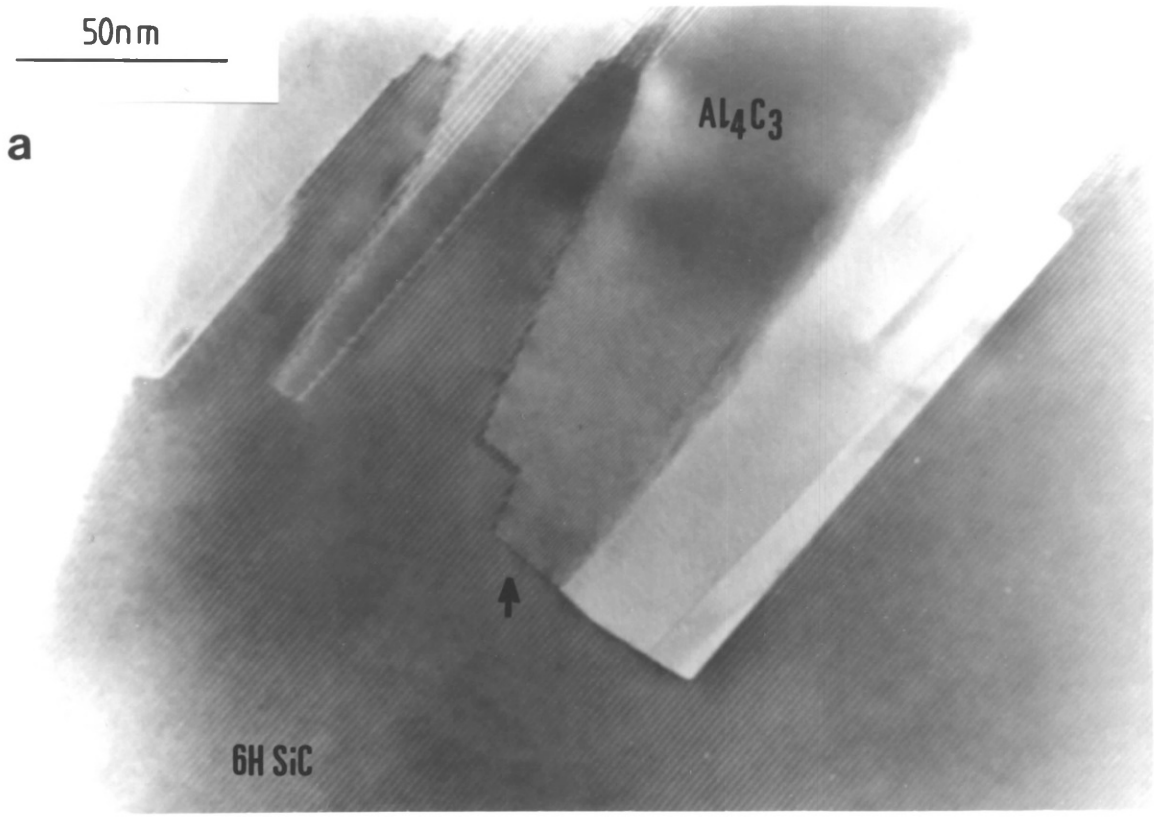
a. Interface between 6H SiC and Al_4C_3 . The parallel sets of fringes imaged are from {00.1} 6H SiC with a spacing of 1.5nm, and {00.3} Al_4C_3 with a spacing of 0.83nm. The portion of the interface arrowed is analysed in figure 4.12. The bright area of the Al_4C_3 shows a minor misorientation from a simple orientation relationship with the SiC. Note the large proportion of basal SiC facets at the interface.

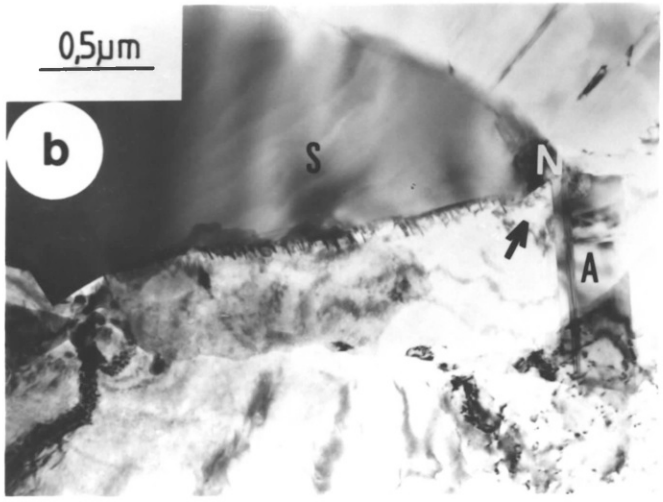
b. 6H SiC 'S' on a $<1\bar{2}.0>$ zone, with an Al_4C_3 crystal 'A' nucleated at 'N'. Note the fine needle-like interface product. The area arrowed is enlarged in **c** below.

c. Region of the interface as in **b** above, showing generally oriented needle-like interface phase eg. at 'P'. Note the region of SiC arrowed where the Al_4C_3 crystal 'A' meets the 6H SiC 'S' is highly disrupted ie. crystal 'A' appears to have nucleated at a region of 'crushing damage' where the SiC shows fine scale displacements, and rotations ({00.6} 6H SiC fringes imaged in the micrograph are poorly reproduced) with respect to the bulk of the SiC.

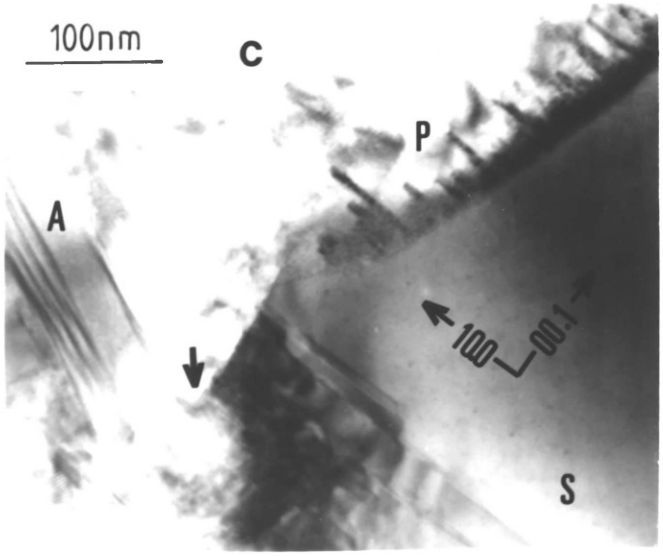
d. 4H SiC 'S' on a $<1\bar{2}.0>$ zone showing reaction product Al_4C_3 labelled 'A' at asperities. All the 'A' crystals shown are also on, or close to $<1\bar{2}.0>$ type zones.

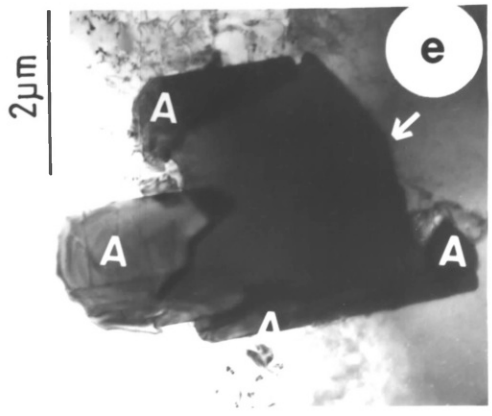
e. The SiC particle at the centre of the micrograph is on a $<1\bar{2}.0>$ zone. All the Al_4C_3 product crystals labelled 'A' are on or close to $<1\bar{2}.0>$ type zones. Note the large proportion of interface not covered by reaction product after 10 000minutes eg. as arrowed.


50nm
a
Al_4C_3
6H SiC


0,5µm
b
S
N
A


2µm
d
A
S
A
A
A
A
A
A
A


100nm
c
P
A
100
00.1
S


2µm
e
A
A
A
A

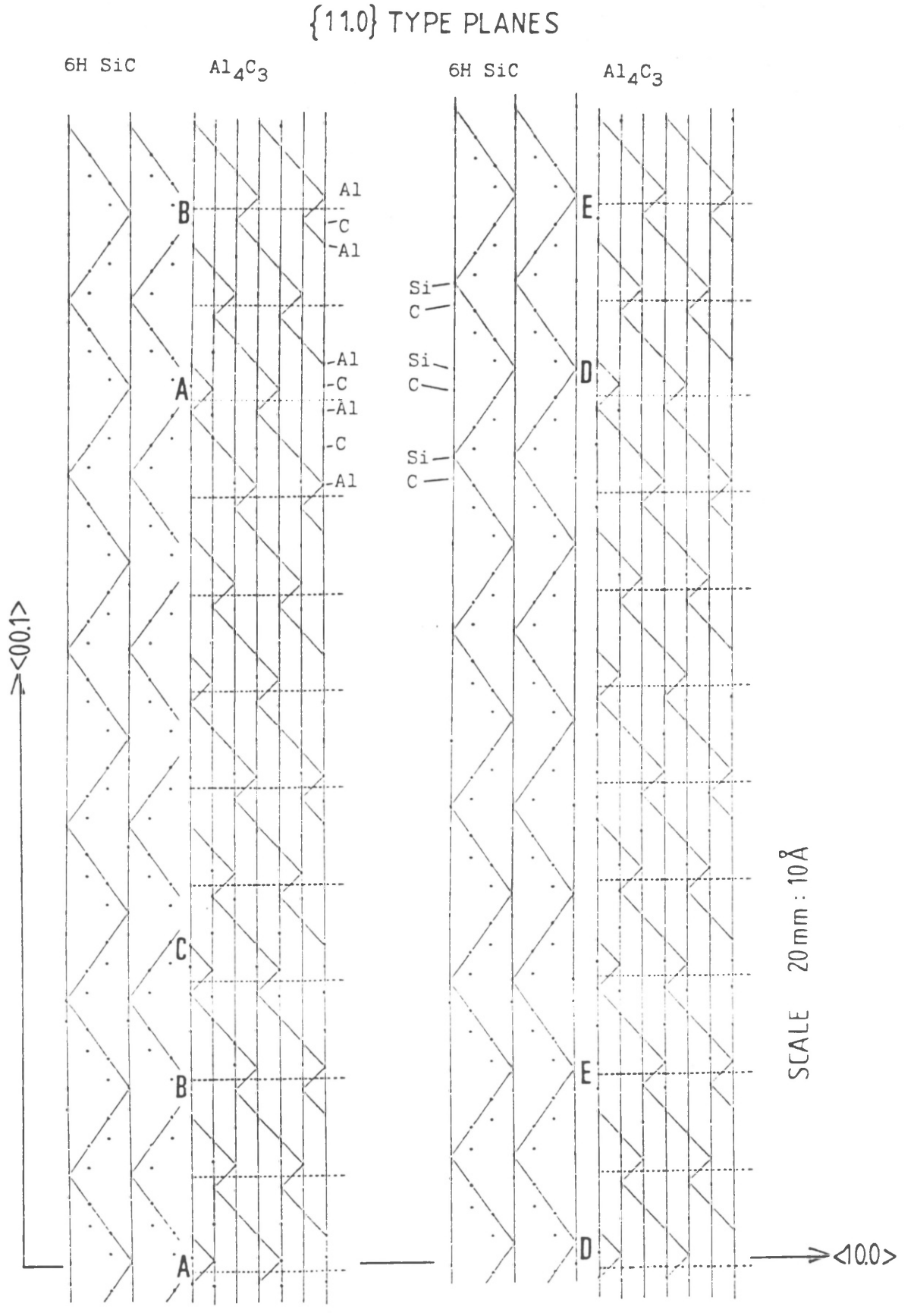


FIGURE 4.12

Suggested sites (lettered) at which coherency could exist between groups of atoms in the 'simple' epitaxial SiC-Al_4C_3 relationship

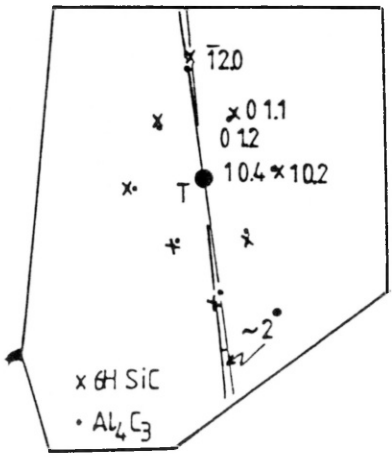
Diagram constructed from data principally in references [51] and [78].

Figure 4.13

TEM micrographs of CP.Al - SiC (MH85-S) following re-melting for 10s at 800°C

The isothermal re-melt of 10s at 800°C followed a heating period of 25s from the initial matrix liquidus temperature ~650°C.

a. Al_4C_3 crystal at 'A' with adjacent 6H SiC 'S'. Stacking faults,eg.as arrowed, are present in the SiC at a high density in the region of 'S'. The SADP (λl=2.52nm.mm) shows [10.$\bar{1}$] 6H SiC zone mixed with a [20.$\bar{1}$] Al_4C_3 zone, as indexed: the rotation between the <1$\bar{2}$.0> directions is ~2°.



b. SiC 'S' exhibits a large expanse of basal cleavage surface at the interface devoid of reaction products,whilst extensive coverage of the non-cleavage facets by Al_4C_3 , eg. at 'A', has occurred.

c. Al_4C_3 at 'A' on asperities at the SiC particle 'S' surface. The reaction product and the parent SiC were simply oriented, or else showed minor misorientations.

d. SiC 'S' showing prolific early reaction eg. at 'A'. Examples of asperities are arrowed, which are present around the interface generally.

e. The SiC particle at the centre of the micrograph shows contrasting extents of reaction product formation around its surface. Extensive reaction product has been produced at 'A' in the vicinity of asperities (arrowed) whereas faceted regions such as at 'C' are Al_4C_3 -free. The region at 'B' is detailed in **d** above.

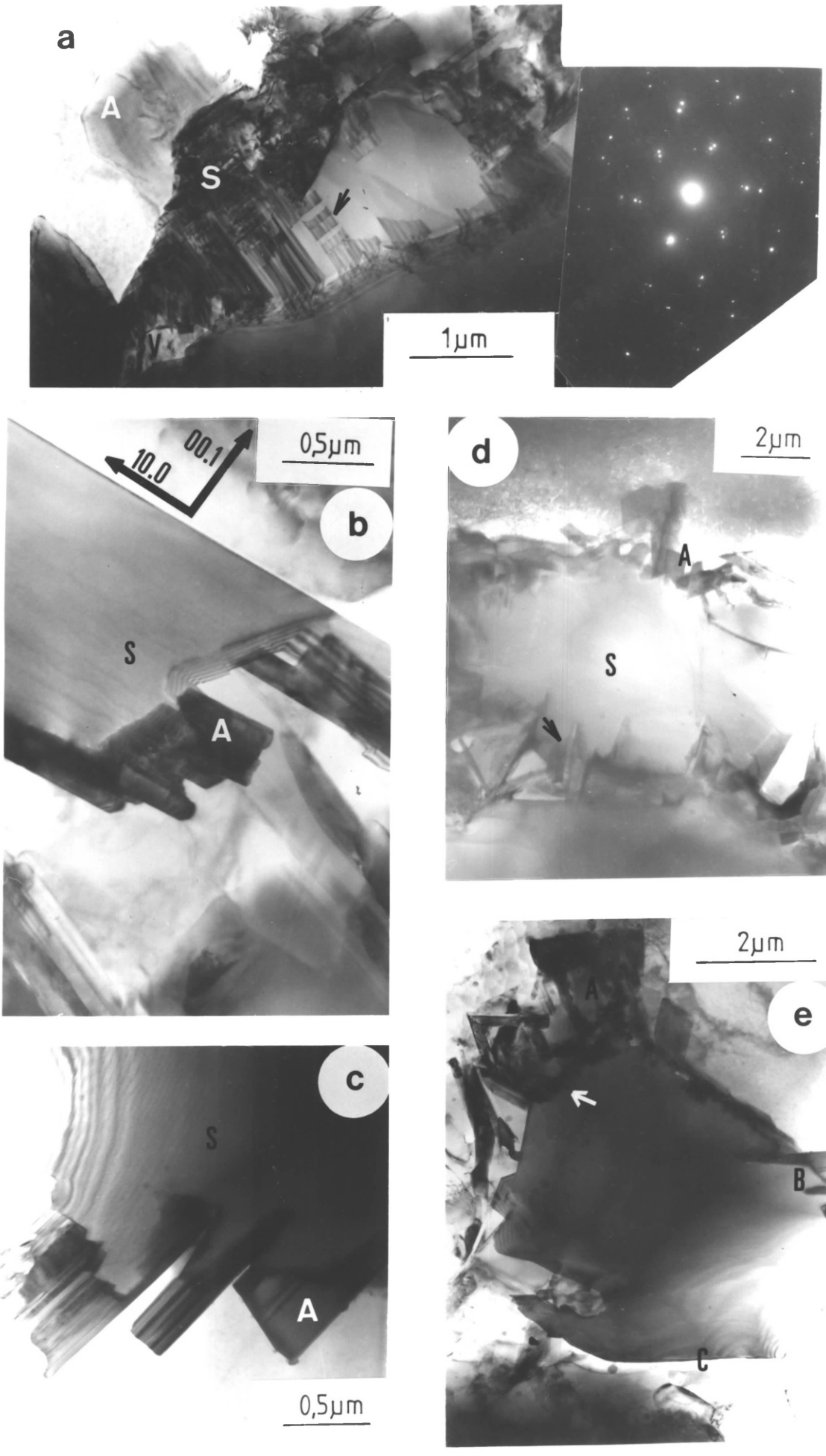

a
A
S
V
1µm
b
00.1
10.0
0,5µm
S
A
c
S
A
0,5µm
d
2µm
A
S
e
2µm
A
B
C

Figure 4.14

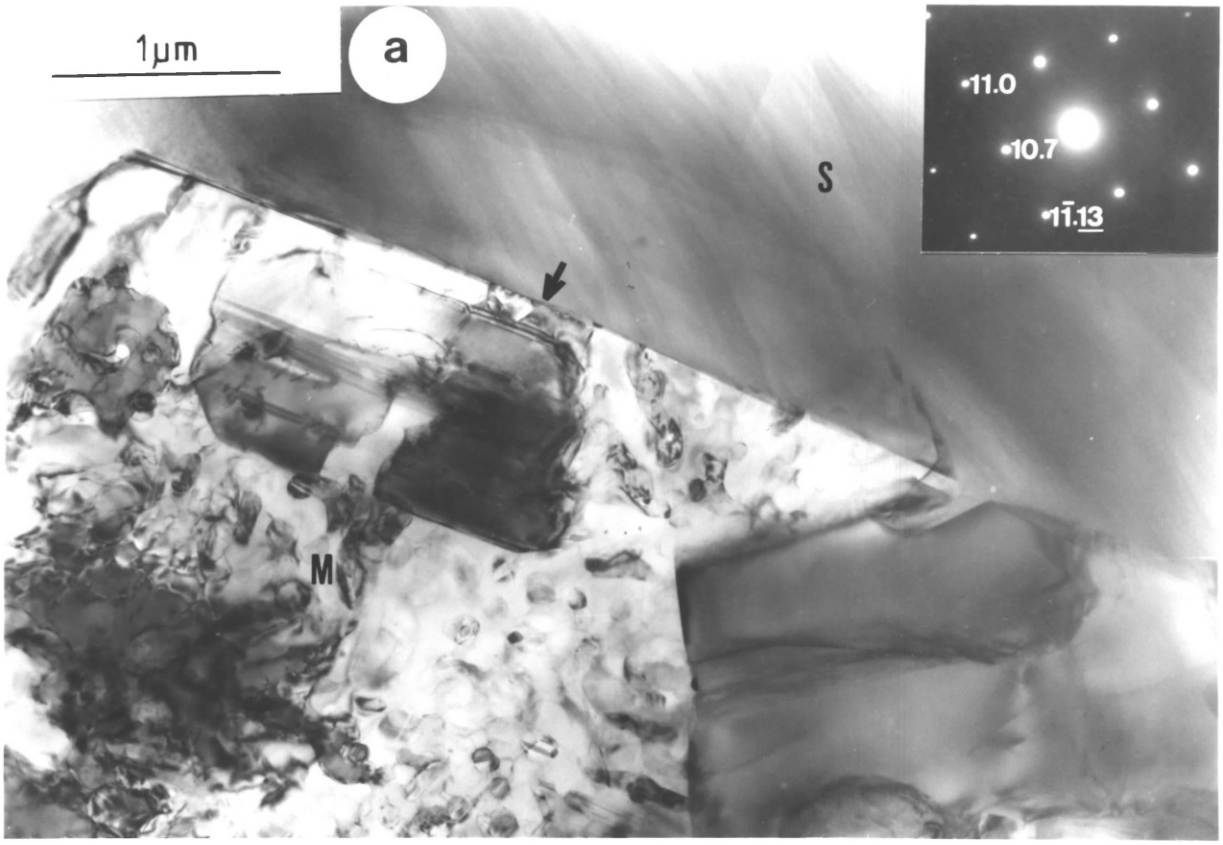
TEM micrographs of CP.Al - SiC (MH87-S) re-melted at 800°C for 1000minutes and WQ

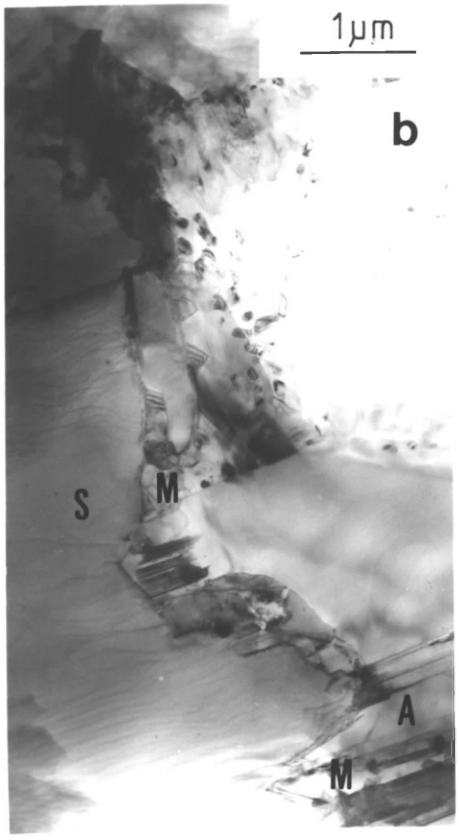
a. 15R SiC labelled 'S' on an ~[$\bar{7}$7.1] zone (see inset SADP with λl= 2.52nm.mm), showing a reaction product free interface of {11./ } type SiC as arrowed. The region of the micrograph labelled 'M' is quench-modified Al-Si eutectic.

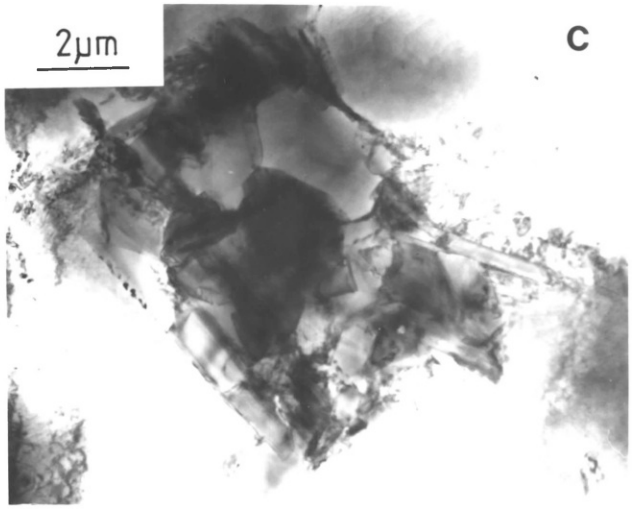
b. SiC particle 'S' showing a nearly continuous coverage of Al_4C_3 eg. at 'A' with the matrix still penetrating to the SiC surface at positions 'M'.

c. An example of an irregularly reacted particle showing the continuous facet developed on the Al_4C_3 on the left-hand side of the polycrystalline aggregate.

d. Al_4C_3 at 'A' showing facets developing on the polycrystal where facet 1~{10.1}; 2~{10.4}; 3~{10.$\underline{10}$}; 4 = {00.1}; and 5~{10.8}. The polycrystal is on a [1$\bar{2}$.0] zone axis as indexed in the SADP inset (with a camera constant λl=2.54nm.mm).


1µm
a
S
M
11.0
10.7
11.13


1µm
b
S
M
A
M


2µm
c

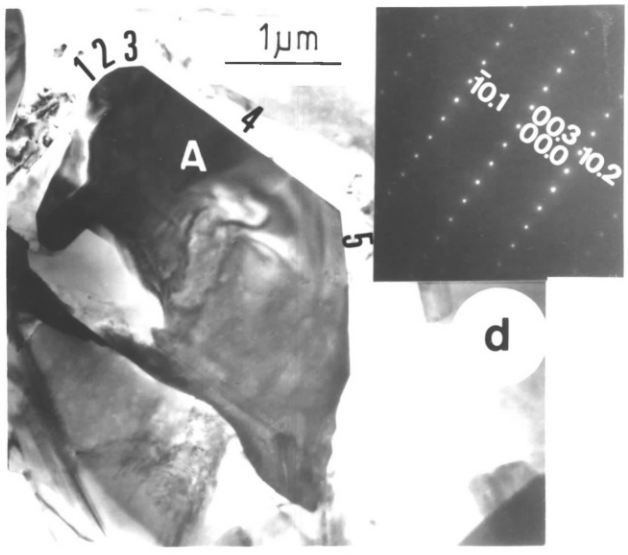
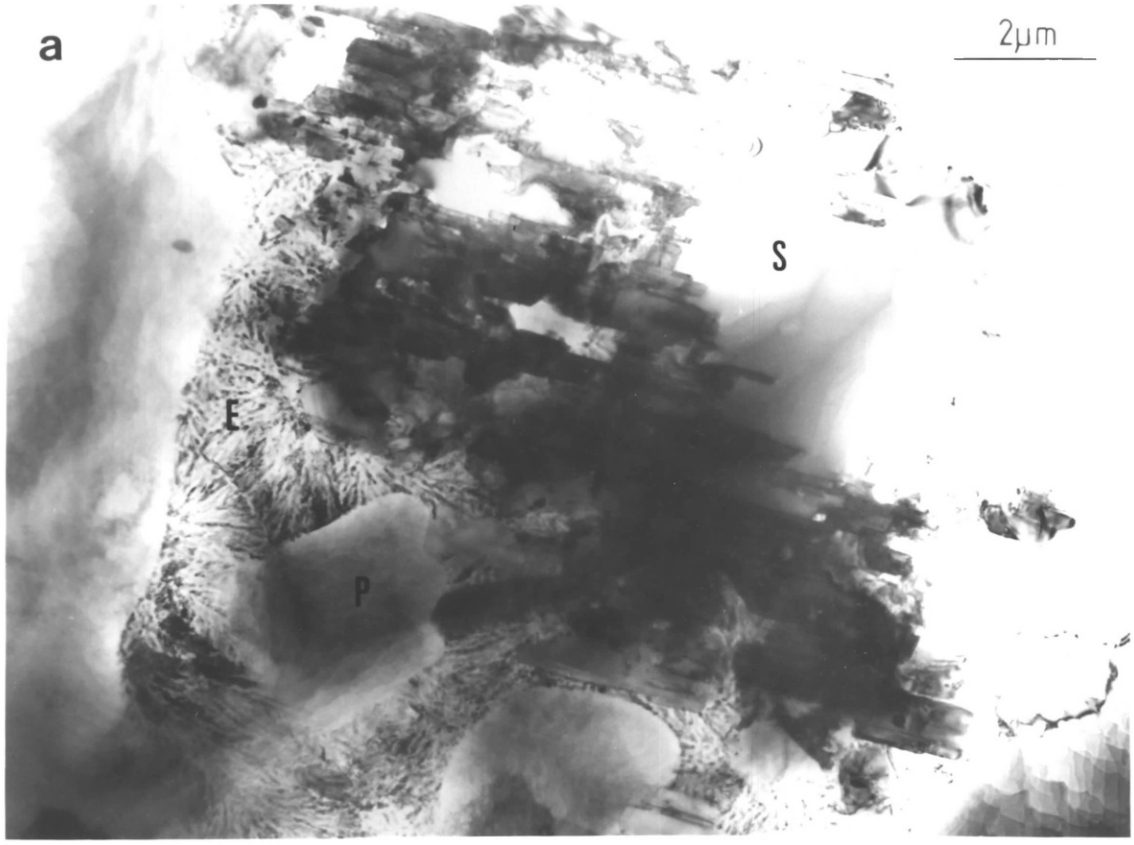

1µm
1 2 3
4
A
5
10.1
00.3
00.0
10.2
d

Figure 4.15

TEM micrographs of CP.Al - SiC (MH87-S) re-melted at 1000^{o}C for 1000minutes and WQ

a. SiC at 'S' on $<1\bar{2}.0>$ type zone with the Al_4C_3 reaction product also on or close to a $<1\bar{2}.0>$ type zone, and generally exhibiting a simple orientation relationship with the SiC 'S'. Some Al-Si eutectic is at 'E' and part of an Al dendrite is at 'P'.

b. SiC at 'S' showing general reaction product 'A' with large numbers of voids 'V' at both SiC - Al_4C_3 interfaces and at Al_4C_3 - Al_4C_3 interfaces. Al-Si eutectic is at 'E'.


a
2µm
S
E
P

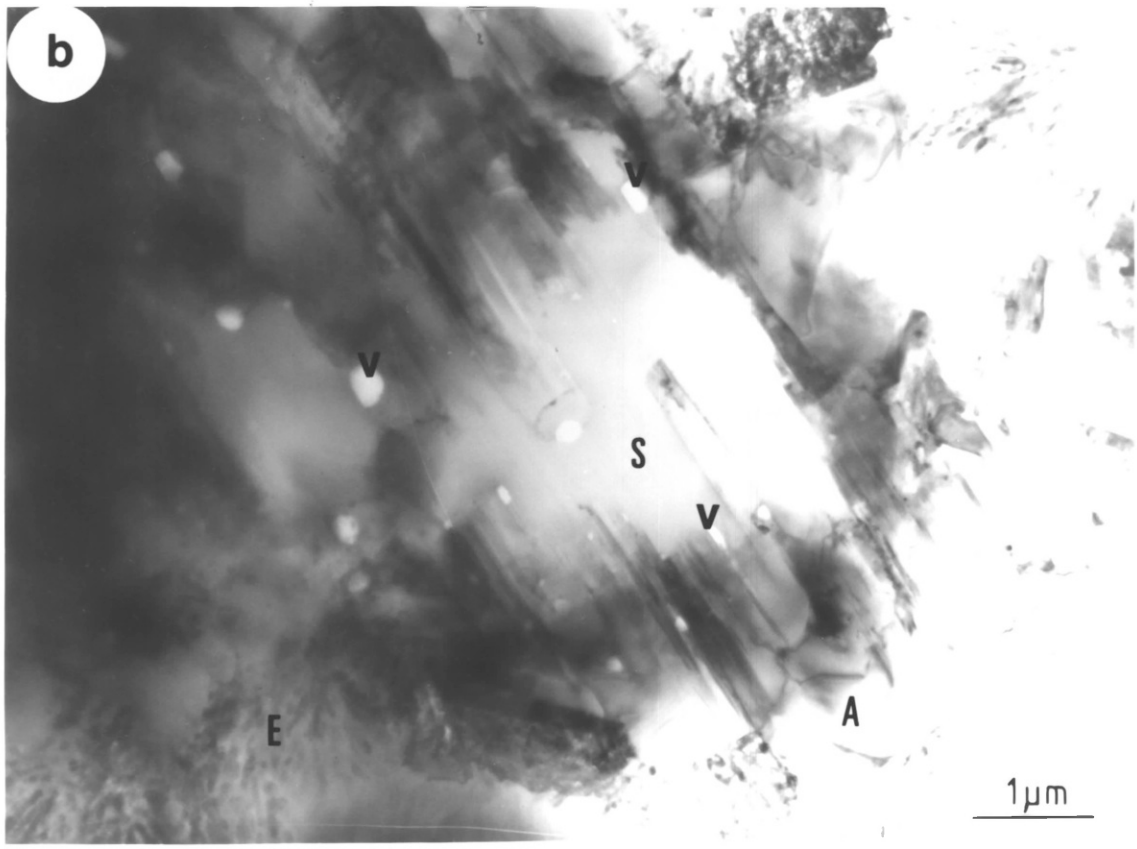

b
V
V
S
V
E
A
1µm

Figure 4.16

TEM micrographs of CP.Al - SiC (MH87-S) re-melted at 1000°C for 1000minutes and WQ

a. Continuous interface product Al_4C_3 a 'A' showing a plate-like subgrain structure. The Al_4C_3 is oriented with the SiC which was on a $<1\bar{2}.0>$ type zone. Note the presence of interface voids. The region marked 'X' is Al filled.

b. Al_4C_3 crystal at 'A' showing dislocations at the interface with an unidentified particle marked '?'.

c. SiC particle 'S' with oriented interface product Al_4C_3 at 'A' unpenetrated by the liquid melt. The Al_4C_3 at 'B' is at an alternative orientation to the rest of the interface product.

d. Al_4C_3 crystal showing dislocations and what appear to be low angle boundaries (arrowed). The region marked 'X' is on an $\bar{}$[05.2] zone according to the indexing of the inset SADP (λl = 2.51nm.mm). The 01.5 and 20.5 indexing was preferred to 10.7 and 20.7 on the basis of the interplanar angles.

e. As in **d**. above with the Al_4C_3 re-oriented (see positions 'X' and 'T' for reference). A SiC particle is at 'S'.

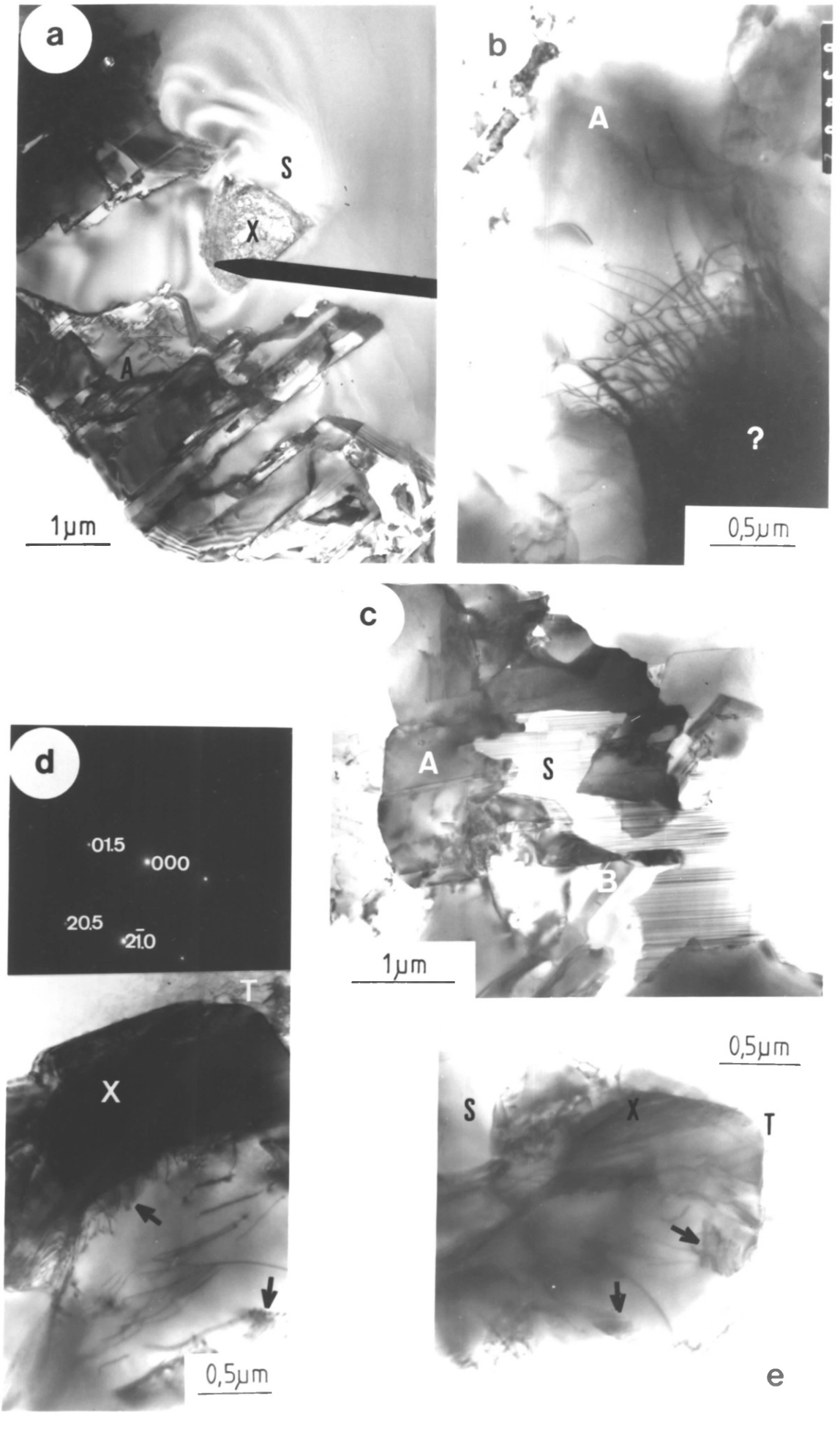

a
S
X
A
1µm
b
A
?
0,5µm
c
A
S
B
1µm
d
01.5
000
20.5
21̄.0
T
X
0,5µm
0,5µm
S
X
T
e

Figure 4.17

Electron diffraction patterns

a. TEM BF image of rotation twins in Al_4C_3 .The specimen was slightly tilted away from the orientation at which the SADP was produced in order to increase the contrast between the twins. The SADP shows the mixed $<1\bar{2}.0>$ type zones from an area incorporating a twin boundary.

b. Mixed SADP of $<1\bar{2}.0>$ type 6H SiC and Al_4C_3 zones.

c. Mixed SADP of a $<1\bar{2}.0>$ type 6H SiC zone with two Al_4C_3 zones of the same type. A fourth zone has been indexed as $[\bar{2}\bar{1}1]$ Al.

d. Mixed SADP of $<1\bar{2}.0>$ type 6H SiC and Al_4C_3 zones.

e. Mixed SADP of $<1\bar{2}.0>$ type 6H SiC and Al_4C_3 zones.

f. Mixed SADP across an Al_4C_3 - 6H SiC interface. The SiC zone is $<1\bar{2}.0>$ type.

g. Mixed SADP across an Al_4C_3 - 6H SiC interface. The SiC zone is $<1\bar{2}.0>$ type.

h. Reflections appearing in **f.** above attributed to Al_4C_3 .

i. 6H SiC zone as in figure **4.10b** and **4.10d.**

j. Al_4C_3 as in figure **4.10b.**

k. Mixed Al_4C_3 and alpha-SiC $[00.\bar{1}]$ zones.

Please find the 'key' to figure 4.17
on the page following the figure itself.

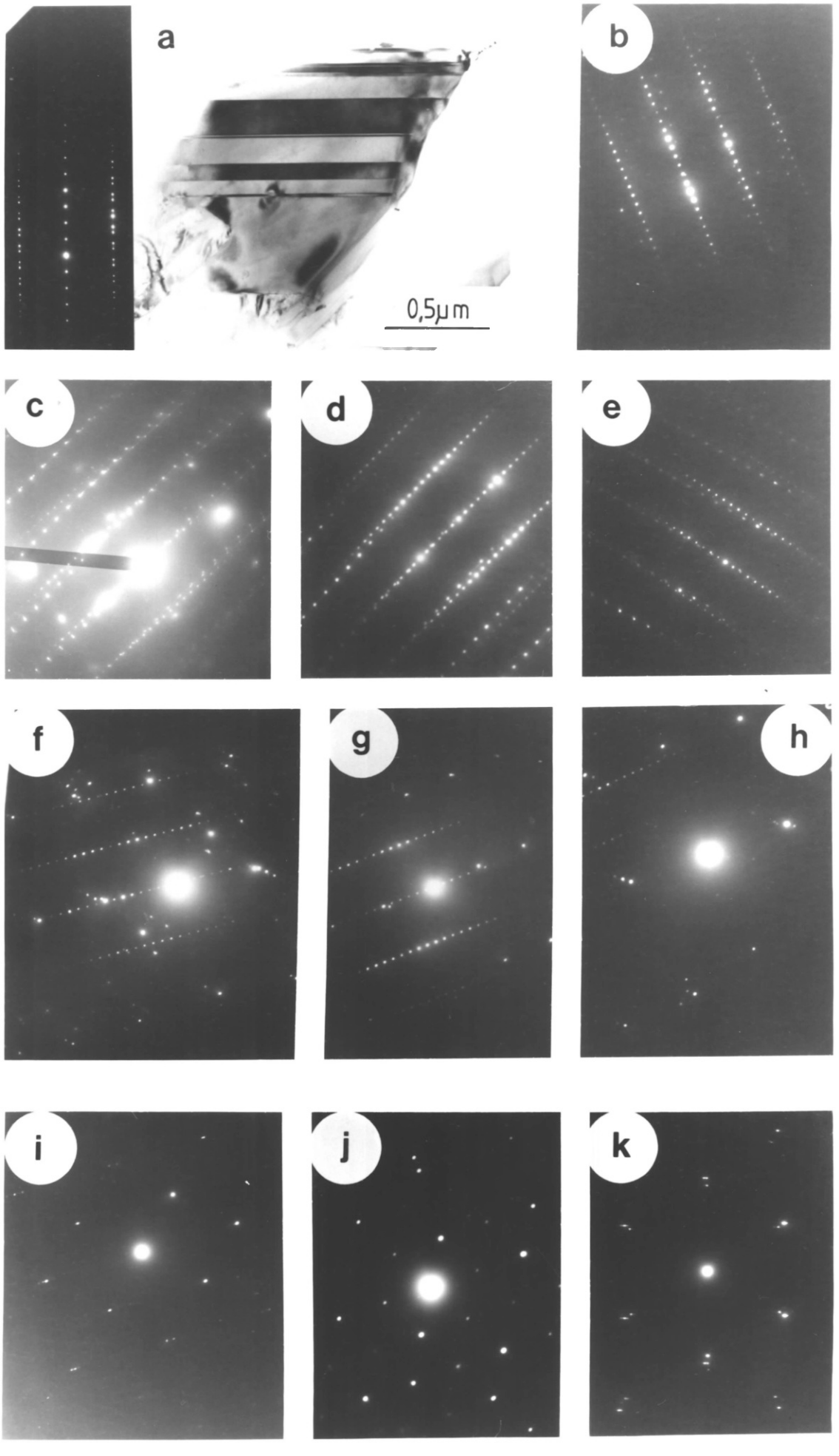
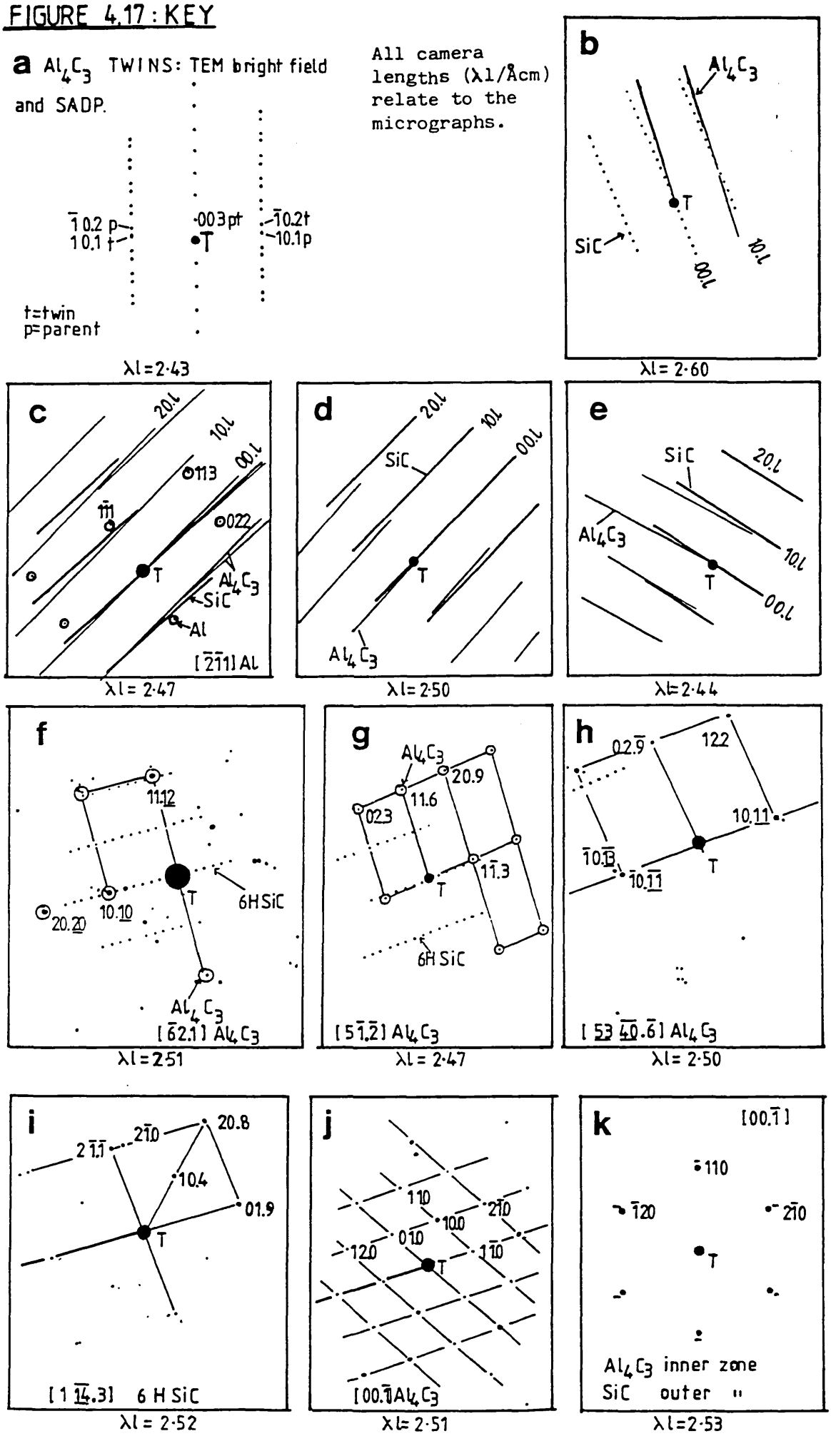

a
0,5µm
b
c
d
e
f
g
h
i
j
k

FIGURE 4.17 : KEY



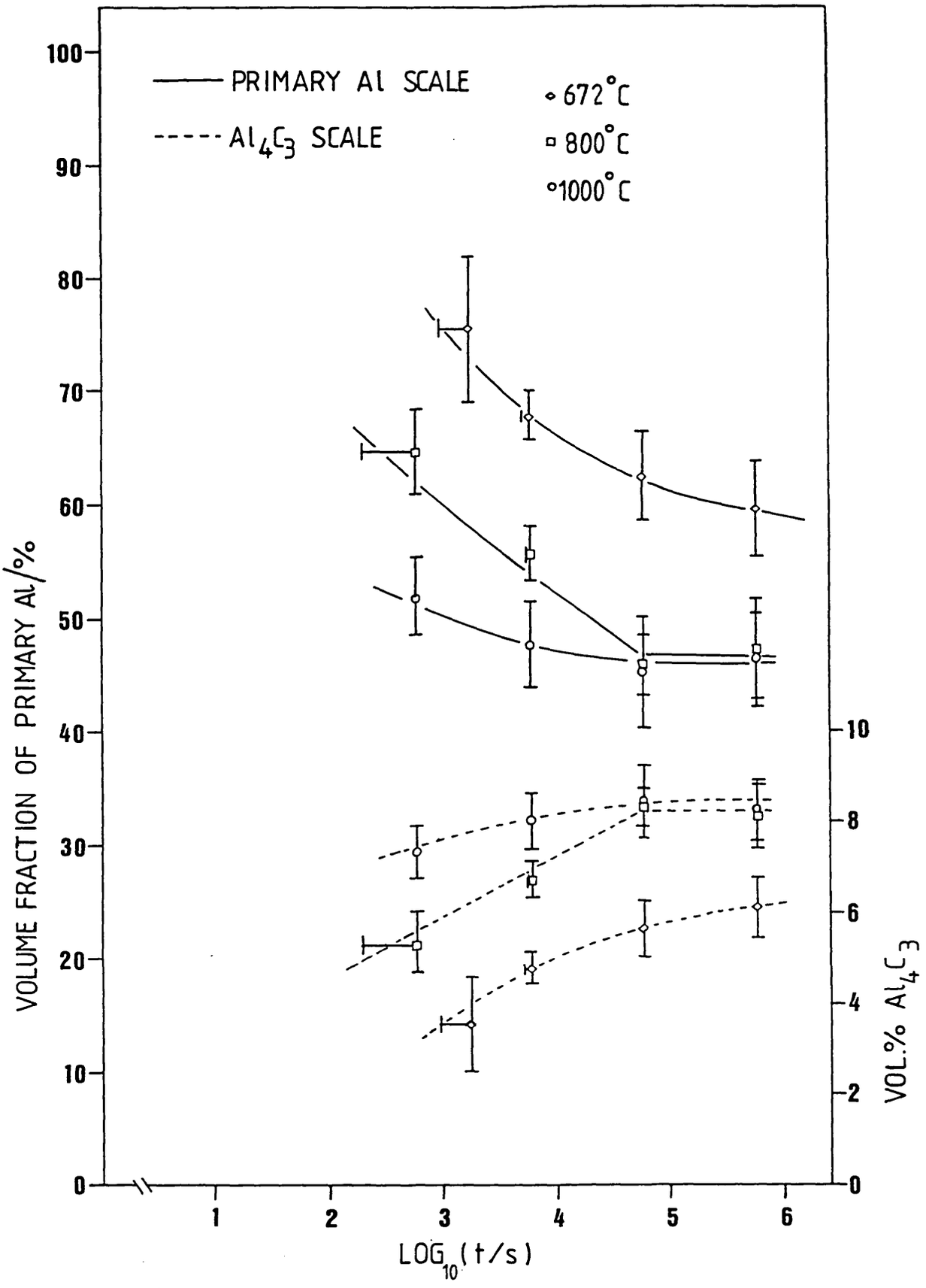
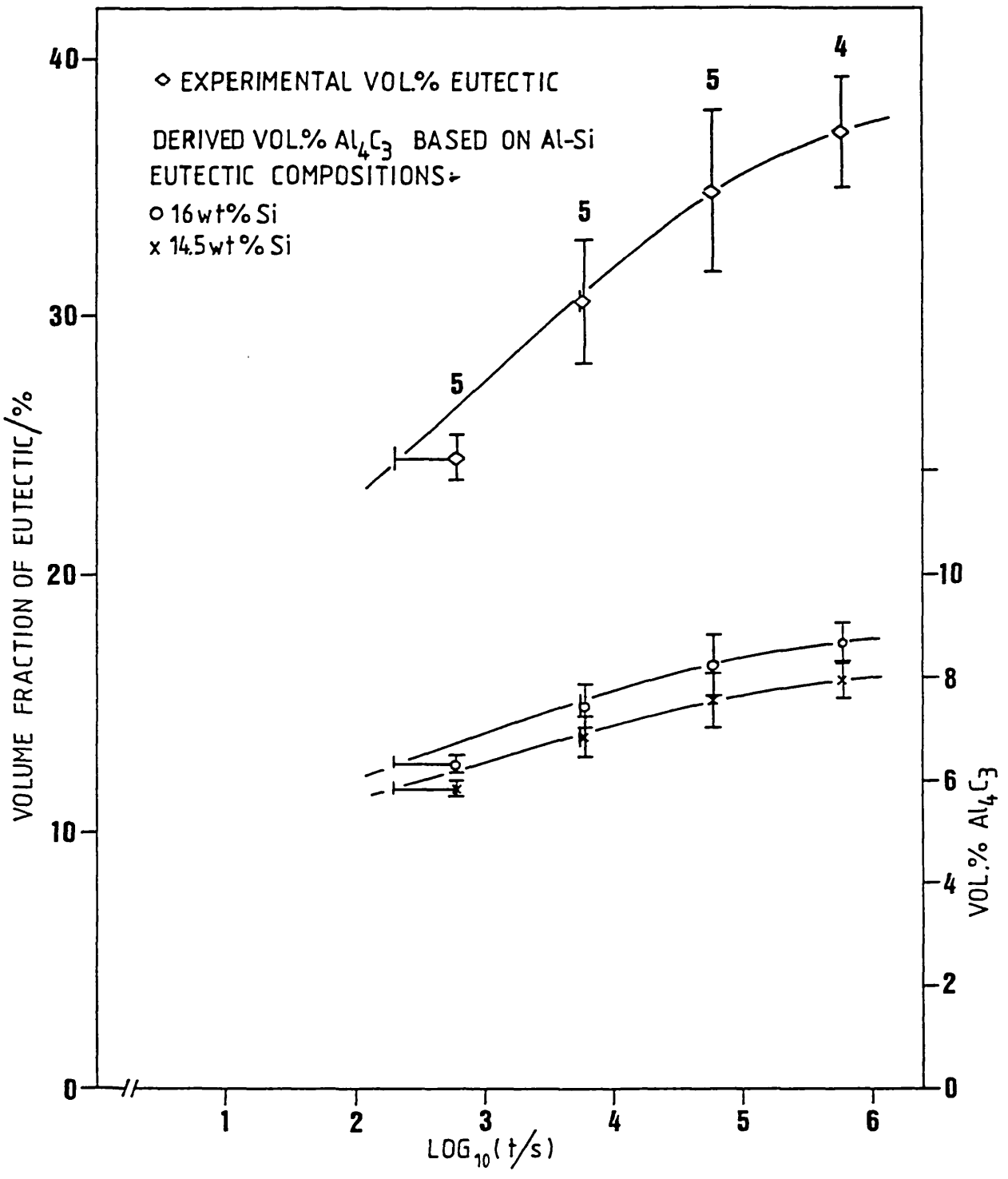


FIGURE 4.18 Experimental isothermal kinetics: the volume fraction of primary Al in re-melted CP.Al-SiC (MH87-S) samples, which were air-cooled, as a function of the re-melt time. The corresponding 'derived' volume fractions of Al_4C_3 areincluded.

FIGURE 4.19 The volume fraction of eutectic in samples of CP.Al+SiC (MH87-S) re-melted at 800°C and water-quenched as a function of the re-melt time. The volume fraction of quenched Al-Si eutectic in the matrix was converted to the corresponding volume fractions of Al_4C_3 assuming the eutectic compositions indicated.



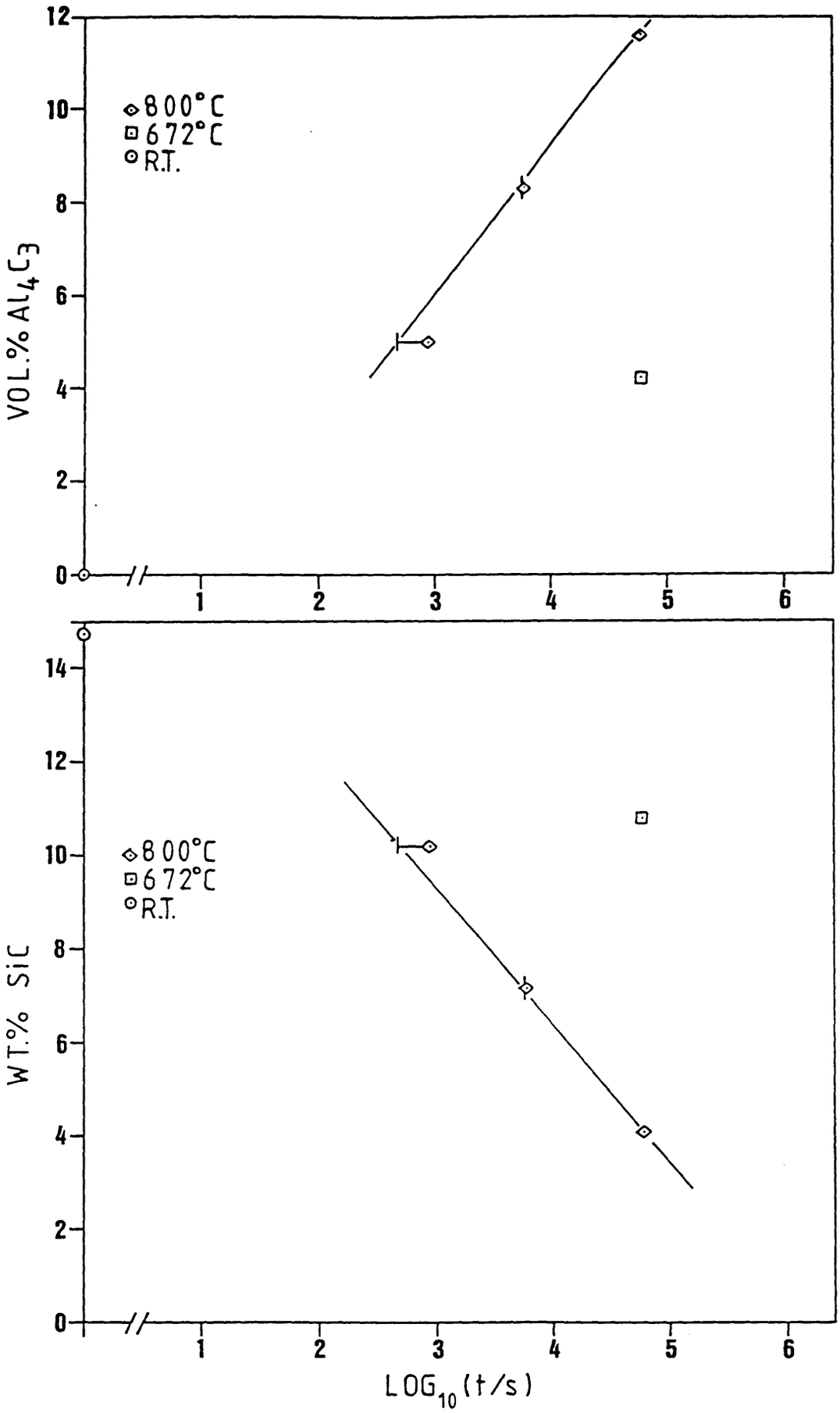


FIGURE 4.20 Experimentally determined wt%SiC in CP.Al+SiC (MH85-S) as a function of the re-melt time(bottom). The corresponding volume fractions of Al_4C_3 are also displayed (top) following their computation.

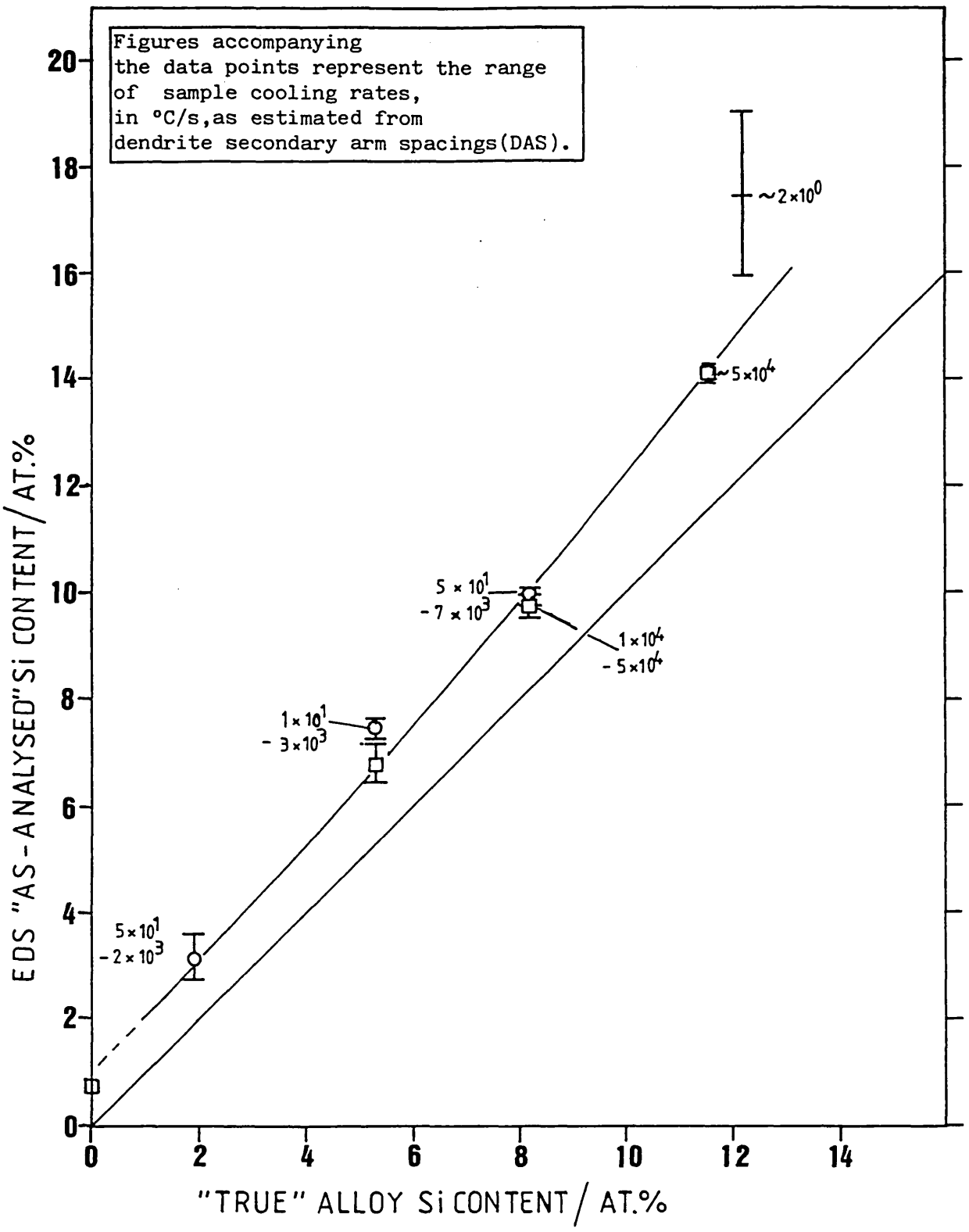


FIGURE 4.21 Calibration curve for the EDS analysis of cast Al-Si alloys. The "as-analysed" EDS results have been ZAF corrected.

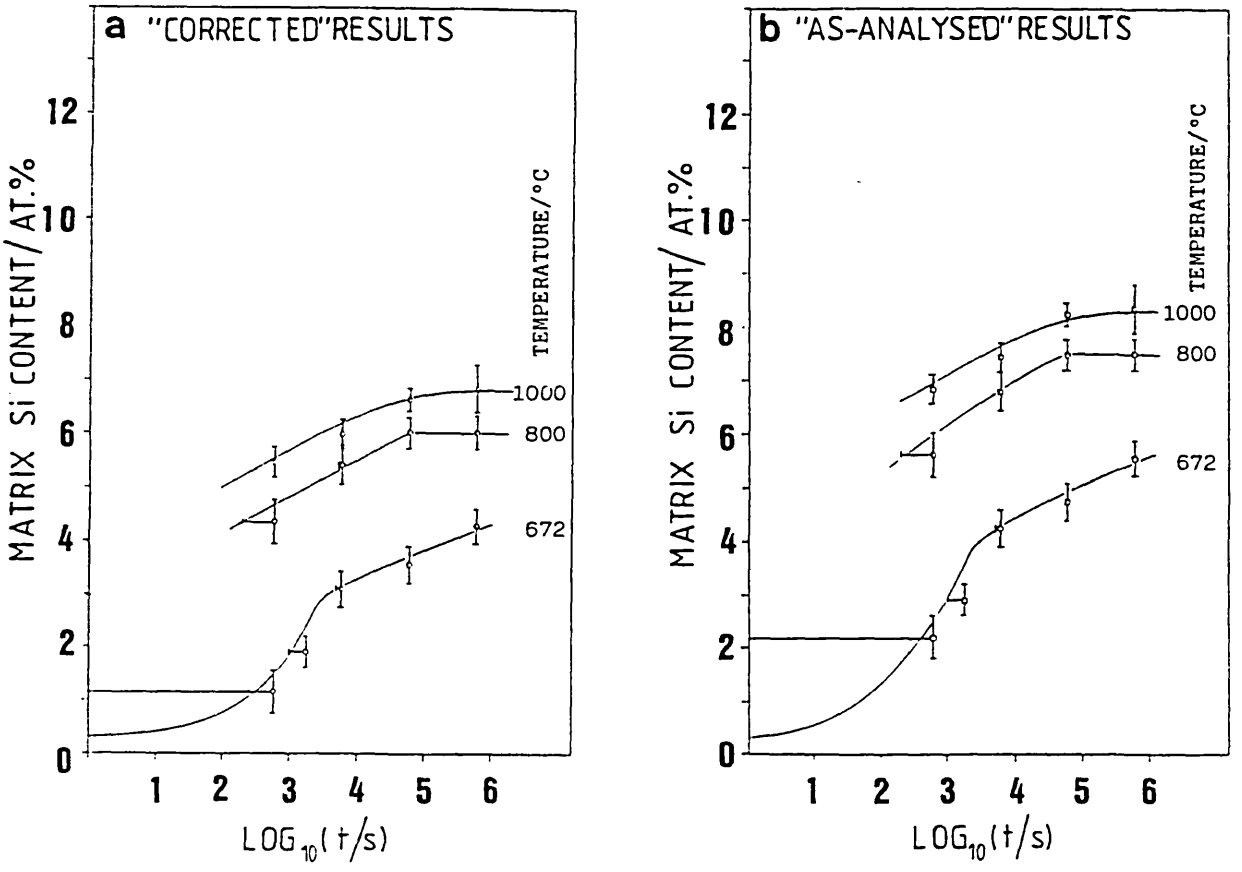


FIGURE 4.22 EDS (energy dispersive X-ray spectroscopy) analysis results.

The Si content of the matrix of re-melted and WQ samples of CP.Al+SiC (MH87-S) is displayed as a function of the re-melt time.

a.EDS results corrected via figure 4.21

b.Original "as-analysed" EDS results prior to correction.

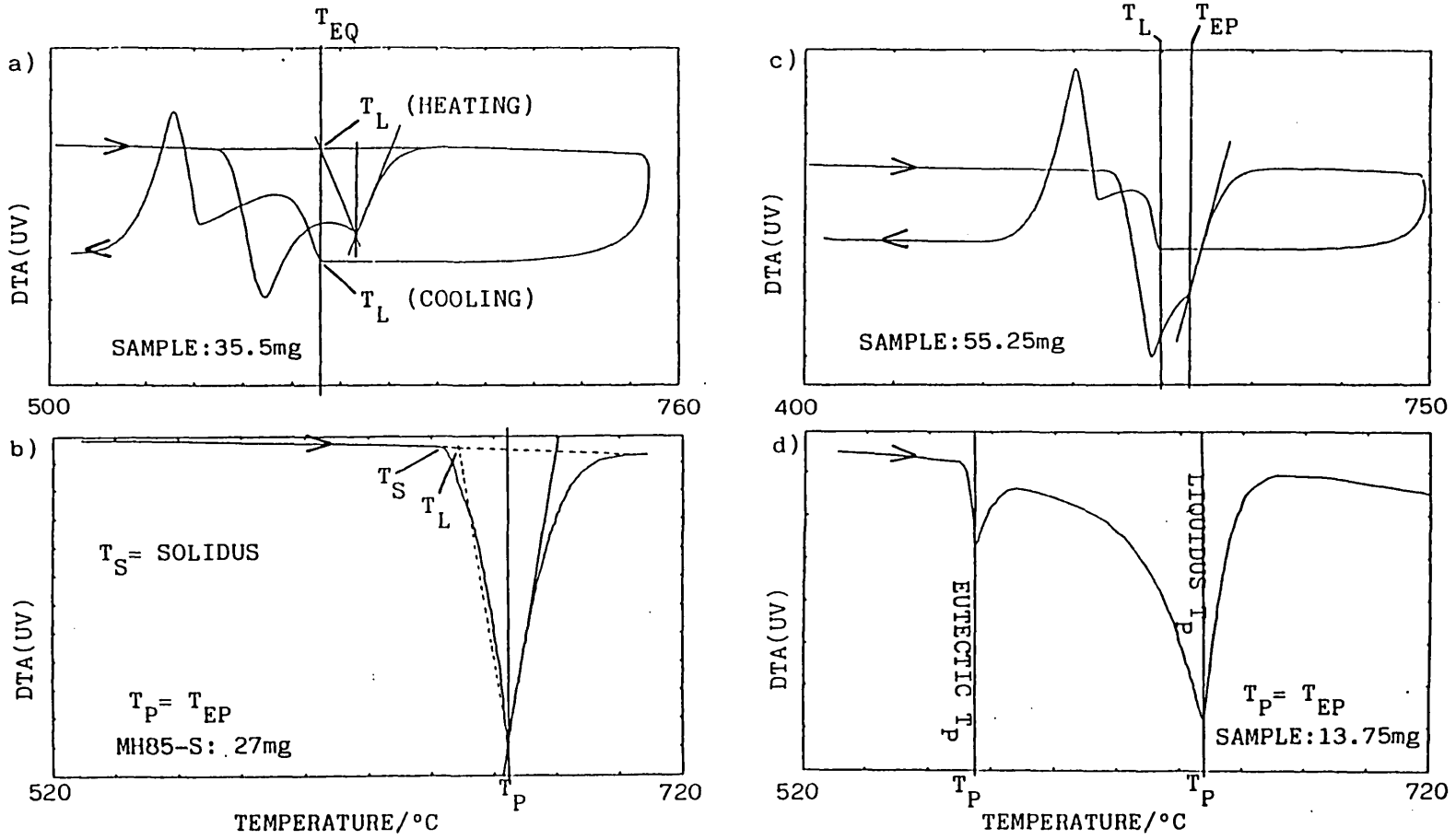
FIGURE 4.23 ANALYSIS OF DTA TRACES.

a) 'Peak construction' with the estimation of the 'equilibrium' liquidus temperature T_{EQ} with the coincidence of T_L(HEATING) and T_L(COOLING).

b) Initial CP.Al-SiC melting peak with the estimation of T_L from 'peak construction'.

c) T_{EP} found for a heavily reacted sample, and definition of T_L.

d) T_P determinations for a low-mass sample.



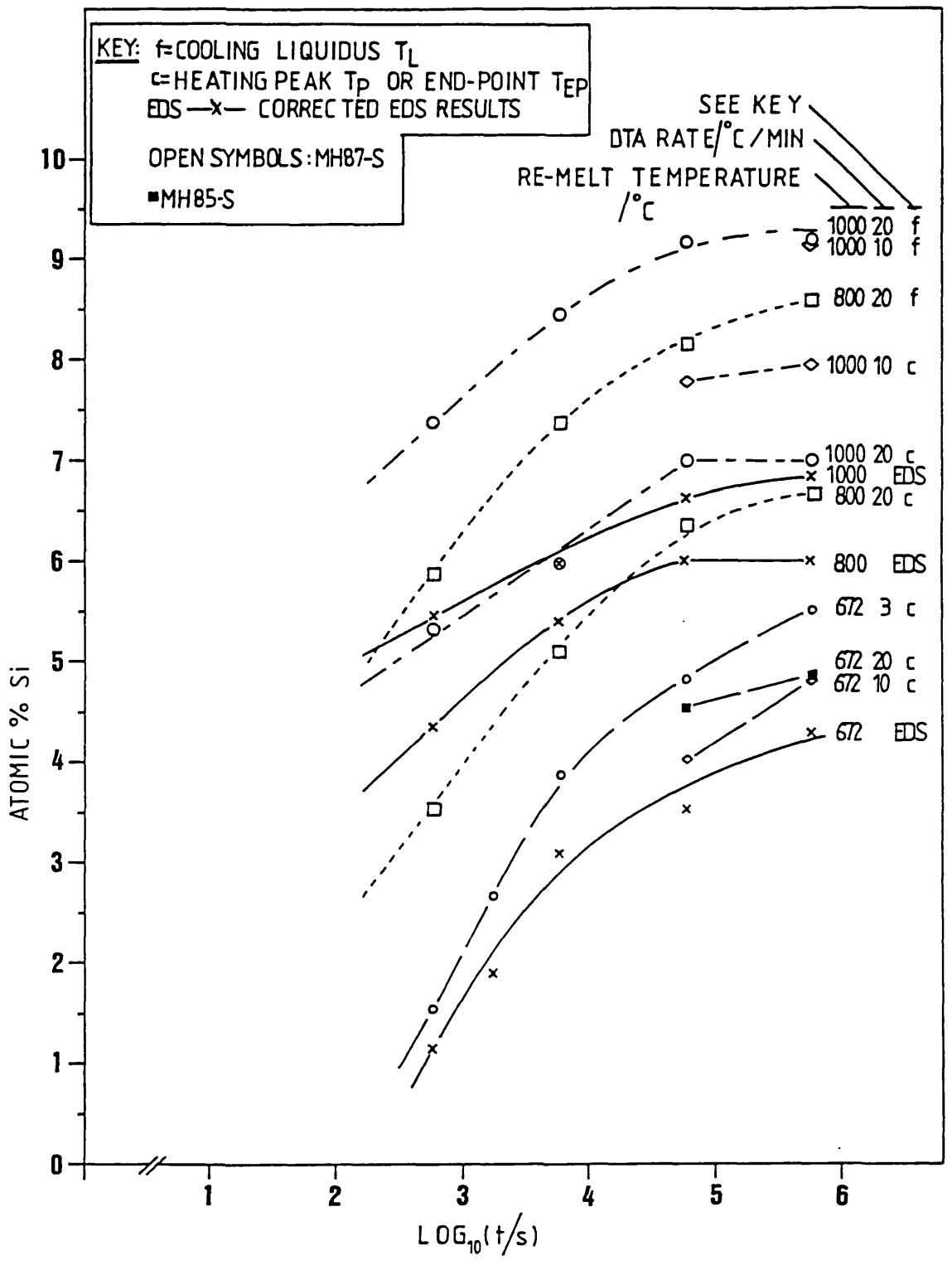


FIGURE 4.24 Comparison of liquid composition results derived from DTA trace temperatures. The temperatures T_L and T_{EP} (=T_P when the sample mass is 'small') were converted into compositions (atomic %Si) via direct application of the Al-Si binary equilibrium diagram.

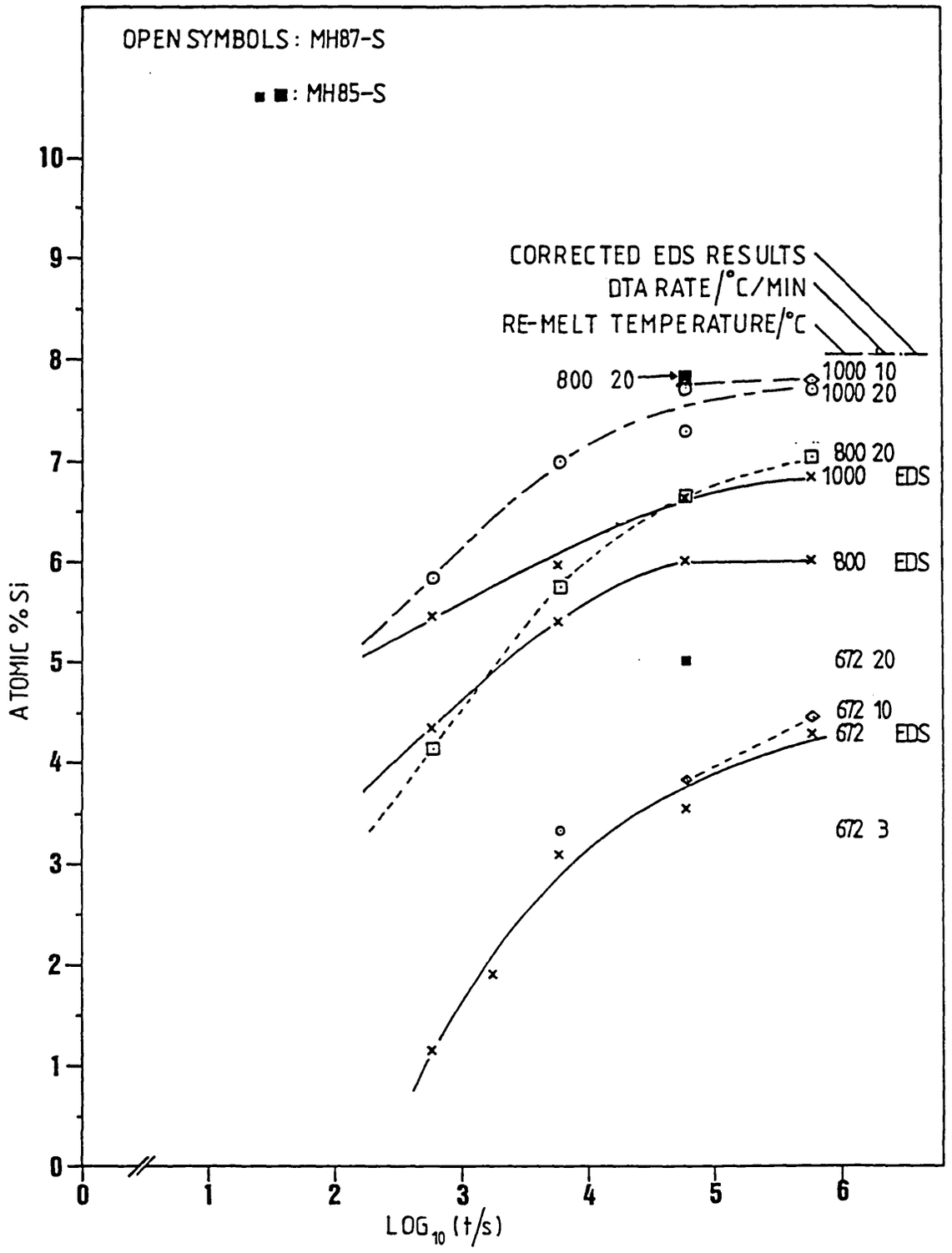


FIGURE 4.25 Comparison of liquid composition results derived from the change in the estimated liquidus temperature with the EDS results. Temperature changes T_L -649°C were converted to atomic%Si via the use of a 'floating' Al-Si equilibrium liquidus.

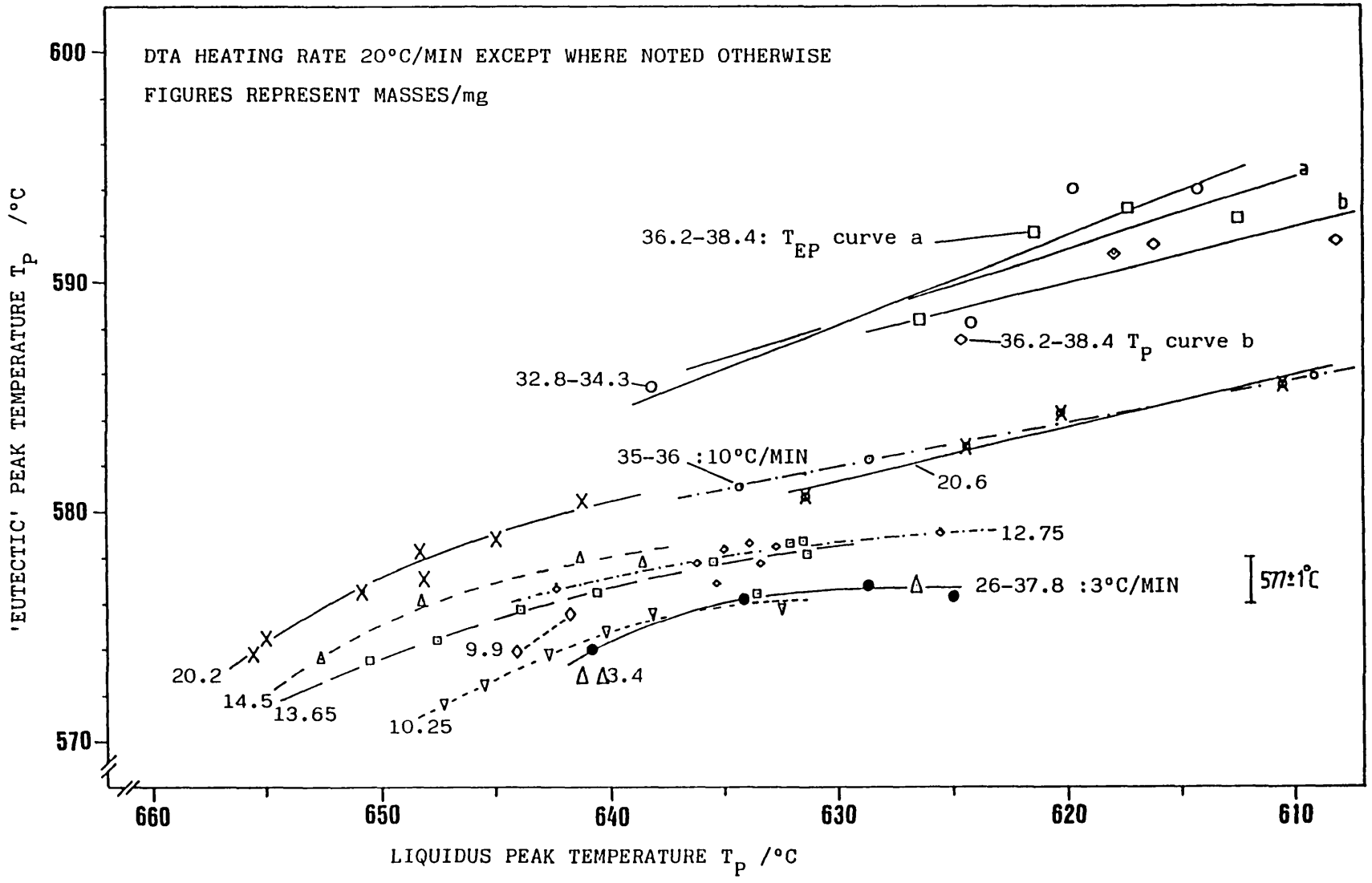
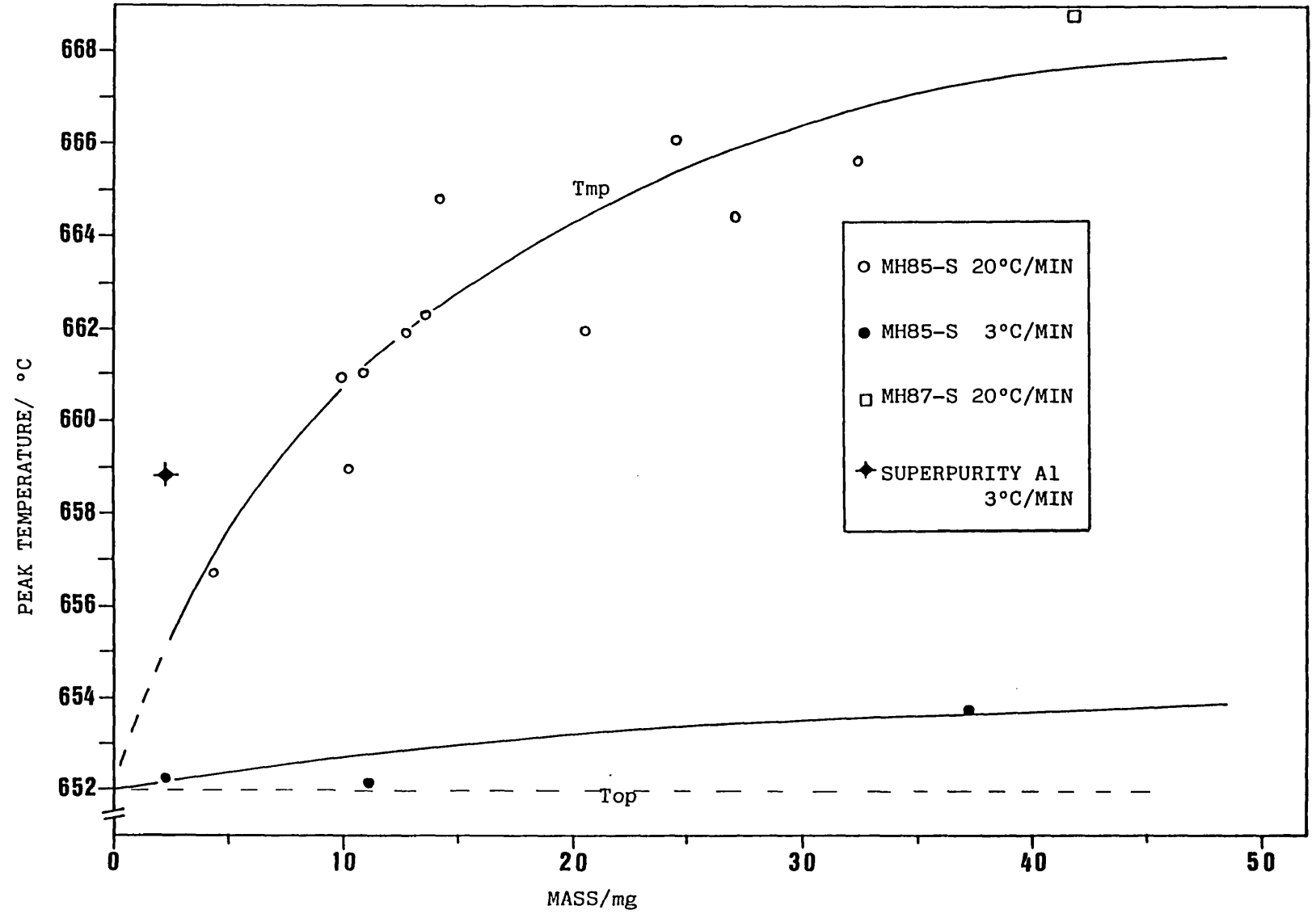


FIGURE 4.26 Curves illustrating the increase in the 'eutectic' DTA peak temperature as the liquidus peak temperature decreases.

FIGURE 4.27 CP.Al-SiC composite DTA peak temperatures found upon heating versus DTA sample mass.



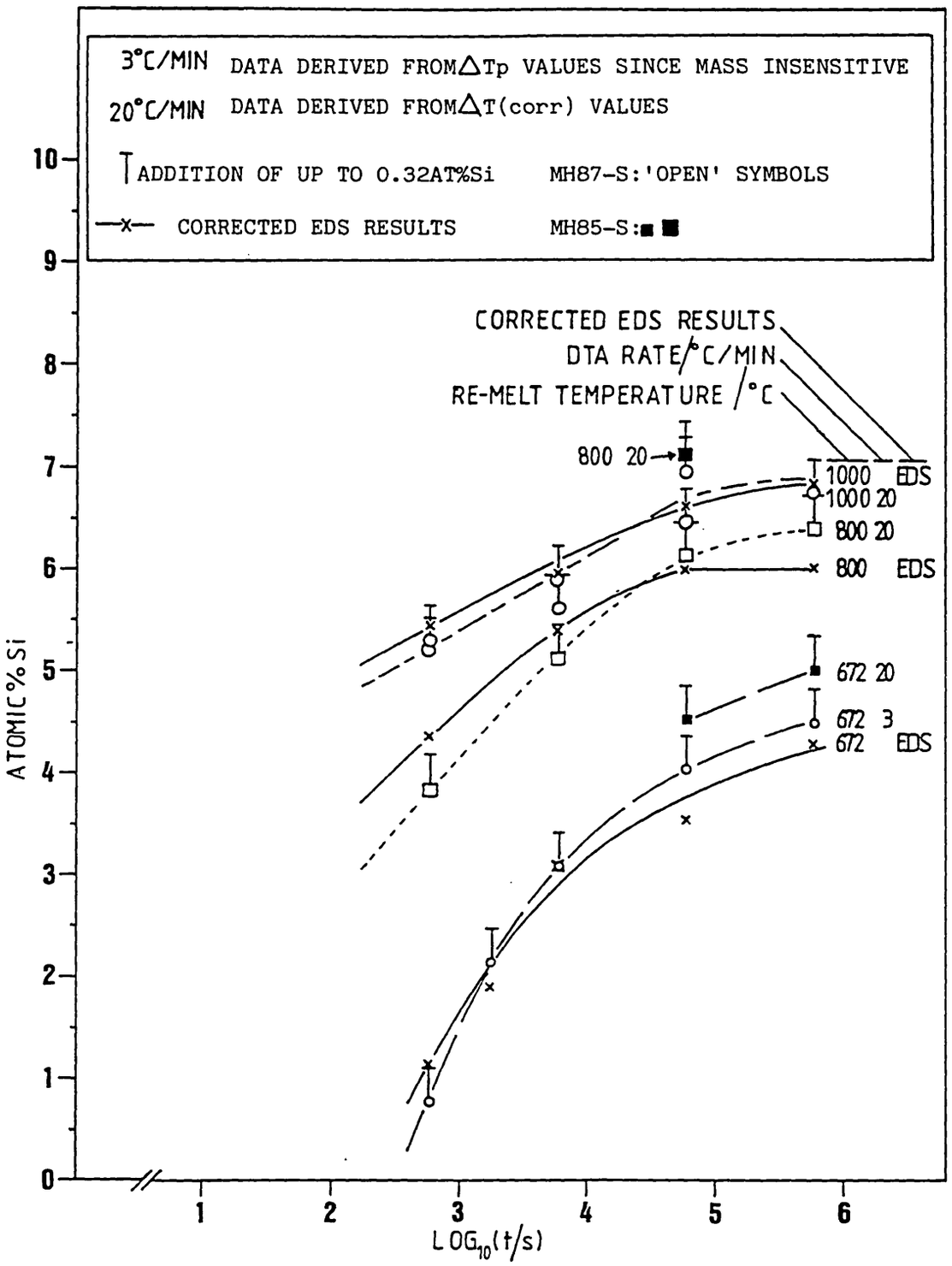


FIGURE 4.28 Comparison of liquid composition results derived from the corrected change in the DTA 'primary' peak temperature ΔT(corr) with the EDS results.

FIGURE 4.29 Comparison of data produced by various techniques and converted to volume fractions of Al_4C_3 for Al-SiC composite reacted at 672°C

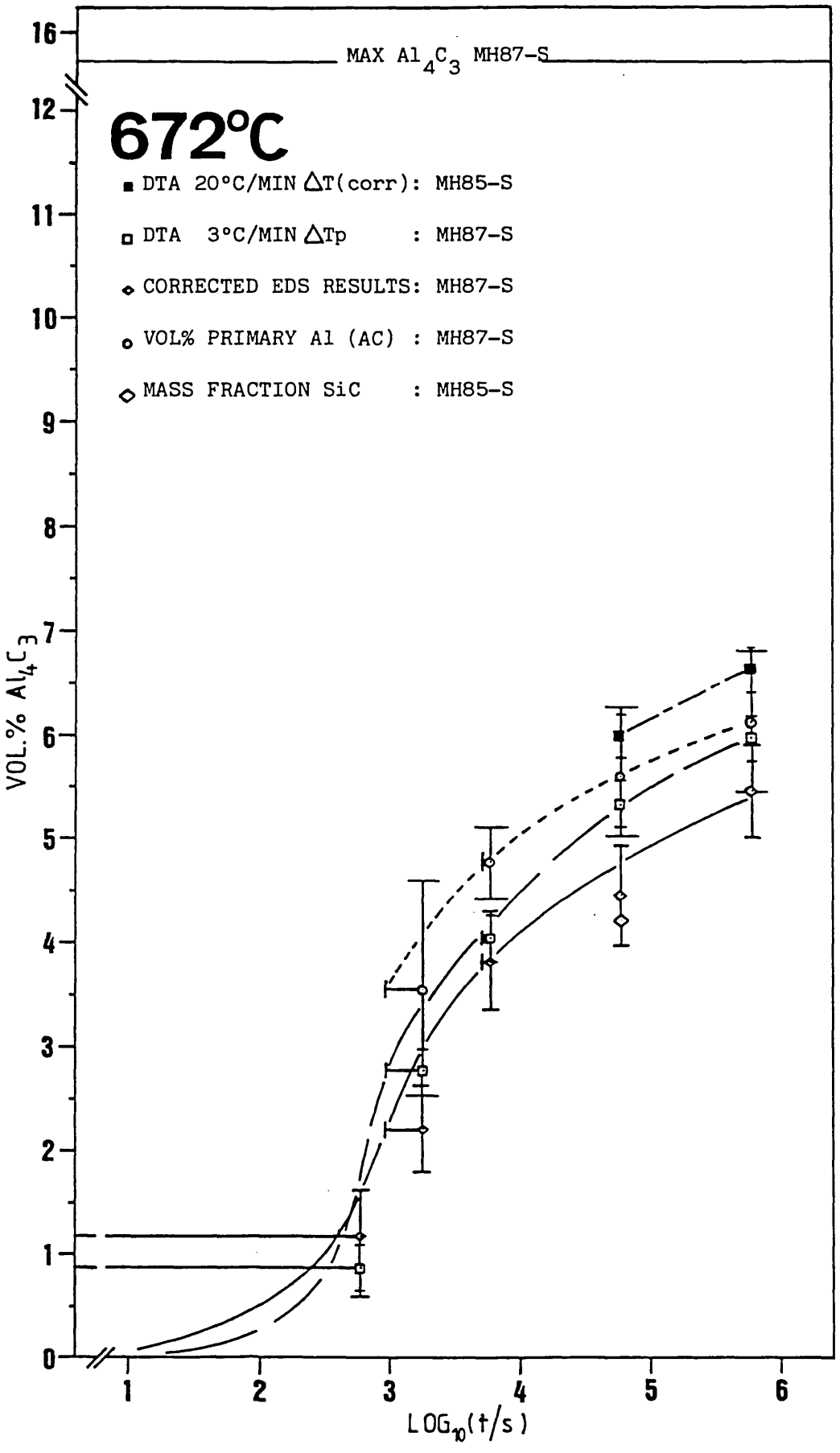


FIGURE 4.30 Comparison of data produced by various techniques and converted to volume fractions of Al_4C_3 for Al-SiC composite reacted at 800°C

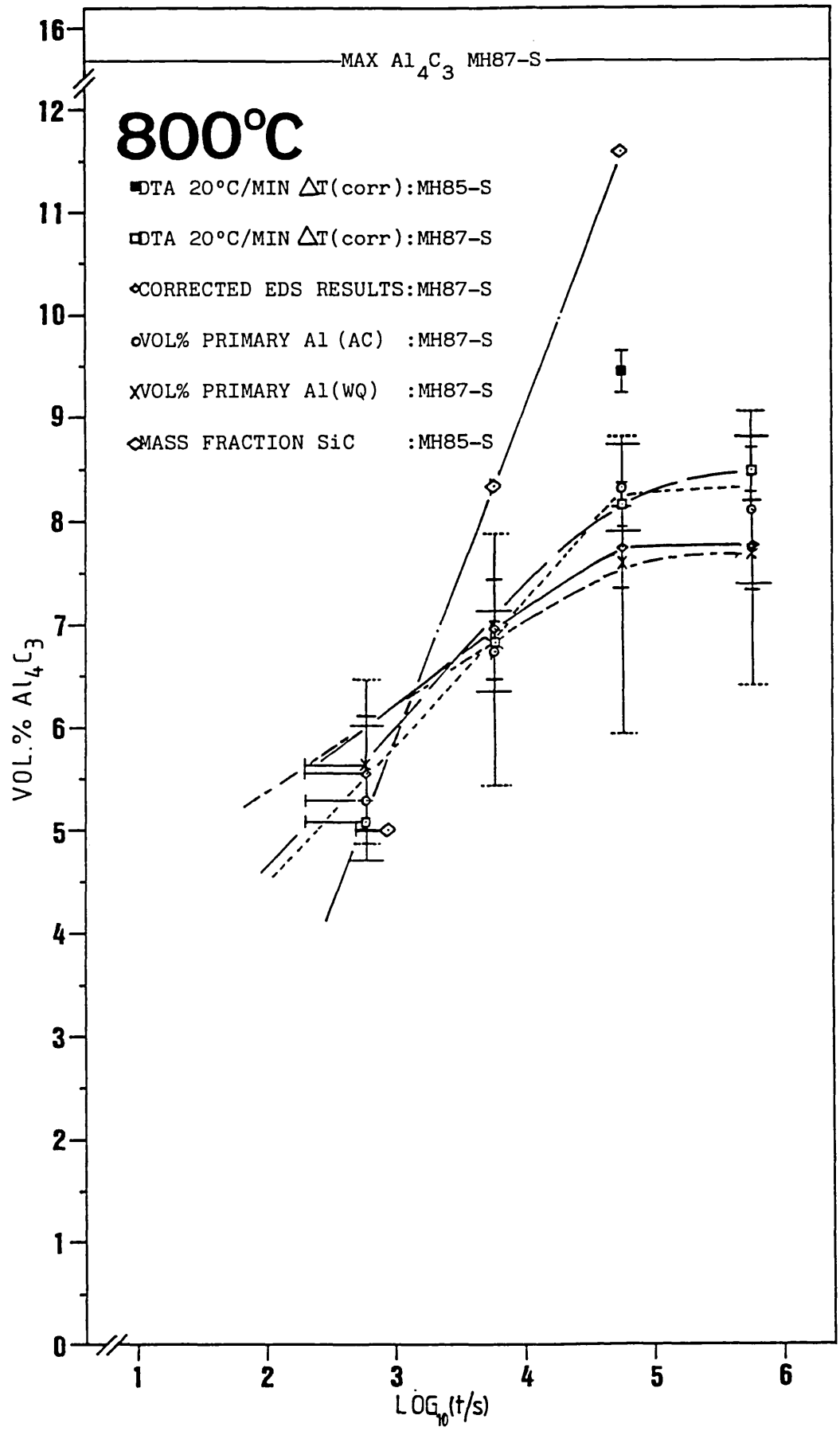


FIGURE 4.31 Comparison of data produced by various techniques and converted to volume fractions of Al_4C_3 for Al-SiC composite reacted at 1000°C

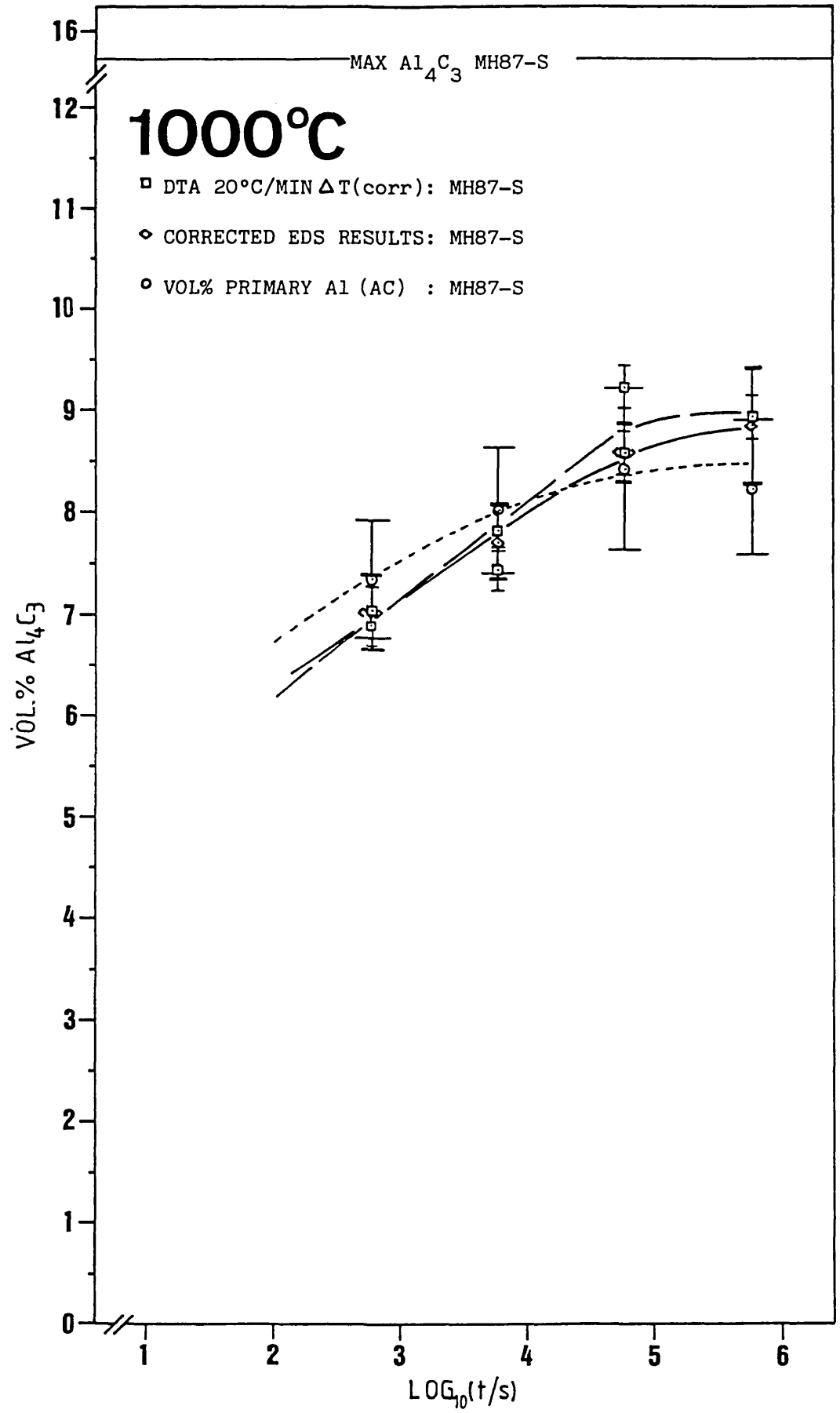
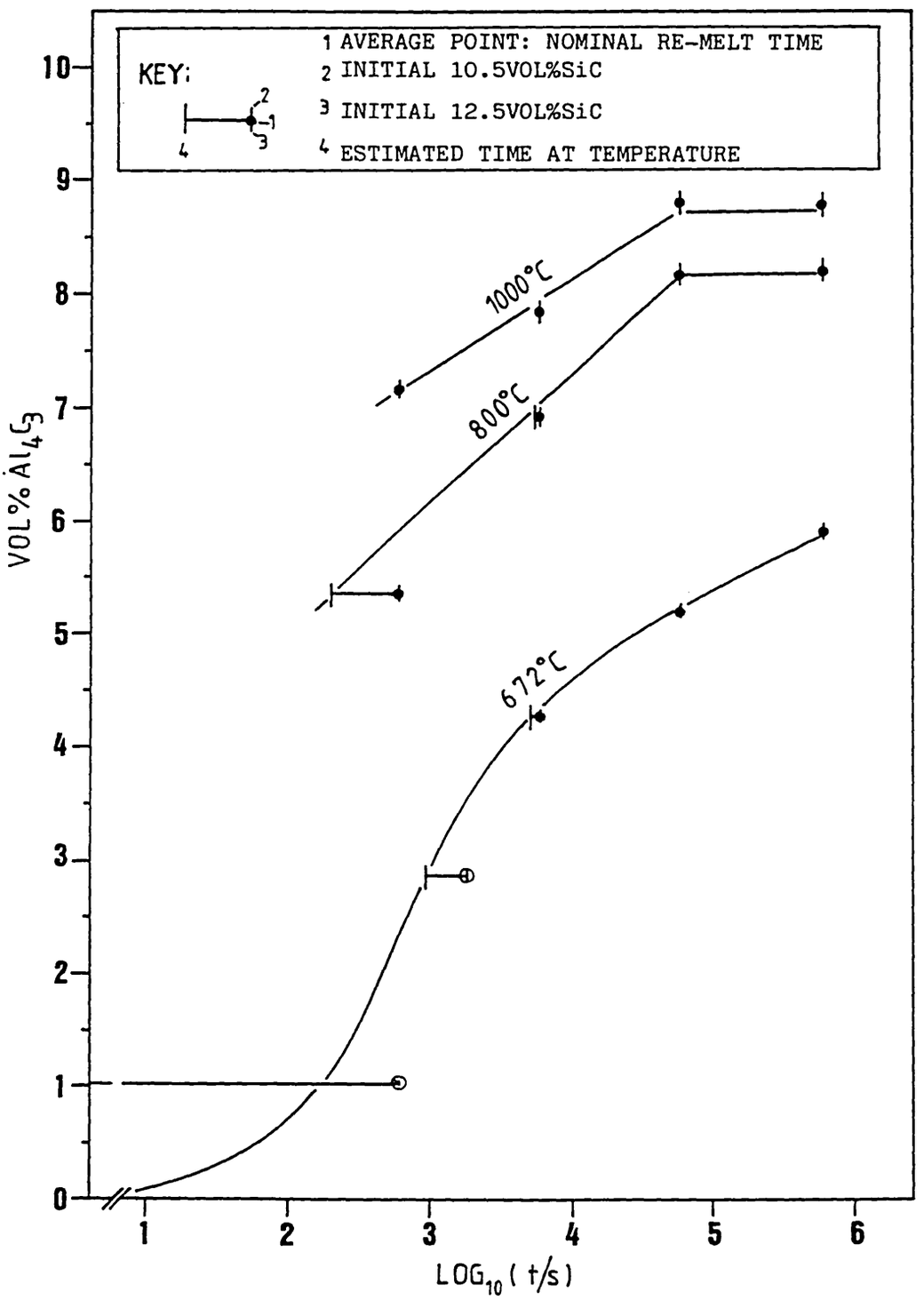


FIGURE 4.32 Averaged results for MH87-S using DTA, EDS and the volume fraction of primary Al in AC samples data. The effect of taking an initial volume fraction of SiC estimate of 10.5 or 12.5vol% to calculate the volume fractions of Al_4C_3 is shown



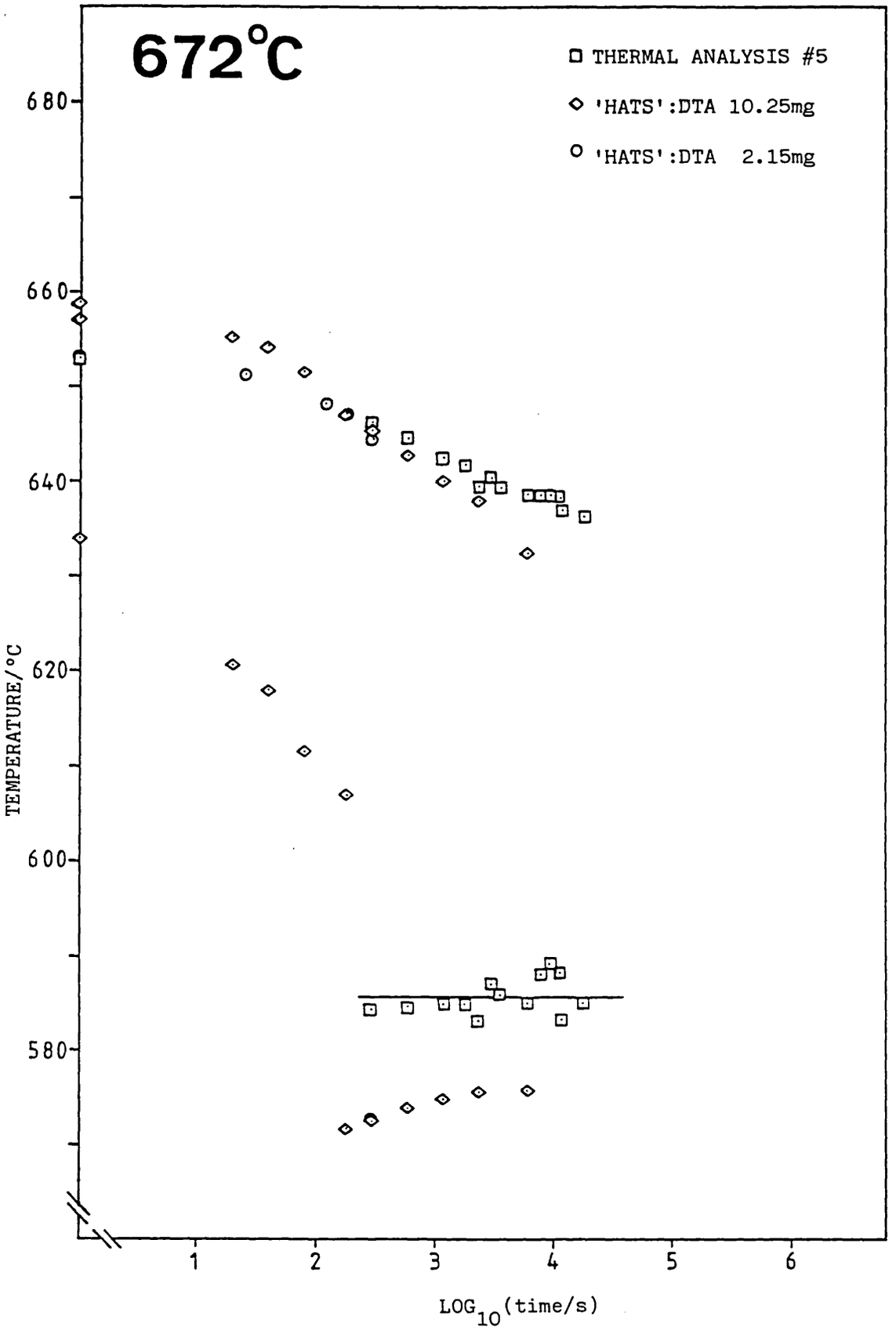


FIGURE 4.33 Plots of DTA peak temperatures and thermal arrest temperatures recorded on heating versus the re-melt time for samples of MH85-S re-melted at 672°C

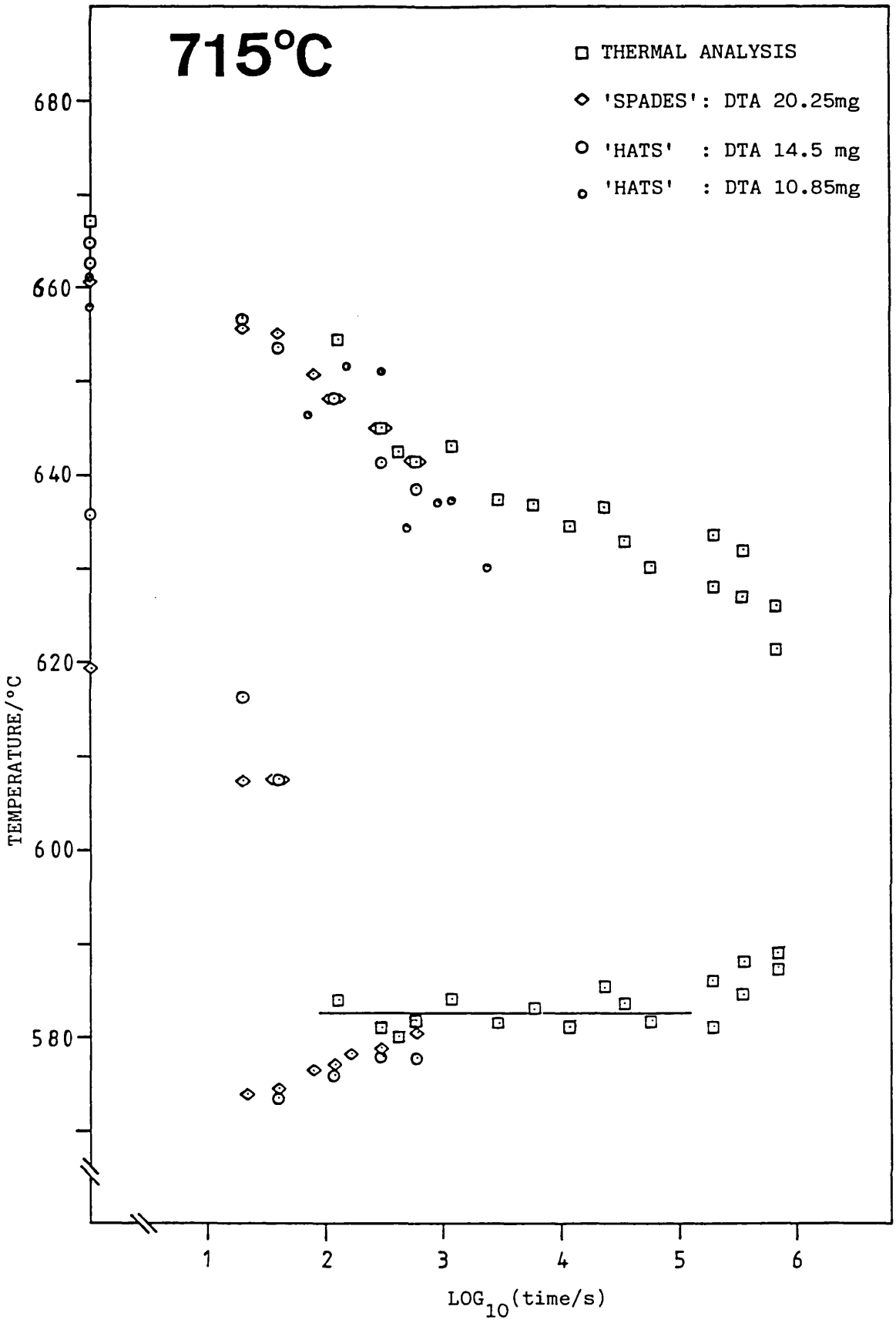


FIGURE 4.34 Plots of DTA peak temperatures and thermal arrest temperatures recorded on heating versus the re-melt time for samples of MH85-S re-melted at 715°C

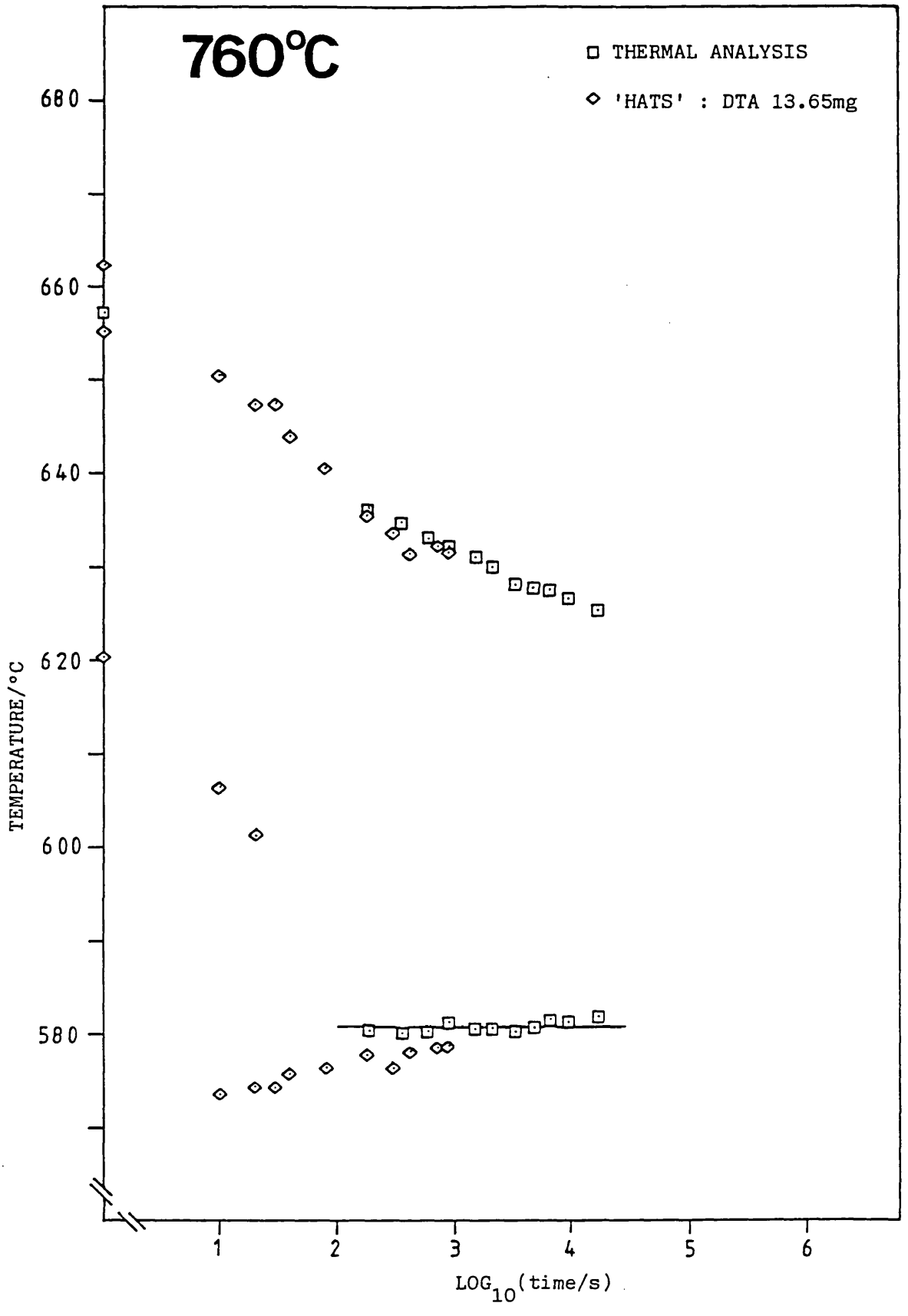


FIGURE 4.35 Plots of DTA peak temperatures and thermal arrest temperatures recorded on heating versus the re-melt time for samples of MH85-S re-melted at 760°C

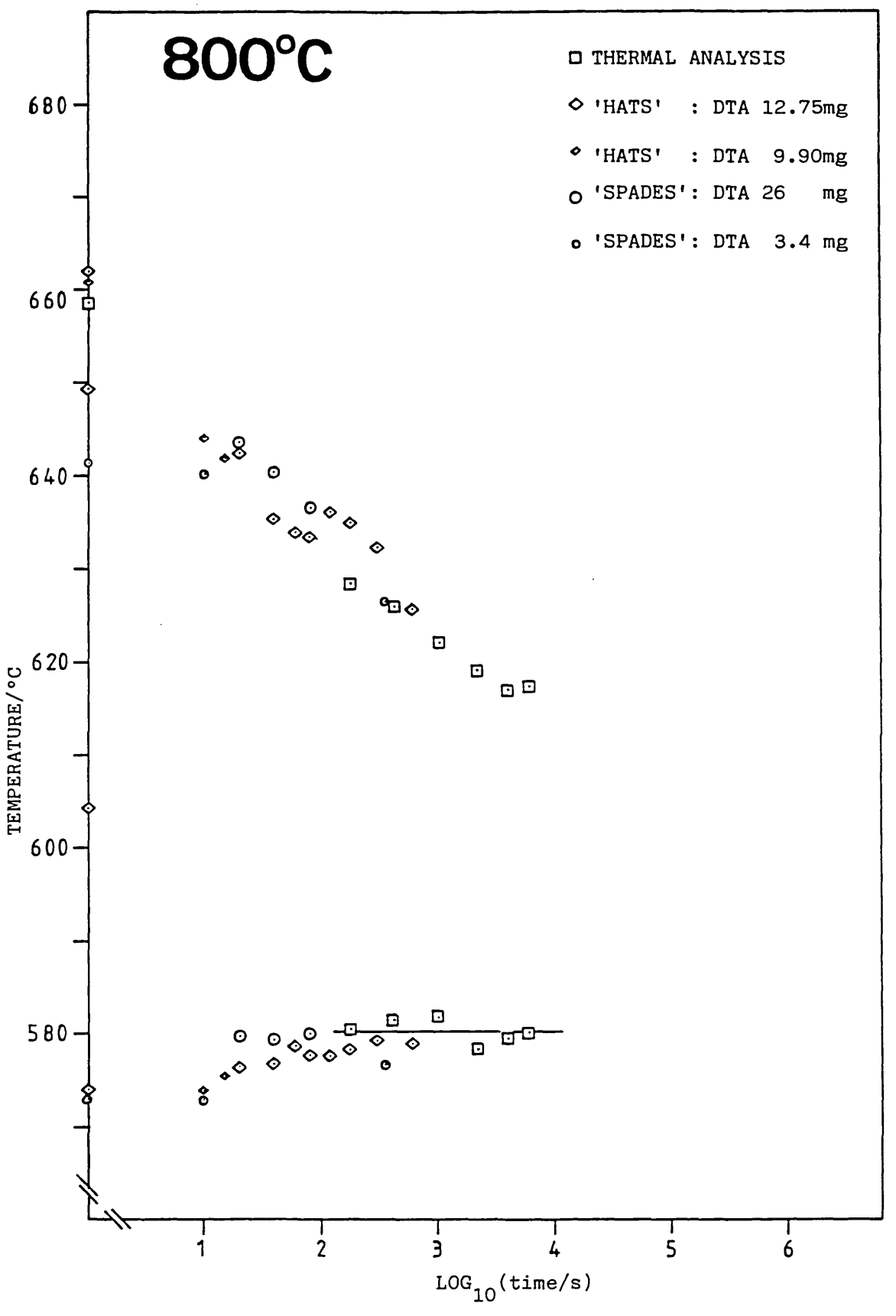


FIGURE 4.36 Plots of DTA peak temperatures and thermal arrest temperatures recorded on heating versus the re-melt time for samples of MH85-S re-melted at 800°C

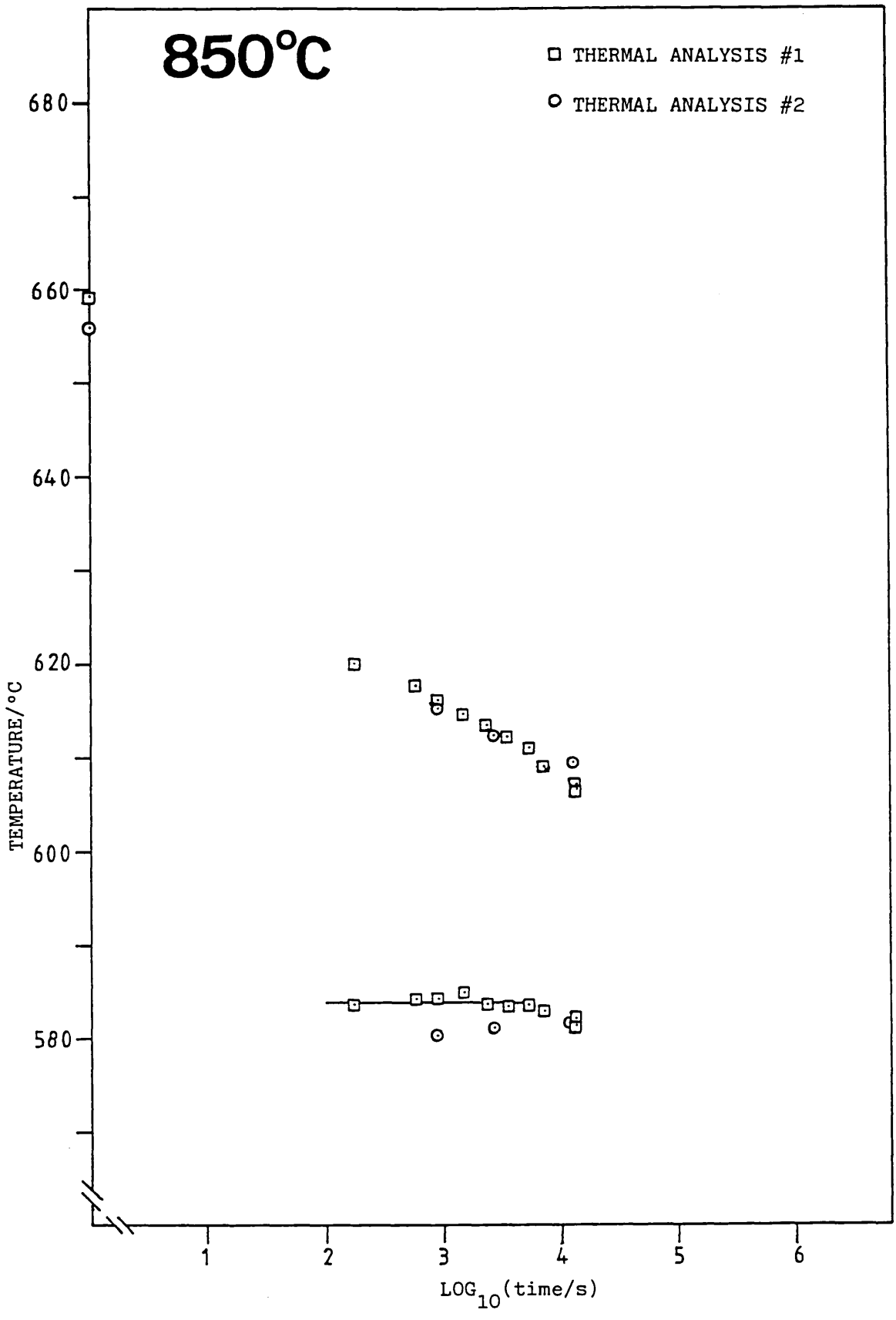


FIGURE 4.37 Plots of DTA peak temperatures and thermal arrest temperatures recorded on heating versus the re-melt time for samples of MH85-S re-melted at 850°C

FIGURE 4.38 Comparison of the thermal analysis data obtained for the different isothermal treatments. The difference between the liquidus and average 'eutectic' thermal arrest temperatures is plotted against the re-melt time

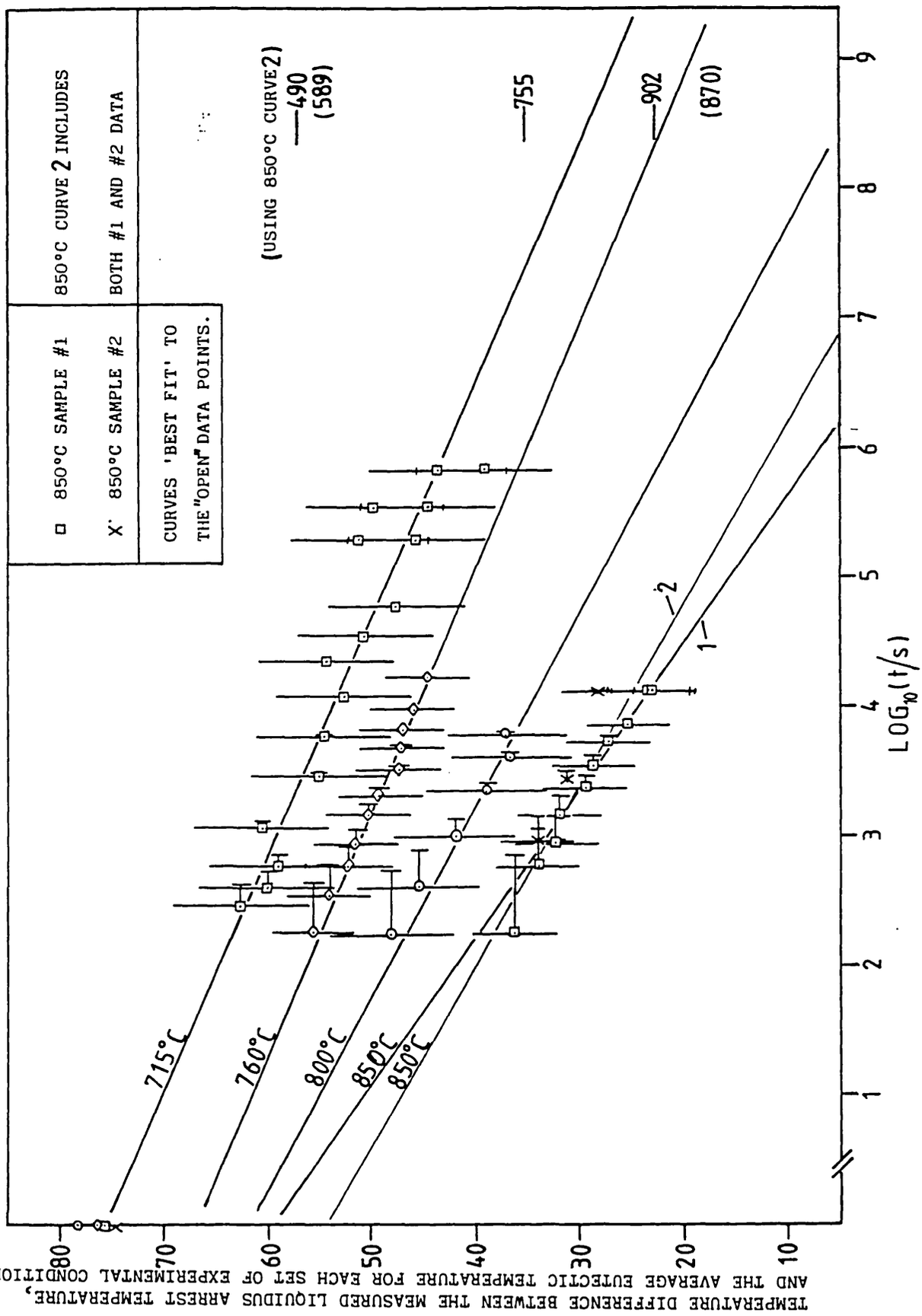
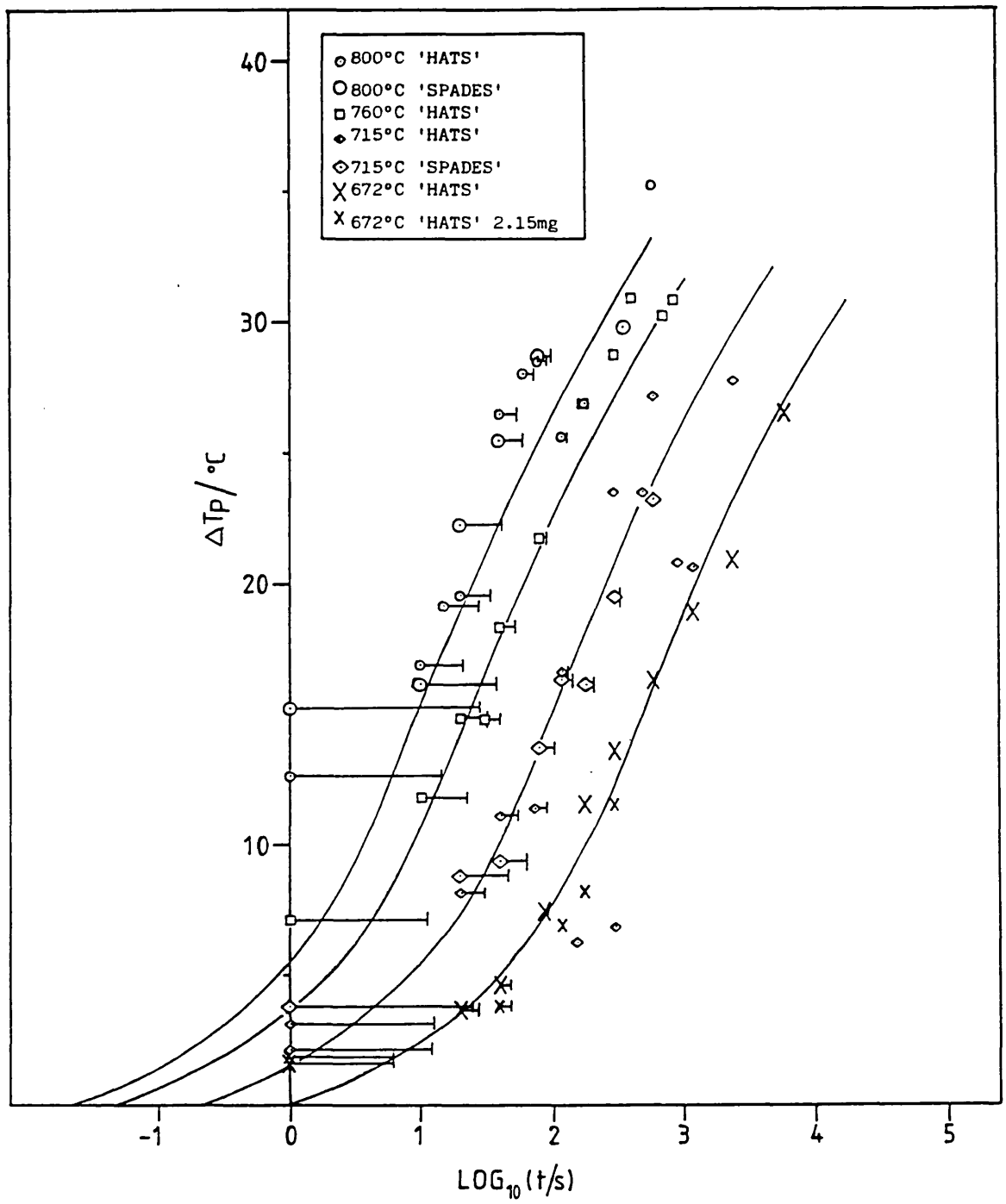


FIGURE 4.39 Decrease in the DTA peak temperature associated with the liquidus recorded on heating ΔT_p for MH85-S 'rapidly heated re-melted samples' as a function of the re-melt time. The curve shown is approximately fitted to the 672°C data and translated to coincide with the other data sets



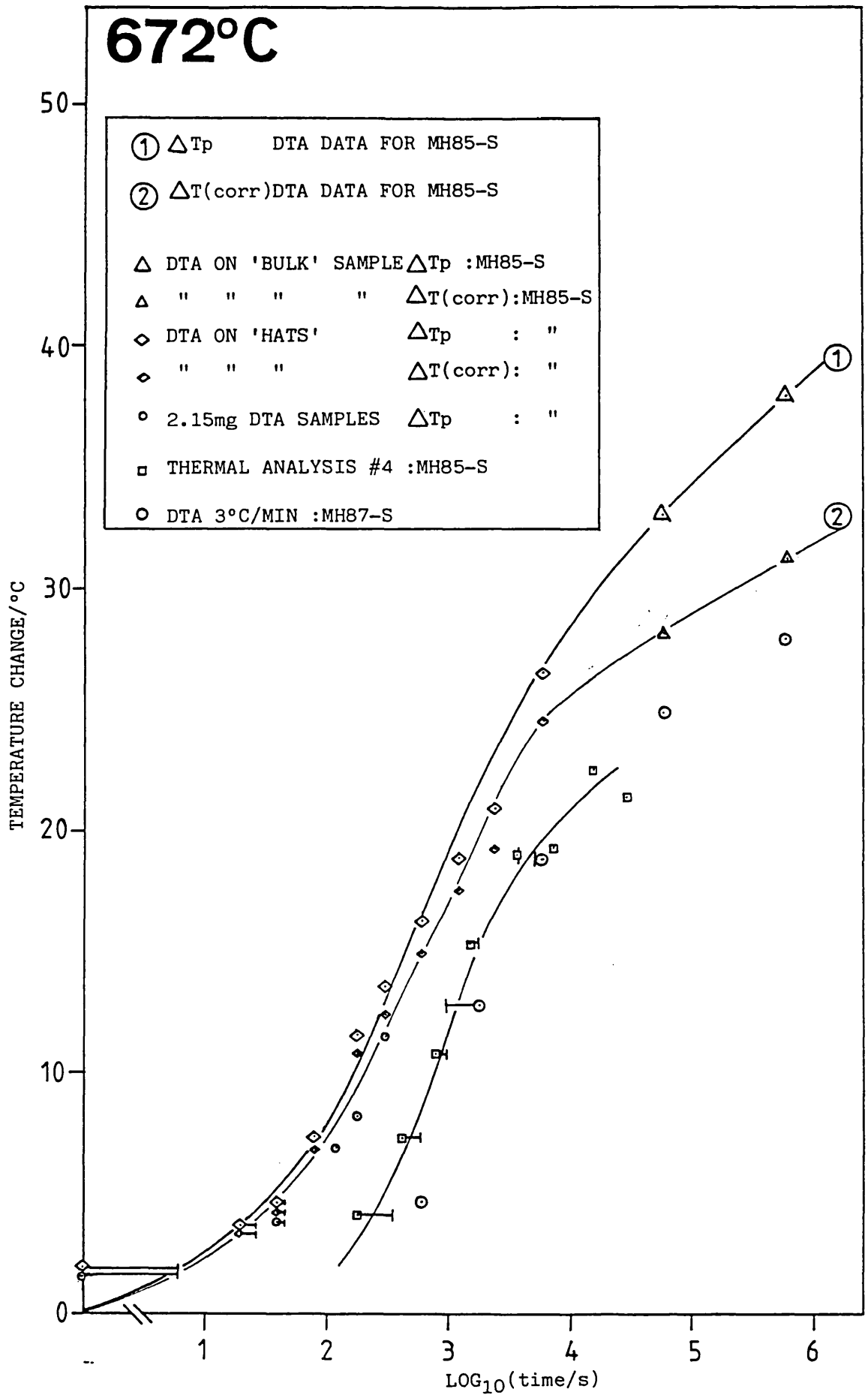


FIGURE 4.40 Kinetic curves derived from the thermal analysis and DTA based methods for reaction (4.1) at 672°C

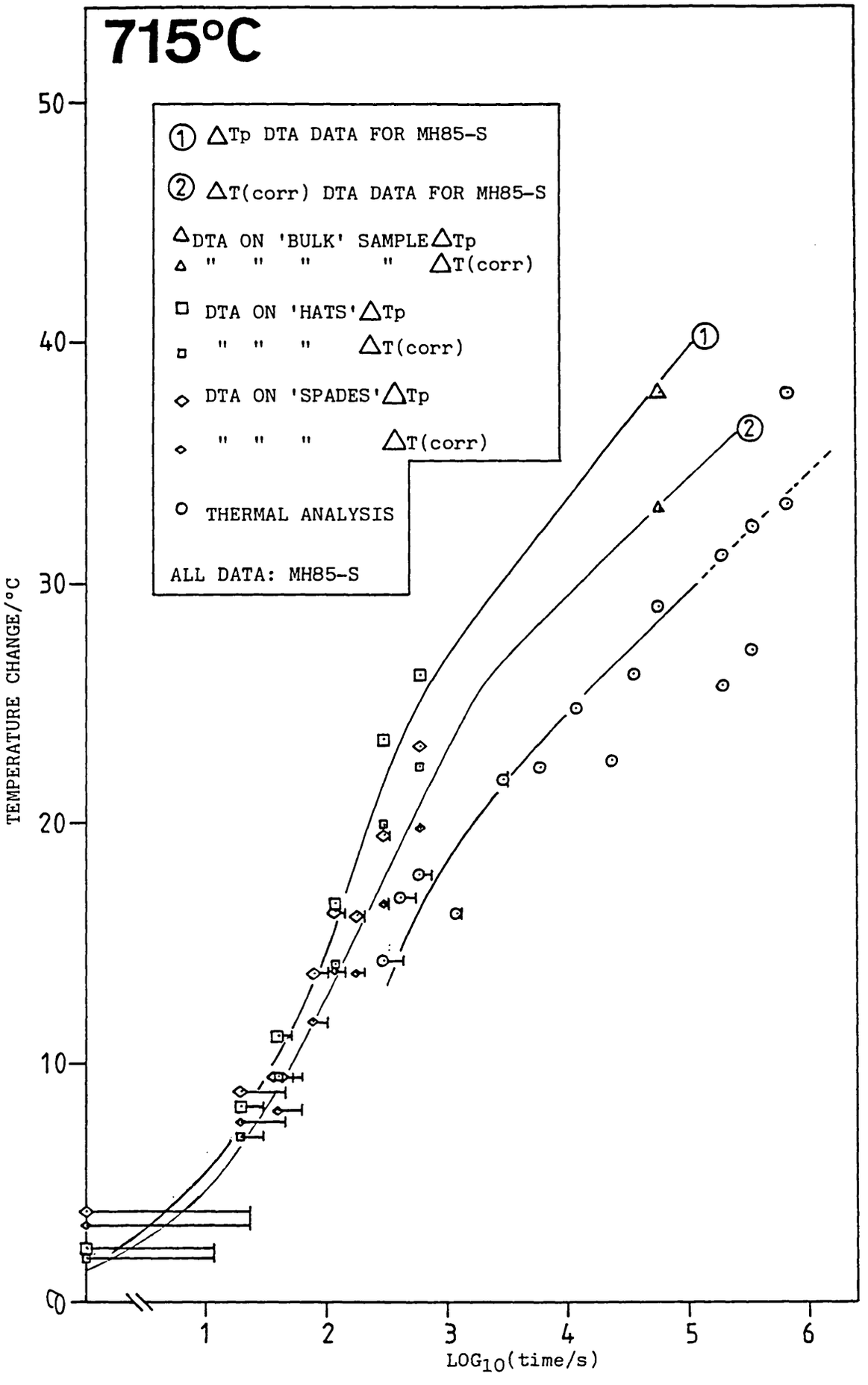


FIGURE 4.41 Kinetic curves derived from the thermal analysis and DTA based methods for reaction (4.1) at 715°C

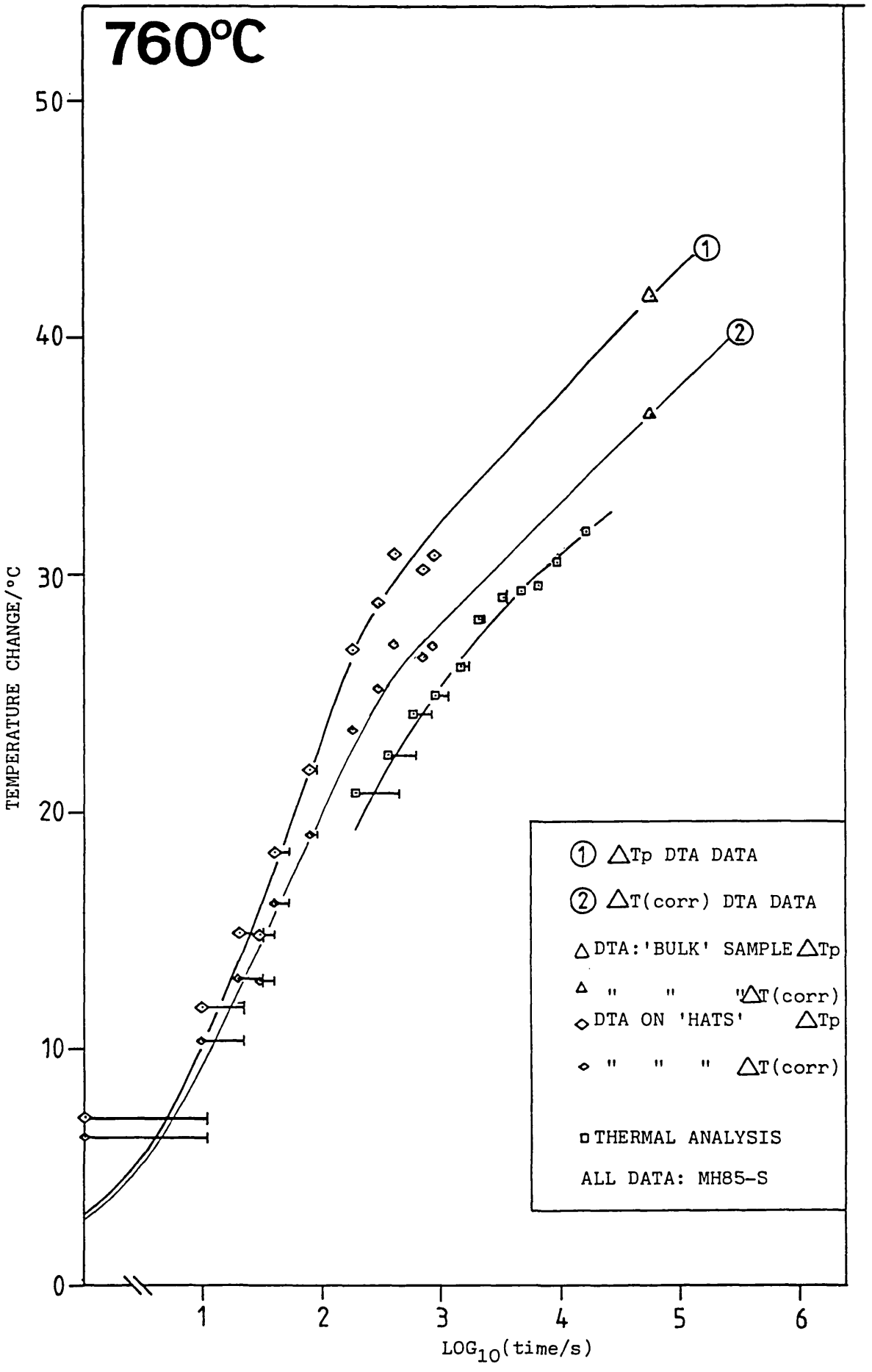


FIGURE 4.42 Kinetic curves derived from the thermal analysis and DTA based methods for reaction (4.1) at 760°C

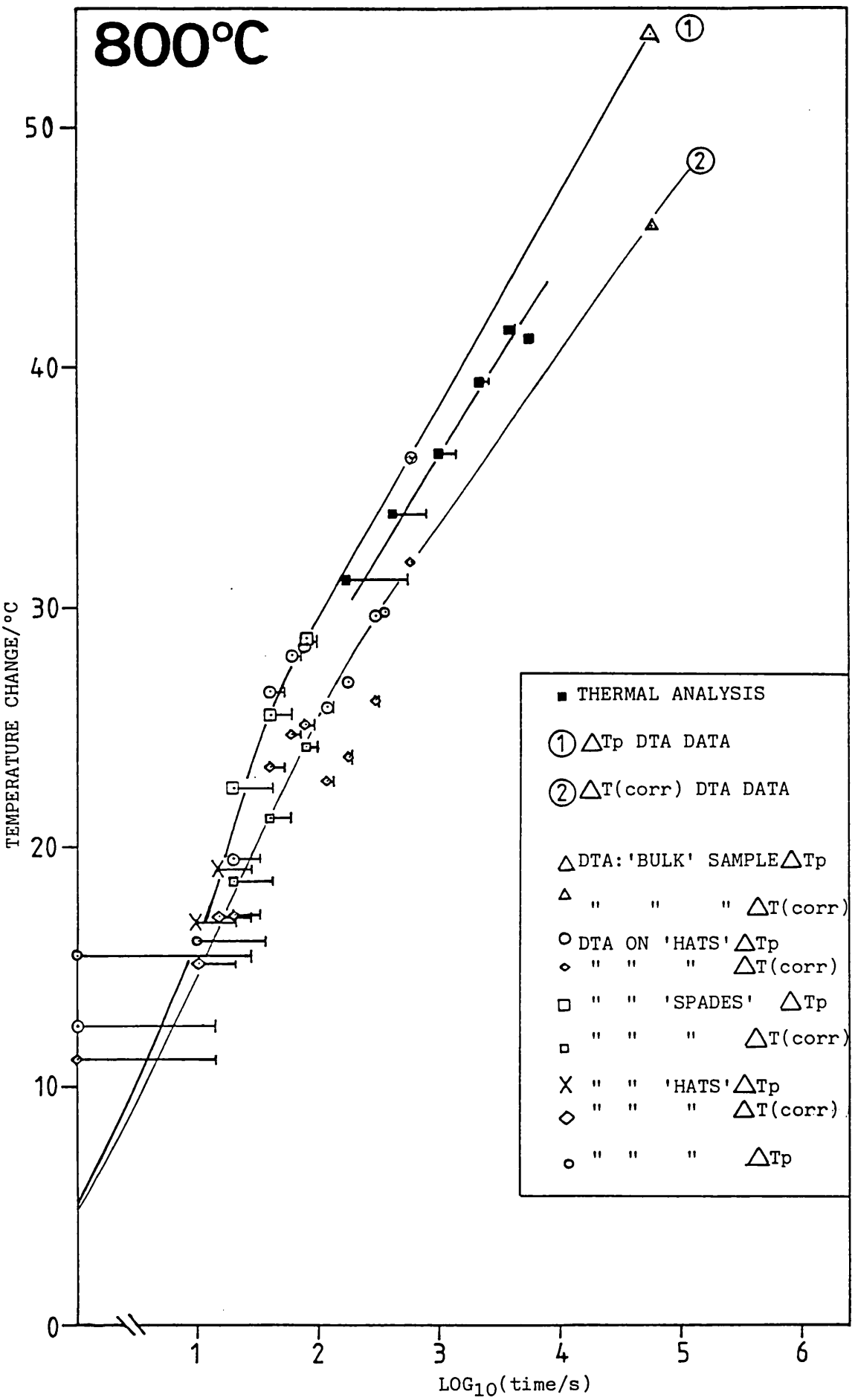


FIGURE 4.43 Kinetic curves derived from the thermal analysis and DTA based methods for reaction (4.1) at 800°C

FIGURE 4.44 Linear extrapolations of the kinetic data presented in figures 4.40 - 4.43. The curves are extrapolated to the temperature change for a sample of MH85-S re-melted for 1000mins at 800°C estimated to be at the 'end of the stage 2 kinetics' at which point the activation energy for the rate controlling reaction mechanism is estimated

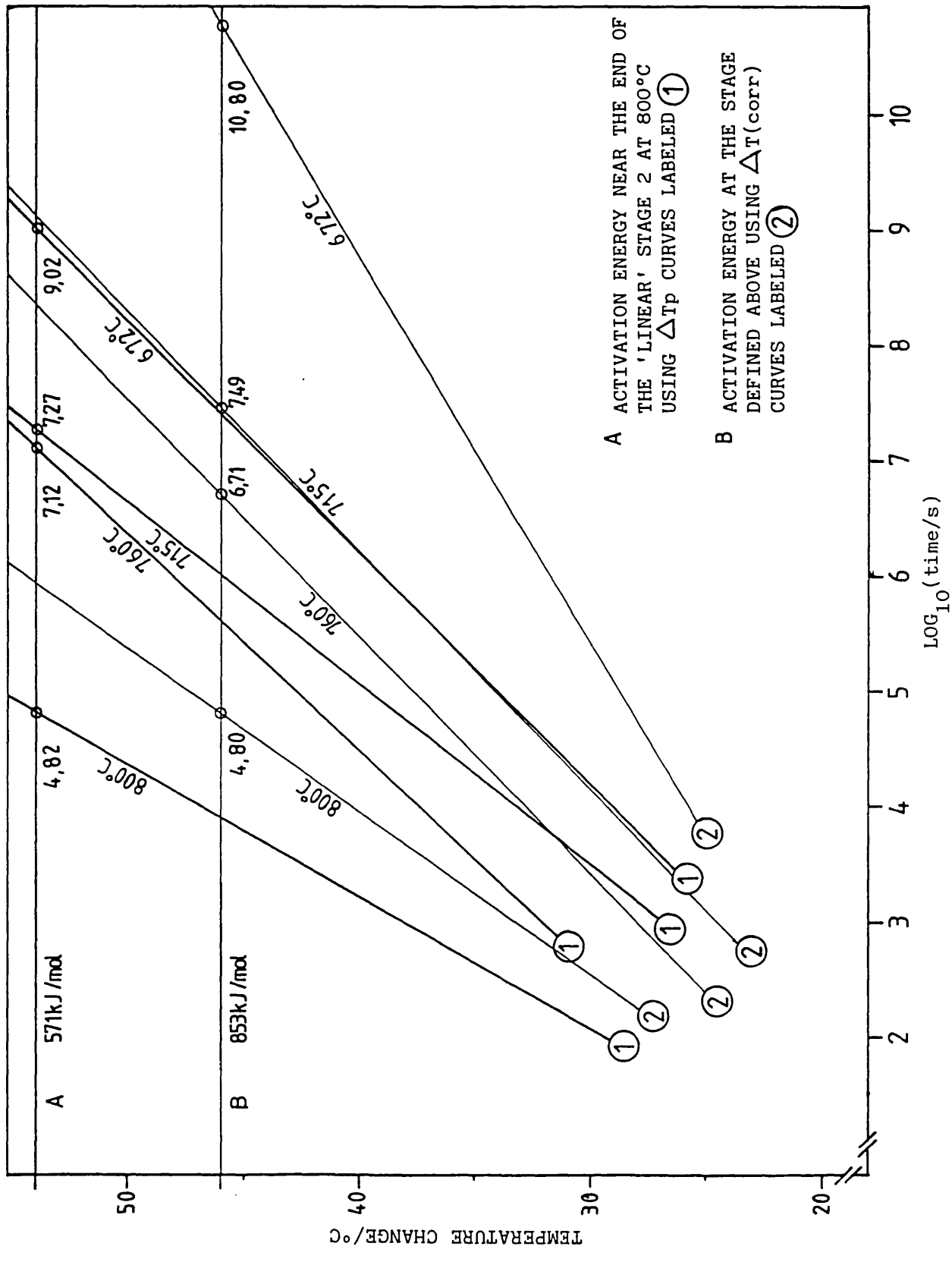


FIGURE 4.45 Decrease in the liquidus DTA peak temperature versus the re-melt time. The data shown covers the 'stage 1' kinetics, although 'stage 1' at 672°C is considered to be incomplete until after 1000s

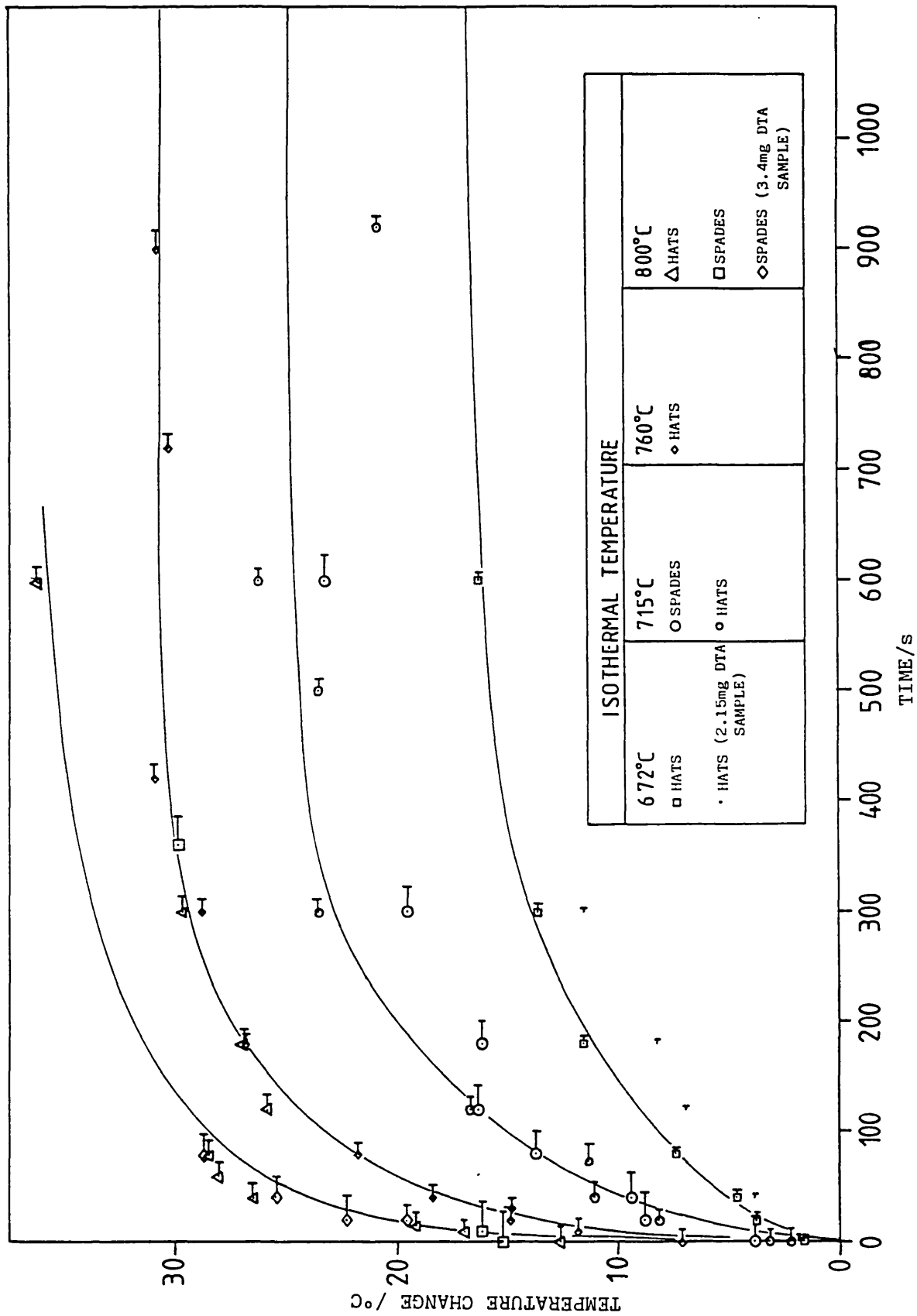


FIGURE 4.46 Arrhenius plots. The log of the time to a given change in the DTA peak temperature, or the log of the time to a given change in the thermal analysis arrest temperature is plotted against the reciprocal of the absolute re-melt temperature. Examples of 'stage 1' and 'stage 2' plots are given.

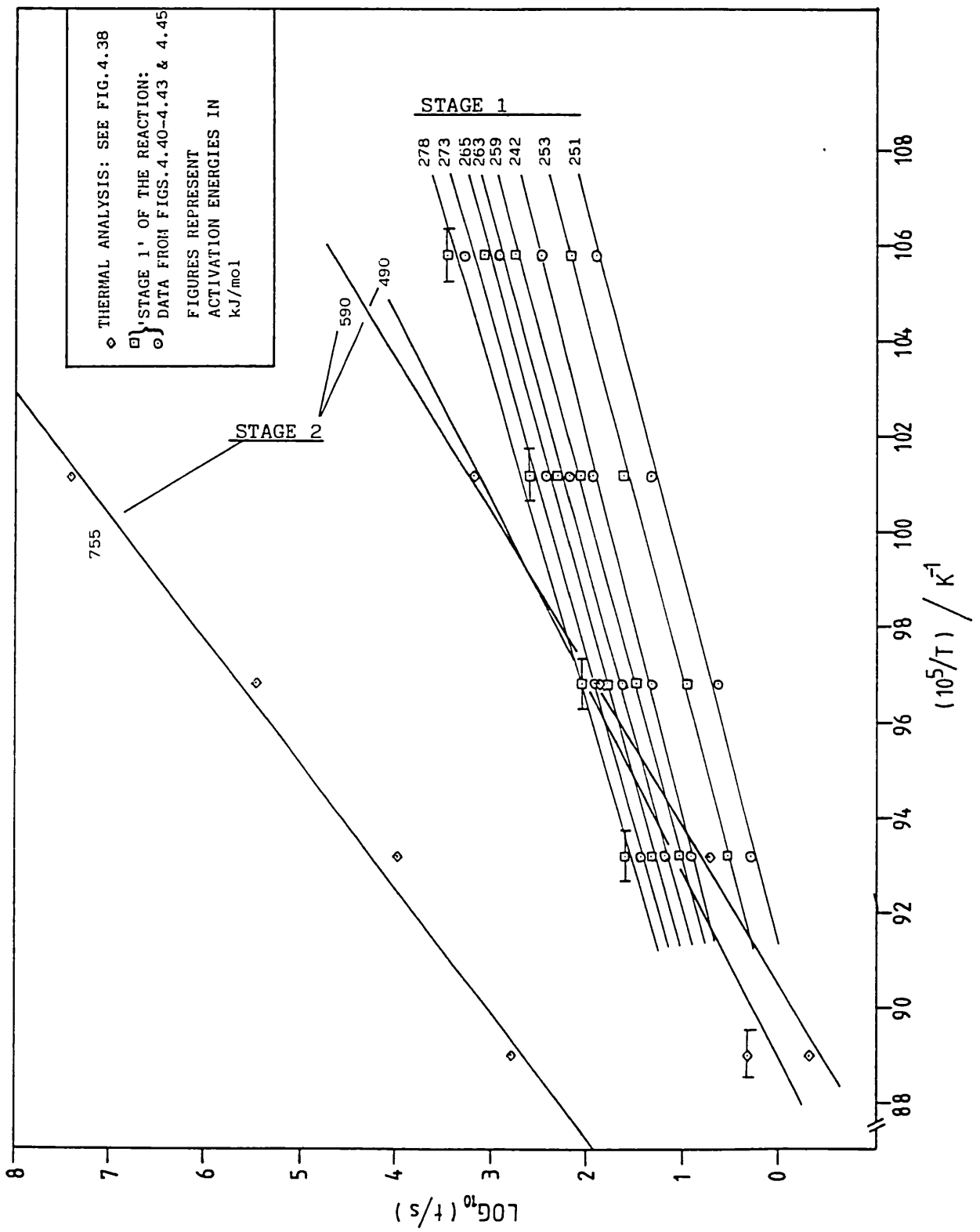


FIGURE 4.47 CP.Al-SiC liquid (matrix) composition as a function of time and temperature. Points a and b = appearance of Al_4C_3 in LM13 +SiC and Al-12Si+SiC respectively. End of the reaction matrix compositions shown by curves marked t=∞

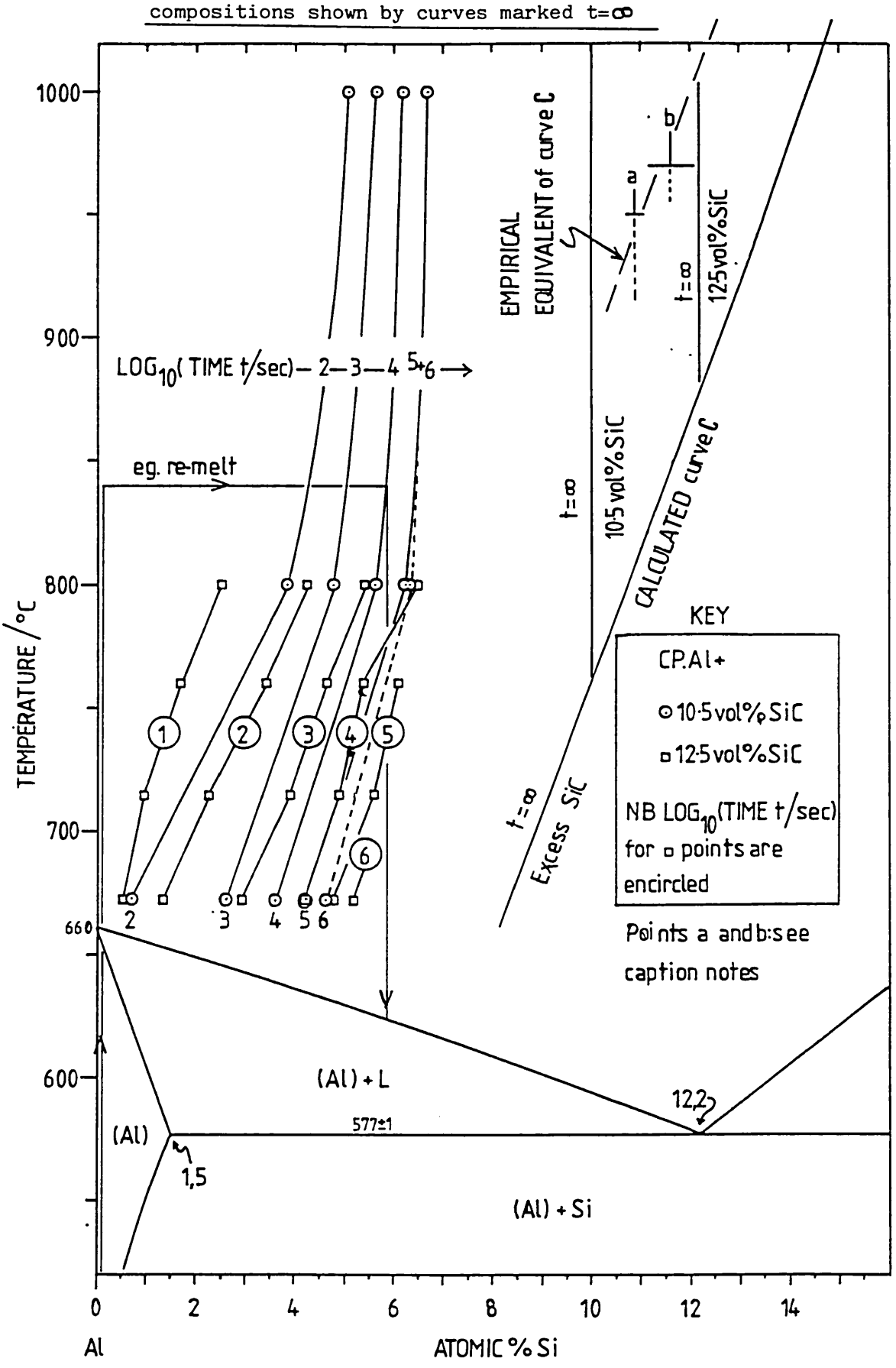


FIGURE 4.48 The volume fraction of Al_4C_3 produced in CP.Al-SiC composites as a function of the re-melting time and temperature .Data in figure 4.32 (CP.Al+10.5vol%SiC) and figures 4.40-4.43 (CP.Al+12.5vol%SiC) were used to construct the diagram.

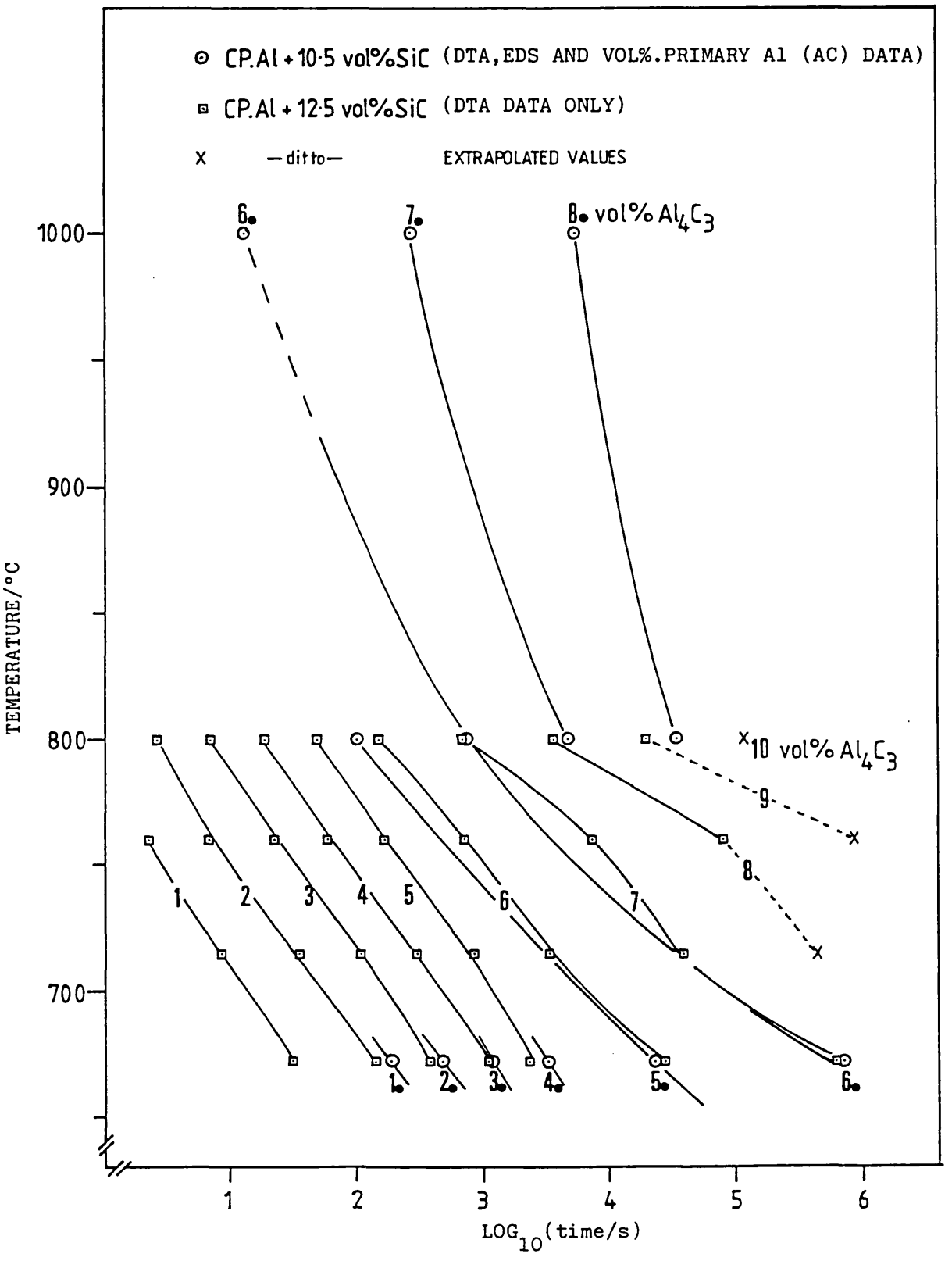


FIGURE 4.49 TTT diagram for the reaction between CP.Al and 10.5vol%SiC and 12.5vol%SiC of F600 grit grade particulate. 100% transformation is defined with respect to the appropriate t=∞ curves in figure 4.47 for each composite. Data in figure 4.32 (CP.Al+10.5vol%SiC) and figures 4.40-4.43 (CP.Al+12.5 vol%SiC) were used to construct the diagram.

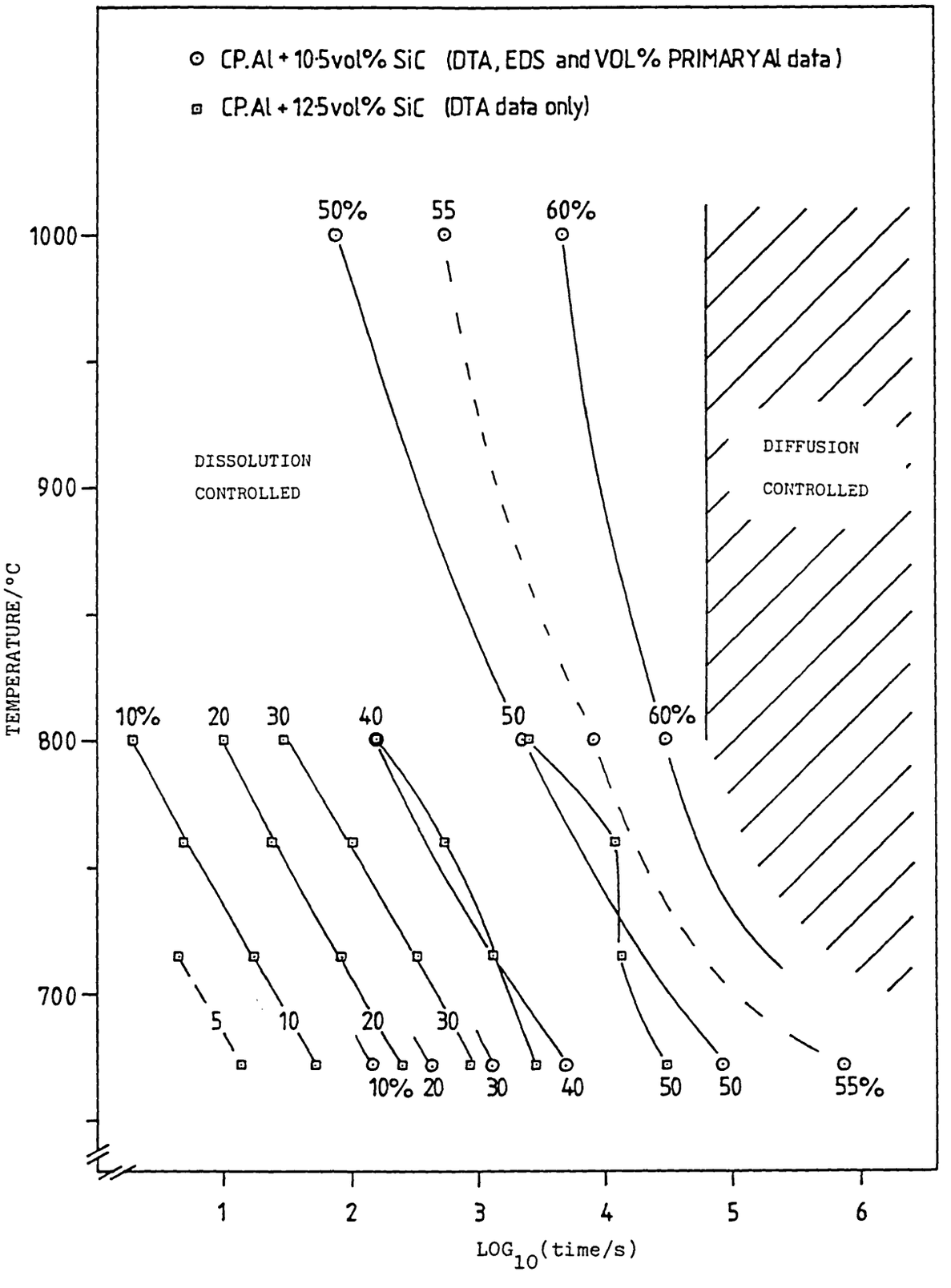


FIGURE 4.50 TTT diagrams for the two composites in which the 100% transformation has been taken as being the same so that a comparison can be made between the extents of reaction. The figure is not the equivalent of 4.49 and 4.48 since only DTA based results have been used.

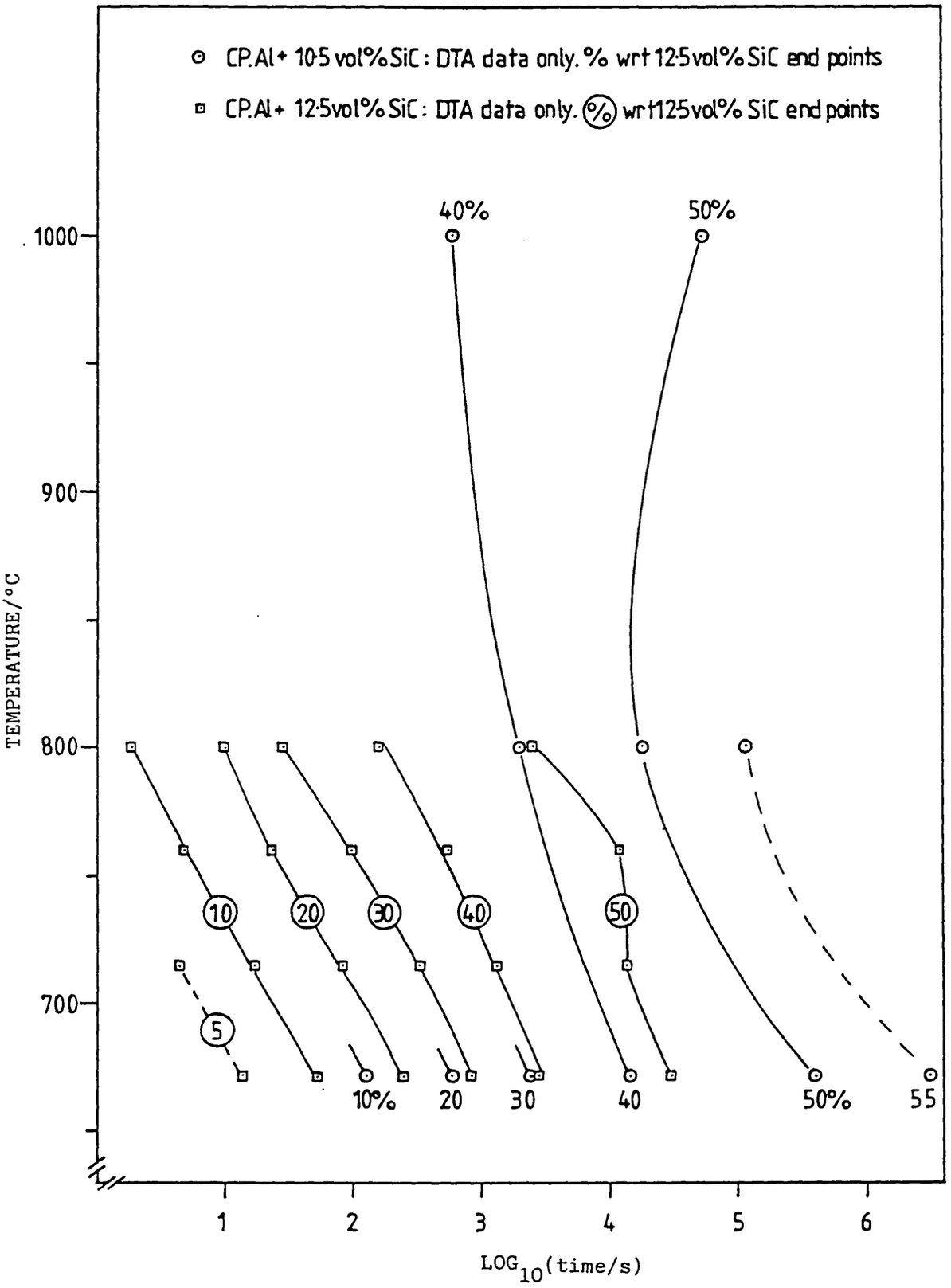


FIGURE 4.51 TTT diagram for the CP.Al+10.5vol%SiC composite alone. The transformation 100% has been defined by an extrapolation of the EMPIRICAL EQUIVALENT of curve C (and the t=∞curve for 10.5vol%SiC) in figure 4.47

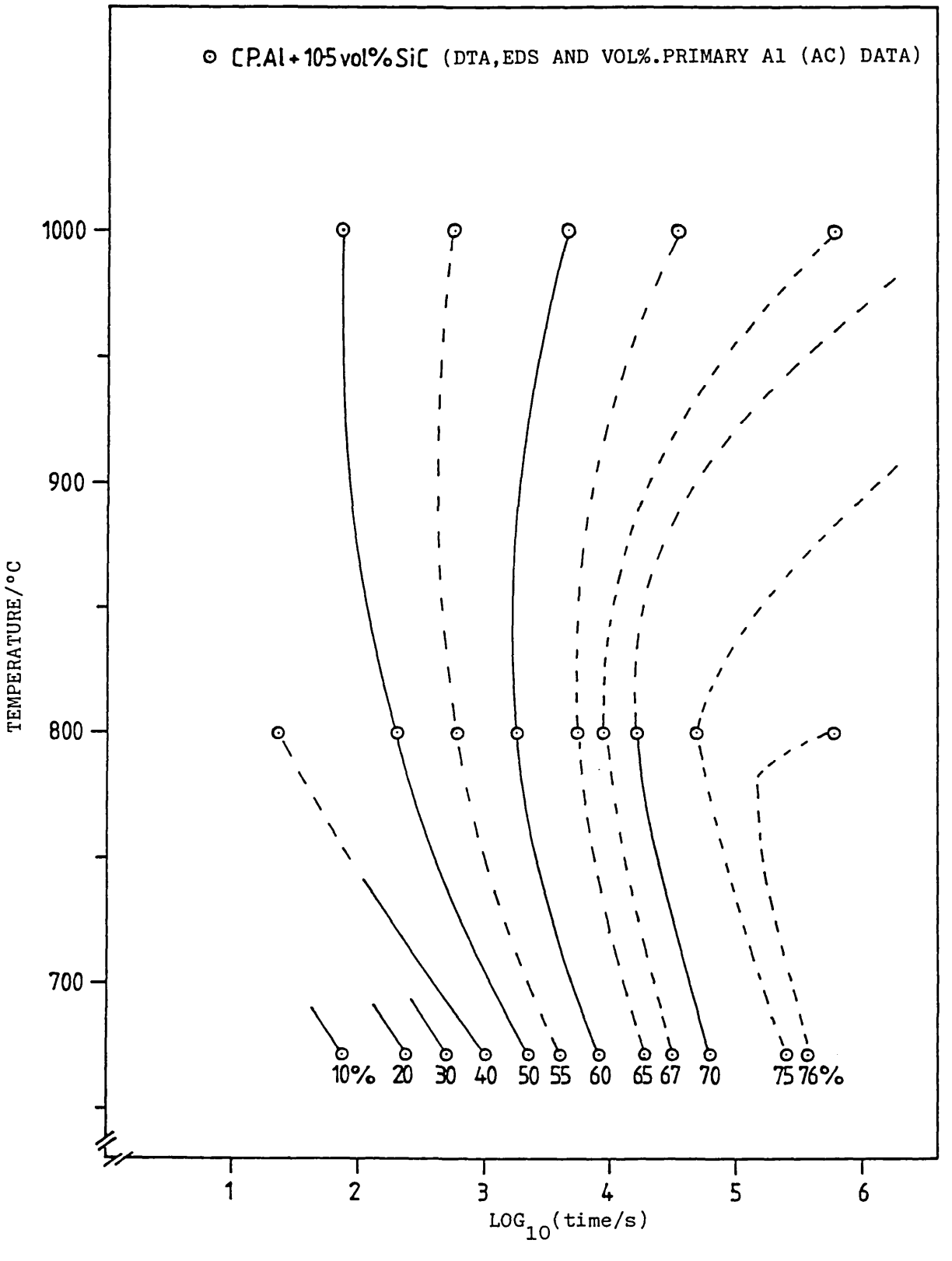
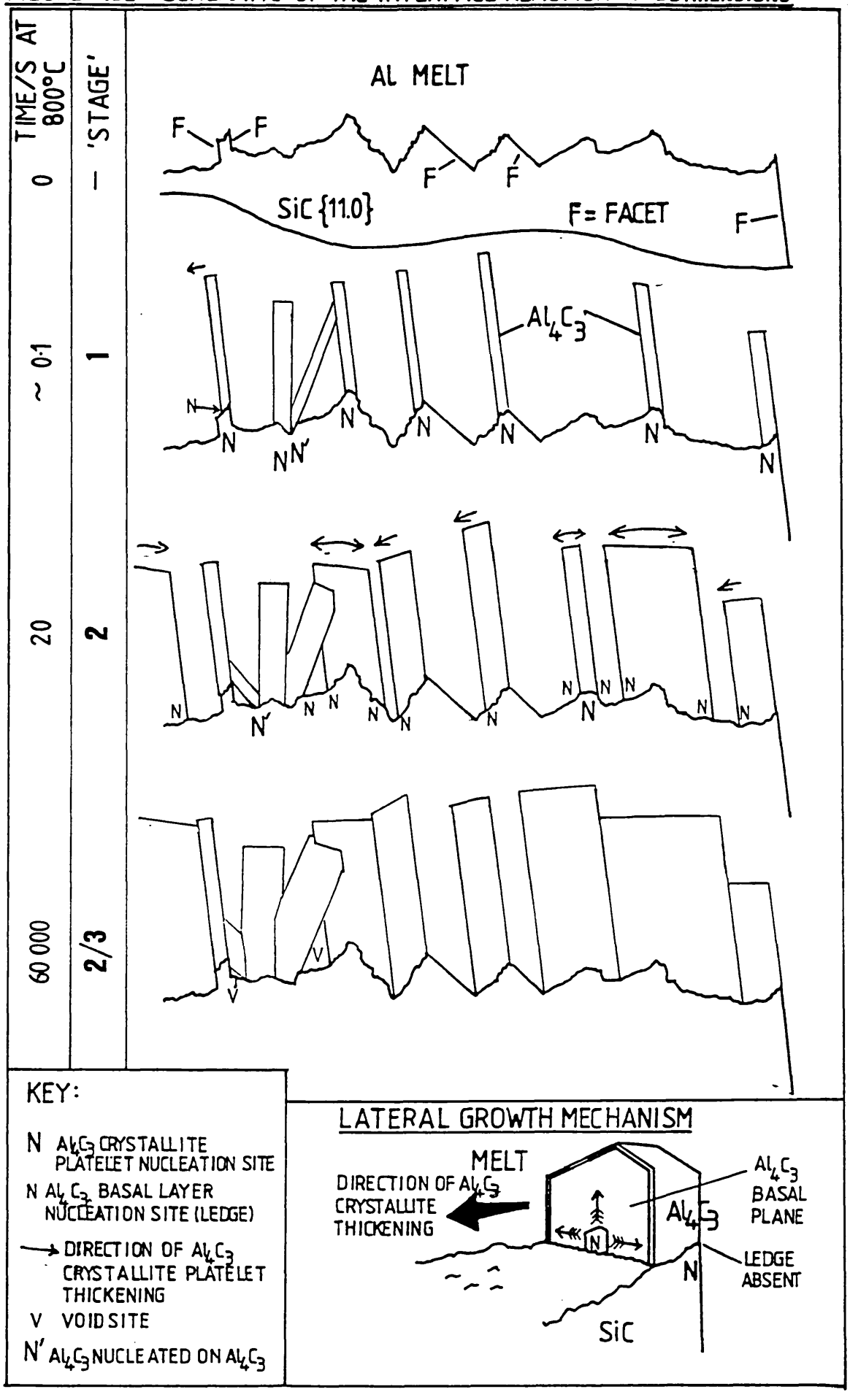


FIGURE 4.52 SCHEMATIC OF THE INTERFACE REACTION IN 2DIMENSIONS



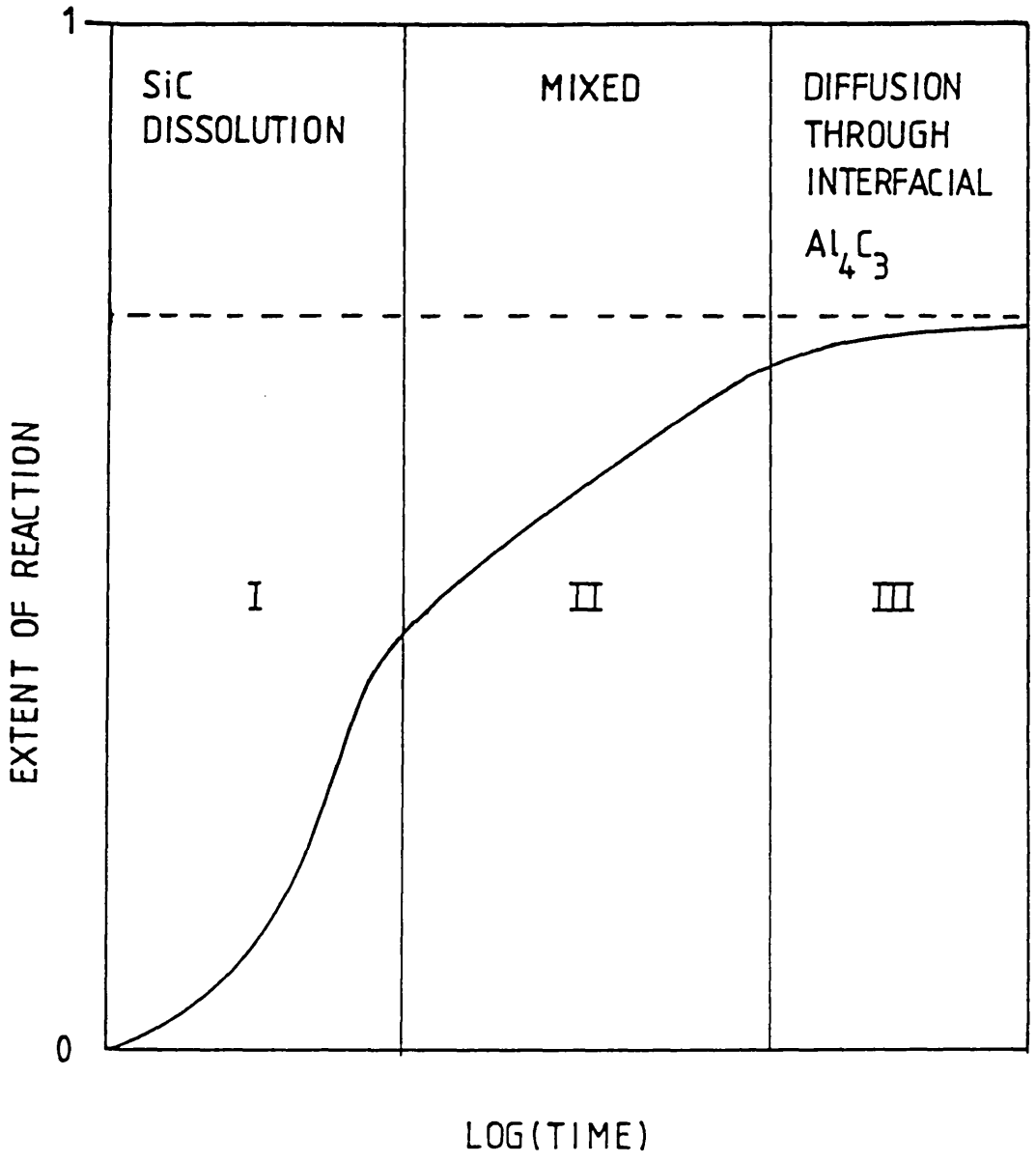


FIGURE 4.53 Summary of the three stages in the kinetics of the reaction $4Al(l) + 3SiC(s) \longrightarrow Al_4C_3(s) + 3Si(l)$ and the rate controlling mechanisms operating at each stage

TABLE 4.1 Initial results of the re-melting of the composites

COMPOSITE	RE-MELT TEMPERATURE/°C	TIME/MINS	COOLING CONDITIONS	PHASES IDENTIFIED BY XRD
CP.Al+SiC	-	-	-	∝SiC (4H,15R,6H, trace of 2H)
"	1000	1000	AC	∝SiC as above Al_4C_3 ,Si
"	$>$2000?	$<5\frac{1}{2}$	Q	Al_4C_3 ,Si
LM13+SiC	-	-	-	∝SiC,Si
"	848	1000	AC	∝SiC,Si
"	1000	1000	AC	∝SiC,Si,Al_4C_3

TABLE 4.2 Estimate of the transformation temperature at which L-SiC equilibrium (metastable) is replaced by L-SiC-Al_4C_3

Al-Si ALLOY	ALLOY COMPOSITION EXPRESSED AS A BINARY /AT%Si	TEMPERATURE/°C	
		REACTION PRODUCTS APPEAR	Al_4C_3 FORMATION GENERALLY
LM13	10.8 ∓ 0.5	~915	$>$950
Al-12Si	11.6 ∓ 0.5	~950	$>$970-990
Al-19Si	-	NOT OBSERVED BELOW 1100	

TABLE 4.3 Intermetallic phases in CP.Al+SiC composites MH85-S, and MH87-S following re-melting.

	ELEMENTS ANALYSED	RE-MELT						SPRAY-CAST NO.
		MH85-S					MH87-S	
		30MINS 800°C					1000MINS 672°C	
PLATE-LIKE PHASE		1°C/MIN					10°C/MIN	COOLING RATE
	Al	66.3	66.7	67.2	67.5	68.4	66.5	
	Si	18.1	17.4	17.7	17.6	17.0	18.7	
	Fe	15.3	15.5	15.0	14.7	14.5	14.7	
	Mn	0.3	0.3	0.1	0.2	0.1	0.1	
	Cu	0.0	0.1	0.0	0.0	0.0	0.0	

	ELEMENTS ANALYSED	RE-MELT				SPRAY-CAST NO.
		MH85-S	MH87-S			
		30MINS 800°C	TO 1320°C	100MINS 800°C		
SCRIPT-LIKE PHASE		1°C/MIN	10°C/MIN	20°C/MIN		COOLING RATE
	Al	73.3	76.0	75.3	73.6	
	Si	10.0	9.8	10.5	9.2	
	Fe	15.9	13.3	13.5	16.4	
	Mn	0.4	0.2	0.4	0.4	
	Cu	0.4	0.7	0.4	0.3	

(ALL COMPOSITIONS IN ATOMIC %)

TABLE 4.4 Mole fraction of Si in liquid Al when L-SiC-Al_4C_3 equilibrium is established

T/°C	T/K	ΔG_1 kJ/mol	$3\Delta G_2$ kJ/mol	ΔG kJ/mol	MOLE FRACTION Si
661	934	21533	67654	89187	0.081
672	945	22326	66665	88991	0.083
800	1073	31561	55125	86686	0.107
827	1100	33509	52687	86196	0.112
1000	1273	45989	37054	83043	0.143
1100	1373	53203	28024	81227	0.161

Table 4.5 Misorientations

SADP figure 4.17	Experimental angle /° +/- 0.2° measured between SiC and Al_4C_3 orders of reflections {10./} {00./} {$\bar{1}$0./}	Orientation Relationship {6H SiC} // {Al_4C_3}	Predicted Angle /°
c	0 0 0	10.0 // 10.0	0.000
(k	- - -	- - -	0.000)
c	- 1.7 -	10.0 // 40.1	1.653
d	2.5 2.2 2.3	10.0 // 30.1	2.204
c	2.4 2.3 2.0	10.0 // 30.1	2.204
e	3.5 3.3 2.8	10.0 // 20.1	3.304
c	3.5 3.5 -	10.0 // 20.1	3.304
b	6.6 6.4 6.0	10.0 // 10.0	6.586

Table 4.6 Initial volume fraction of SiC

Composite	Approximate composite sample mass/g	Number of determinations n	Method*	Vol%SiC +/- σ_{n-1}
MH87-S	1.2-1.5	4	NaOH/HCl D	10.5+/-0.3
	0.7	4	NaOH F	11.7+/-0.5
MH85-S	1.3-1.5	2	NaOH D	13.6+/-1.3
	1.5	1	Acid mix GF1	12.7
	1.5	1	NaOH/HCl F	12.5
200-12	0.9	1	Acid mix F	14.6
	3.8	1	Acid mix GF2	13.5
202-19	2.3	1	Acid mix F	11.6
	2.9	1	Acid mix GF2	16.1

*D=decanting; F=gravity filtration (paper); GF1=vacuum filtration (glass fibre filter); GF2=gravity filtration (glass fibre filter). Reagents are as described in section 3.5.4.

Table 4.7 Al - Si liquidus slope

Silicon interval at%Si	Average slope over interval at%Si per °C	Temperature interval °C
0 - 2	0.168	0.00 - 11.9
2 - 4	0.157	11.9 - 24.6
4 - 6	0.149	24.6 - 38.0
6 - 8	0.143	38.0 - 52.0
8 - 10	0.138	52.0 - 66.5
10 - 12	0.127	66.5 - 82.2
12 - 12.2	0.127	82.2 - 83.8

Table 4.8 Empirical activation energies

MH85-S composite data

Stage	Extent of reaction		Figure	Activation energy kJ/mol
1	any		4.39	258+/-30
	ΔTp=	7	4.45	251
		10	4.45	253
		14	4.45	242+/-24
		16	4.45 ,4.40	259
		18	4.45 , 4.40	263
		20	4.45 , 4.40	265
		22	4.45 , 4.40	273
		24	4.45 , 4.40	278+/-30
	Average			260+/- 12
2	ΔTp=	46	4.44	853 (631 672°C data)
		54	4.44	571 (566 excluded)
	ΔTp	~18-21	4.38	490 (590 includes 850°C)
	ΔTp	~40-43	4.38	755 (data from)
	ΔTp	~53-56	4.38	900 (870 sample #2)

MH87-S composite data

Stage	Extent of reaction		Figure	Activation energy kJ/mol
2	vol%Al_4C_3	5.75	4.32	425
		8.0	4.32	692

Chapter V

Al-Si-SiC Composites

5.1 Introduction

The composite material discussed in the previous chapter contained only impurity levels of silicon in the initial matrix alloy. It is well known that pre-alloying the matrix with sufficient silicon can inhibit reaction between SiC and liquid aluminium as a result of the complete stability of the Al-Si liquid alloy-SiC system. In this chapter three alloys are examined in which Al_4C_3 is not predicted to be produced until high alloy liquid superheats are obtained.

The results of a brief investigation into the origin of the Osprey ^{TM} Preform Process spray-cast microstructure exhibited by the Al-Si matrix composites are presented. The formation of Al_4C_3 at the necessarily high superheats is discussed in terms of the changes in microstructure and the distribution of this product compared to that formed in the CP.Al-SiC composite, and a mechanism is suggested to account for the observed differences. General results of the re-melting experiments are presented, with comments on the observed phenomena, emphasising the influence of the SiC particles on the solidification microstructure.

5.2 Al-19Si-SiC composite

5.2.1 *Al-19Si-SiC as-sprayed microstructure*

The composite preform 202-19 (CP.Al-19Si-SiC) showed bands of porosity separated by less porous regions. A significant, regular variation in the volume fraction of the SiC was observed to occur, peaking every 3-5mm radially through the preform billet: such variation would require the general quantitative approach to the study of the reaction kinetics performed on the CP.Al-SiC composites to be heavily modified in order to obtain reliable results. The average volume fraction of the SiC was found to be ~13.9+/- 3 vol.%SiC. The source of the silicon carbide was as for the previously discussed composites.

Figure 5.1a shows a region relatively SiC lean, and what may be described as a coarse microstructure with respect to the matrix silicon phase. Deep etching of the composite with NaOH(aq) revealed that some of the silicon polyhedral particles exhibited simple geometric shapes. Figure 5.1b shows what appears to be a small primary Si crystal on the surface of a SiC particle. Some smaller simple Si crystals, correllated with eutectic Si , were also seen in the matrix of ~1 micron diameter, though in general these crystals formed larger polycrystalline aggregates. The distinction between primary, and eutectic silicon was made possible following TEM examination, as indicated in figure 5.2.

The commercial purity matrix alloy allowed various impurity phases to form upon solidification. These were dimensionally refined. The often observed association of the intermetallic phases with the SiC, eg. figure 5.1c, may be simply the result of particle pushing by primary Al, or due

to the preferential nucleation of the intermetallic phases on the SiC: these points are examined further later in this chapter.

In association with porous regions, the occasional rapidly solidified matrix alloy particle was found as shown in figure 5.1d. The particle, <1.5microns across, showed a microcrystalline structure with a crystal size of typically <5nm, and a correspondingly diffuse diffraction pattern as in figure 5.1e: rings consistent with Al were present though the broader halos remain unindexed, and were probably not due to Si. The particles were most likely to be Si, coarsened into shells as a result of multiple recalescence.

In general the microstructure showed "primary" Si polycrystals, typically both more equiaxed and coarser (~5-15microns) than the "eutectic" Si polycrystals which tended to exhibit a wider variety of sectional shapes, as shown in figure 5.1f. The primary Si were found to be associated with SiC particles; the eutectic scale Si being more uniformly distributed. The plate-like intermetallics, probably Al_5FeSi, were typically <10microns long.

5.2.2 *Synthesis of the as-sprayed microstructure*

The Osprey^{TM} preform process as used to produce the composite studied created a micostructure consisting of refined primary Si, and non-silicon intermetallics with a very coarse Al-Si eutectic structure. A crude experiment to synthesise this microstructure was carried out and the results are presented in figure 5.3. Splatting the re-melted composite as described in the experimental procedures could readily provide microstructure on a finer scale than that presented in the "spray-cast" microstructure as shown in figures 5.3a and d. Judging from the Al-Si calibration alloys also splat in a similar manner, cooling rates upto ~$5x10^4$ $^oC/s$ (as represented in 5.3a as judged with respect to the hypoeutectic alloys splatted), and more typically ~10^2 to 10^3 $^oC/s$ (as in 5.3d as also judged by comparison with the hypoeutectic alloys splatted) could be produced. Primary Si is barely seen to be nucleated in 5.3a, though in 5.3d the longer local solidification time allowed the begining of the formation of the primary Si crystal branching to be evident.

The microstructural results in figures 5.3b, c, e, and f show that microstructures remarkably like the spray-cast ones are readily produced when the splat material is annealed at temperatures at, or very close to, the Al-Si eutectic temperature in under one minute as in figures 5.3c and f. Heat treatment for five minutes at 550^{o}C had only produced a degree of spheroidisation similar to that in 5.3b; five minutes at 578^{o}C produced incipient melting in the samples.

It is suggested that in order that the microstructure be produced in the preform 202-19 the cool between the solidus and 550^{o}C must be very sluggish, and that the microstructural evolution is practically completed at temperatures very close to, if not at, the solidus. The initial cooling rate required to refine the microstructure would be readily provided by the gas jet

carrying the melt and particles~10^4-10^6 $^oC/s$ [143]. In the particular spray-cast studied it is further suggested that both the macroscopic variations in the porosity and the scale of the matrix microstructure was due to a variable spray-density [143]. Simple experiments of this type performed on suitable alloys may provide useful data to supplement the complex models being developed to describe the spray-casting process.

5.2.3 *Primary silicon in re-melted Al-Si-SiC composites*

Following the re-melting and water-quenching of Al-19Si-SiC, primary Si is seen to nucleate preferentially on SiC and in a prolific manner, figure 5.4a. As the cooling rate decreases, figure 5.4b, fewer nucleation events occur and the primary Si crystals have developed faceted branches bound by {111} planes typical of unmodified primary Si crystals which are of a sufficient size for this branching to occur [67]. When the samples are cooled naturally, massive primary Si polycrystals result as in figure 5.4c. Figure 5.4d suggests that isolated SiC crystals can be associated with Si crystal nucleation events: however, primary Si crystals are often observed to nucleate on any surfaces where, in accordance with the Gibbs Adsorption Isotherm, segregation of the Si will occur.

Due to the tendency for Si to form twins, the few TEM observations made are unlikely to provide large numbers of sections showing direct SiC-Si epitaxy if it exists. Nucleation of the Si at low undercoolings does not appear to be significantly affected by the prescence of the SiC in general.

Figure 5.4c shows that SiC particles are incorporated into the growing Si crystal, as also evidenced by figure 5.4b. It appears that the SiC particles are not merely trapped between the Si branches, but are engulfed by the Si which preferentially grows around the SiC particles which occurs at both high (figure 5.4b) and low (figure 5.4c) Si growth rates. Si-SiC interface formation is favoured above the formation of Si-liquid Al alloy and Al-SiC interfaces. It is suggested that captured SiC particles are often not wholly surrounded by Si due to Si growth constraints, and as the eutectic solidifies Al-SiC interfaces are produced. When Al-Si eutectic is solidified at 1^oC/min as in section 5.10 the eutectic Si contains the SiC with very few Al-SiC interfaces present ie. eutectic Al rejects the SiC particles.

The thermodynamic approach to the problem of particle capture or rejection by a solidifying phase will lead to the correct prediction of whether the phenomenon can occur [171]. When SiC is wet by liquid Al in a wetting experiment, the wetting is driven by the interface reaction : if the reaction is necessary for wetting to occur spontaneously then for SiC already present in the melt, initial dissolution of the SiC into either an Al or Al-Si melt will prevent spontaneous wetting of the SiC by the solidifying Al since a chemical equilibrium state will have been established in the melt system. Solute will be rejected from the solidifying solid at the interface, so that for the

SiC to be captured a reaction would need to occur between the SiC and the solidifying Al at the interface for spontaneous wetting.

It is proposed that the extremely slow solidification of an Al-Si eutectic-SiC composite with a high temperature gradient to produce planar Al interfaces ie. region 'A' in Day and Hellawell [63] should be performed to test as to whether Al will capture SiC or not, when it is known that the dissolution reaction is complete. Equilibrium will be attained in the particle-melt system and then 'equilibrium' solidification performed ie. conditions where heat and mass transport rates are high compared with the rate of solidification.

Primary Si in LM13 is seen to nucleate in association with SiC particles, but more so with what appear to be either oxides eg. spinel MgO_4Al_2 or possibly AlP (the P level of most commercial Al-Si alloys being sufficiently high for primary formation of this compound which aids the dispersion of primary Si [70]) when the cooling rate is not high eg.$<1^oC/s$. These particles were observed at high superheats eg. towards 1000^oC under which conditions the LM13 becomes hypereutectic with respect to Si as a result of SiC dissolution. This suggests that inclusions other than SiC are present and represent more favourable sites for Si nucleation than the SiC- liquid interface.

5.3 Al-12Si-SiC composite

5.3.1 *As-sprayed Al-12Si-SiC*

The microstructure of the as-sprayed Al-12Si-SiC preform 200-12 was as shown in figure 5.4e and f. The features were as for the Al-19Si-SiC preform as discussed in section 5.2 except that primary Si polyhedra were absent. The uniformly distributed eutectic Si polyhedra can be observed without the interference of the primary Si phase. The composite contained ~14 +/- 0.8vol%SiC. Figure 5.4f shows a low volume fraction of SiC particles and figure 5.4e shows none: the region of 5.4e was on the outermost part of the preform and suggests that the highly fluid eutectic alloy could flow enough to separate from the particles during consolidation.

5.3.2 *Re-melted Al-12Si-SiC*

Figure 5.5a shows a typical re-melted and solidified Al-12Si-SiC microstructure. An occasional primary Si crystal, and narrow Al_5FeSi plates (analysed by EDS in the as-cast condition as $Al_4(FeSi)_2$) are seen along with the Al-Si flake eutectic and a low volume fraction of primary Al.

As the re-melting temperature is raised the solidified composite suffers from increasing gross particle segregation for a fixed holding time. The effect of 100minutes re-melting and solidification in-situ were compared. At 850^oC there was little apparent settlement, allowing for the initial SiC volume fraction variations. By 950^oC large regions especially about the sample periphery are devoid of particles ie. the sample has separated into high SiC volume fraction regions and large regions devoid of all but the occasional SiC particle. A sample melted for

100minutes at 1000°C under argon had separated into regions highly populated by SiC particles and regions SiC free, the distribution of which could not be accounted for by gravity induced settlement alone. In the 1000°C sample it was noted that the almost all the porosity was associated with the SiC: this may represent porosity retained from the spray-cast as much of the alloy shrinkage would have been accounted for by the formation of a large pipe in a SiC-free region.

5.3.3 *Al_4C_3 formation in Al-Si-SiC melts*

The results presented in figure 4.6 indicate that Al_4C_3 is not produced until superheats >950°C for the LM13 based composite studied (Al + 10.8wt%Si when expressed as a binary) and >970-990°C for the Al-12Si-SiC. For the Al-19Si-SiC composite thermodynamic calculation suggests that the Al-19Si-SiC composite will need to be heated to >1290°C for Al_4C_3 formation.

Some SiC dissolution will occur to attain SiC - L equilibrium. According to the liquidus published by Viala *et al* [73] the carbon should be deposited as SiC upon cooling, however the proposed peritectic does not operate at the cooling rates used in this study, as is evident from all the preceding results (Chapter 4), and any C in solution would almost certainly be deposited as Al_4C_3. Alloying with Si is reported to increase the activity of C in Al such that less C would need to dissolve into an Al-Si melt to form Al_4C_3 at the same temperature as a superheated liquid Al-SiC system.

Al_4C_3 formed in Al-12Si-SiC at adequately high temperatures is as shown in figures 5.5b and e. The large faceted crystals are rapidly produced eg. less than 10minutes at 992°C. Generally the Al_4C_3 crystals appear as in figure 5.5d, but some are observed to contain fine particles as in figure 5.5c. The Al_4C_3 particles are distributed uniformly amongst the SiC particles (figure 5.5e) though the number per unit volume would appear to be low compared to the number of SiC particles present. The Al_4C_3 morphology and distribution are evidently different when compared to the Al_4C_3 produced in the re-melted CP.Al-SiC composites.

TEM studies of the Al_4C_3 clarify several features. Figure 5.6a shows a large Al_4C_3 crystal exhibiting predominantly {10.0} facets: no orientation relationship with the 15R SiC denoted 'S2' appears to exist and the particle could have been 'captured' by the growing Al_4C_3 which would not be suprising with the SiC particle dissolving when the crystals met. The interface in figure 5.6b appears smooth though it is difficult to judge whether the edge of the SiC is actually visible in this case. The structures within the Al_4C_3 crystal at the interface could represent the effect of the change in Al_4C_3 growth which would occur as liquid is ejected from the SiC-Al_4C_3 interface: the faceted portions of the Al_4C_3 at the interface could be of a different and more favourable orientation with respect to the SiC which would have been initially contacted at a random orientation.

Figure 5.6c shows Al_4C_3 nucleated on 6H SiC with an orientation relationship of the type often observed in this study in the CP.Al -SiC system in which Al_4C_3 has formed. Other oriented SiC-Al_4C_3 crystals were also found during the HVEM study suggesting the same type of orientation relationship. The Al_4C_3 crystal infigure 5.6c shows what appear to be large numbers of dislocations, some of which cut through the {00.1} facet: there also appears to be a general contrast change across the centre of the crystal suggesting that the crystal section seen is composed of at least two misoriented portions separated by a low angle boundary.

Figure 5.7 shows what is evidently polycrystalline Al_4C_3 with two associated faulted SiC particles, both predominantly 4H SiC and neither showing a simple orientation relationship with the surrounding Al_4C_3, though SiC particles outside the plane of the foil might have done so. The number of Al_4C_3 to the right of 'S1' in figure 5.7b suggests that several nucleation events have occurred. The similarity between particles at 'P' in figure 5.7b and the cluster of fine particles within the polycrystalline Al_4C_3 structure in figure 5.5c suggests that the particles are associated with a mechanism which influences the nucleation or growth of the Al_4C_3 .

What appear to be large numbers of dislocations perpendicular to the Al_4C_3 facets are evident in figure 5.7c along with numerous stacking fault-like structures running radially within the crystals. The SiC particle 'S2' in figure 5.7d could represent another 'captured' SiC particle, though part of the SiC interface (where a fracture surface runs across faults) appears to be highly stepped where the Al_4C_3 meets the SiC and would be identified with a nucleation site in the re-melted CP.Al - SiC system.

5.3.4 *Suggested mechanism for the nucleation and growth of Al_4C_3 in Al-Si-SiC composites*

The basic processes by which the Al_4C_3 nucleates and grows in the Al-Si-SiC melts can be considered to be the same as in the re-melted CP.Al-SiC composites ie. refer to figure 4.52. However, in order to explain why there is a difference in the distribution and morphology of the Al_4C_3 product in the Al-Si matrix composites compared to the CP.Al matrix case a significant increase in the difference between the rates of Al_4C_3 crystallite nucleation and growth, in the early stages prior to impingement, has to be postulated (figure 5.13): such divergences are seen when saturated solutions are supercooled, which leads to a larger average crystal size as a result of the crystal growth rate increasing more rapidly with supersaturation than the nucleation rate [174].

If it is assumed that the C supersaturation in the melt will be controlled by the dissolution rate of the SiC, as shown for the liquid CP.Al - SiC system, then the growth rate of a nucleated Al_4C_3 crystal will follow the dissolution rate. The nucleation rate will depend on several factors which will also increase exponentially with temperature which are the same as the factors involved in the growth rate eg. the dissolution rate controlling the level of supersaturation, and the

diffusion rate which will determine both the rate at which atoms enter into a proto-nucleus and the rate at which atoms attach to a growing crystal surface. A possible factor which will reduce the nucleation rate could be an increase in the interface energy due to increasing mismatch between the parent and Al_4C_3 product phase: this type of factor could result in a greater critical nucleus size and hence reduce the rate of nucleation below that expected.

Geometric factors which remain constant are the spacing of the most favourable nucleation sites, which will be of the same number as in the reaction initiated at low temperatures by the definition of 'most favourable': these sites include the asperities etc. discussed in the preceding chapter. The effect of reduced nucleation and a high growth rate will be the early impingement of the platelets nucleated on SiC particles with several potent nucleation sites, and a complete absence of the narrower platelets observed in the reaction nucleated at lower temperatures.

The consequence of early impingement is the appearance of the large equiaxed Al_4C_3 crystals in general, the internal structure suggesting the polycrystalline origin of the particles: part of the growth of the Al_4C_3 polycrystals already exhibiting low index facets leading to their final shape could be accomodated by the dislocation mechanism proposed by Frank [172], the dislocations produced by the impingement of the discrete Al_4C_3 platelets [173] which often are only slightly misoriented from each other as shown in the preceding chapter. Several platelets with similar orientations could impinge and produce large crystals exhibiting simple hexagonal prism shapes, as opposed to the plate-like hexagonal habit of Al_4C_3 grown freely in the melt. It could be possible for dislocations to be transmitted from the substrate into an Al_4C_3 nucleated or growing over the site where dislocations emerge at the surface eg. from an area of 'crushing damage' assuming that the interface is maintained: the nucleation of the dislocation will only be spontaneous if, for example, there is an energetic advantage in maintaining epitaxy with the substrate at the expense of dislocation production. However, the defects are introduced, the Al_4C_3 crystal in figure 5.6c has apparently elongated in the 'c' direction under the influence of dislocations.

Nucleation would take place preferentially at the nucleation sites described in chapter IV eg. asperities. The distribution of such sites with both single, and multiple, sites of preferred dissolution would dictate the distribution of the large Al_4C_3 crystals observed in the re-melted Al-Si-SiC composites. If a single nucleation event were to occur on a SiC particle then a simple thickened hexagonal Al_4C_3 platelet can be produced, following rapid lateral coarsening as in figure 4.52. If several simply oriented Al_4C_3 platelets were to impinge a simple faceted prism results often surrounding a highly irregular SiC particle similar to the SiC particle in figure 4.11d which were observed on polished sections following reaction in the LM13 based composite: such SiC particles are excellent nucleation sites, the original shape of the substrate remaining largely unaltered throughout the reaction.

The nucleation of Al_4C_3 on several adjacent siteswhere there is no relative orientation relationship leads to what is evidently polycrystalline Al_4C_3, some of the features identifiable with thickened plates and interface porosity as evident in the heavily reacted CP.Al-SiC system.

Since the growth rates are so high and the ultimate extent of the reaction limited, the reaction can take place without the complete coverage of the SiC-melt interfaces which allows equilibrium to be attained unlike in the CP.Al-SiC system studied at a similar superheat ($^{-}1000^{o}C$).

5.3.5 *Anomalous structures*

The fine particles observed in figure 5.5c within the Al_4C_3 crystals were observed quite frequently: these could be the result of sectioning through highly irregular SiC particles. However, in these commercial materials containing various other inclusions eg. figure 5.7 and in figure 5.9, it would not be suprising if other nucleation sites are present in these materials or are produced at high superheats: some of the observed inclusions could simply be the effect of internal oxidation due to trapped gas especially around clusters of SiC with the subsequent coincidental association with Al_4C_3 .

5.4 LM13+ 18-20vol%SiC *composite*

5.4.1 *As-sprayed LM13+ 18-20vol%SiC*

The as-sprayed microstructure generally showed similar features to the Al-12Si-SiC as in figure 5.8a. The only real difference was due to the additional matrix phases resulting from the high-alloying element content of the matrix LM13 alloy as in figure 5.8b.These phases, below the resolution of the bulk EDS technique at 20kV, were qualitatively analysed and subjected to light metallography, and found to include: Si spheroids; large plates resembling $(FeNi)_2Al_9$; segments of a blue/black script identified with Mg_2Si, and Fe,Mn containing spheroids some of which appeared in the SEM to be partially peritectically transformed. The Al matrix contained Mg, Cu and Si, and irregularly shaped constituents rich in Ni,Cu and Si were also found using EDS.

A typical TEM micrograph is shown in figure 5.8c. Particles containing heavy elements are on the cell boundaries - the Al cells being roughly equiaxed. The eutectic Si spheroids show parallel twins as in the 200-12 preform Si, and other Si-Si interfaces within the Si crystal aggregates. The SiC-matrix interface shown in figure 5.8d shows no sign of reaction as in the other as-sprayed composites. Figure 5.8e shows an unidentified intermetallic phase (SADP in figure 5.8f) wetting a SiC particle (SADP in figure 5.8g) with which there appears to be an epitaxial relationship. The micrograph also shows some finer precipitation in the matrix due to decomposition of the matrix solid solution at some stage between preform spraying and TEM examination.

5.4.2 *Re-melted LM13 + 18-20vol%SiC*

The composite was re-melted to temperatures up to 1000^{o}C and for times up to ~1week in air or under argon. The samples were cooled on the bench (AC), WQ or cooled in a more controlled manner in the furnace or DTA apparatus. A search was conducted for the temperature at which Al_4C_3 precipitation started. As this temperature is approached C from SiC dissolution released into the melt would precipitate as carbides on cooling. Small volume fractions of precipitated particles would be expected, and any peculiar structures that were noted are discussed below.

When the composite was re-melted at 848^{o}C for 1000 minutes under argon and AC, very little internal oxidation could be found (figure 5.9a): the amount of oxide introduced from the SiC particle surfaces and the sprayed melt droplet surfaces would have been very low. The inclusions would probably be Al_2MgO_4 identified in LM13 by X-ray diffraction when LM13 was oxidised for ~1week at 733^{o}C and the inclusions extracted. At 915^{o}C the content of coarse inclusions was still low (figure 5.9b), and a few equiaxed Al_4C_3 particles were present. At 1000^{o}C there was relatively abundant Al_4C_3 as in figure 5.9e. The ring structure apparently of carbides, in figure 5.9c is comparable in dimensions to the aforementioned inclusion structures. The structure in figure 5.9f shows yet another variation of a ring structure.

It is possible that pre-solidified sprayed droplets could introduce poorly bonded interfaces into the composite to which oxygen migrates during the subsequent re-melting of the composite. Oxide , and oxycarbide precipitation could result at these interfaces, either coarsening at the re-melt temperature or precipitating on cooling, mainly prior to matrix solidification, which leaves the structures undisturbed.

There was sufficient Al_4C_3 in the LM13 re-melted at 1000^{o}C for X-ray diffraction identification when the Al_4C_3 particles were concentrated with the SiC and Si following matrix dissolution with nital. The Al_4C_3 particles were similar to those found in the Al-12Si-SiC composite and would have developed as discussed in section 5.3.4. No effect of the other alloying elements on the course of the reaction was apparent, other than that the lower Si level compared with the Al-12Si-SiC allows the reaction to start ~950^{o}C as previously mentioned.

The increasing Si level with SiC dissolution increased the occurrence of primary Si crystals, which appeared to nucleate on inclusions other than the SiC particles. Identification of the temperature at which the Al-Si-SiC reaction started was hindered by interference produced by particles which appeared as in 5.9d. The 'rogue' particles were of approximately the same size as the SiC particles, but were present at a very low volume fraction, representing ~1 in every 10 000 particles.In the vicinity of these particles from ~940^{o}C in the LM13 there appeared abundant faceted crystals identified with Al_4C_3 by light microscopy. Any apparent Al_4C_3 particle detected in the temperature range 850-950^{o}C was attributed to these inclusions. That

these particles were softer, darker, and were corroded by the melt at temperatures approaching those necessary for general SiC dissolution, suggests that they are either impure SiC with excess C or simply C particles. C dissolution is itself reduced by Si alloying of the Al melt [69].

Similar particles were found in the Al-SiC composite, though much less frequently since owing to the general appearance of reaction products there was nothing unusual in the bulk microstructure to draw the attention to them.

5.4.3 *Intermetallics in re-melted LM13 + 18-20vol%SiC and in LM13*

Intermetallics found both in the LM13 and the composite were characterised by EPMA as in table 5.1. The intermetallics found in the composite matrix were also characterised by polishing and etching as in table 5.2. The composite matrix showed several phases expected in LM13 [175] following re-melting and cooling at various rates eg. AC, 20°C/min and 1°C/min as in figure 5.10a. The composite matrix showed primary Al (with Cu, Mg and Si in solution), with flake Si (ie. unmodified), Mg_2Si eutectic and at least five other intermetallics in the castings.

The intermetallics included $Al_{15}(FeMn)_3Si_2$ (intermetallic 1 in table 5.1) in a primary polyhedral form, figure 5.10b, seen to wet the SiC particles, and at higher cooling rates in a eutectic script form. The primary particles tend to contain Fe:Mn in the atom ratio 1:1, but in the script eutectic Mn is reduced with both Fe and other transition metals taking its place eg. Ni (Cu is known to substitute for Si [155]). There was no primary $Al_{15}(FeMn)_3Si_2$ in the base LM13 supplied for comparison with the composite, indicating that there was less Mn and a lower total Mn + Fe content in the base LM13. This was verified by the appearance of $Al_4(FeSi)_2$ as in figure 5.11d in the base LM13 (intermetallic 6 in table 5.1) which takes up some Ni and Mn.

The composite matrix showed abundant $(FeNi)_2Al_9$ (intermetallic 2 in table 5.1) with a lesser amount of the intermetallic 3. Intermetallic 3 (also in table 5.1) was not identified with any of the intermetallics in the literature, and crystallographic data on the phase would be required for a fuller characterisation (a resembl nce is noted with the compound described as Al-Mn-Fe-Ni-Cu (II) as given in [176]) : it appears to be related to $Al_4(FeSi)_2$, figure 5.11d shows intermetallic 3 apparently as a peritectic product of $Al_4(FeSi)_2$ in a similar manner observed of $(FeNi)_2Al_9$. Intermetallic 3 is similar chemically to $(FeNi)_2Al_9$ but contains significantly more Si and marginally more Ni, Mn and Cu. More of intermetallic 3 was seen in the LM13 than in the composite: the eutectic Al-intermetallic 3 composition was analysed as ~81wt%Al, 9.8wt%Ni, 3.2wt%Fe, 3.0wt%Si, 2.1wt%Cu, 0.7wt%Mg and 0.4wt%Mn.

The composite also contained AlCuNi compounds as in figures 5.10c and d. Both $Al_3(CuNi)_2$ (intermetallic 4 in table 5.1) and the ternary Al_6Cu_3Ni (intermetallic 5 in table 5.1) which is

reported to exhibit a range of compositions centred on this formula [177]: Al_7Cu_4Ni is given as an alternative [178].

The base LM13 alloy showed $CuAl_2$ (not identified in the composite) and possibly the ternary AlCuNi compound in the form of a fine eutectic script , the overall eutectic composition was ~84.6at%Al, 10.0at%Cu, 4.3at%Ni and 1.1at%Si. The LM13 also showed a Mg-Si-Al-Cu-Ni phase (intermetallic 8 in table 5.1) and an Al-Si-Mg-Ni-Fe-Cu phase (intermetallic 9 in table 5.1) and a generally greater abundance of the Mg_2Si phase compared with the composite matrix.

It was suspected that the as-supplied base LM13 alloy had a lower Mn:Fe ratio, less Ni, and more Cu and Mg than the composite matrix LM13. The apparent differences between the phases present in the re-melted composite, and the supplied LM13 were probably solely due to allowable variations in the alloy composition according to BS.1490.

The morphologies of the intermetallics appeared to be generally unaltered by the numerous interdendritic SiC particles, except that the SiC resided in all the intermetallic phases at a higher volume fraction than in the Al. When the intermetallic eutectics were coarse enough to accommodate the SiC particles, the Al in the eutectic rejected the SiC into the intermetallic phases to leave only a small fraction of the total SiC surfaces in contact with the Al. The intermetallic phases generally showed a tendency to facet on one or more set of interfaces with the Al: it appears that Al-SiC interfaces could readily be eliminated from the composite with a sufficient volume fraction of non-Al phases, if the Al alloy is solidified at a low rate.

From the observations on the solidified Al-X eutectic-SiC systems, where examples of X are Si, $Al_{15}(FeMn)_3Si_2$, $(FeNi)_2Al_9$ or intermetallic 3, several important results can be inferred. The Al and eutectic X phase will grow at the same interface velocity, and the X phase captures SiC and the Al does not. A range of thermal properties will be exhibited by the X phases quoted. The liquid bulk alloys will be similar except in the immediate vicinity of the solidifying interface at finite interface velocities: forces in the liquid, preventing contact between the SiC particles and the two coupled solidifying phases in the same system, will not vary much at all between adjacent eutectic interfaces, and the effect of the particle on diffusion fields (heat or mass) will be eliminated as a variable. That one eutectic phase is faceted (singular) at the liquid interface, and the shape of the Al-liquid interface depends on the local undercooling and on the need to maintain mechanical equilibrium at the phase junctions, will be largely unimportant when the SiC particles themselves have highly irregular surfaces. A simpler comparison of the effects of variations in physical properties of solidifying phases can be made in eutectic systems, in which the maintenance of a near-coplanar eutectic-liquid interface will imply that the various transport phenomena can be eliminated from the comparison of the two eutectic phases. The remaining major variables are thermodynamic ie. interface energies with peculiarities such as

the formation of low energy interfaces via epitaxial relationships in some systems, and interface reactions in which products other than an interatomic interface bond is formed.

In a system Al-Si-Z with SiC particles in which X is a eutectic phase formed during solidification with Al the various wetting reactions are as follows where the interface energy is γ(interface), and the work of adhesion is given as Wa(n) for each reaction considered 1 to n:

$$\gamma(\text{SiC-L}) + \gamma(\text{Al-L}) - \gamma(\text{SiC-Al}) = \text{Wa(1)};$$
$$\gamma(\text{SiC-L}) + \gamma(\text{X-L})_{hkl} - \gamma(\text{SiC-X}) = \text{Wa(2)}.$$

If phase X presents a faceted interface to the melt and it is inferred that:

$$\gamma(\text{X-L})_{hkl} > \gamma(\text{Al-L}) \qquad \text{----------(5.1)}$$

on the assumption that the enthalpy of vapourisation of the Al is likely to be lower than that of the intermetallic or Si phases at the eutectic temperature, and that the solid-liquid interface energies of these phases will increase with the enthalpy of vapourisation. It is shown empirically that the liquid-vapour surface energy of pure metals increases with the enthalpy of vapourisation, and it is suggested that a similar increase in the solid-liquid metal surface energies will be implied [113].

If it is also assumed that:

$$\gamma(\text{SiC-X}) <= \gamma(\text{SiC-Al}) \qquad \text{----------(5.2)}$$

since nothing is known about these relationships then:

$$\text{Wa(2)} > \text{Wa(1)}$$

which means that the eutectic X phase is more likely to entrap SiC, or for SiC to exist at the X-Al interface if wetting is incomplete due to excess SiC and geometric constraints, to reduce overall the SiC-Al interface area and the total energy of the system.

If the reaction SiC ---> Si + C is necessary for SiC to be wet by the Al-Si-Z melt, which contributes an energy change of Δh per unit area, then :

$$\gamma(\text{SiC-L}) + \gamma(\text{Al-L}) - |\Delta h| - \gamma(\text{SiC-Al}) = \text{Wa(3)};$$
$$\gamma(\text{SiC-L}) + \gamma(\text{X-L})_{hkl} - \gamma(\text{SiC-X}) = \text{Wa(4)}$$

which combined with assumptions (5.1) and (5.2) above further increases the wetting advantage of the eutectic phase X over the solidifying Al phase irrespective of contact angles:

$$\text{Wa(4)} > \text{Wa(3)}.$$

Unknown reactions driving wetting of the SiC by the X phase could also occur to increase the adhesion, though the most significant finding is simply the formation of some epitaxial X-SiC interfaces for which preliminary results are presented in section 5.5 below. It is suggested that the thermodynamic effects will far outweigh the kinetic factors typically invoked in order to attempt to predict particle pushing in the metal-ceramic systems currently of interest. The kinetic particle pushing models will not be applicable to most composite systems that are being developed where there is a significant liquid phase interface reaction contributing to wetting as in the Al-SiC system. Progress will only be made by the continued work to determine solid-liquid interface energies, both theoretically and empirically.

One minor practical result of the incorporation of the SiC into the intermetallic eutectic phases formed at low cooling rates is that the outlines of the phases are broken-up so as to lose the 'morphological aid' to identification.

5.5 Orientation relationships

The orientation relationships presented in figure 5.12 suggest that the Al melt -SiC interface is a suitable site for phases to nucleate with epitaxial relationships with the SiC substrate. The apparent Si-SiC relationship shown in figure 5.12a could have occurred purely by chance: the SiC did not appear to play an active role in the nucleation of Al-Si eutectic colonies in general : in the 'wheatsheaf' type Al-Si growth Si will tend to re-nucleate on Si to start a new colony (the Al itself undergoes numerous re-nucleations in each colony) [67]); this type of eutectic was often observed in the AC samples of Al-12Si-SiC.

Figure 5.12b shows the intermetallic $Al_{15}(FeMn)_3Si_2$ with a very precise and simple relationship with the SiC. It is interesting to compare this result with the primary $Al_{15}(FeMn)_3Si_2$ phase as shown in 5.10b for which SiC could well have acted as a nucleant. That this phase occurs in many alloys (cubic alpha (FeSi)) suggests that this observation may be important as far as microstructure control is concerned for cast Al alloy composites.

Figures 5.12b, d, and e show that an unidentified intermetallic with some interplanar spacings closely matching those of the SiC could also have nucleated preferentially on the SiC.

It is evident that some phases nucleate and grow on SiC substrates in the melt, and that particle pushing by both primary and eutectic Al are not the sole mechanisms causing SiC to be engulfed by intermetallic compounds in the eutectics: the SiC is preferentially wetted by many of the intermetallic compounds in the eutectics.

5.6 Summary : Chapter V

The preform microstructures were found to have originated, from solid state coarsening of the Si in the matrix, at temperatures at or near to the matrix solidus.

The large number of SiC-melt interfaces in a composite will strongly influence the distribution of primary Si crystals in a spray cast, and in the conventional casting of composites employing high cooling rates.

At low cooling rates the lower numbers of non-SiC inclusions appear to behave as more potent nucleation sites for primary Si.

Al_4C_3 growth in Al-Si-SiC composites leads to a different Al_4C_3 morphology due to the greater increase in growth rate of the product crystals with temperature compared with the increase in the nucleation rate over the same temperature range. A consequence of the greater growth rate is the involvement of the dislocation growth mechanism in determining the ultimate shape of the Al_4C_3 product crystals.

It is suggested that from the metallography of cast composites that both the primary and eutectic Al reject SiC particles: any of the phases in the Al alloy systems studied tend to wet the SiC in order to reduce the total Al-SiC interface area which appears to be directly linked by the tendency of all these phases to facet. It is suggested that thermodynamic effects will far outweigh the kinetic factors invoked to account for particle pushing phenomena, and that solidifying Al will not wet SiC suspended in the melt.

The common intermetallic phase $Al_{15}(FeMn)_3Si_2$ found in Al alloys can exhibit the following orientation relationship with SiC :
$<41\bar{2}>$ int. //<11.0> alpha SiC;
<021> int. //<00.1> alpha SiC;
$<\bar{3}2\bar{5}>$ int. //<10.0> alpha SiC.

5.7 Further work

1. The unidirectional solidification of an Al-Si eutectic melt containing a suspension of SiC particles at various solidification rates, including the Al-Si solidification conditions classified as region 'A' according to Day and Hellawell [63], could be undertaken to provide fundamental data on the interactions of SiC particles with a various Al interface geometries.

2. The mechanical properties of hybrid directionally cast eutectic Al-Si-X alloy-SiC particle systems could be examined and compared with the Al-Si eutectic -SiC system following similar casting procedures, and a quantitative evaluation of the interfacial characteristics of the systems could be correlated with the basic mechanical properties. The intermetallic phase modulus can be enhanced whilst retaining the benefits of the ductile matrix by eliminating particles from the Al.

3. The bonding between phases that wet SiC from the melt is potentially better than Al. Ductile-ductile eutectics plus SiC particulate systems could be investigated with the aim of entrapping particles preferentially into one phase in order that the dispersion can be controlled by controlling the eutectic spacing.

4. The synthesis and crystallographic characterisation of intermetallic 3, could be carried out in order to determine whether the phase is an unknown compound, or a known compound taking-up various alloying elements into solution.

6. Physical and chemical characterisation of the 'rogue' particles, found in the composites, could be carried out in order to determine their origin.

7. A kinetic study of the formation of Al_4C_3 in the Al-Si-SiC system would potentially provide data to determine whether alloying with Si effects the initial reaction rate as well as the thermodynamics.

8. Pure Al-Si-SiC alloys, initially containing a low free-Si content (eg. 0-5wt%Si), could be melted at temperatures below the melting point of pure Al to procure information on the constitution of the Al-Si-C system in the temperature range from 577^{o}C to 660^{o}C.

Figure 5.1

As-sprayed Al-19Si-SiC

a. Light micrograph : polished and etched 15s in 0.5HF(aq). The phases present include: SiC as dark-grey particles; Si as mid-grey particles, and the Al matrix appears white.

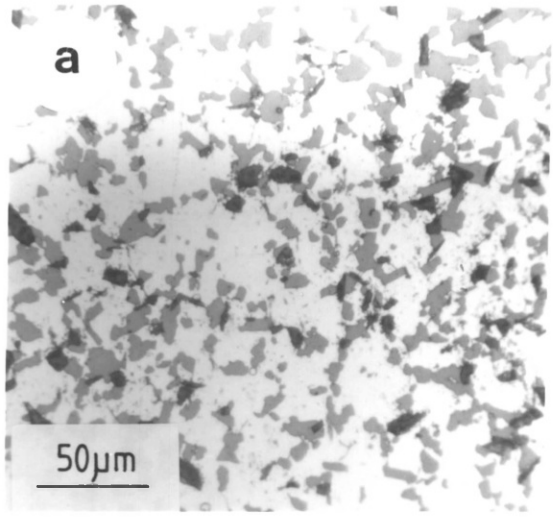
b. SEM secondary electron image (SEI) at 25kV. A simple Si polyhedron is shown on the surface of a SiC particle : the sample was deep etched in 10wt%NaOH(aq).

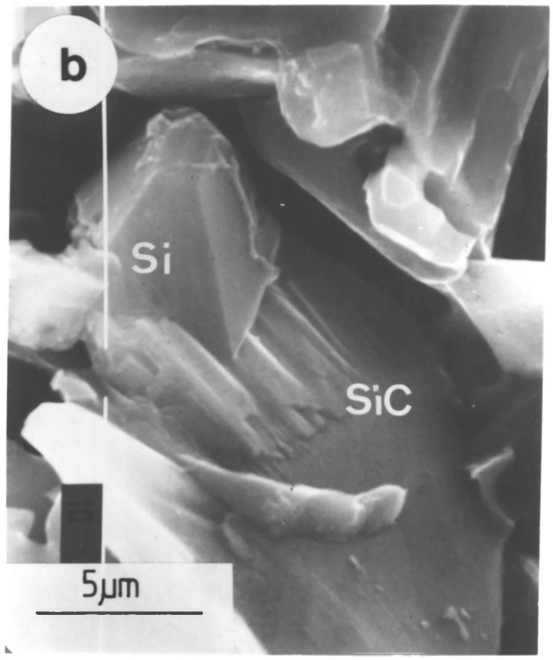
c. TEM micrograph taken in the bright field mode (BF). Impurity intermetallic phases (black) at the SiC-matrix interface.

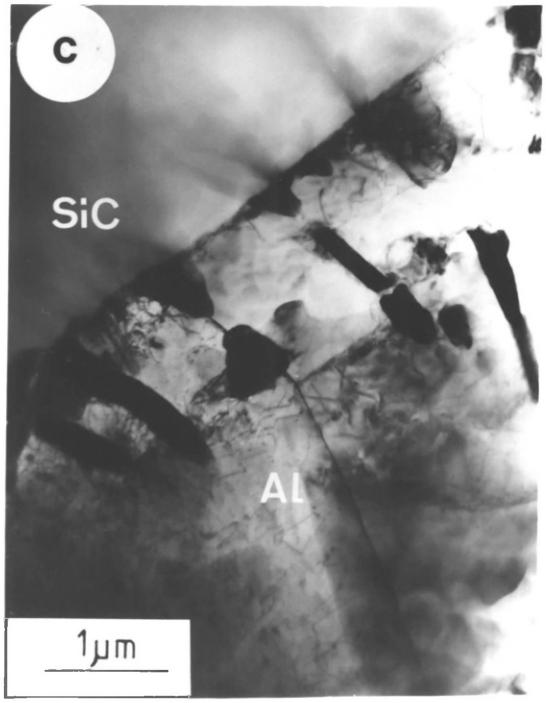
d. TEM BF micrograph showing what is presumably a rapidly solidified Al-19Si powder particle incorporated into the composite.

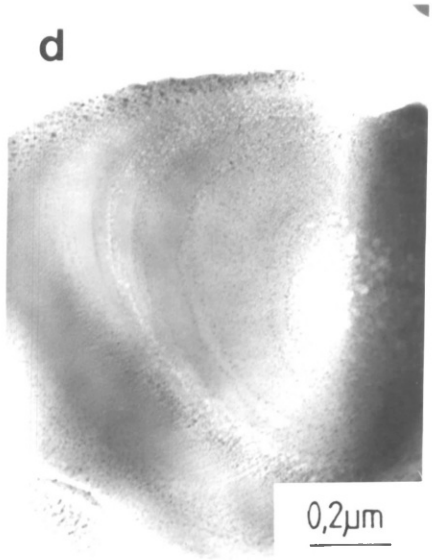
e. Selected area diffraction pattern (SADP), with a camera length $\lambda l = 2.595$nm.mm, taken from the particle shown in **d.** above. Four rings indexed as Al, though none correspond directly with Si.

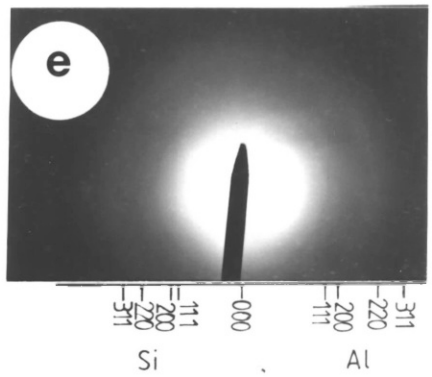
f. SEM SEI at 25kV. The features present in this micrograph include: pale-grey, angular SiC particles; pale-grey acicular impurity phase(s); mid-grey Si; dark-grey Al,and a number of pale-grey sub-micron particles corresponding to the polishing medium.


a
50µm


b
Si
SiC
5µm


c
SiC
Al
1µm


d
0,2µm


e
000
111
200
220
311
111
200
220
311
Si
Al

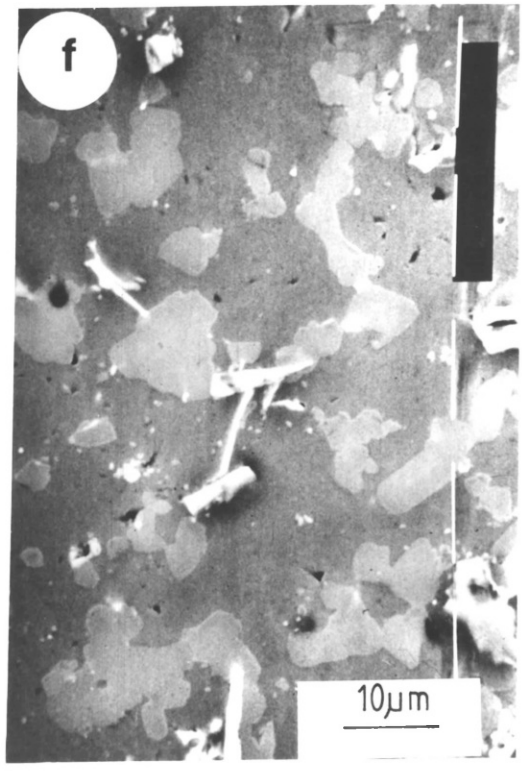
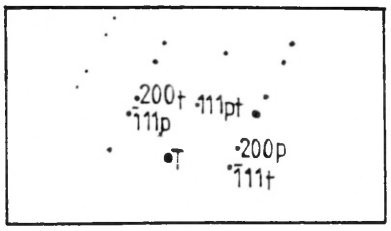

f
10µm

Figure 5.2

As-sprayed Al-19Si-SiC

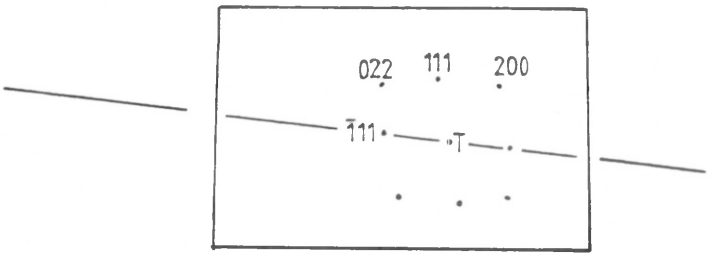
a. TEM BF image showing a twinned 'eutectic' Si crystal.

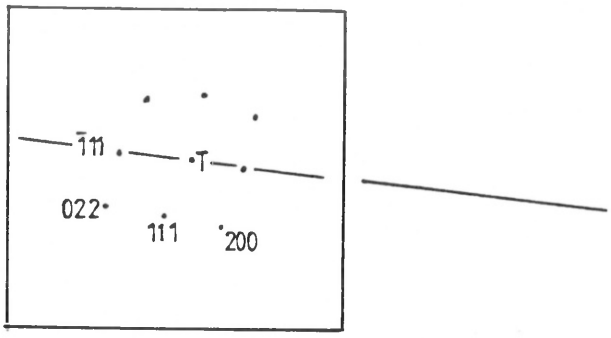
b. TEM BF of 'eutectic' Si containing parallel twins, similar to **a.** above. The inset SADP (λl=2.476nm.mm) taken from across the twin boundary is oriented with the BF image. Both parent (p) and twin (t) <110> zones are identified in the SADP key and indicate that the twin boundary is {111} type.



c. TEM BF image showing a 'primary' Si spheroid composed of pyramidal Si portions. The crystal surfaces tend to be approximately {111} type facets as deduced from the SADPs presented in **d.** below

d. TEM BF image showing a detail from **c.** above. SADPs from areas marked 1 and 2 are indexed as Si <110> zones as in the key and the orientation of the SADPs (λl= 2.58nm.mm) with the BF strongly suggests that the boundary between regions 1 and 2 is a {111} Si twin plane.





Note: the morphology of the 'primary' Si crystals shown here corresponds to that described for un-modified primary Si crystals at a stage of growth prior to the formation of instability induced branches [67].

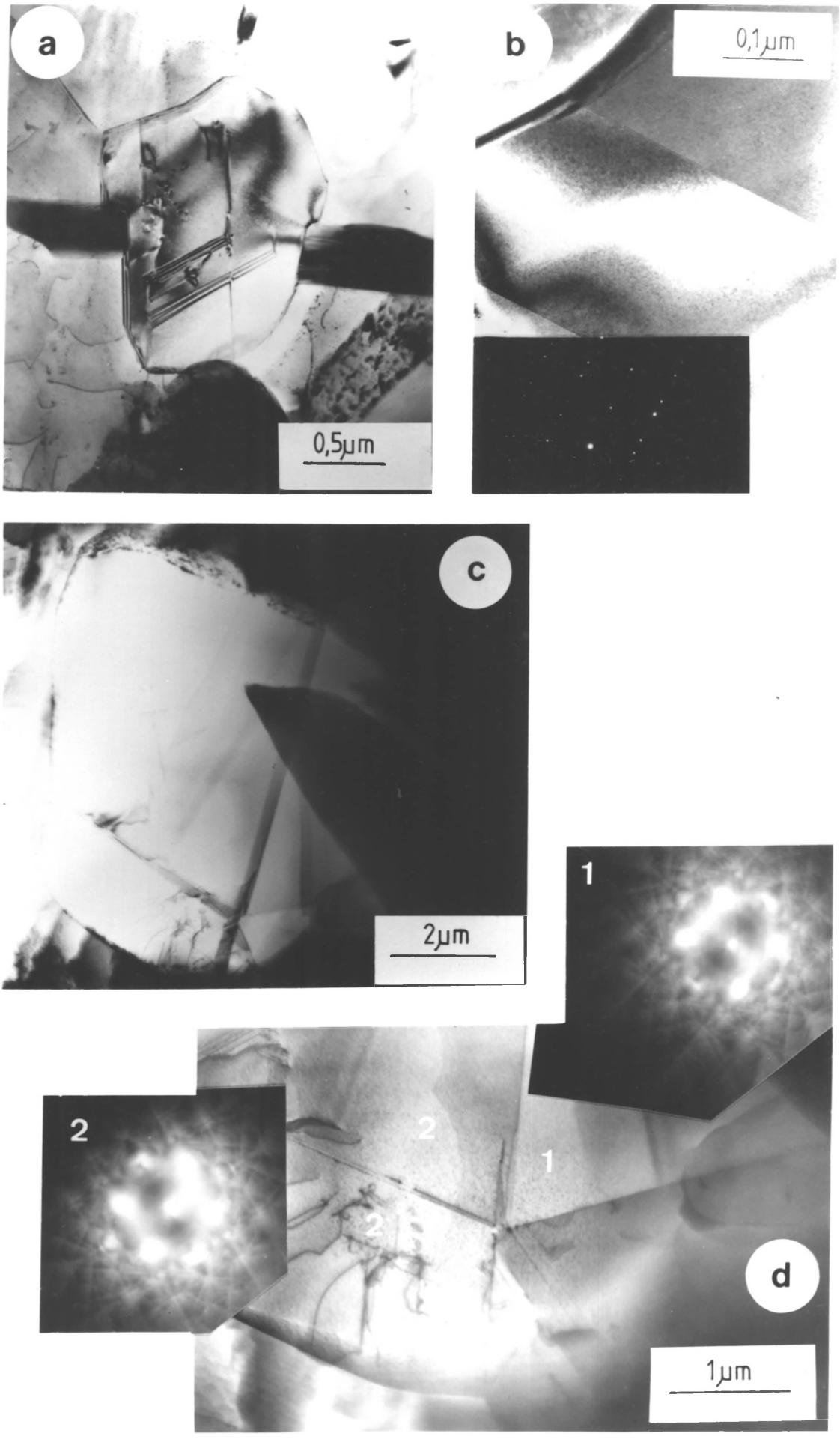

a
0,5µm
b
0,1µm
c
2µm
1
2
2
1
2
d
1µm

Figure 5.3

Synthesis of the as-sprayed Al-19Si-SiC microstructure

a. Light micrograph of a polished and etched (0.5%HF(aq)) sample of Al-19Si-SiC that has been splat-quenched following re-melting at 750^{o}C. Smooth, grey SiC particles can be seen in the very fine, Al-Si eutectic which appears mottled-grey. A primary Si particle 'P' is arrowed.

b. Light micrograph of an area of the sample prepared as above which was then annealed for 0 - 10s at 578^{o}C. The dark-grey particles are SiC, and the mid-grey particles are Si: the polished sample was unetched. The larger Si particles seen, corresponding to primary Si crystals, were probably already coarser and more numerous prior to annealing compared with the structure shown in **a**. It is suspected that the splatted structure was not quite as fine as in the area in **a**. above.

c. Light micrograph of an area of the sample prepared as in **a**. above and then annealed for a total of 50 - 60s at 578^{o}C. The phases seen are as identified in **b**. above.

d. Light micrograph of a different area of the sample shown in **a**. in which the splatted structure is much coarser. The features seen are: dark-grey SiC particles; large, mid-grey, faceted, primary Si crystals, and the matrix consisting of a readily resolved Al-Si eutectic.

e. Light micrograph of an area of the splatted material which has been annealed 0 - 10s at 578^{o}C. The phases are as in **d**. above. Note that the scale has changed.

f. Light micrograph of an area of the splatted material which has been annealed 50 - 60s at 578^{o}C. Phases are as identified as in **d**. above. The scale is the same as in **e**.

Note: it is suggested that regions of the matrix with a fine scale splatted-composite microstructure respond to the short anneals as in the sequence **a-c**, and that coarser parts of the splatted-composite microstructure correspondingly follow the sequence **d-f.** The scale of the as-sprayed composite structure generally varied between that shown in **c** and in **f**. The area of figure **5.1a** is more typical of the coarser structure in the preform, the finer composite matrix microstructure was typically associated with porous parts of the preform.

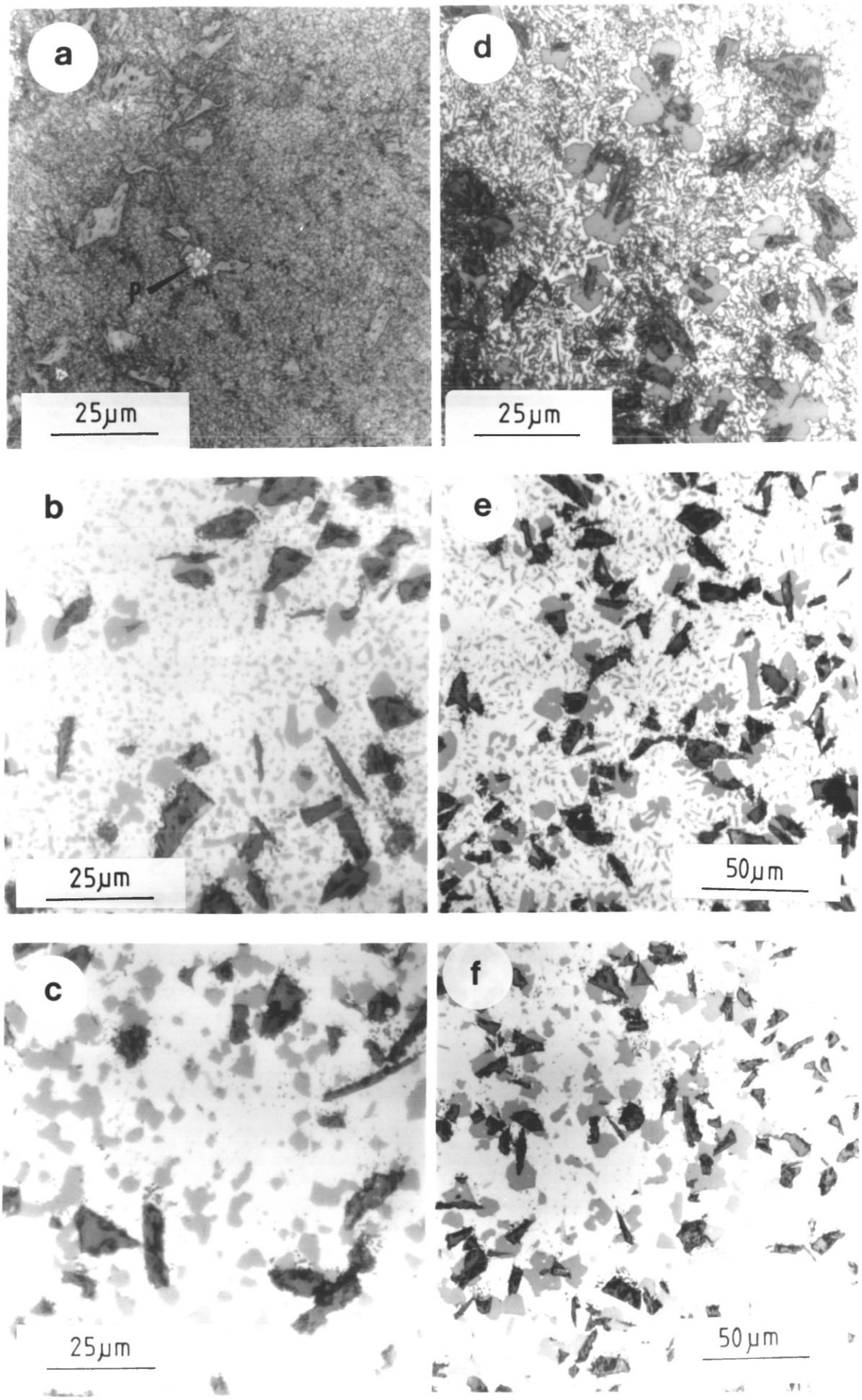

a
P
25μm
d
25μm
b
25μm
e
50μm
c
25μm
f
50μm

Figure 5.4

Primary Si - SiC interactions and as-sprayed Al-12Si-SiC

a. Light micrograph of an unetched, polished section from an expanded outer-shell of composite material created during the water quenching of a re-melted sample of Al-19Si-SiC (100minutes at 857^{o}C). The numerous primary Si particles, eg. 'S' as arrowed, reside at the SiC-matrix interface. The Al-Si eutectic in the matrix is unresolved.

b. Sample as in **a**. above: region from within the bulk of the sample. SiC particles are dark-grey, and the faceted, primary Si crystals are mid-grey. The primary Si crystals have developed blocky branches.

c. Light micrograph of Al-19Si-SiC re-melted for 100minutes at 857^{o}C and air-cooled (AC). The etched features shown include SiC particles (black), primary Si (mid-grey, blocky faceted crystals), and eutectic Si (mid-grey with a 'flake' morphology). Note that SiC particles can be seen surrounded either partly, or completely by the primary Si.

d. Light micrograph of an unetched sample of Al-12Si-SiC re-melted at 950^{o}C for 100minutes and AC. Si particles (mid-grey, faceted) nucleated on isolated SiC particles (dark-grey) in the melt.

e. SEM SEI of a polished, and lightly etched SiC-free region of the Al-12Si-SiC (200-12) preform. The delineated particles are Si, and the bright plates are impurity phase(s).

f. SEM SEI of another area of the sample shown in **e**. above in which there is a locally low volume fraction of SiC particles (bright); the other features are as identified in **e**.

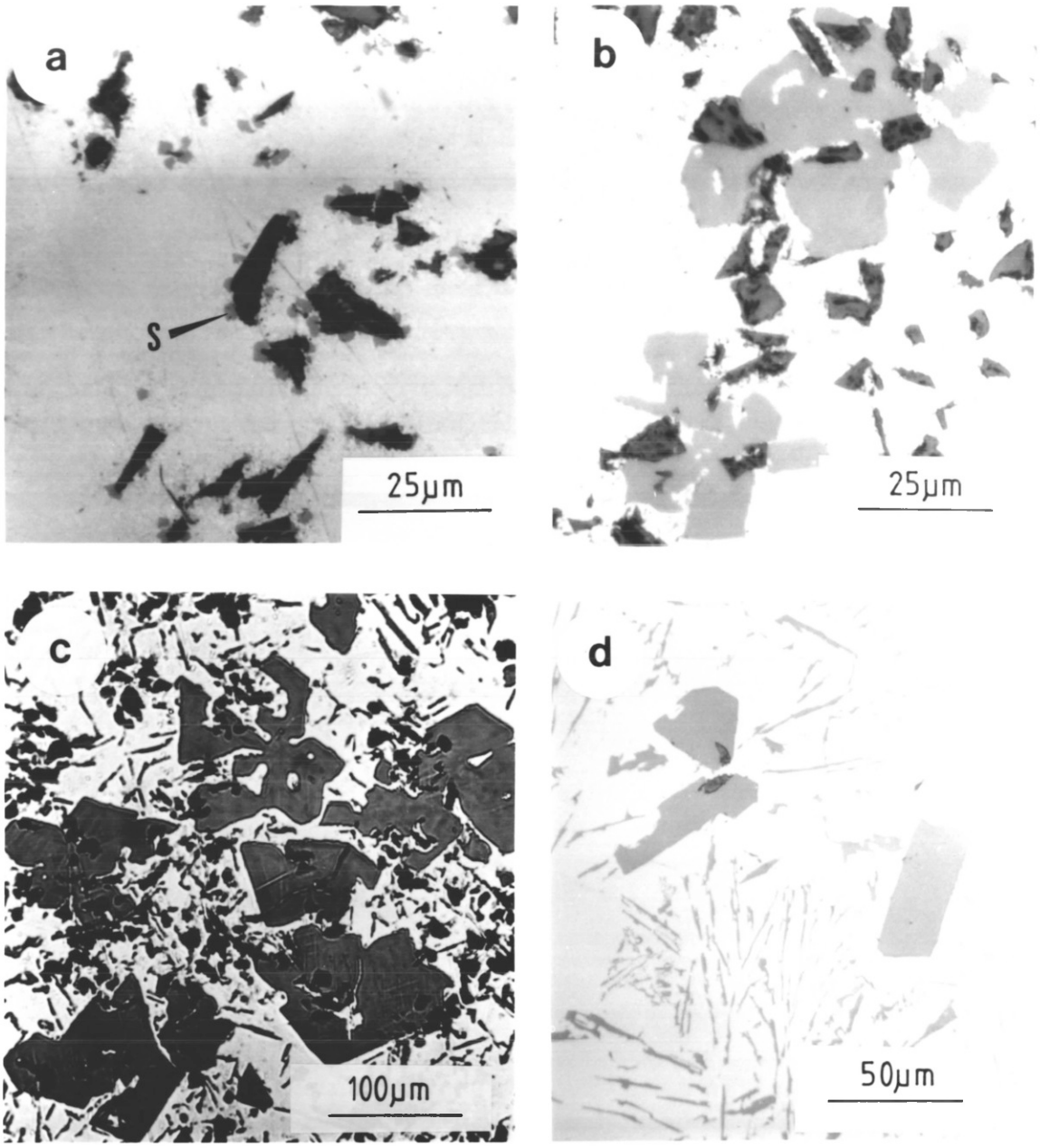

a
S
25µm
b
25µm
c
100µm
d
50µm
e
10µm
f
50µm

Figure 5.5

Re-melted Al-12Si-SiC

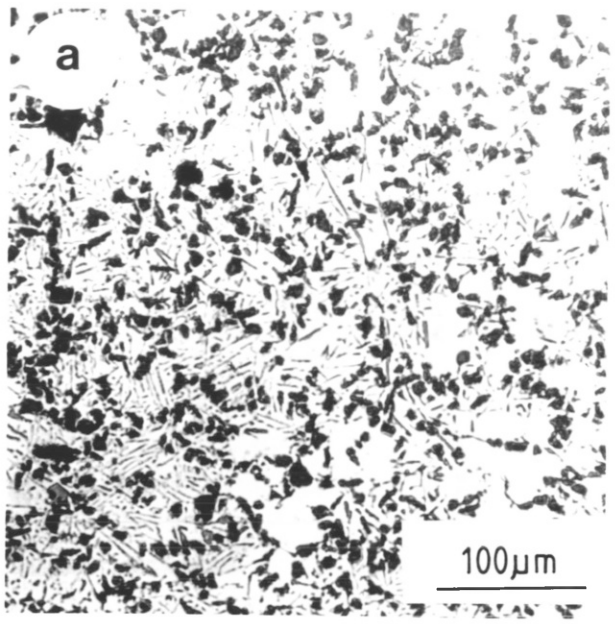
a. Light micrograph of an unetched sample of Al-12Si-SiC following re-melting for 100minutes at 855^{o}C and AC. Resultant SiC distribution: the SiC particles are dark, the eutectic Si is mid-grey and the Al pale-grey. Al dendrites are also present.

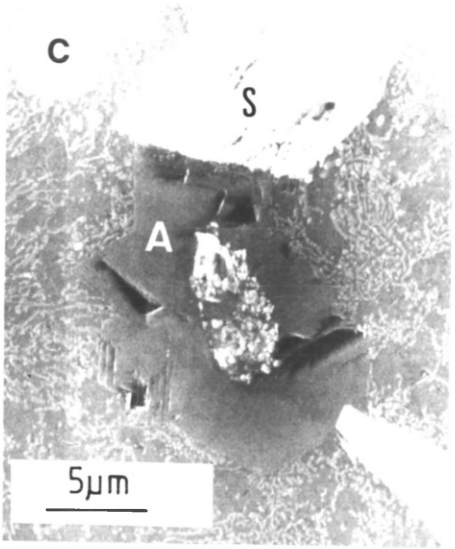
b. SEM SEI micrograph of an Al-12Si-SiC sample re-melted for <10minutes at ~1005^{o}C, and splat quenched: the polished section was lightly etched in 0.5HF(aq). The phases are: bright SiC particles, surrounded by the dark-grey, faceted Al_4C_3 crystals in an Al matrix of a slightly paler grey than the Al_4C_3 , containing bright eutectic Si particles.

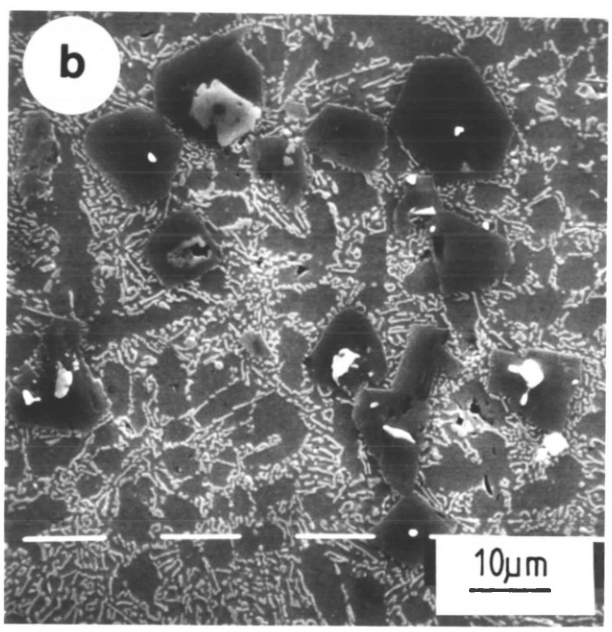
c. As **b**. above. The Al_4C_3 is marked 'A' and the SiC 'S'. Note the granular, bright particles in the centre of phase 'A'.

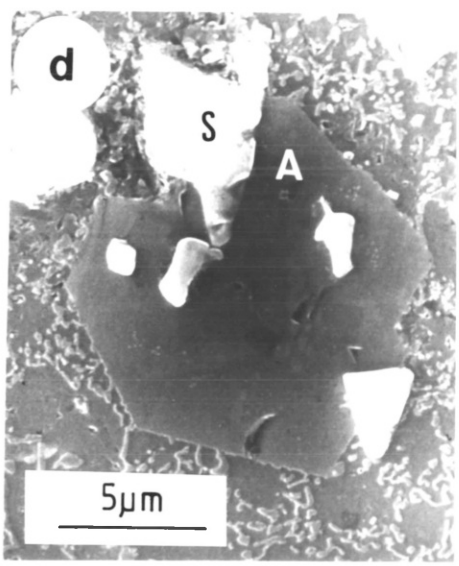
d. As **c**. above. The more typical Al_4C_3 crystal section through 'A' lacks the finer internal particles present in the section in **c**.

e. Light micrograph of an Al-12Si-SiC sample re-melted, whilst argon encapsulated, at 1000^{o}C for 100minutes and AC. The micrograph shows an area into which the SiC particles were segregated, along with the Al_4C_3 crystals nucleated on them (eg. at 'A'). Note that the Al_4C_3 crystals do not cover the SiC particle surfaces generally, unlike in the re-melted CP.Al-SiC system.


a
100μm


c
S
A
5μm


b
10μm


d
S
A
5μm

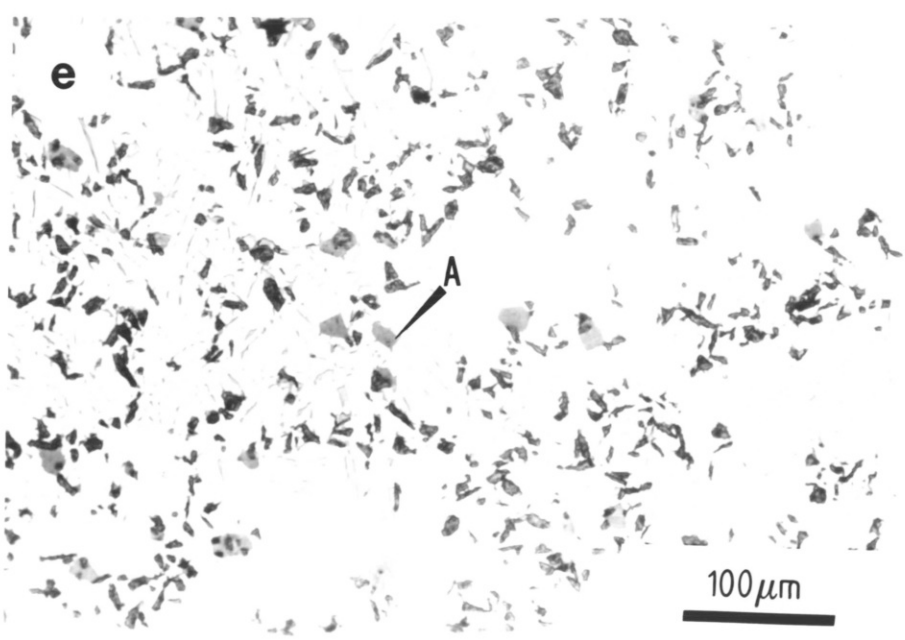
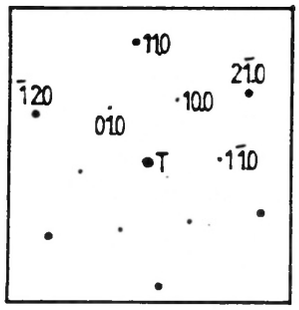

e
A
100μm

Figure 5.6

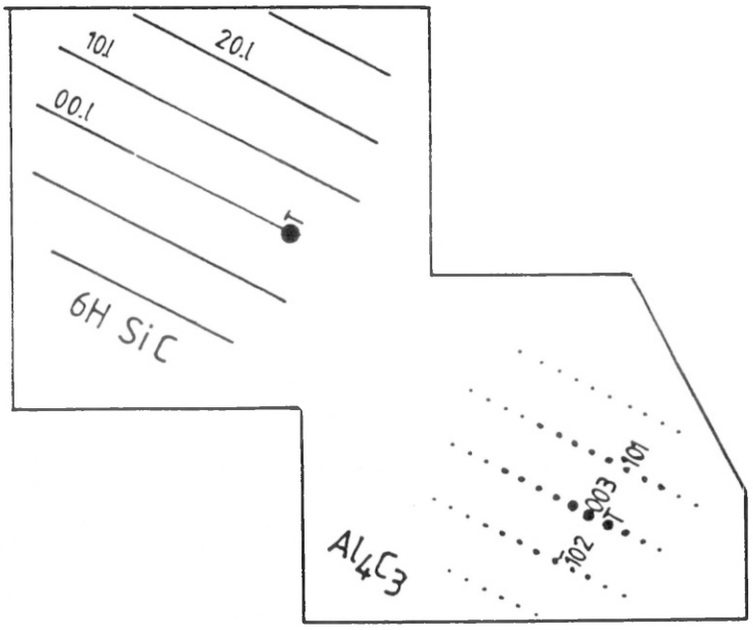
Re-melted Al-12Si-SiC

a. TEM BF image of an Al_4C_3 crystal in a sample of Al-12Si-SiC re-melted under argon for 100minutes at 1000°C and AC. Al_4C_3 'A' is on a <00.1> zone as indicated by the inset SADP (λl=2.68nm.mm), which also enables the lower left Al_4C_3-matrix interface to be identified as a {10.0} Al_4C_3 facet. Two SiC particles are present labelled 'S1' with interface voids at 'V', and 'S2' which was 15R SiC.



b. As in **a.** but ion beam milled for 3minutes longer. TEM BF image of the interface between SiC particle 'S1' and the Al_4C_3 crystal 'A'.

c HVEM BF image produced at 500kV of a sample as shown in **a.** above. A 6H SiC particle and an SADP from it (top right) and an adjacent Al_4C_3 crystal oriented with the SiC and its SADP is shown (bottom right with λl=2.15nm.mm) indicating that the principle axes (see key) are misoriented by only a few degrees as commonly observed in the re-melted CP.Al-SiC system. Note the high defect density in the Al_4C_3 crystal.



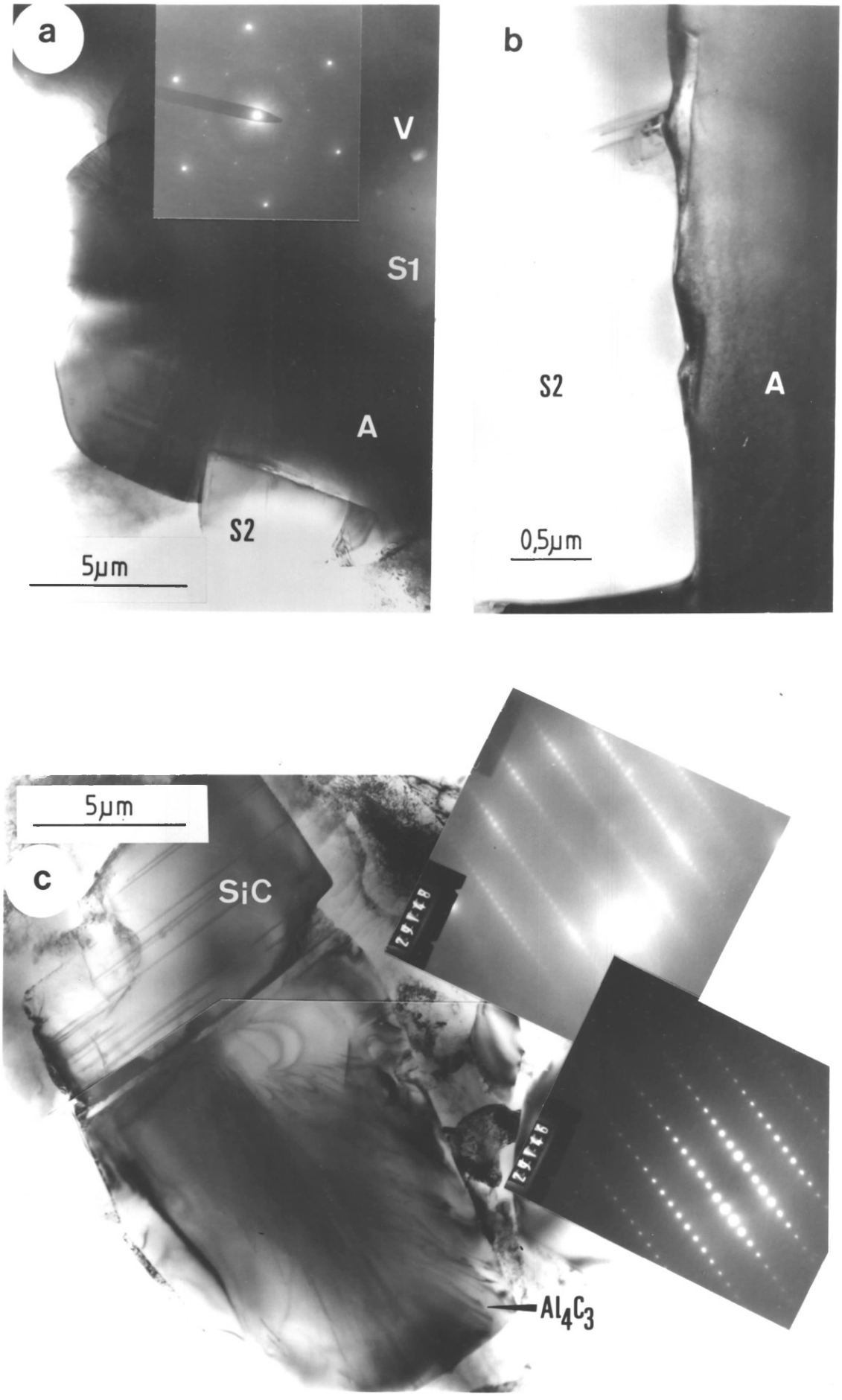

a
V
S1
A
S2
5µm
b
S2
A
0,5µm
5µm
c
SiC
Al_4C_3

Figure 5.7

Re-melted Al-12Si-SiC

TEM BF micrographs at 100kV of the Al-12Si-SiC composite following re-melting at 1000^{o}C for 100mins and AC.

a. Group of Al_4C_3 crystals 'A' and SiC particles 'S1' and 'S2'.

b. As in **a**. above but ion milled 12minutes more. The central SiC particle 'S1' is heavily faulted and was found to be 4H SiC as indicated by a <11.0> type zone axis diffraction pattern. Note the polycrystalline material at 'P' with associated voids.

c. Periphery of the Al_4C_3 area shown in **a**. but 5minutes ion beam milling earlier than in **a**. Note what are apparently dislocations in the Al_4C_3 as arrowed, and the high density of faults in the lower portion of the figure.

d. As in **c**. Al_4C_3 at 'A' shows a defect structure. The SiC particle 'S2' showing stacking faults was found to be a 4H polytype.

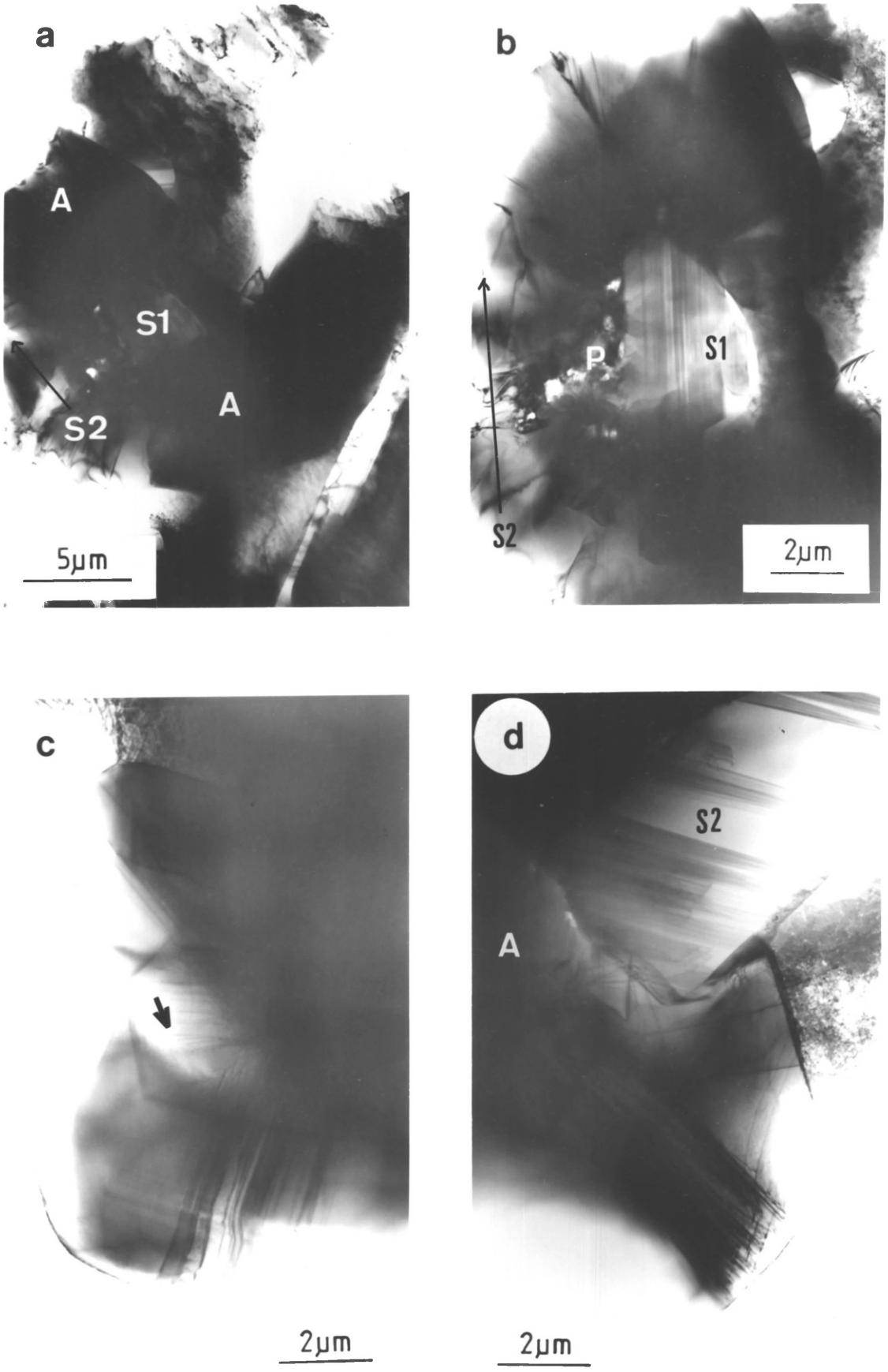

a
A
S1
S2
A
5µm
b
P
S1
S2
2µm
c
2µm
d
S2
A
2µm

Figure 5.8

As- sprayed LM13+18-20vol%SiC

a. Light micrograph of unetched MH35-L

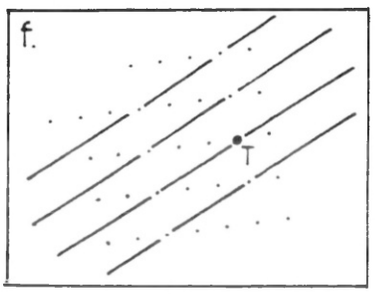
b. Light micrograph of unetched MH35-L showing the following phases: SiC (dark angular particles with a black outline); mid-grey Si spheroids; and Al (pale grey). Various intermetallic phases can also be seen.

c. TEM BF image of a general area of the as-sprayed composite. Intermetallic particles appear as dark sub-micron spheroids and cuboids; SiC particles are the large dark angular phase, Si is faceted and twinned, and the remaining matrix is mainly Al.

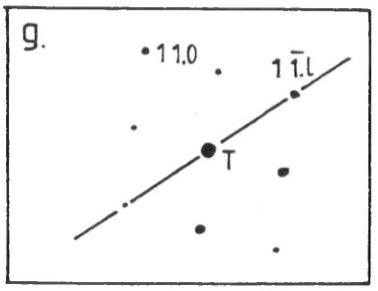
d. TEM BF image of a SiC-matrix interface. The SiC is at 'S' and pale-grey, twinned Si crystals are imaged in the matrix.

e. TEM BF micrograph showing an unidentified intermetallic 'I' seen to wet SiC 'S'. Precipitates formed in the solid-state in the matrix at 'M' are visible.

f. SADP from intermetallic 'I' as oriented in **e.** above (λl=4.92nm.mm).



g SADP from the SiC (λl=4.92nm.mm) adjacent to the intermetallic 'I' in **e.** above at the same orientation. The SADPs in **f** and **g** suggest that an orientation relationship exists between the two phases.



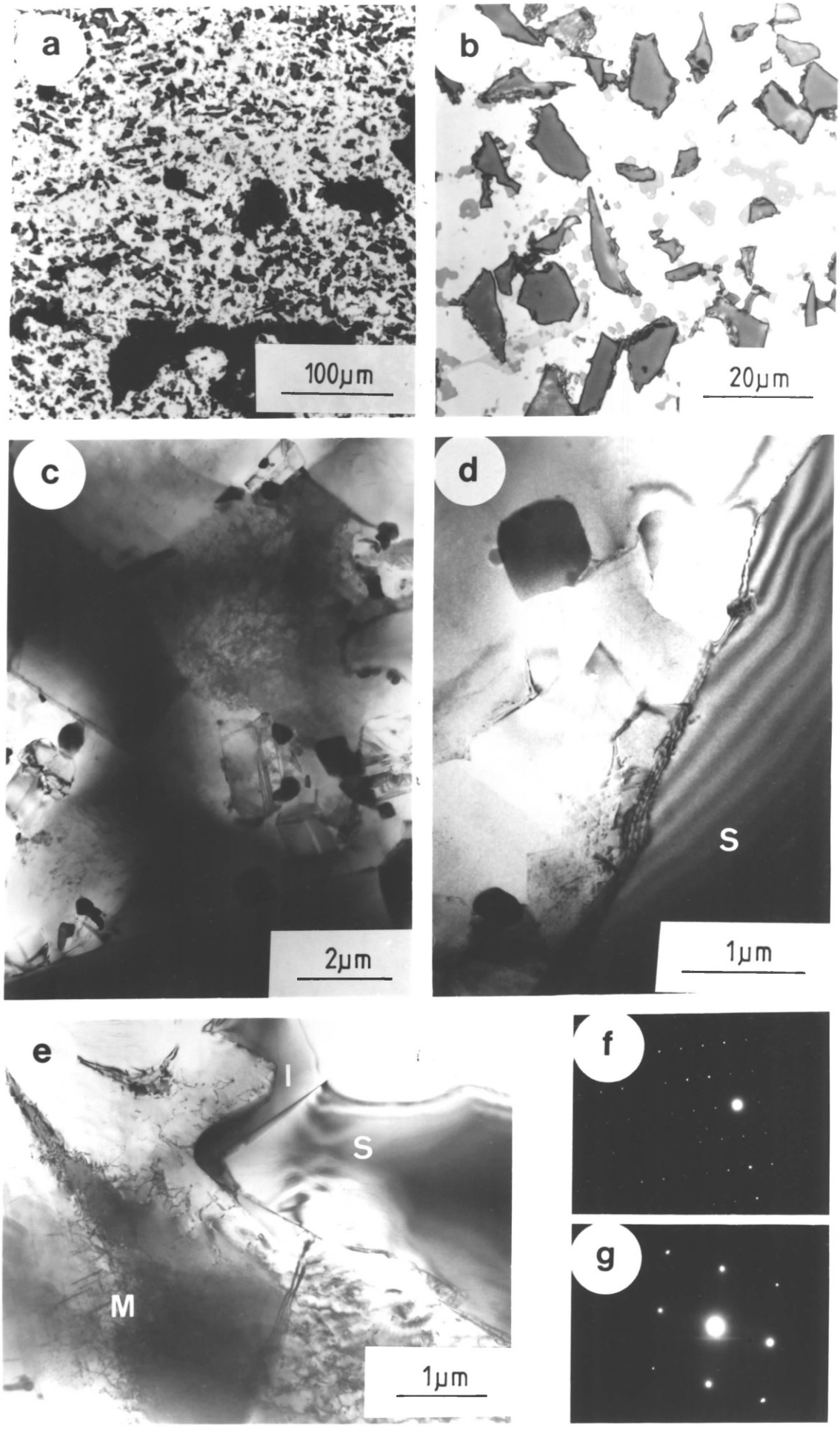

a
100µm
b
20µm
c
2µm
d
S
1µm
e
I
S
M
1µm
f
g

Figure 5.9

Re-melted LM13+18-20vol%SiC

a. Light micrograph of LM13+SiC composite following a 1000minute re-melt at 848^{o}C and AC: the re-melting was carried out under argon. A string of inclusions (arrowed) was found on the as-polished section.

b. Light micrograph of LM13+SiC composite following a 1000minute re-melt at 915^{o}C and AC: the re-melting was carried out under argon. The ring of inclusions (arrowed) was found on the as-polished section, and there appear to be three types of particles present in the ring: '1' SiC particles; '2' mid-grey faceted particles (Al_4C_3); and '3' dark particles (spinel?) .

c. Light micrograph of LM13+SiC composite following a 1000minute re-melt at 1000^{o}C and AC: the re-melting was carried out under argon. The ring structure (arrowed) appears to be composed of Al_4C_3 alone.

d. Light micrograph of LM13+SiC composite following a 100minute re-melt at 940^{o}C and WQ: the re-melting was carried out in air. A highly reactive 'rogue' particle labelled 'R' is seen to be surrounded by a localised concentration of Al_4C_3 particles (arrowed) when Al_4C_3 is generally absent from the matrix.

e. SEM BEI (backscattered electron image) micrograph of LM13+SiC re-melted 1000minutes at 1000^{o}C and AC. Several constituents can be seen including: black, faceted Al_4C_3 particles eg. at 'A'; dark-grey particles of SiC; mid-grey matrix Al; pale-grey, poorly defined, eutectic Si; and 'white' eutectic phases rich in transition elements Fe, Mn, Ni etc. Note the similarity in the distribution and morphology of the Al_4C_3 in both the LM13 and the Al-12wt%Si matrix composite (see figure **5.5e**).

f. Light micrograph of LM13+SiC composite following a 1000minute re-melt at 1000^{o}C and AC: the re-melting was carried out under argon. A ring of fine needle-like or platelet phases are present in the solidified structure.

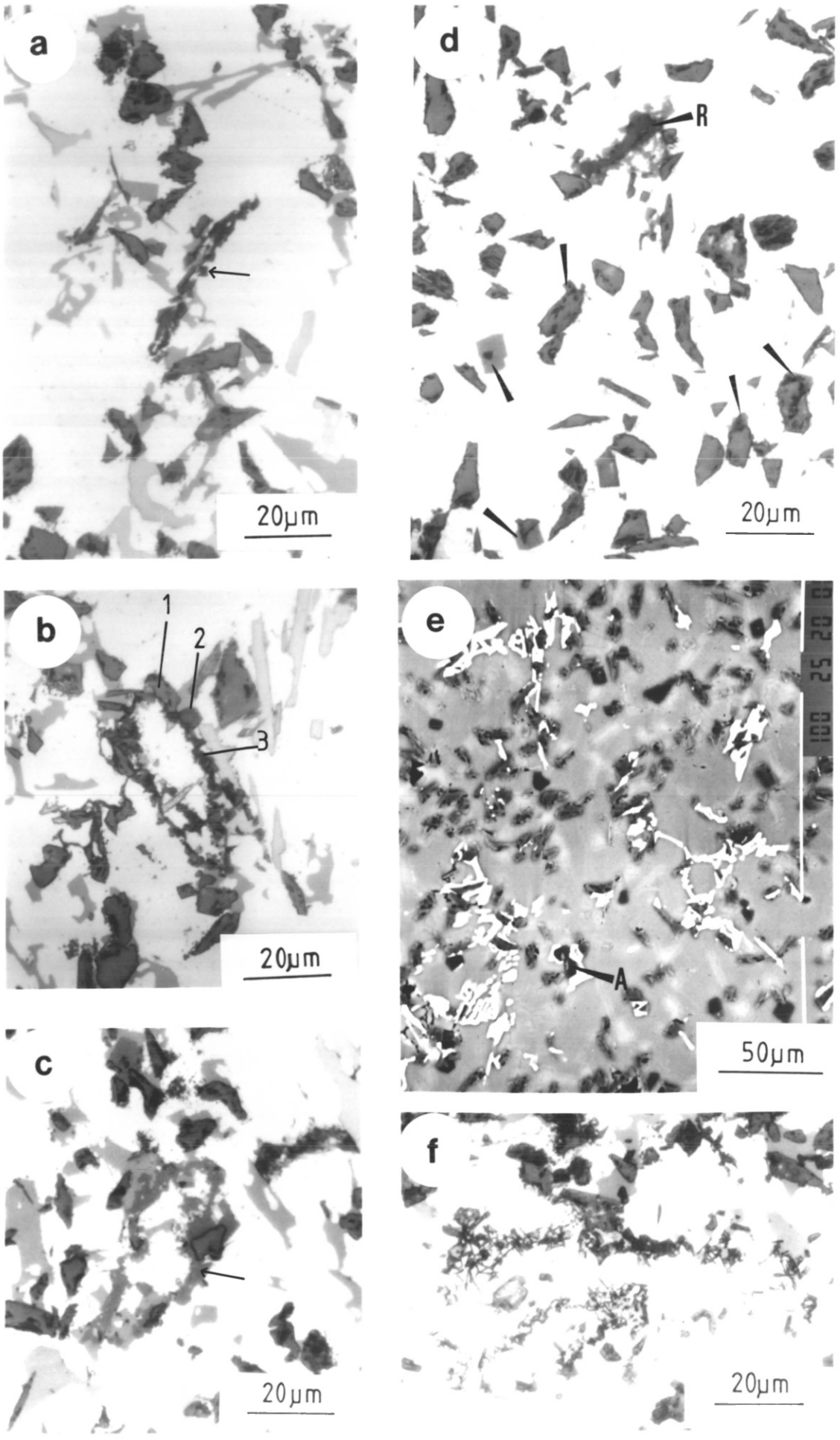

a
20μm
d
R
20μm
b
1
2
3
20μm
e
A
50μm
c
20μm
f
20μm

Figure 5.10

Re-melted LM13+18-20vol%SiC

Note: intermetallics are numbered as in table 5.1.

a. SEM BEI of a sample of LM13+SiC re-melted for 30minutes at 800^{o}C, furnace cooled to 600^{o}C, then cooled at 1^{o}C/min to 515^{o}C and finally AC to RT (typical LM13 solidification range is 560 - 525^{o}C). The phases present include: 'black' porosity; 'dark-grey' SiC; 'pale-grey' Al; and 'bright' intermetallic phases.

b. Conditions as in **a** above. The main mid-grey tone region of the micrograph is an $Al_{15}(FeMn)_3Si_2$ primary spheroid (several of which are evident in micrograph **a**). SiC particles within the spheroid are dark in contrast. Note the 'crazing' of the intermetallic spheroid.

c Condition as in **a** above. Porosity appears black in the micrograph along with SiC as dark-grey particles, Al as the mid-grey matrix and various pale-grey intermetallic phases. The SiC particles lie segregated within the interdendritic eutectic phases and porosity.

d The same area as in **c** is shown revealing the segregation of the(Al Cu Ni) phases which show the highest contrast (with the exception of the low fraction of Pb particles).

e Condition as in **a** above. The micrograph shows an intermetallic phase into which the SiC particles have segregated so producing a large proportion of intermetallic-SiC boundaries: the intermetallic phase surrounds or links all the SiC particles the eutectic colony contains.

f SEM BEI image of intermetallic phases in the base LM13 alloy re-melted and cooled with the sample described in **a** above. The bright phase is $(FeNi)_2Al_9$ (intermetallic 2) and the greyer script is $Al_{15}(FeMn)_3Si_2$ (intermetallic 1).

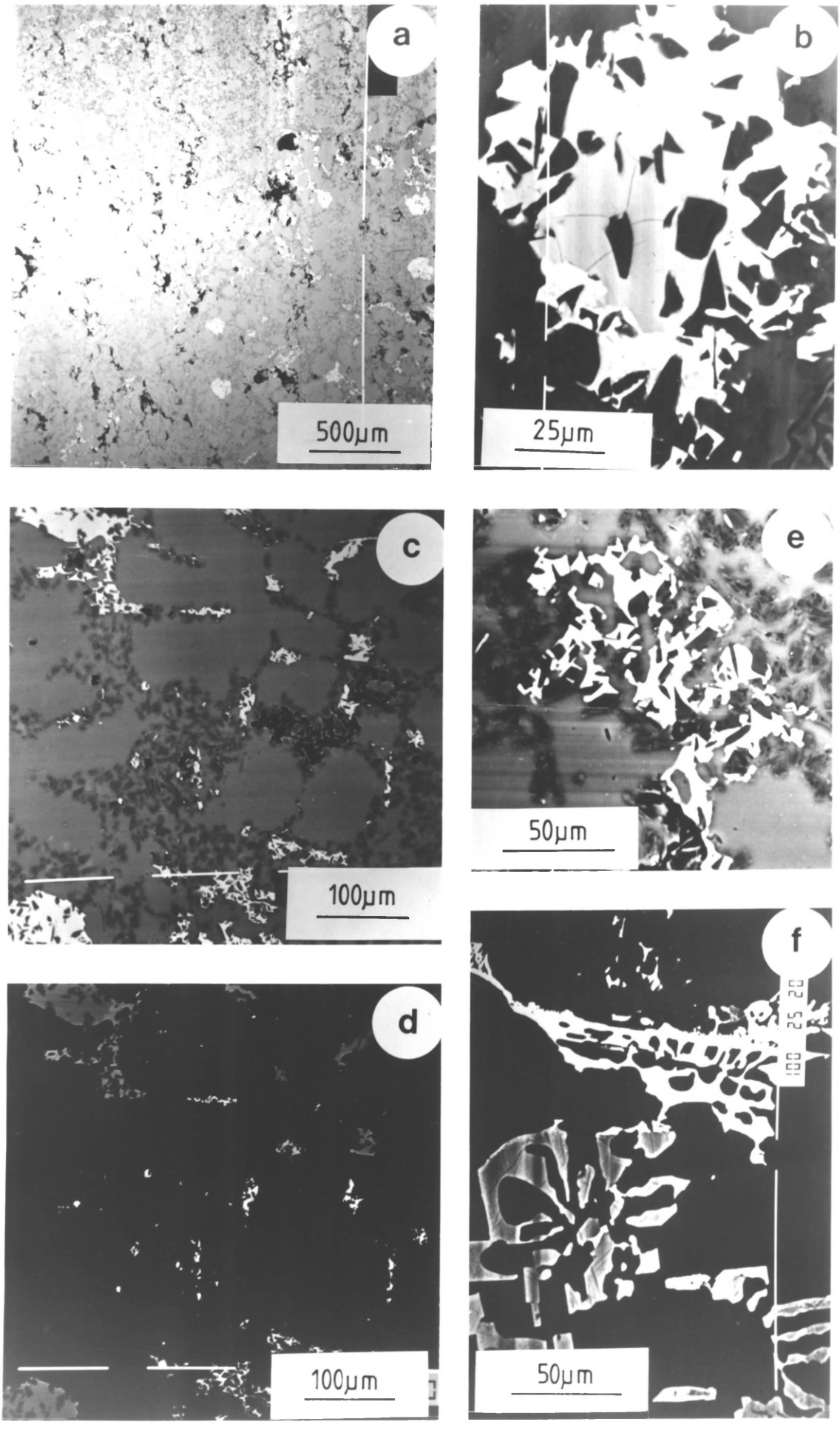

a
500µm
b
25µm
c
100µm
e
50µm
d
100µm
f
50µm

Figure 5.11

Phases in LM13

Note: intermetallics are numbered as in table 5.1.

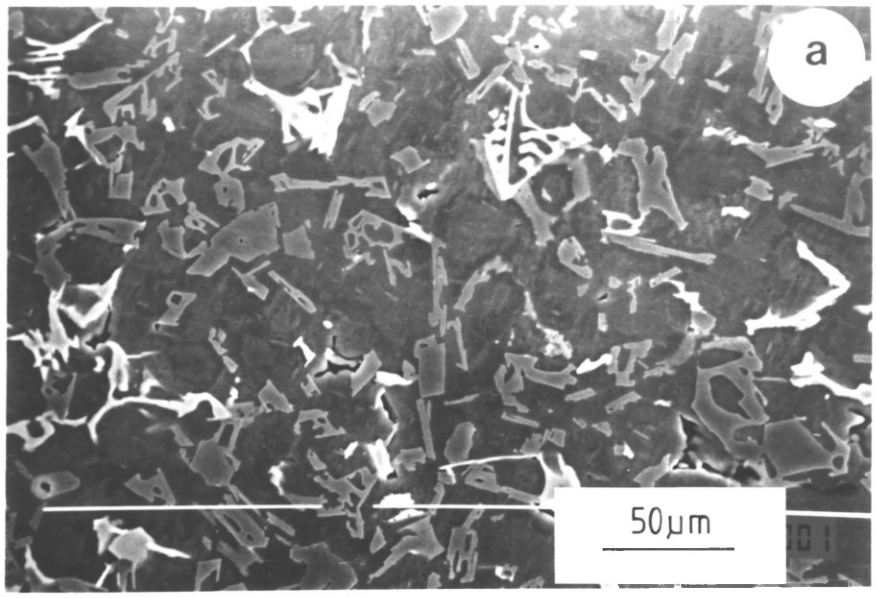
a SEM SEI micrograph of the as-cast LM13 base alloy. Brightly contrasted intermetallic phases are seen amongst the generally distributed flake Si (mid-grey/faceted) in the Al matrix (dark-grey).

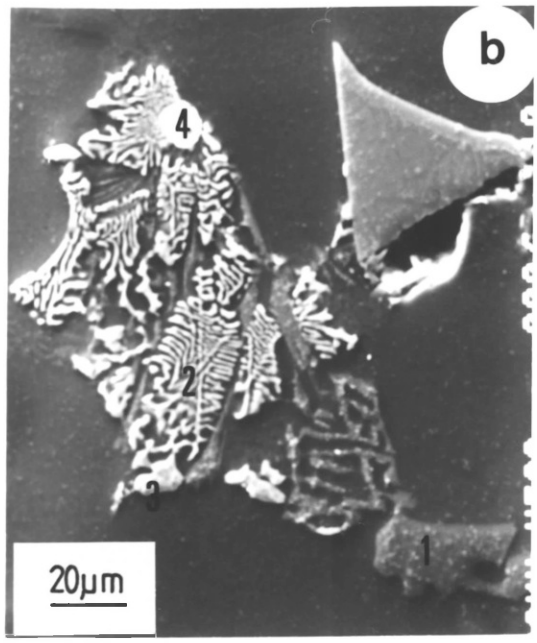
b SEM SEI micrograph of the LM13 alloy re-melted for 30minutes at 800^{o}C, furnace cooled to 600^{o}C, then cooled at 1^{o}C/min to 515^{o}C and finally AC to RT (typical LM13 solidification range is 560 - 525^{o}C). The phase labelled '1' is Al-Mg-Si-(Fe-Ni-Cu) which is intermetallic 9, the composition being comparable with $Al_8Mg_3Si_6Fe$. The eutectic '2' contains Al-Cu-Ni: the bright phase is likely to be $NiCu_3Al_6$ (intermetallic 5) judging from the overall composition of the colony and the presence of $CuAl_2$ particles at '3' (intermetallic 7). A particle of Pb found is labelled '4'.

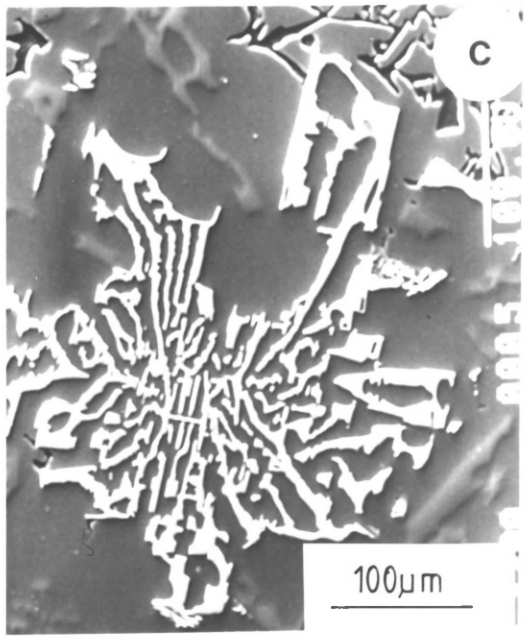
c Conditions are as in **b** above. A typical eutectic colony of Al-Ni-Si-Fe-Mn-Cu phase designated intermetallic 3 is the bright phase dominating the micrograph. The phase appears to present more facets to the matrix than the $(FeNi)_2Al_9$ in figure 5.10f and does not tend to generally produce the 'tight' script associated with the $(FeNi)_2Al_9$ though both phases have a basic plate-like morphology. The dark script in the micrograph beneath the figure label 'c' is likely to be Mg_2Si.

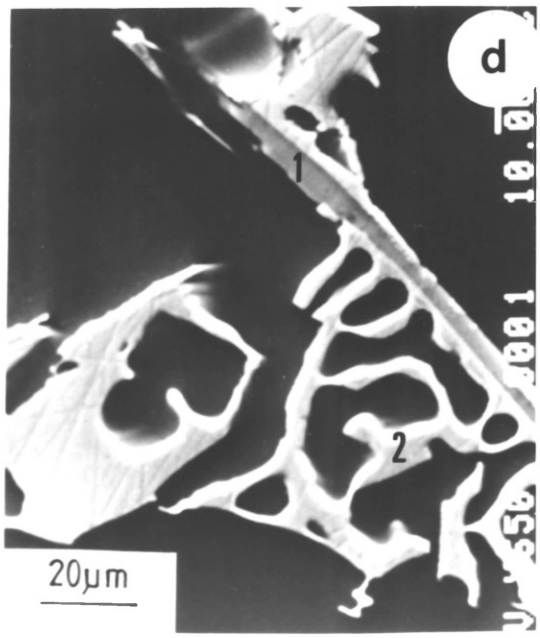
d Conditions are as in **b** above. The micrograph shows $Al_4(FeSi)_2$ labelled '1' (intermetallic 6) upon which intermetallic 3, labelled '2' has formed.

e Conditions are as in **b** above. The micrograph shows: ' 1'$(FeNi)_2Al_9$ (intermetallic 2); '2' $CuAl_2$ (intermetallic 7); '3' Mg-Si-Al-Cu-(Ni) phase (intermetallic 8) the composition of which suggests $Al_5Si_6Mg_8Cu_2$ (decomposition in the solid state into a two-phase structure appears to have occurred). The script at 'M' is likely to be Mg_2Si.


a
50µm


b
4
2
3
1
20µm


c
100µm


d
1
2
20µm

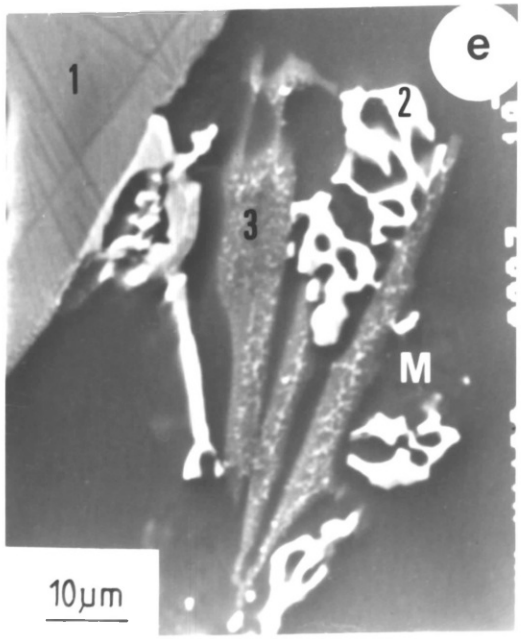
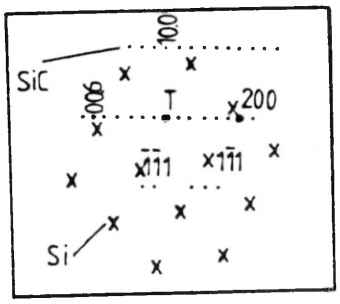

e
1
2
3
M
10µm

Figure 5.12

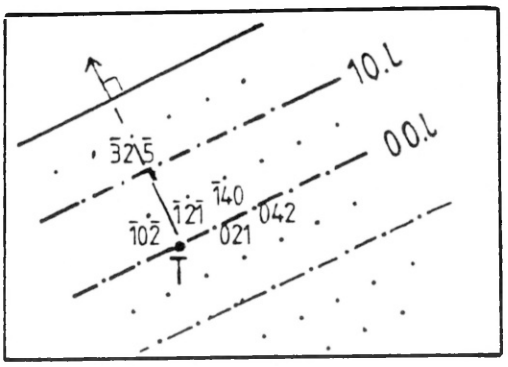
Orientation relationships between SIC and matrix phases

a TEM BF showing a 6H SiC particle 'S' and a Si flake 'I' in MH87-S re-melted for nominally 30minutes at 672^{o}C and AC. The SADP inset (with a camera length λI=2.415nm.mm and not oriented with the BF) shows a mixed diffraction pattern with a [$\bar{1}$2.0]6H SiC zone and a [0$\bar{1}\bar{1}$] Si zone as indexed in the key. The following orientation relationship is suggested:



[$\bar{1}$2.0] 6H SiC // [0$\bar{1}\bar{1}$]Si;
[10.1] 6H SiC // [01$\bar{1}$]Si (~1 - 1.2^{o} away);
[$\bar{1}$0.8] 6H SiC // [$\bar{3}\bar{1}$1]Si (ditto).

b TEM BF showing SiC 'S' and $Al_{15}(FeMn)_3Si_2$ 'I' in a sample of Al-12Si-SiC re-melted at 1000^{o}C for 100minutes. The mixed SADP (λI=2.12nm.mm) inset in the micrograph and oriented with the BF is indexed in the key and the SiC is on a [1$\bar{2}$.0] zone and the cubic intermetallic phase is on a [41$\bar{2}$] zone. The following orientation relationship is suggested:



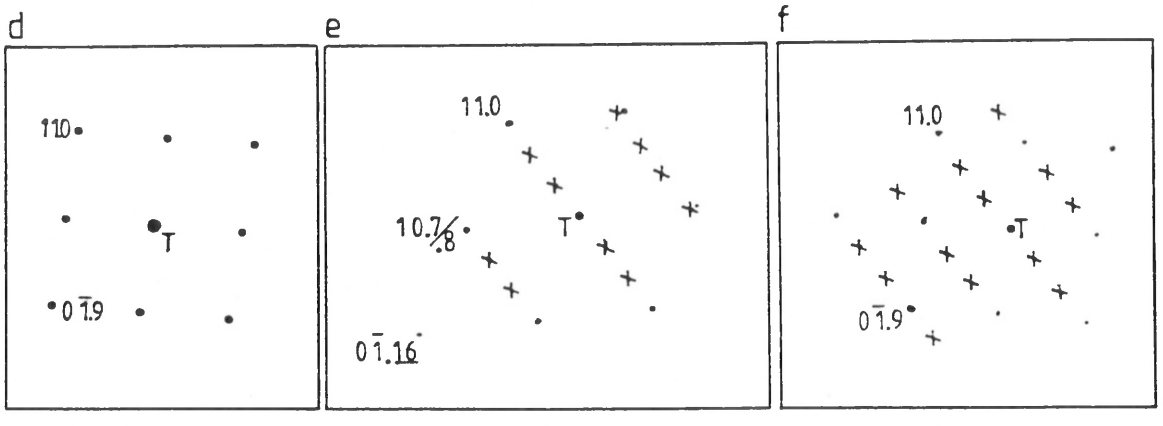
[1$\bar{2}$.0] alpha SiC // [41$\bar{2}$] $Al_{15}(FeMn)_3Si_2$;
[00.1] alpha SiC // [021] $Al_{15}(FeMn)_3Si_2$;
[10.0] alpha SiC // [$\bar{3}\bar{2}\bar{5}$] $Al_{15}(FeMn)_3Si_2$.

c TEM BF showing an unidentified intermetallic 'I' and adjacent SiC 'S' in a sample of Al-12Si-SiC re-melted at 1000^{o}C for 100minutes and AC. SADPs from these phases are presented in **d**, **e** and **f** below.

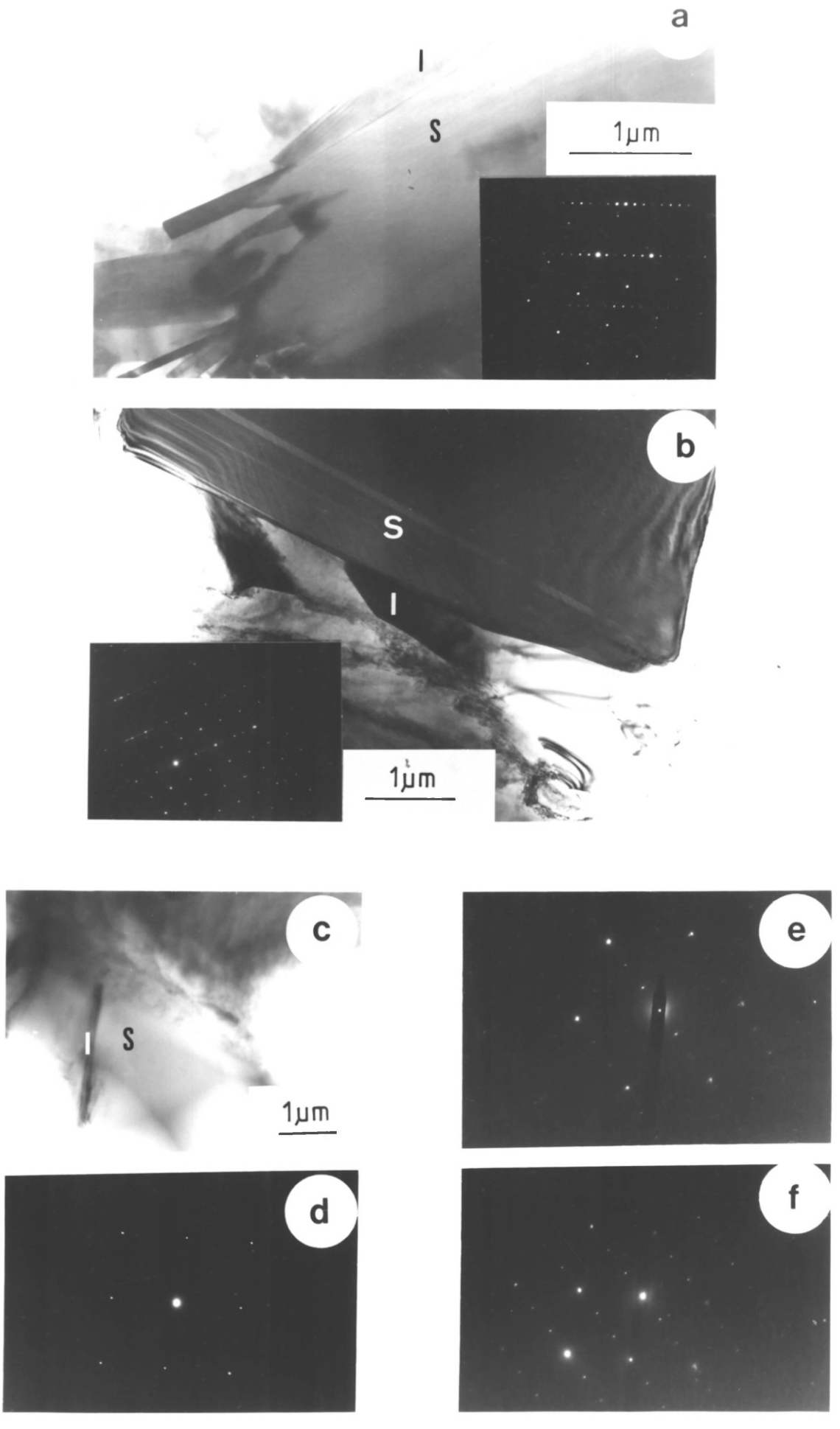
d SADP (λI=2.425nm.mm) from the 6H SiC in **c** indexed as a [$\bar{9}$9.1] zone.

e Mixed SADP (λI=2.425nm.mm) from the 6H SiC on a [$\bar{16}$ $\underline{16}$. 1] zone and a set of reflections from the intermetallic in **c** : rows of intermetallic reflections are parallel with the <11.0> SiC direction and close coincidence of spots can be seen (see key).

f Mixed SADP taken from the SiC and intermetallic phase in **c** in which the SiC is tilted back onto the [$\bar{9}$9.1] zone via a rotation about the <11.0> direction which reveals other intermetallic phase planes with interplanar spacings closely matching those of the SiC. Some 'd' spacings suggested from the SADPs for the intermetallic are, in angstroms: 4.676-4.687, 2.77, 2.10 , 1.875 and 1.64 which could not be correlated sucessfully with phases in the powder diffraction files.



SiC=• ; INTERMETALLIC=x ; T = TRANSMITTED BEAM.


a
I
S
1µm
b
S
I
1µm
c
I
S
1µm
e
d
f

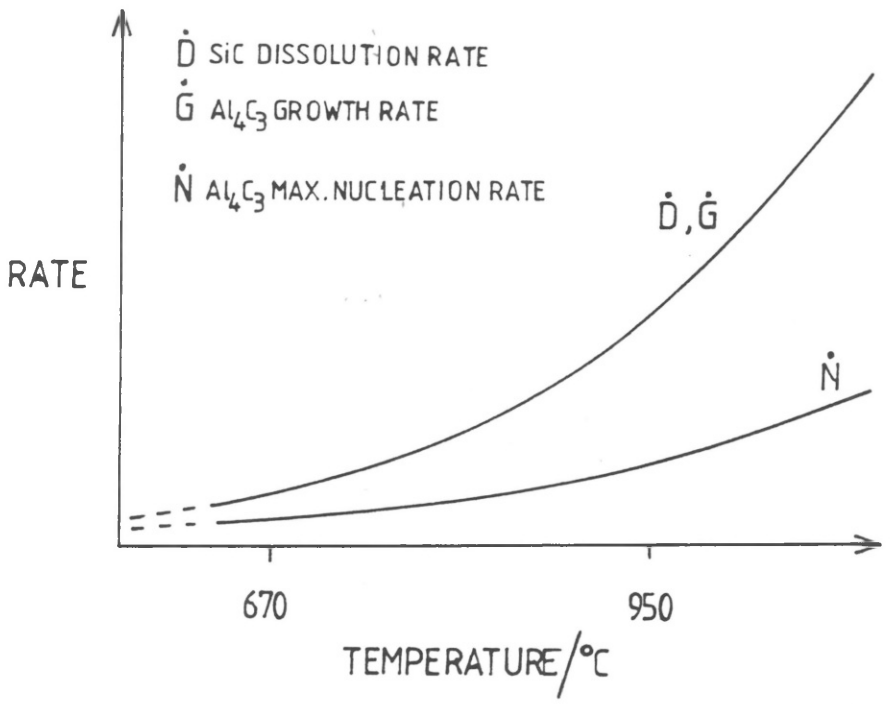


FIGURE 5.13 Proposed temperature dependence of rate phenomena early in the reaction:

$4Al(l) + 3SiC(s) \longrightarrow Al_4C_3(s) + 3Si(l)$

TABLE 5.1 Intermetallic phases in LM13+18-20vol%SiC (MH35-L) composite following re-melting, and in conventional LM13.

(ALL COMPOSITIONS IN ATOMIC %)

	ELEMENTS	RE-MELT													
		LM13+18-20VOL%SiC (MH35-L)												LM13	
	ANALYSED	8800MINS. 733°C AC					100MINS. 868°C AC			100MINS. 972°C AC		30MINS. 800°C COOLED 1°C/MIN				
INTERMETALLIC 1	Al	70.4	72.4				68.6	69.8	69.1	69.9	70.2	70.1	70.7	70.3	70.7	70.2
	Mg	0.5	0.9				1.1	0.7	1.3	1.3	0.9	0.0	0.6	0.3	0.4	0.6
	Si	10.7	10.9				12.4	10.9	9.8	11.2	11.1	10.6	11.3	10.9	10.3	10.6
	Mn	8.5	6.1				8.4	9.0	5.7	7.9	8.0	7.1	8.5	8.1	5.6	5.8
	Fe	8.9	8.3				8.8	8.7	11.2	8.6	8.9	10.7	8.5	8.5	11.8	11.2
	Ni	0.6	0.8				0.4	0.5	1.7	0.7	0.6	0.6	0.2	0.4	0.5	0.7
	Cu	0.3	0.6				0.3	0.4	1.1	0.4	0.3	0.1	0.1	0.3	0.7	0.9
	Zn	0.1	–				–	–	–	–	–	–	–	–	–	–
	Cr	–	–				–	–	–	–	–	–	–	0.9	–	–
	V	–	–				–	–	–	–	–	–	–	0.2	–	–
		p	p				p	p	s	p	p	s	p	p	s	s
INTERMETALLIC 2	Al	80.1	79.3	80.9	82.4	79.8	79.5			79.4	81.0	79.5			78.3	77.5
	Mg	0.9	0.9	1.2	1.2	1.3	1.7			1.3	0.9	0.0			0.0	1.1
	Si	0.4	1.3	1.7	1.0	0.7	1.8			1.4	1.6	1.9			2.3	2.9
	Mn	0.6	0.6	0.6	0.3	0.5	0.5			0.4	0.3	0.4			0.6	0.4
	Fe	1.7	3.4	3.0	2.5	2.0	4.0			3.9	3.6	5.0			4.7	6.0
	Ni	15.0	13.7	11.8	11.8	14.7	11.8			13.1	11.9	12.7			12.7	11.6
	Cu	1.3	0.8	0.8	0.7	1.0	0.6			0.5	0.6	0.3			0.5	0.6

NOTE: for INT.1 p denotes primary , s denotes 'script'.

TABLE 5.1 cont.
(ALL COMPOSITIONS IN ATOMIC %)

	ELEMENTS	RE-MELT									
		LM13+18-20VOL%SiC (MH35-L)					LM13				
	ANALYSED	8800MINS. 733°C AC			100MINS. 972°C AC		30MINS. 800°C COOLED 1°C/MIN				
INTERMETALLIC 3	Al	71.0	71.6	71.6	70.2	70.0	70.0	70.1	69.3	69.0	70.0
	Mg	1.3	1.2	1.2	1.0	1.4	0.6	0.6	0.6	1.2	0.6
	Si	5.9	6.1	5.3	5.6	6.4	6.3	5.5	6.5	6.3	5.9
	Mn	1.1	0.9	0.7	1.5	0.7	0.7	0.8	0.8	1.0	0.9
	Fe	4.5	4.3	3.4	3.6	4.3	4.9	4.5	5.5	5.2	4.4
	Ni	14.1	13.7	15.5	14.9	15.2	15.4	16.6	15.1	14.9	15.1
	Cu	2.1	2.1	2.4	3.1	2.1	2.2	1.9	2.1	2.4	2.9
	Zn	-	-	-	-	-	-	-	-	-	-

	ELEMENTS	RE-MELT		
		LM13+18-20VOL%SiC (MH35-L)		
	ANALYSED	8800MINS. 733°C AC	100MINS. 972°C AC	
INTERMETALLIC 4	Al	65.2	59.4	56.7
	Mg	1.7	6.6	5.9
	Si	0.2	5.2	3.3
	Mn	0.0	0.0	0.0
	Fe	0.1	0.0	0.1
	Ni	15.2	14.7	18.1
	Cu	17.6	14.0	15.9

	ELEMENTS	RE-MELT	
		LM13+18-20VOL%SiC (MH35-L)	
	ANALYSED	8800MINS. 733°C AC	100MINS. 972°C AC
INTERMETALLIC 5	Al	62.8	69.8
	Mg	1.9	2.8
	Si	0.2	0.0
	Mn	0.1	0.0
	Fe	0.3	0.1
	Ni	9.9	5.7
	Cu	24.8	21.7

TABLE 5.1 cont.

(ALL COMPOSITIONS IN ATOMIC %)

		RE-MELT															
		I.M13															
		30MINS. 800°C COOLED 1°C/MIN															
		INTERMETALLIC 6				INTERMETALLIC 7				INTERMETALLIC 8				INTERMETALLIC 9			
ELEMENTS	ANALYSED																
Al		67.5	66.7			65.2	66.3			18.2				43.8	43.4		
Mg		0.0	0.3			0.0	0.0			41.1				23.3	24.4		
Si		16.3	17.1			3.1	1.3			31.1				26.9	26.1		
Mn		1.3	2.0			0.0	0.0			0.0				0.1	0.3		
Fe		13.1	12.6			0.0	0.0			0.0				2.4	1.9		
Ni		1.6	1.1			0.8	1.2			0.4				2.9	3.6		
Cu		0.1	0.1			29.8	31.2			9.1				0.5	0.3		
Zn		0.0	0.1			0.0	0.0			0.0				0.1	0.0		

Table 5.2 Identification of intermetallic phases in LM13+18-20vol%SiC (MH35-L) composite following re-melting

Intermetallic (refer to table 5.1)	Compound formula (literature)	Cast morphology	Colour	
			As-polished on colloidal SiO_2	Etched 0.5HF(aq)
Int.1	$Al_{15}(FeMn)_3Si_2$	Labyrinthine/ chinese script eutectic and polyhedral primary grains.	Pale grey	Pale brown-pale blue(with Cu)
Int.2	$(FeNi)_2Al_9$	Partially faceted script and plates	Pale grey/ relieved	Dark brown
Int.3	-	Connected narrow plates and script	Pale grey/ relieved	Black/brown
Int.4	$(CuNi)_2Al_3$	Compact form as unresolved in light microscope	Pale green tint/mottled/ relieved	Unattacked
Int.5	Cu_3NiAl_6	Irregular interdendritic pools	Pale pink tint/relieved	Unattacked
-	Si	Plate-like eutectic Polyhedral primary	Grey	Darkened
-	Mg_2Si	Script-like	Blue/black	Etched-out
Int.6 - Int.9	not identified in the composite			

Chapter VI

Fractography

6.1 Introduction

Following the reaction between liquid Al and particulate SiC in which the interface product Al_4C_3 is formed, and Si is released into the liquid matrix, the mechanical properties of the subsequentaly solidified composite may be detrimentally affected by the changes in the interface structure between the matrix and ceramic particles, and the change in the alloy matrix chemistry. Simple preliminary experiments were performed to provide samples for fractographic characterisation with a view to deciding whether the presence of Al_4C_3 plays a role in determining the path of the fracture, and thereby inferring whether Al_4C_3 is an effective embrittling agent.

6.2 General remarks on the tensile results

Engineering stress-strain curves for the four tests conducted are reproduced in figure 6.1a. Failure strains and the maximum engineering stresses reached during the tests are tabulated in figure 6.1b. The ductility is seen to decrease in figure 6.1 from conditions A through to D, as might be expected as the volume fraction of ductile primary Al is decreased, and the total volume fraction of brittle phases SiC, Si and Al_4C_3 is increased. Samples A and B had undergone workhardening prior to fracture, whereas samples C and D had not undergone significant workhardening. Samples B, C and D failed in a macroscopically brittle manner. In the next four sections a detailed account of each sample's fractographic examination will be given in turn.

6.2.1 *Test A*

The main microstructural features of the CP.Al-SiC material (MH85-S) prior to testing were as follows:

i. approximately 12.5vol% of irregularly shaped SiC particles with a characteristic dimension ~13microns;

ii. bands in the extrusion direction into which SiC particles are concentrated ;

iii. clusters of SiC particles ~60microns across;

iv. porosity, typically associated with particle clusters and particle-particle contacts in general;

v. cracked SiC due to the combination of clustering and the hot extrusion processing step;

vi. Fe rich impurity phases at the SiC-matrix interface;

vii. and an Al matrix with a grain size of the order of the SiC particle spacing and impurity levels of Si in solution or combined in a very low volume fraction of Al -Fe-Si particles.

Despite the inherent flaws the highly ductile matrix, and the relatively low volume fraction of rigid SiC particles allowed the sample to be strained to~24% with a low workhardening rate, as in figure 6.1, compared to the other test conditions.

Examination of the fractured sample showed several features. The test piece had taperred significantly at mid-gauge, but there was no localised neck (figure 6.2a). The fracture involved a mixture of tensile and shear failures (figure 6.2a), though some parts of the fracture surface were parallel to the tensile axis (figure 6.2e) which can be correlated with the banding in the particle and porosity distribution in the original material. The fracture surface showed deep, equiaxed dimples on the tensile portion (figure 6.4a) and shallower dimples, elongated in the direction of shear on the shear surfaces (figure 6.5a). Fracture of the SiC particles below the fracture surface was rarely seen to open into extended voids, except , for example, as in figure 6.3a. Generally the void population immediately below the fracture surface did not appear to differ significantly from that along the length of the test piece. Many of the dimples on the tensile fracture surface did show SiC particles in their bases. The particles revealed at the base of the dimples were not generally completely free from the matrix: some particles were revealed as a 'bump' covered in a rough layer of Al. The particle shown in figure 6.5a on a sheared area of the fracture surface illustrates that the Al can remain adhered to the SiC: the multiple dimples on the SiC surface may correspond to interface associated particles such as the iron rich impurity phases. However, generally much of the shear surface was quite smooth, except where the occasional particle was exposed, and where particles had been drawn across the surface leaving furrows. Parts of some particles exposed on the shear surface were completely matrix free, apparently not due to particle fracture: the transverse metallographic sections showed many instances where the matrix has 'peeled away' from the particle at the point where the shear surface meets the particle. It is suggested that many of the features observed are as an inevitable consequence of the shear crack cutting through poorly bonded regions of the composite eg. the SiC particle 'banding'. Although fracture of the SiC particles was by no means prevalent, many of the SiC particles at the fracture surface contained secondary cracks.

6.2.1.1 *Test A : summary*

The fractured sample showed ductile characteristics, though the lack of any localised necking shows that high local straining does not occur on the scale of the test piece dimensions. Damage resulting from the passage of the shear crack is limited to a very narrow zone, of the order of the particle spacing. There is no evidence that voids were produced at the SiC-matrix interface during the test. It is likely that many of the voids involved in the fracture, which produced the dimples on the tensile fracture surface, were present prior to the test.

6.2.2 *Test B*

Following a re-melting treatment to produce a low volume fraction of Al_4C_3 at the SiC-matrix interface it was estimated that the matrix contained less than 1at%Si which upon solidification would give rise to less than 5vol% of Al-Si eutectic (by application of the Scheil equation [163] with a partition coefficient estimated at 0.11). Less than 1vol% Al_4C_3 would have been produced during the re-melt (see figure 4.32).

The bands of porosity and SiC in the microstructure were as in the original material , though the volume fraction of the porosity may have increased marginally with the addition of casting porosity, though the SiC particles do not appear to have been redistributed significantly (figure 6.26). Thermocouple readings indicated that complete melting occurred in the vicinity of the thermocouple junction inserted into one end of the sample during re-melting, where the temperature reached ~15^{o}C above the liquidus: the whole sample was assumed to have melted. The apparent lack of SiC particle redistribution suggests that either melting was incomplete or that particle pushing was limited. The Al-Si eutectic and impurity phases were insufficient in quantity to be seen associated with all the SiC particles, and many of the SiC particles were free from eutectic although the particle surfaces had been attacked by the melt producing Al_4C_3. Many particles could have been trapped between dendrite arms, though the primary Al grain size would need to be small in order to prevent long range particle pushing. Overall very little particulate redistribution was evident though no grain size measurements, nor observations on the positions of particles with respect to grain boundaries were made. The small amount of Al_4C_3 required for the experiment was produced in the re-melt, and the amount of extraneous phases such as flake Si, and the Al-Fe-Si phases in the cast structure was minimal.

The large volume fraction of primary Al with Si in solution produced significant ductility despite the high flaw content of the composite (see figure 6.1). The sample failed by shearing-off at one end of the gauge length, as in figure 6.2b. The occurrence of fracture surfaces parallel to the tensile axis again, as in test A, show that the banded porosity and particles have influenced the crack path. No necking of the sample was apparent and the sample failed at a maximum engineering stress of ~160MPa. This figure was higher than in test A; however the true stress at failure in test A is higher than the 109MPa in figure 6.1b, and as test sample A was observed to have necked the stress at failure for tests A and B would probably be much closer than suggested by the engineering stress values. With the pre-existance of voids and particle fractures in the material it would be difficult to determine whether the test conditions created significant damage immediately below the fracture surface, as with condition A.

Fractured SiC particles, which had separated just below the fracture surface, and particles which had fractured in association with sub-fracture surface voids were observed to a greater extent in test B compared with test A. Examples of sub-fracture surface damage are SiC-SiC fracture, Al_4C_3-SiC debonding and Al-SiC debonding as evident from figure 6.3b: in the figure 6.3b it is not possible to say which fracture event had occurred first, though Al_4C_3-SiC debonding definitely takes place. Further examples of debonding were observed several particle spacings below the main, sectioned, fracture surface in association with the opening-up of a large (pre-existing) pore.

Generally the fracture surface itself showed shallow dimples and fractured SiC particles as in figures 6.4b, c and d : the abundant flat fracture of the SiC seen was in marked contrast to the fracture surface in test A. Direct evidence for the role of the Al_4C_3 platelets in the transition in fracture behaviour is sparse as described below.

Figures 6.5c and 6.5d show interfacial voids which have been produced due to the debonding of the matrix from the interface phase. For example the particle labelled 'A' in figure 6.5c appears to be intact, but fully exposed: the bright rim of material between 'A' and the SiC particle 'S' suggests that a void had been present around particle 'A' prior to the fracture of the adjacent SiC. A further feature of interest on the fracture surface is the appearance of the flat region of matrix material surrounding SiC particles as in figure 6.5d. Following SiC fracture, the crack will extend into the surrounding phases at the interface until the ductile matrix is met where the crack will be blunted. A void is created extending through the SiC particle, with the final local separation of the sample taking place by the ductile failure of the Al matrix. Prior to the fracture of the SiC particles it is suggested that the interface voids have formed via interface phase-matrix debonding or interface phase-SiC detachment.

6.2.2.1 *Test B: summary*

Failure involves the fracture of the SiC particles in the path of a shear crack. SiC-matrix interfacial phases appear to nucleate voidseither by detaching from the SiC or by debonding from the matrix: subsequent void growth along the SiC-matrix interface is limited prior to SiC fracture, and the SiC-Al matrix bonding appears to be strong. There is no evidence that the fracture of Al_4C_3 precedes SiC fracture. Comparing the mechanical behaviour of test samples B and A, the workhardening rate of material B was greater than in the A sample, the strain to failure was much lower, though the true failure stress was considered to be similar.

6.2.3 *Test C*

Following re-melting to produce a substantial increase in the volume fraction of Al_4C_3, compared with test B, but not to produce a continuous interface phase layer, the sample for test C contained ~6.7at%Si in the matrix giving ~39-44vol% eutectic with ~8.1vol%Al_4C_3 . The local volume fraction of particulate material ie. SiC covered in Al_4C_3 within the eutectic would be ~40vol%. The tensile test curve in figure 5.1a suggests that rapid workhardening had taken place place followed by early brittle failure of the test piece without necking. The apparent ductility recorded (figure 6.1a) is probably somewhat high since machine elasticity was not taken into account.

Figure 6.2c shows extensive porosity, and the original directionality of the SiC banding still remains evident although much of the particulate has been redistributed upon solidification.

Figure 6.3c shows sub-fracture surface SiC fractures which were occasionally seen. Typically, a damage zone exists just below the surface in which Si flakes have fractured: the Si flakes are more often found showing multiple fractures as the fracture surface is approached. Al-Fe-Si crystals are also found to be fractured. Regions of the matrix between the fractured phases remain intact as ductile ligaments. Concentrations of sub-surface fractures occurred in conjunction with porosity opening below the main crack path, whereas the damage zone over 'sound' portions of the test piece fracture surface is extremely narrow, typically of the order of the Si flake spacing. The fracture surface itself, figure 6.4c, shows features identifiable with the major microstructural constituents. Much of the fracture surface is covered in eutectic Si, which had cleaved, divided by ductile ridges or cusps corresponding to eutectic Al. Isolated regions of dimpled morphology can be seen which would correspond to primary Al. Generally, the surface roughness is on a finer scale compared to the fracture surface morphologies resulting from the preceding tests.

The eutectic Si, comprised of volumes of parallel flakes, present variable fracture morphologies: flat areas of the fracture surface, where the fracture path has passed along Si flakes, are the result of {111}Si cleavage planes as is generally observed in fractured, unmodified Al-Si alloys [64]; with the Si flakes lying approximately parallel to the tensile direction the flakes fracture occurs across the narrow dimensions (transversely), the cracks eventually linking-up as the separating eutectic Al fails in a ductile manner.

A closer examination of the fracture surface as in figure 6.6a shows what are considered to be fractured SiC particles as flat islands, surrounded by the often discontinuous flat regions at the SiC-matrix interface corresponding to Al_4C_3: within the interface region bright cusps, likely to be Al are also seen. The SiC-Al_4C_3 aggregates tend to contain more than one SiC particle linked together by Al_4C_3 bridges [154] which can fracture together. That the SiC-Al_4C_3 aggregates within the Al-Si eutectic fracture, often with secondary cracking, is not suprising considering the high local volume fraction of particles in the eutectic through which the fracture would tend to run. Figure 6.6b, taken from a water-quenched sample of MH85-S which had been re-melted at 800^{o}C for 1000minutes, and fractured in a simple impact experiment, shows the 'flat' failure of the SiC-Al_4C_3 aggregates amongst the finely dimpled Al and quench modified Al-Si eutectic. Secondary cracking can occur at the SiC-interface phase boundary, figure 6.6a, and through the SiC-Al_4C_3 aggregates generally, figure 6.6b.

6.2.3.1 *Test C: summary*

The failure of sample C would have been initiated from the extensive porosity produced during solidification. Large volumes of unmodified Al-Si eutectic containing 'flake' Si in which SiC-Al_4C_3 aggregates were concentrated, allow a fracture path to travel through the brittle eutectic [64], inevitably encountering the SiC-Al_4C_3 aggregates which are then induced to fracture. There is some evidence to suggest that the SiC-Al_4C_3 interface is suceptible to fracture.

However, it is suggested that the porosity and the eutectic Si are responsible for the overall fracture behaviour. Increased constraints upon deformation of the eutectic imposed by the rigid particulates, and the possibility that the Si cracks do not run through the SiC-Al_4C_3 aggregates spontaneously means that the presence of the particulate material does not necessarily reduced the toughness: quantification is necessary in order to assess the influence of the particulate. Extensive sub-surface damage, usually as Si and Al-Fe-Si phase fractures, with some Si-SiC failures, are likely to be related to casting porosity which has either opened-up independently away from the main crack, or as an extension of the casting porosity, which forms much of the fracture surface proper, out of the plane of the metallographically prepared section.

6.2.4 *Test D*

Test D was conducted to provide a fracture specimen containing the SiC in a flake Si eutectic, without the Al_4C_3, to act as a comparison with test C with respect to the type of fracture mechanisms exhibited. The sample D matrix is almost of eutectic composition so that the local SiC volume fraction in the eutectic is practically the same as in the composite, whereas in sample C the eutectic particulate concentration was 3-4 times higher than in the composite due to the particle pushing induced segregation.

Large volumes of porosity as in figure 6.2d probably dictated the early failure of the sample, as indicated in figure 6.1a. Subsurface damage resulted from porosity extension as in figure 6.3d, in which both SiC fractures and Si flake cracking are seen. The sample had not been subjected to any prior working ie. no extrusion, and so SiC particle fractures are less likely to be linked with the composite manufacture but could result from defects in the SiC grit as supplied by the grit producers. Figure 6.4d from test D shows a coarser surface structure than in figure 6.4c from test C which is related to the coarseness of the Si flake -Al eutectic structure as seen by comparing figures 6.3c and 6.3d. Flat Si fractures were present in sample D more frequently, and on a larger scale than in test C , as in figure 6.4d, which also shows that sample D contained regions with unbonded SiC particles.

Closer examination of the fracture surface as represented in figures 6.6c and 6.6d show multiply fractured Si flakes, and what appear to be fractured SiC particles on the surface: these features correspond to those observed sub-surface in figure 6.3d. Figure 6.6d also shows that where SiC particles remain bonded to the Al, they have fractured and debonded from the adjacent Si crystals.

6.2.5 *Corrosion induced cracking*

Polished samples left in the atmosphere suffered surface deformation as a result of the

hydrolysis of the large particles of Al_4C_3 in which:

$$Al_4C_3(s) + 12H_2O(l) \longrightarrow 4Al(OH)_3(s) + 3CH_4\ (g)$$

occurs [81], accompanied by a volume change of a factor 2.1 to 2.7 times for the solid products: the density of the hydroxide is 2.42g/cc [180,181], and with a mw. 78.0g/mol whereas the density of Al_4C_3 is given as either 2.36g/cc [180,181] or as the theoretical density 2.99g/cc (as used throughout this study) with a mw. 144.0g/mol. When the volume fraction of Al_4C_3 was high, and the matrix necessarily contained a high Si content, complete disintegration of the cast samples readily occurred over a period of several weeks.

6.3 Discussion

6.3.1 *General*

The aim of this study was to look at the influence of the Al_4C_3 interface phase on the fracture behaviour of the composites. Despite the limitations in the tests performed and of the sample preparation, eg. in situ re-melting and solidification, conclusions can be drawn.

In order to rationalise the observations in the multiphase systems the 'potential' individual contributary failure pathways for each test condition are tabulated in figure 6.7: the 'tables of failure pathways' are necessarily symmetrical about the 'leading' diagonal. In figure 6.7 the constitution is summarised for each test in terms of phase morphology and volume fraction: differentiation is made between primary and eutectic Al, since the segregation of the particulate phases to the eutectic is considered a very important variable. Porosity has been excluded.

The main results highlighted in figure 6.7 are:

i) the transition from test A to test B involving a 'minor' constitutional change;
ii) the apparent lack of Al-Al_4C_3 debonding in test C although present in test B;
iii) the apparent absence of Al_4C_3-Si/β (FeSi) debonding in test C, but with the observation of SiC-Si/β (FeSi) debonding in test D.

Each point is discussed below.

6.3.1.1 *Fracture mechanism transition from test A to test B*

The transition in the fracture behaviour was drastic although the constitutional change was relatively minor (figure 6.7). The important feature in the transition appears to be the debonding of Al_4C_3 plates from Al to form voids at the SiC particle-matrix interface. In test A voids were deeper than in test B on tensile regions of the fracture surface: the pre-existing voids in test A would be 'stable' and join by ductile coalescence at a critical strain. In test B the nucleation of voids by SiC cracking leads to catastrophic failure at a strain much lower than that necessary to connect the pre-existing porosity in sample B: growth of voids nucleated at the Al-SiC interface could be inhibited by the existence of a 'strong' Al-SiC interface bond. The SiC-Al debonding (table 6.1) for test B appears to occur only as a consequence of interface phase debonding, and the subsequent limited spread of the voids through the SiC-Al interface.

The suggested test B fracture mechanism (see figure 6.8) involves the nucleation of interface voids (exaggerated in figure 6.8) and the subsequent intensification of shear bands from the spreading crack tip towards the 'free surfaces' represented by the interface voids: in this way the main spreading crack will be directed towards SiC particles.

The sequence of interface void nucleation followed by SiC particle fracture is proposed since voids are unlikely to form at the SiC-matrix interface once the strain has been relaxed by SiC particle fracture. The interface voids were not observed (by light microscopy) below the fracture surface: it is hypothesised that the debonding is induced only under the direct influence of the spreading crack's tip: the further opening of voids would also be restricted except as the fracture surface itself is created.

Differences between samples for tests A and B also included the matrix Si content. The increased Si content of the sample B matrix would lead to a greater yield strength, and workhardening rates would be increased by the increased volume fractions of reaction product particles, and impurity phases, especially in the immediate vicinity of the SiC particles: a reduction in strain relaxation by dislocation mechanisms could simply lead to SiC particle fracture. Further work proposals 2-4 are designed to provide clarification of the role of the interface debonding in the overall fracture process for test B.

6.3.1.2 *Lack of Al-Al_4C_3 debonding in test C when present in test B*

With the increased Si 'flake' levels in sample condition C compared with B, the Al-Al_4C_3 fracture apparent in test B does not appear: strain relaxation occurs earlier via Si cleavage. In test C Si 'flake' fractures have a very high probability of meeting SiC-Al_4C_3 aggregates. The debonding sequence in table 6.1 is an attempt to show which failures occur first ie. at the lowest strains: where large 'flake' Si crystals are present early cleavage of this phase dictates the extent to which other less brittle constituents contribute to the fracture path. Confirmation and quantification of the individual contributing failure paths ('phase fracture' and debondings as in figure 6.7) would be required to support the suggestion that the SiC-Al_4C_3 fractures occur no more than would be expected by chance.

6.3.1.3 *Apparent absence of Al_4C_3- Si/β(FeSi) debonding in test C*

Al_4C_3-Si/β (FeSi) debonding in test C was apparently absent although SiC-Si/ β(FeSi) debonding was observed in test D: one difference between samples C and D was the scale of the Si 'flakes': the flakes were much coarser in test D than in test C. It was therefore more likely that greater individual areas of Si-SiC interface existed in D , and that individual areas of Al_4C_3-Si bonding would be small in comparison (irrespective of basic differences in the interfacial bonding). Further effects would be due to the increased size of the Al_4C_3-SiC aggregates

which may induce them to fracture as opposed to undergoing matrix-Al_4C_3 interface debonding generally.

6.3.2 *Al_4C_3 on fracture paths*

Al_4C_3 was found to play a role in void formation principally via Al-Al_4C_3 and SiC-Al_4C_3 debonding when the Al_4C_3 was in the form of small, discrete plates at the SiC-matrix interface: this phenomenon is suspected to be a critical event responsible for the change in the dominant fracture paths from that of the starting composite used in test A to that of the same material following a limited amount of re-melting induced SiC dissolution. The fracture of SiC particles in test B would introduce sharp cracks to the interface phases, including Al_4C_3, and would induce further fracture or debonding: however, it was impossible for Al_4C_3 plate fracture to be detected in this work. The fracture of Al_4C_3 crystals, prior to the fracture of SiC, which would introduce a sharp crack to the interface with the SiC possibly inducing the SiC to fracture, could be a contributory factor in the fracture process, especially if the cleavage planes of both the interface product and the SiC are aligned. The observation that cracking of the massive Al_4C_3 plates during the polishing of the arc-melt experiment sample in which cracks ran along the Al_4C_3 plates, and not across them (leading to large pieces of the matrix falling out from between interconnected plates), does suggest that the basal planes of the Al_4C_3 are suceptible to cleavage, and that continuous SiC-Al_4C_3 cleavage cracks would contribute to the aggregate failures as a consequence of the commonly observed alignment of basal planes across the SiC-Al_4C_3 interface.

Fracture of the Al_4C_3-SiC aggregates in test C could produce Al_4C_3-Al_4C_3 ,Al_4C_3-SiC and SiC-SiC fractures. As mentioned above, crack initiation in these aggregates would probably result from the presentation of a Si cleavage crack to the Al_4C_3: all the above failure paths appear to be possible (see figure 6.7), though the predominance of any one, or the fracture sequence (table 6.1) has not been established. The extent to which SiC-Al_4C_3 aggregate fracture events contribute to fracture nucleation and the total fracture path in systems without the brittle Si 'flake' constituents (chill-cast or chemically modify the alloy) could be studied. Unrelaxed strains, introduced into the Al_4C_3-SiC aggregates during cooling from the re-melt temperature, the oriented growth of the Al_4C_3 on the SiC (with respect to the alignment or otherwise of cleavage planes in each phase and the type of Al_4C_3-SiC interface predominating), and the irregularity of the interface phase thickness although nearly continuous, would together lead to the aggregate fracture being a complex function of orientation (with respect to the local stress conditions) and re-melt temperature and time. The formation of Al_4C_3-bridged aggregates (ultimately creating networks) can further increase the contribution of the phase to the fracture paths.

6.3.3 *Comparison with the literature*

SiC particle-matrix interface or near-interface failure of the type observed in test A has been observed by several authors [181,182,183,18,23] some of whom did so under conditions of superplasticity [7,184]: processing-produced voids were largely held responsible for the failure mode of the composite in some cases [23,7,184]. SiC particle fracture is accounted for by the existence of 'Griffith flaws' in the SiC [18,185] which leads to a particle size dependence. The types of failure mechanism typically observed in discontinuously reinforced SiC-wrought Al alloy matrix composites have been summarised [186]; however, the literature on the fracture of similar casting alloy based composites is scarce.

Few studies specifically mention the Al_4C_3 interface product with respect to mechanical properties in Al alloy-SiC composites produced by foundry methods, except [38]. In contrast, the Al-graphite literature has established a link between the fracture strength of the composites and the amount of interfacial Al_4C_3 formed during heat treatment [87,88,90,91,187], generally suggesting that a defect is formed at the interface either due to non-uniform dissolution of the fibre or cracking of the interface product: from the general Al-SiC reaction observations in this study the dissolution of the SiC would only superficially deepen pre-existing notches in the SiC particle surfaces, and other mechanisms leading to SiC fracture as discussed above would be more important. Interface product cracking was shown to account for the observations of Baker et al [88]. T.Eturk et al [92] have noted that Al_4C_3 can become detached from the graphite fibre leading to pull-out.

The type of fracture surface appearance exhibited by fracture sample B was observed by Stephens et al [188] for 30micron B_4C particles in an A356 alloy matrix. These authors described void formation and growth around "matrix precipitated particles in the reaction zone at the B_4C/matrix interface" [188]; the interface products included Al_4C_3 and three other compounds.

6.3.4 *Summary*

The fracture results are summarised in table 6.1.

6.4 Further work

1. Al_4C_3 at low levels <0.5vol% could probably be tolerated in many cast alloys used for non-critical applications, although with proper matrix selection and process control the reaction product should not be formed. If Al_4C_3 is to be formed in wrought Al alloys then the corrosion rates, and static corrosion induced cracking behaviour at various Al_4C_3 contents, in different environments and different matrix microstructure conditions should be established.

2. An Al-1wt%Si-12vol%SiC composite system (with the same SiC grit as supplied for the composites studied in the present work) with similar initial workhardening and strength levels

as the Test B condition to initially test the hypothesis that the Al_4C_3 associated interface voids are necessary to induce SiC fracture.

3. TEM study of sub-fracture surface Test B material would be required to confirm whether Al_4C_3 debonding from the matrix occurs generally or only at the fracture surface, and to show the Al_4C_3 plate cleavage planes and whether these are likely to account for SiC particle fractures.

4. In order to provide direct evidence in support of the provisionally proposed fracture mechanism for the failure of sample B, in-situ HVEM tensile experiments would need to be conducted.

5. Whether fractures follow SiC-Al_4C_3 interfaces or not could be investigated by using a fractured sample of re-melted Al-SiC in which both halves of individual SiC-Al_4C_3 aggregates are identified and then subjected to EDS analysis in an analytical SEM in which the Si and Al distribution on the fractured aggregate surface could be simply mapped: low beam accelerating voltage could be used to increase the resolution. Precautions to reduce the amount of fluorescence from the surrounding matrix would probably be necessary on account of the fracture surface topography, combined with the loss of signal if a low accelerating voltage is used eg. bring the EDS detector closer to the sample.

6. The same experiment as above could be more sucessful if a surface technique eg. SAM (Scanning Auger-electron Microscopy) was used in place of a standard SEM.

7. Samples of cast Al-Si alloys containing the 'equiaxed' Al_4C_3 particles could be produced in which fracture at the SiC-Al_4C_3 interface could be more readily observed if it occurs, owing to the simpler SiC-Al_4C_3 aggregates produced in these systems.

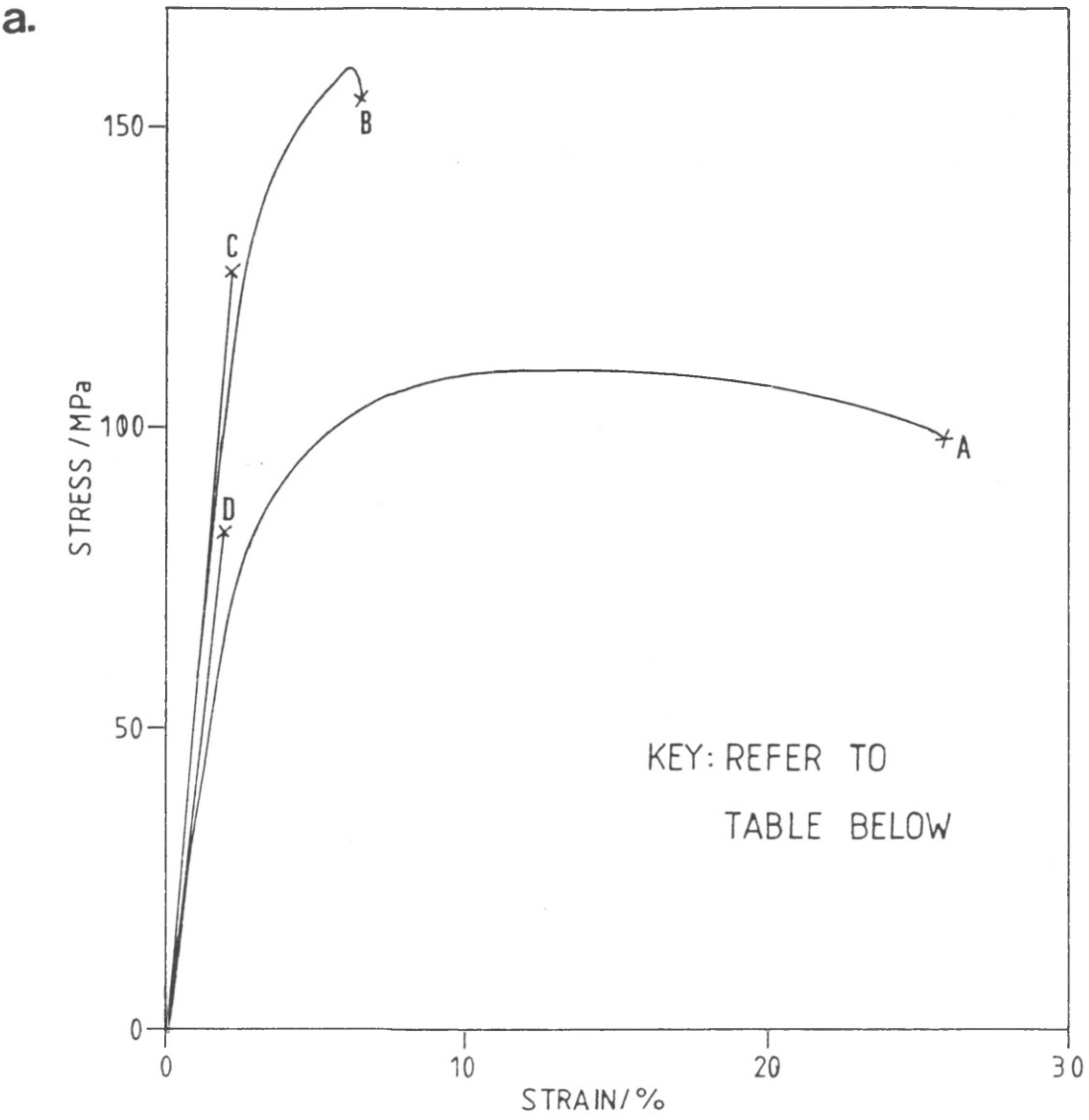
8. By using fracture crack arrest techniques, or stopping a tensile test following a level strain just prior to fracture, samples of heavily reacted, chill-cast and annealed Al-Si-SiC-Al_4C_3 could be examined in an attempt to see where cracks initiate in SiC-Al_4C_3 aggregates in the absence of the 'flake' Si constituent, and to supply complimentary evidence for suggestions 5 and 6.

9. LM13-SiC fractography could be carried out in order to assess the effect of the presence of the SiC particles within the various primary and eutectic phases in cast, HIPped (Hot Isostatic Pressing) and heat-treated conditions: recommendations for closer alloy control for such systems could be made. The influence of SiC particles on thermal fatigue crack growth in such alloys could be investigated.

10. Fracture toughness test specimens could be produced from HIPped (Hot Isostatic Pressing) of cast Al-alloy SiC composites in which Al_4C_3 is produced. Chemical and quantitative microstructural characterisation of the composites could be used to formulate Al-alloy-SiC composite controls.

11. Differences in the intrinsic toughness of various types of SiC particles could be investigated. The usual particle parameters could be used ie. size distribution and volume fraction to produce composites in an Al matrix. Polycrystalline SiC, standard grits, platelets and spheres, if obtainable with comparable powder characteristics, could be tried. SiC powder could be sintered with additives designed to weaken the grain boundaries to provide a source of equiaxed SiC following careful crushing, if a source does not exist commercially. Using a spectrum of matrix strengths, the fracture behaviour of each type of composite could be examined: elimination of variations in the particle distribution that each type of reinforcement may introduce could be achieved by blending the different morphologies in the cases where they can be readily distinguished (for identification and the quantification of fracture events).

a.



b.

TEST	COMPOSITE	CONDITION	10^4 x INITIAL STRAIN RATE $/s^{-1}$	ENGINEERING PEAK STRESS /MPa	ENGINEERING STRAIN TO FAILURE /%
A	MH85-S CP.Al+SiC	AS-SPRAYED+ HOT EXTRUDED	2.7	109	~ 24
B	MH85-S CP.Al+SiC	HEATED TO ~666°C AND AIR COOLED	4.6	160	~ 5
C	MH85-S CP.Al+SiC	190MINS. 800°C AIR COOLED	5.2	126	~ 0
D	200-12 Al-12Si-SiC	190MINS. 800°C AIR COOLED	5.2	83	~ 0

FIG.6.1 Tensile test results.

Figure 6.2

Fractography via light microscopy

The tensile axis for all the specimens shown in this figure was approximately as indicated by the arrow in **6.2a.**
The scale for the micrographs **6.2a-6.2d** inclusive is as indicated in **6.2b**.

a Sample A: hot-extruded CP.Al+12.5vol%SiC (MH85-S). Note the following: the particles and porosity are banded along in the tensile direction; the fracture specimen tapers; and the fracture surface itself appears to be comprised of a tensile region 'T' and a sheared region 'S'.

b Sample B: materials as for sample A but heated to 666^{O}C and air-cooled (AC). Note the following: the elongated porosity and particle bands along the tensile axis; the failure appears to have been predominantly by shear at one end of the gauge length; the apparent increase in the porosity compared to sample A.

c Sample C: material as for sample A but heated to 800^{O}C for 190minutes and AC. The fracture surface is 'flat' at ~90^{O} to tensile axis at the mid-gauge length position. Porosity in the bulk sample is seen to extend radially as well as along the tensile axis.

d Sample D: as-sprayed Al-12Si-SiC (200-12) was heated to 800^{O}C for 190minutes and AC. Extensive porosity in the sample is evident from the micrograph.

e Sample A: as in **a** above. Fracture surface regions parallel to the tensile axis on which exposed SiC particles are visible have been marked on the micrograph: note the high pore density.

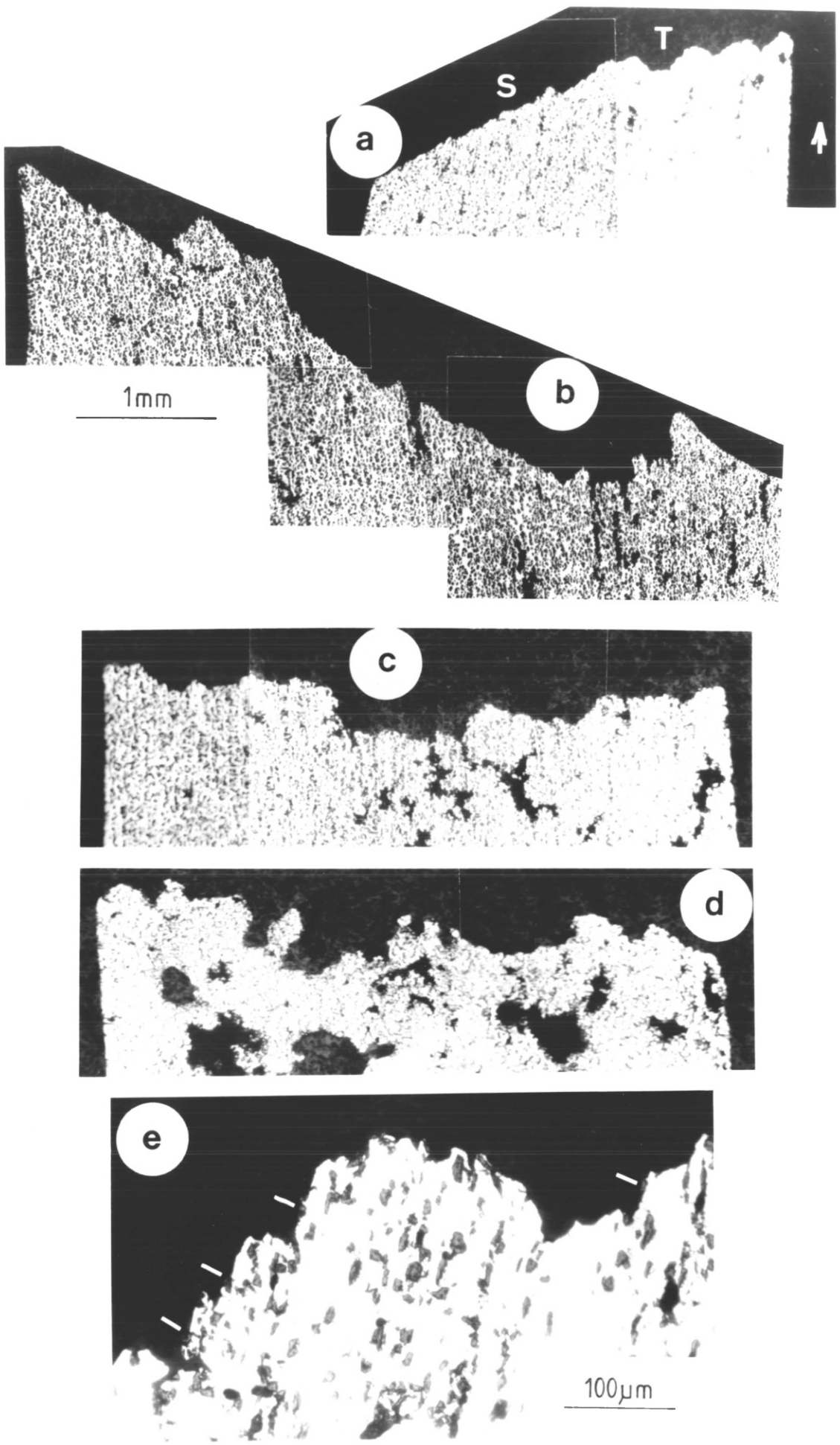

T
S
a
1mm
b
c
d
e
100µm

Figure 6.3

Fractography via light microscopy: transverse sections

a Sample A: rarely observed sub-surface SiC particle fractures at 'A'.

b Sample B: several examples of sub-surface interface failure are shown in the micrograph. Al_4C_3 at 'A' is separated from the parent particle 'P'; fractured SiC with apparent SiC-Al debonding is seen at 'D'. Debris above 'D' suggests that the SiC-Al debonded particle is associated with a band of poorly bonded SiC particles.

c Sample C: sub-surface SiC fractures are arrowed. The micrograph shows less sub-surface damage in the eutectic than was typical. Exposed SiC-Al_4C_3 aggregates on the fracture surface are at the positions indicated by the white markers.

d Sample D: subsurface SiC fractures appear above 'A' and where arrowed. An example of Si 'flake' fracture is at 'B'. The sub-surface damage shown in the micrograph appears to be related to the void on the left hand side which has opened and has promoted failure at 'A' and 'B': the damage extends towards the right of the micrograph. Much of the sub-surface damage in this sample can be related to casting porosity opening under load.

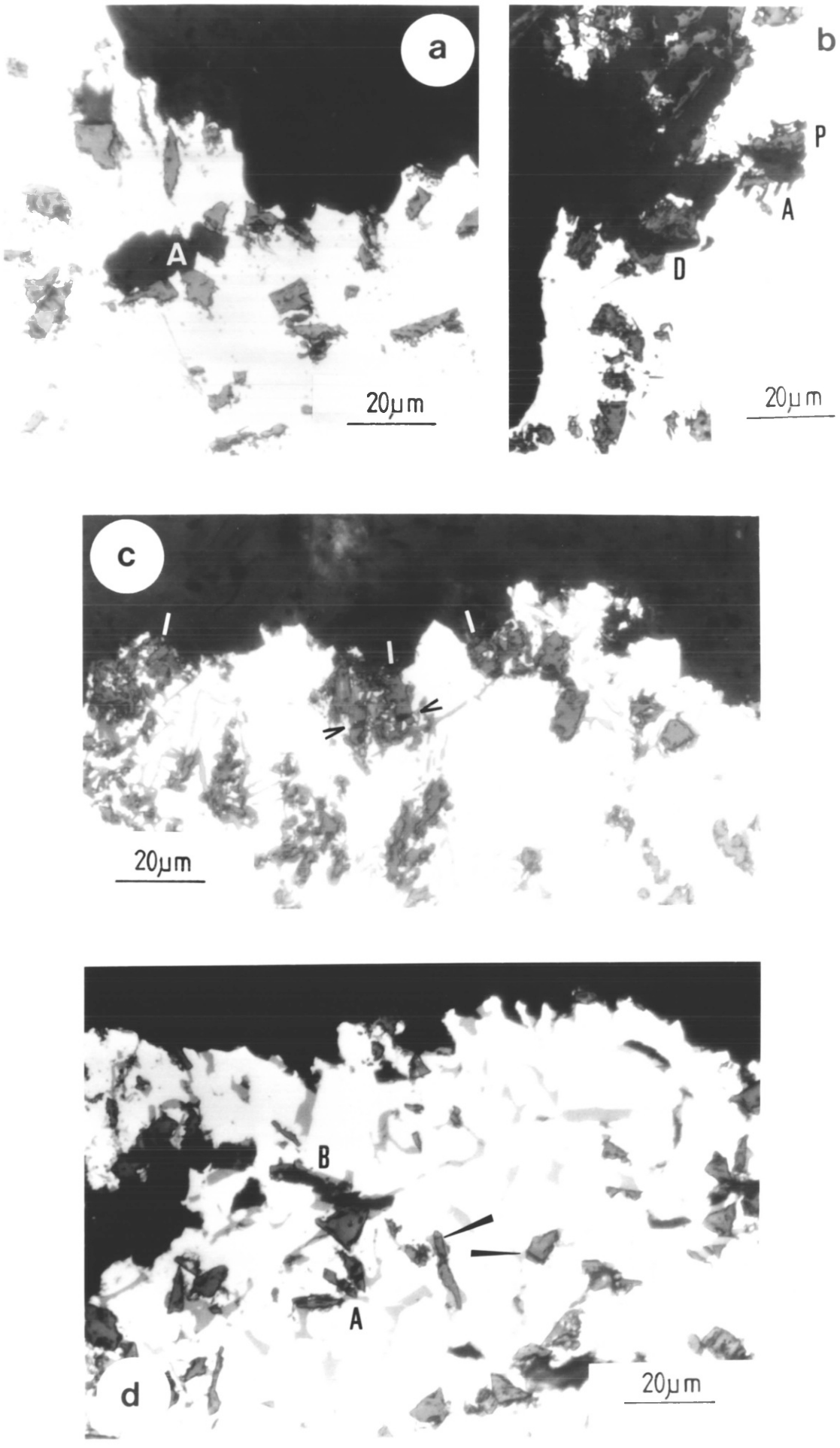

a
A
20μm
b
P
A
D
20μm
c
20μm
B
A
d
20μm

Figure 6.4

SEM of fracture surfaces

Micron bars: the vertical white lines to the right of each micrograph represent 50microns.

a Sample A: tensile failure region. A generally equiaxed dimple morphology is shown, and SiC particles are often seen exposed in the base of the larger dimples.

b Sample B: the micrograph shows shallow dimples in which large amounts of particulate phases can be seen, the large fractured particles corresponding to SiC.

c Sample C: the sample surface is less uniformly rough compared to the preceding samples. The following suggestions are made for the identification of fractured constituents:

'P'- examples of ductile failure of primary Al;

'F'- flat regions of 'flake' Si (appears black);

'V'- examples of fractured Al_4C_3-SiC aggregates at the apices of the 'V's.

d Sample D: generally eutectic Al forms ductile ridges separating 'flake' Si fractures. Large areas of flat 'flake' Si cleavage are seen around points marked 'F' (appears black). Unbonded SiC particles are present on the fracture surface at 'U': generally SiC particles could not be readily distinguished from the other phases on this type of fracture surface.

a
25KU X500 50µm 000004
b
25KU X500 50µm 000045
c
P
F
25KU X500 50µm 000022
d
F
25KU X500 50µm 000045

Figure 6.5

SEM of fracture surfaces

a Sample A: part of the shear surface. Note the occasionally exposed SiC particle on the surface, as above 'A' in the micrograph: the Al appears to be partly pulled away from the SiC particle.

b Sample B: note the high density of flat fractured SiC particles eg. at points marked 'S'. At point 'F' there appears to be the rare appearence of fractured Si. (This sample had been exposed to the atmosphere).

c Sample B: example of fractured SiC particle at 'S' with the surrounding phase, presumably Al_4C_3 as at 'A'. The plate at 'A' appears to have been debonded from the matrix leaving the crystal intact: the bright ridge between 'A' and 'S' suggests that Al was not readily debonded from the SiC. (The sample surface was in a 'freshly' fractured condition).

d Sample D: change in the contrast of the interface constituents compared with **c** above due to atmospheric exposure of the fracture surface. The SiC is situated at 'S', with the surrounding interface phase debonding evident: note that the ligaments remain between the debonded phases. Also, note the flat regions marked 'F' in the surrounding matrix.

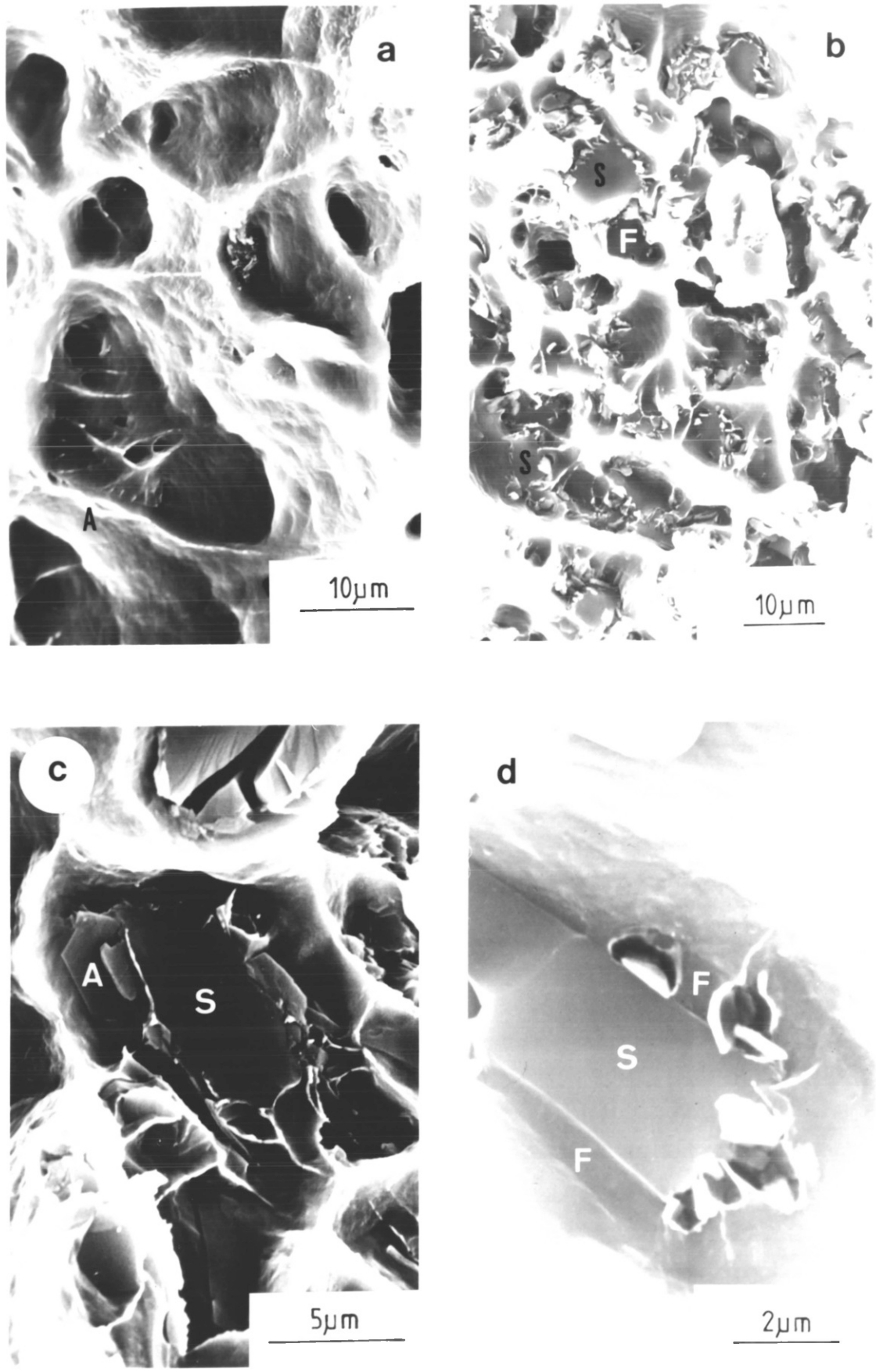

a
A
10µm
b
S
F
S
10µm
c
A
S
5µm
d
F
S
F
2µm

Figure 6.6

SEM of fracture surfaces

Micron bars: the vertical white lines to the right of each micrograph represent 10, 5 ,10 and 10microns for micrographs **a - d** respectively.

a Sample C: examples of fractured SiC at points marked 'S' where the SiC has suffered cleavage and is surrounded by polycrystalline Al_4C_3 and Al. The white arrow points to a SiC-Al_4C_3 fracture. Generally the surface shows fractured Si crystals divided by the bright ridges of the Al phase.

b Sample C: MH87-S re-melted at 800^{o}C for 1000minutes and water quenched. The sample was simply notched and fractured. The surface shows a flat region at 'S' corresponding to SiC, sheathed in Al_4C_3. Tiny, bright ridges amongst the Al_4C_3 suggest that some Al is present eg. immediately above 'S'. Around the 'flat' region is the fine Al-Si eutectic, and dimpled Al. The arrows indicate facets on the Al_4C_3 .

c Sample D: large region of fractured Si flake: it is difficult to identify SiC in this condition by colour/morphology alone.

d Sample D: a more typical region than in **c** above ie. more typical of the fractured regions in a sample composed of large voids. SiC particles are indicated with a white 'X': identification is uncertain however. The white arrow indicates a fractured SiC particle which is apparently detached from the Si but remains bonded to the Al. Generally the surface shows the aligned phases of the 'flake' eutectic Al-Si penetrating the fracture surface at various angles.

a
S
S
20KV X1,500 10µm
b
S
c
25KV X1,500 10µm 000042
d
+
+
+
+
20KV X2,000 10µm 000020

FIGURE 6.7 POTENTIAL AND OBSERVED FAILURE MECHANISMS

TEST A

	VOL% ~87P* Al	~12.5 SiC	<1 AlFeSi
Al (matrix)	F	Ⓓ	D
SiC(particulate)	Ⓓ	Ⓕ	D
AlFeSi(particles)	D	D	F

TEST B

	VOL% ~86P* Al	~12 SiC	~1 Al_4C_3	<1 Si	<1 β(FeSi)
Al (matrix)	F	D	D	D	D
SiC(particulate)	D	F	D	D	D
Al_4C_3 (discrete plates)	D	D	F	D	D
Si (flake)	D	D	D	F	D
β(FeSi) (acicular)	D	D	D	D	F

TEST C

	VOL% ~80# Al	~8 Al_4C_3	~6 SiC	5-6 Si	~1 β(FeSi)	#46-42P* 34-38E*
Al (matrix)	F	D	–	D	D	
Al_4C_3(interface layer)	D	F	D	D	D	
SiC(particulate)	–	D	F	–	–	
Si (flake)	D	D	–	F	D	
β(FeSi) (acicular)	D	D	–	D	F	

TEST D

	VOL% ~73E* Al	~14 SiC	~12 Si	~1 β(FeSi)
Al (matrix)	F	D	D	D
SiC(particulate)	D	F	D	D
Si (flake)	D	D	F	D
β(FeSi) (acicular)	D	D	D	F

KEY:
F = PHASE FRACTURE
D = INTERFACE DEBONDING
– = NO INTERFACES
□ = OBSERVED
○ = " BUT SUSPECTED TO PRE-EXIST
■ = DOMINANT NON-Al FAILURE
⬚ = UNOBSERVED/INSUFFICIENT DATA/DOES NOT OCCUR
P*= PRIMARY Al VOL%
E*= EUTECTIC Al VOL%

FIGURE 6.8 SHEAR CRACK GROWTH

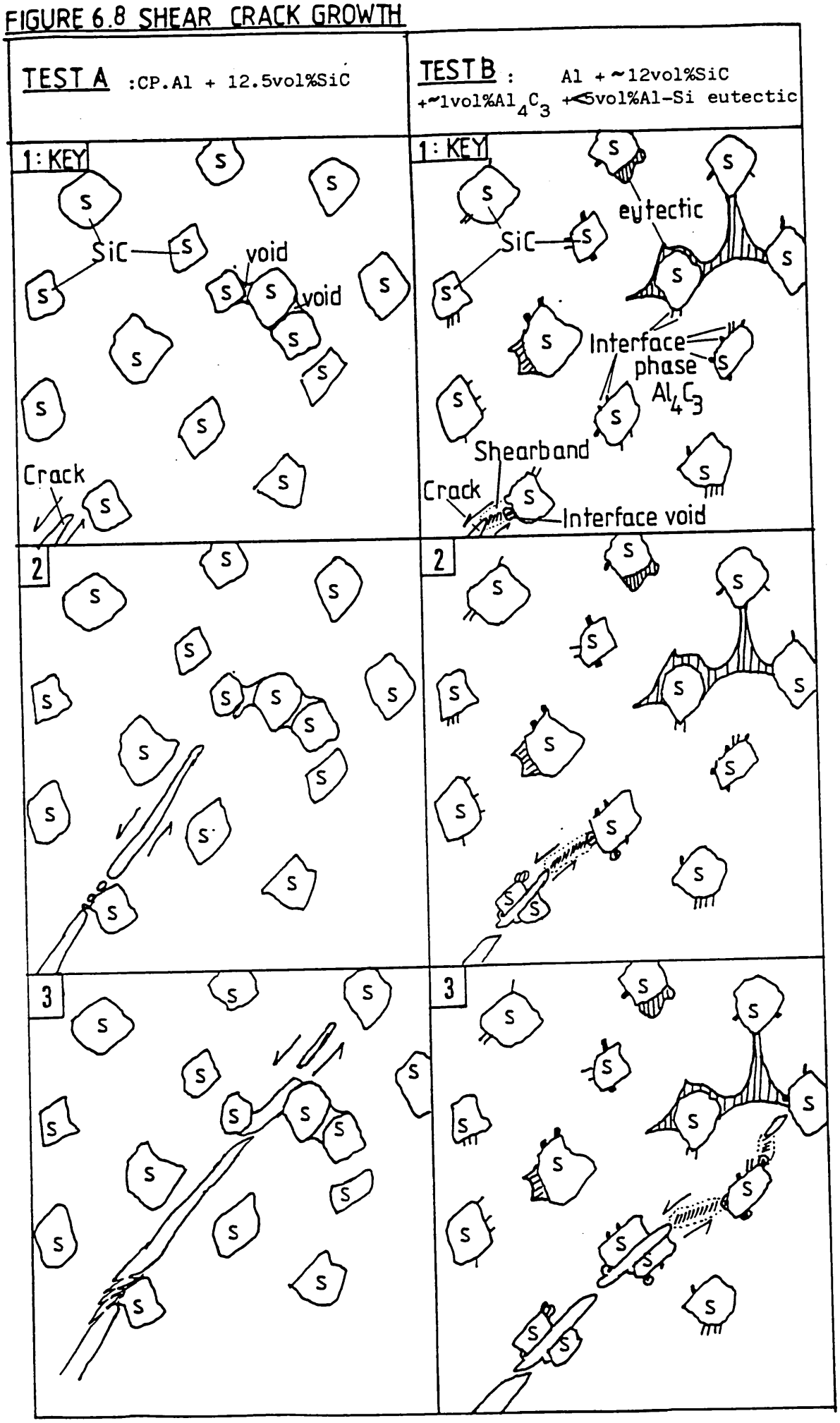


TABLE 6.1 Fractography results summary and proposed dominant mechanisms

TEST	MICROSTUCTURAL CONSTITUENTS	DOMINANT FRACTURE PATH	DEBONDING SEQUENCE: STRAIN | LOW / HIGH ()=ORDER NOT DETERMINED	DOMINANT MECHANISM
A	CP.Al matrix +12.5vol%SiC +porosity +few fractured SiC particles	Al matrix	Al-Al	DUCTILE COALESCENCE OF PRE-EXISTING VOIDS
B	Al(Si SS) +~12vol%SiC + ~1vol%Al_4C_3(discrete plates at SiC-matrix interface) + <5vol%Al-Si 'flake' eutectic +porosity +few fractured SiC particles	Al matrix and SiC-SiC	(Al_4C_3-Al) (Al_4C_3-SiC) SiC-Al SiC-SiC Al-Al	COALESCENCE OF INTERFACE NUCLEATED VOIDS FOLLOWING SiC FRACTURE (PROVISIONAL)
C	Al(Si SS) +~6vol%SiC +~8vol%Al_4C_3(nearly continuous SiC-matrix interface phase) +39-44vol%Al-Si 'flake' eutectic +extensive casting porosity +few fractured SiC particles	Casting porosity linked by fracture through eutectic	Si-Si β(FeSi)-β(FeSi) (SiC-SiC) (Al_4C_3-SiC) (Al_4C_3-Al_4C_3) Al-Al	DUCTILE COALESCENCE OF Si 'FLAKE' CLEAVAGE CRACKS
D	Al-Si 'flake' eutecic +~14vol%SiC + extensive casting porosity	Casting porosity linked by fracture through eutectic	Si-Si β(FeSi)-β(FeSi) (Si-SiC) (SiC-SiC) (β(FeSi)-SiC) Al-Al	DUCTILE COALESCENCE OF Si 'FLAKE' CLEAVAGE CRACKS

β(FeSi)=acicular Al_5FeSi

Chapter VII

Conclusions & references

7.1 Conclusions

Chapter IV

4.1) CP.Al reacts with Acheson process manufactured SiC particles in the temperature range studied, from the CP.Al liquidus ~650^{o}C to 1000^{o}C , resulting in the precipitation of Al_4C_3 at the reaction temperature, and the taking of Si into solution in the melt.

4.2) The Al_4C_3 product resides at the SiC-liquid alloy interface.

4.3) Following the re-melting of CP.Al+10.5-12.5vol%SiC composites, and cooling at practical rates ~0.01^{o}C/s - ~10^4 ^{o}C/s, the composite matrix alloy solidifies as a conventional Al-Si based alloy (the Si being produced in the reaction during re-melting) would do under the same conditions.

4.4) Neither SiC or Al_4C_3 support the nucleation of primary Al under the cooling conditions given in 4.3) above.

4.5) Both SiC particles, and Al_4C_3 covered SiC particles, are 'pushed' ahead of growing primary Al dendrites during solidification in the range of cooling rates as given in 4.3) above.

4.6) Al_4C_3 nucleation occurs epitaxially at the SiC - liquid aluminium interface, and initially results in discrete Al_4C_3 crystals.

4.7) The most common, simple Al_4C_3-alpha SiC epitaxial relationship is:
{10.0} Al_4C_3 // {10.0} alpha SiC
{00.1} Al_4C_3 // {00.1} alpha SiC
{11.0} Al_4C_3 // {11.0} alpha SiC.

4.8) Misorientations (at least up to ~7^{o} relative rotation about a <11.0> direction) away from the orientation relationship in 4.7) above are very frequently observed.

4.9) Some Al_4C_3-Al_4C_3 nucleation also occurs giving rise to orientation relationships between the Al_4C_3 crystals.

4.10) SiC surfaces which act as the preferred Al_4C_3 nucleation sites are identified with the tips of SiC asperities: the asperities are produced during the intragranular fracture of the SiC during the crushing process to produce the SiC particulate.

4.11) Any SiC surface which has been created by the same fracture process as at the tip of an asperity also acts as a site of preferred nucleation: the fracture process involves a fracture path running across a macroscopically defined SiC surface, especially macroscopically defined {10.0} planes, that are as far as possible from any of the main cleavage surfaces observed ie. actual {11.0} and {00.1} planes.

4.12) Extended areas of any SiC cleavage surface eg. {00.1} and {11.0} (not exclusively) do not support Al_4C_3 nucleation, and are resistant to coverage by Al_4C_3 crystals growing from adjacent parts of the same SiC crystal surface.

4.13) The Al_4C_3 crystals have a plate-like morphology exhibiting large, pinacoidal, basal facets.

4.14) As a consequence of 4.7), 4.8) and 4.13) the Al_4C_3 initially generally undergoes rapid growth into the melt away from the SiC surface, due to crystal anisotropy, until low index facets are established generally on the Al_4C_3 crystal.

4.15) Following the establishment of population of Al_4C_3 crystals at the SiC-liquid interface, deep channels through the Al_4C_3 interface product can still remain allowing SiC-liquid contact.

4.16) When the SiC interface is covered in Al_4C_3 crystals voids are found within the polycrystalline interfacial Al_4C_3 product, and at the SiC-Al_4C_3 interface when the interface is examined at room temperature.

4.17) The reaction tends to create SiC facets at the SiC-Al_4C_3 interface.

4.18) The reaction in CP.Al-SiC composites between an initially CP.Al liquid and 10.5 - 12.5vol%SiC particulate by which Si and Al_4C_3 are formed, there are at least three stages in the temperature range 672^{o}C to 800^{o}C:

i) an initially rapid stage with an activation energy of 260+/- 42kJ/mol;

ii) a slower stage where the activation energy increases from 270kJ/mol up to ~570 - 900kJ/mol;

iii) a very slow stage where either the overall reaction has saturated or the activation energy of the continuing reaction is>=570 -900kJ/mol.

4.19) The first stage of the reaction in 4.18) i) is SiC dissolution controlled, the SiC being in direct contact with the melt; the second stage in 4.18) ii) involves an increasing proportion of the SiC dissociation products undergoing a solid-state diffusion step, with direct SiC dissolution into the melt taking place proportionately less; the third stage 4.18) iii) involves all the dissociation products undergoing a solid-state diffusion step in the course of the continuing reaction.

4.20) The epitaxial nucleation, and initial growth of the Al_4C_3 crystals at the interface is the dominant feature of the first stage of the reaction 4.18) i) : the nucleation sites in 4.10) and 4.11) are correlated with areas of the SiC surface assumed to have a high dissolution rate per unit area.

4.21) Sites that do not support nucleation 4.12) are correlated with areas of the SiC surface assumed to have a low dissolution rate per unit area.

4.22) The transition from the kinetics of the first to the second stage of the reaction, as in 4.18) i) and ii), can be correlated with nucleation site saturation.

4.23) The second stage of the reaction 4.18) ii) is dominated by the remaining lateral growth of the Al_4C_3 product ie. growth in directions parallel to the SiC surface: this process leads to the gradual separation of the dissolving SiC from the liquid Al alloys, blocking the last of the direct SiC-liquid alloy dissolution sites.

4.25) The final stage of the reaction, 4.18) iii), in which the SiC is completely separated from the melt by the polycrystalline Al_4C_3 interface product: 'stable' Al alloy liquid-SiC facets are present at the beginning of this stage.

4.26) The reaction 4.18) at 672^{o}C for 10 000minutes does not reach the third stage of the reaction, and there is insufficient evidence to say whether the overall reaction has saturated or not at this condition.

4.27) The Si content of Al in commercial purity based Al-Si binary alloys determined using three methods: i) quantitative metallography; ii) EDS with appropriate cast alloy standards; and iii) melting point changes from DTA (with a 20^{o}C/min heating rate) using the binary equilibrium Al-Si liquidus gradient as a calibration, taking both impurities, and the changing proportions of primary Al and Al-Si eutectic, into account. Close agreement in the results from the three methods shows that they can be used with some confidence in the systems studied for Si contents below ~9at%Si at least, and typically within an error of +/-1at%Si. The DTA method used with a heating rate ~3^{o}C/min could potentially produce more reliable Si content results.

4.28) The change in the DTA peak temperature as the extent of reaction increases can be used to follow the kinetics of the reaction between liquid Al and SiC, and meaningful activation energies derived when the data is analysed by the 'time to a given extent of reaction' method.

Chapter V

5.1) Microstructures produced by splat quenching Al-Si-SiC composite and annealing for one minute at, or near to, the matrix solidus (~575^{o}C+/-3^{o}C) temperature, are very similar to those microstructures produced by the spray co-deposition process used to manufacture the composite.

5.2) The spheroidal eutectic Si in the spray cast Al-19Si-SiC composite consists of Si crystal aggregates showing coarse twinning on {111} planes; the primary Si spheroids in the same material are composed of coarse, twin-related Si crystals radiating from a point, the twin boundaries are again {111} planes.

5.3) SiC-melt interfaces, in an Al-Si-SiC composite with an hypereutectic Al-Si matrix alloy, can behave effectively as primary Si nucleation sites when the composite is cooled through the matrix solidification range at ~10^{3} ^{o}C/s - ~10^{5} ^{o}C/s.

5.4) At low cooling rates (<~10^{3} ^{o}C/s) the lower numbers of non-SiC inclusions appear to behave as more potent nucleation sites for primary Si.

5.5) A small volume fraction of the particulate material reacts prematurely, from ~915^{o}C with the LM13 alloy melt, and from ~940^{o}C in the Al-12wt%Si melt, producing a reaction product resembling Al_4C_3, in its morphology and colour, when examined by light microscopy.

5.6) The Al_4C_3 formed in the re-melted Al-Si-SiC composites can exhibit the same type of epitaxial relationship with the SiC as in the re-melted CP.Al-SiC composites.

5.7) The growth of Al_4C_3, nucleated in Al-Si-SiC composites containing ~10-13wt%Si at temperatures above 915^{o}C, leads to a different Al_4C_3 morphology (blocky hexagonal prisms) compared with that produced when SiC dissolves in CP.Al (hexagonal plates). This effect is suggested to be due to the greater increase in the growth rate of the product crystals with temperature compared with the increase in the nucleation rate over the same temperature range. A consequence of this increase in the growth rate is the greater involvement of a dislocation influenced crystal growth mechanism in the determination of the ultimate shape of the Al_4C_3 product crystals.

5.8) The nucleation of the Al_4C_3 in the Al-Si-SiC composites studied appeared to occur at the same type of SiC-liquid alloy interface sites as in the CP.Al-SiC composites.

5.9) From the metallography of cast composites, both the primary and eutectic Al are seen to reject SiC particles: any of the phases in the Al alloy systems studied tend to wet the SiC in order to reduce the total Al-SiC interface area which appears to be directly linked by the tendency of all these phases to facet in the Al melt. It is further suggested that thermodynamic effects in this system will far outweigh the kinetic factors invoked to account for 'particle pushing' (and particle capture), and that solidifying Al will not wet SiC suspended in the melt.

5.10) The common intermetallic phase $Al_{15}(FeMn)_3Si_2$ found in Al alloys can exhibit the following orientation relationship with SiC :
$<41\bar{2}>$ int. //<11.0> alpha SiC;
<021> int. //<00.1> alpha SiC;
$<\bar{3}2\bar{5}>$ int. //<10.0> alpha SiC.

5.11) Large amounts of an unidentified intermetallic phase is found in LM13 with a composition of approximately 70at%Al, 15at%Ni, 6at%Si, 5at%Fe, 2at%Cu, 1at%Mn and 1at%Mg.

Chapter VI

6.1) The as-supplied hot-extruded CP.Al-12.5vol.%SiC composite fractured by the ductile coalescence of pre-existing voids during a tensile test. SiC fractures were rare.

6.2) A low volume fraction of Al_4C_3 ($\tilde{}$1vol.%Al_4C_3) formed in the CP.Al-12.5vol.%SiC composite during re-melting can induce voids to form at the SiC-matrix interface, during tensile testing, as a result of both Al_4C_3 debonding from its parent SiC, and Al_4C_3 at the SiC-matrix interface debonding from the Al matrix.

6.3) When CP.Al-12.5vol.%SiC is re-melted to produce $\tilde{}$1vol.%Al_4C_3 the fracture path goes through the SiC particles

6.4) When CP.Al-12.5vol.%SiC is re-melted to produce $\tilde{}$8vol.%Al_4C_3, and air-cooled, during tensile testing some SiC-Al_4C_3 debonding can occur, though there is no evidence that the SiC-Al_4C_3 aggregates fracture preferentially when surrounded by the coarse Ai-Si eutectic.

6.5) When a re-melted, and air-cooled, Al-12wt%Si-14vol.%SiC composite is fractured in a tensile test the fracture path tends to go through the Si in the eutectic.

6.6) Si-SiC interface, and Al_5FeSi-SiC interface debonding events can occur when a re-melted, and air-cooled, Al-12wt%Si-14vol.%SiC composite is fractured in a tensile test.

7.2 References

1 **E.A.Feest** : Metals and Materials, Vol.4, No.5, May 1988, 273-278

2 **D.Charles**: Metals and Materials, Vol.6, No.2, February 1990, 78-82

3 **R.S.Ravichandran and E.S.Dwarakadasa**: Journal of Metals. May 1987 pp28-32

4 **A.P.Divecha, S.G.Fishman and S.D.Karmarkar**: Journal of Metals Sept 1981 pp12-17

5 **S.V.Nair, J.K.Tien and R.C.Bates**: International Metals Reviews Vol.30 No.6 (1985) pp275-290

6 **Y.Flom and R.J.Arsenault**: Journal of Metals, July ,1986 pp31-34

7 **M.W.Mahoney and A.K.Ghosh**: Metallurgical Transactions A, Vol.18A April 1987 pp653-661

8 **J.R.Pickens T.J.Langan, R.O.England and M.Liebson** : Metallurgical Transactions A, Vol.18A, February 1987 pp303-312

9 **J.White, I.R.Hughes, T.C.Willis and R.M.Jordan**: 4th International Aluminium Lithium Conference, Paris, June 10-12, 1987 p.C3-347

10 **S.G.Fishman and A.K.Dhingra** in :'Cast Metal Reinforced Metal Composites'. Proc. Int. Symp. on Advances in Cast Reinforced Metal Composites, 1988. Edited by S.G.Fishman and A.K.Dhingra. ASM International. Preface p.v

11 **P.K.Rohatgi, R.Asthana, and S.Das**: International Metals Reviews Vol.31 No.3 (1986) 115-139

12 **P.K.Rohatgi** in :'Interfaces in Metal Matrix Composites, Proceedings of a Symposium sponsored by the AIME-American Society of Metals Composite Committee, held at the Annual Meeting of the Metallurgical Society in New Orleans, Louisiana, March 2-6, 1986. Ed. A.K.Dhingra and S.G.Fishman. The Metallurgical Society Inc . p.185

13 **P.Chesney** : Metals and Materials,Vol.6 ,No.6 ,June 1990 ,373-376

14 **A.R.E.Singer and S.Ozbek**: Powder Metallurgy Vol28.No.2 (1985) 72-78

15 **A.Kelly**: as ref.10, pp1-5

16 **D.Webster**: Metallurgical Transactions A, Vol.13, August 1982 pp1511-1519

17 **J-K .Shang and R.O.Ritchie**: Acta Metallurgica Vol.37 No.8 (1989) pp2267-2278

18 **Y.Flom and R.J.Arsenault** in :Proceedings of the Sixth International Conference on Composite Materials ICCM VI, and the Second European Conference on Composite Materials ECCM 2, held at Imperial College, London, UK, 20-24 July 1987. Edited by F.L.Matthews et al. Vol.2 pp189-198

19 **S.R.Nutt**: as ref.12, p157

20 **T.Kobayashi, M.Yoshino, H.Iwanari, M.Niinomi and K.Yamamoto**: as ref.10, pp205-210

21 **E.Jong**: Imperial College. Unpublished work.

22 **V.C.Nardone**: Scripta Metallurgica Vol.21 (1987) 1313-1318

23 **Y.Flom and R.J.Arsenault**: Materials Science and Engineering, Vol.77,1986,pp191-197

24 **R.J.Arsenault and N.Shi**: Ibid., Vol.81, 1986, pp175-187

25 **Y.Flom and R.J.Arsenault:** Ibid.,Vol.75, 1985, pp.151-167

26 **R.J.Arsenault:** Ibid.,Vol.64,1984, pp.171-181

27 **M.Vogelsang, R.J.Arsenault and R.M.Fisher** : Metallurgical Transactions A, Vol.17A, March 1986,pp.379-389

28 **M.Taya and T.Mori:** Acta Metallurgica, Vol.35, No.1 1987,pp155-162

29 **R.J.Arsenault and R.M.Fisher:** Scripta Metallurgica, Vol.17, 1983, pp67-71

30 **M.Taya and R.J.Arsenault:** Ibid., Vol.21, 1987, pp349-354

31 **B.Derby and J.R.Walker:** Scripta Metallurgica Vol.22 (1988) pp529-532

32 **F.J.Humphreys:** 9th RISO Int. Symp. on Metallurgy and Materials Science: Mechanical and Physical Behaviour of Metallic and Ceramic Matrix Composites. 5-9 Sept. 1988 . pp51-74

33 **T.G.Nieh and R.F.Karlak:** Scripta Metallurgica, Vol.18,1984, pp.25-28

34 **M.A.Bayoumi and M.Suery:** as ref.18, Vol.2 pp 481-490

35 **T.Christman an S.Suresh:** Brown University Report No. NSF-ENG-8451092/1/87 June,1987

36 **M.Skibo, P.L.Morris and D.J.Lloyd** : as ref.10, pp257-261

37 **R.B.Bhagat, M.F.Amateau and E.C.Smith:** as ref.10, pp399-407

38 **D.J.Lloyd, H.Lagace, A.McLeod and P.L.Morris** : Materials Science and Engineering, A107 (1989) pp73 - 80

39 **Encyclopedia of Materials Science and Engineering.** Vol.6. Ed. M.B.Bever, Pergamon Press Ltd. 1986. pp4403-4406

40 **R.W .Olesinski and G.J.Abbaschian** : Bulletin of Alloy Phase Diagrams. Vol.5, No.5 (1984) 486 - 489

41 **N.N.Ault and R.G.Robertson:** Ceramic Bulletin, Vol.65, No.5, 1986, pp.741-742

42 **L.A.Lay:** The Corrosion Resistance of Technical Ceramics, NPL, HMSO, 1983

43 **Arrigo Addamiano** in: 'Silicon Carbide 1973' Proceedings of the Third International Conference on Silicon Carbide held at Miami Beach, Florida, on 17-20 September 1973. Edited by R.C.Marshall, J.W.Faust and C.E.Ryan. University of South Carolina Press, Columbia, South Carolina. 1974. pp 179-183

44 **U.S.Ram, M.Dubey and G.Singh** : Ibid. pp184-190

45 **Y.Tung and J.W.Faust Jr.** : Ibid. pp254-258

46 **J.Ruska, L.I.Gaulkler, J.Lorenz and H.U.Rexer** : Journal of Materials Science, Vol.14 (1979) 2013 - 2017

47 **Z.Inoue, H.Komatsu, H.Tanaka and Y.Inomata** : as ref.43 'SiC 1973' p.191

48 **S.Shinozaki and K.R.Kinsman:** Acta Metallurgica, Vol.26, pp.769 - 776

49 **H.Sato, S.Shinozaki and M.Yessik:** as ref.43 'SiC 1973' pp.230-237

50 **I.Tanaka, Y.Inomata, K.Hara and H.Hasegawa:** Journal of Materials Science Letters, Vol.4, 1985 pp315-317

51 **M.Lancin, F.Anxionnaz, J.Thibault-Desseaux, D.Stutz and P.Griel** : Journal of Materials Science, Vol.22 (1987) 1150 - 1156

52 **T.Sakai, H.Watanabe and T.Aikawa** : Journal of Materials Science Letters, Vol.6, 1987, pp.865-866

53 **C-H.Andersson and R.Warren**: Composites. Vol.15. No.1 January 1984 16-24

54 **D.Pandey and P.Krishna**: as ref.43 'SiC 1973' pp.198-205

55 **Yo Tajima and W.D.Kingery**: Communications of the American Ceramic Society, Feb (1982) C-27 - C-29

56 **J-C.Viala, P.Fortier, B.Bonnetot and J.Bouix**: Materials Research Bulletin Vol.21 (1986) 387-394

57 **J.C.Viala, F.Bosselet, P.Fortier and J.Bouix** : as ref.18. ICCM6 - ECCM2 Vol.2 p147-155

58 **M.Cauchetier, O.Croix and M.Luce**: Advanced Ceramic Materials Vol.3 No.6 (1988) 548- 552

59 **Z.Li and R.C.Bradt** : Journal of Materials Science Vol.21 (1986) pp4366-4368

60 **J.L.Murray and A.J.McAlister** : Bulletin of Alloy Phase Diagrams, Vol.5,No.1 (1984) 74-84

61 **L.M.Hogan and M.Shamsuzzoha**: Materials Forum Vol.10 No.4 (1987) 270-277

62 **R.Elliott** : International Metals Reviews, September 1977. p161-

63 **M.G. Day and A. Hellawell**: Proceedings of the Royal Society A305 (1968) 473-

64 **H.A.H. Steen and A.Hellawell** : Acta Metallurgica, Vol.20 March 1972 pp363-370

65 **H.Fredriksson, M.Hillert and N.Lange**: Journal of the Institute of Metals Vol.101 (1973) 285-299

66 **S.C.Flood and J.D.Hunt**: Metal Science Vol.15 July 1981 287-294

67 **K.F.Kobayashi and L.M.Hogan** : Journal of Materials Science, Vol.20 (1985) 1961-1965

68 **L.Clapham and R.W.Smith**: Acta Metallurgica Vol.37 No.1 (1989) 303-311

69 **T.A.Chernyshova and L.I.Kobeleva**: Journal of Materials Science Vol.20 (1985) 3524-3528

70 **L.F.Mondolfo** :' Aluminium : Structure and Properties'. Butterworths, 1976, pp351-352

71 **L.Kaufman and H.Nesor**: CALPHAD Vol.2 No.4 (1978) p298

72 **L.L.Oden and R.A.McCune**: Metallurgical Transactions A, Vol.18A, December 1987, 2005-2014

73 **J-C. Viala, P.Fortier, C.Bernard and J.Bouix** in : Proceedings of the First European Conference on Composite Materials, Bordeaux, France, 1985, pp583-588

74 **Metals Handbook**, 8th Edition Vol.8 ASM Metals Park Ohio 1973,p.341

75 **L.F.Mondolfo**: ' Aluminium : Structure and Properties'. Butterworths, 1976, p.61

76 **K.Grjotheim et al**: Metals Abstract 7703 420172

77 **'The Chemical Elements and Their Compounds'**: Ed. N.V.Sidgwick. Vol.1. OUP 1962 pp.413-414

78 **M.V.Stackelberg and E.Schnorrenberg** : Z.Phys.Chem., B27.37, pp37 - 49

79 **T.Iseki, T.Kameda and T.Maruyama**: Journal of Materials Science Letters, Vol.2 (1983) 675-676

80 **'Structural Inorganic Chemistry'**: Ed. A.F.Wells. 3rd Edition. OUP .1962 pp760-764

81 **'Advanced Inorganic Chemistry'**: Eds.F.A.Cotton and G.Wilkinson, 5th Edition,1988, John Wiley and Sons. pp.239-240

82 **W.H.Pfeifer** in: 'Hybrid and Select Metal Matrix Composites'. A State-of-the-Art Review Ed. W.J.Renton. American Institute of Aeronautics and Astronautics. N.Y.1977 pp232-252

83 **T.Otani, B.McEnaney and V.D.Scott** : as ref 10, p383

84 **R.B.Bhagat et al.** : as ref.10, pp185-194

85 **G.A.J.Hack**: Metals and Materials Vol.3, No.8 p.457

86 **G.Jangg et al.**: Metals Abstract 7709 140386

87 **I.H.Khan**: Metallurgical Transactions A, Vol.7A Sept 1976, 1281-1289

88 **S.J.Baker and W.Bonfield**: Journal of Materials Science, Vol.13 1978 pp1329-1334

89 **C-H. Andersson and R.Warren**: Composites. Vol.15. No.2. April 1984 101-111

90 **Shojiro Ochiai, Kozo Osamura and Yotaro Murakami**: Z.Mettallkde, Bd.74 (1983) H.2 pp68-73

91 **Shojiro Ochiai and Kozo Osamura**: Metallurgical Transactions A, Vol.18A April 1987 pp673-679

92 **T.Eturk, J.A.Cornie and R.G.Dixon**: as ref.18. ICCM6-ECCM2 (1987) Vol.2 pp156-168

93 **S.R.Nutt and F.E.Wawner**: Journal of Materials Science Vol.20 (1985) 1953-1960

94 **J.C.Viala, P.Fortier and J.Bouix**: Journal of Materials Science Vol 25 (1990) 1842-1850

95 **G.Schneider, L.J.Gauckler, G.Petzow and A.Zangvil**: Journal of the American Ceramic Society Vol.62 No.11-12. (1979) pp574-576

96 **R.G.Behrens and G.H.Rinehart**: Journal of the American Ceramic Society Vol.67 No.8. (1984) pp575-578

97 **B.L.Kidwell, L.L.Oden and R.A.M^{c}Cune**: Journal of Applied Crystallography, Vol.17, 1984, pp481-482

98 **Z.Inoue, Y.Inomata, H.Tanaka and H.Kawabata**: Journal of Materials Science, Vol.15 1980, pp255-256

99 **K.I.Portnoy, V.I.Bogdanov, A.V.Mikhaylov and D.L.Fuks**: Phys.Met.Metall. Vol.50, No.2, (1980) pp182-185

100 **K.I.Portnoi, V.I.Bogdanov, A.V.Mikhailov and D.L.Fuks**: Dokl. Akad. Nauk. SSSR. 240, (1978) 1154-1156

101 **S.K.Lilov**: Crystal Research and Technology Vol.17 No.6. (1982) 783-786

102 **R.J.Arsenault and C.S.Pande**: Scripta Metallurgica, Vol.18, No.10 (1984) 1131-1134

103 **Y.A.Vodakov and E.N.Mokhov** : as ref. 43, 'SiC 1973' pp.508-519

104 **T.Iseki, T.Kameda and T.Maruyama**: Journal of Materials Science Vol.19 (1984) pp1692-1698

105 **K.Kannikeswaran and R.Y.Lin**: Journal of Metals September 1987 17-19

106 **D.J.Lloyd and E.W.Dewing** in: Proceedings of the International Symposium on Advanced Structural Materials, Montreal, Canada, August 28 - 31, 1988; Edited by D.S.Wilkinson. Pergamon Press 1989 . pp 71 - 76.

107 **D.J.Lloyd and I.Jin** : ALCAN International , Kingston Research and Development Centre, Internal Report 20.11.87

108 **D.J.Lloyd and I.Jin** : Metallurgical Transactions A, Vol.19A, (1988) 3107 - 3109

109 **T.Choh and T.Oki**: Materials Science and Technology Vol.3 May (1987) 378-385

110 **I.J.McColm** : Ceramic Science for Materials Technologists, Leonard Hill 1983

111 **M.N.Rahaman, Y. Bolteaux and L.C.de Jonghe**: American Ceramic Society Bulletin, Vol.65 No.8 (1986) pp1171-1176

112 **M.N.Rahaman and L.C.de Jonghe**: American Ceramic Society Bulletin Vol.66 No.5 (1987) pp782-785

113 **F.Delannay, L.Froyen, A.Deruyttere**: Journal of Materials Science Vol.22, 1987 pp1-16

114 **K.G.Kreider and K.M.Prewo** in : 'Composite Materials Vol.4: Metallic Matrix Composites', Edited by K.G.Kreider, Academic Press, N.Y., London 1974 p412

115 **V.M.Bermudez**: Applied Physics Letters, Vol.42 No.1. 1st January (1983)pp70-72

116 **V.M.Bermudez**: Journal of Applied Physics ,Vol.63 No.10. 15th May (1988) pp4951-4959

117 **K. Yoshii, S.Inoue, S.Inami and H.Kawabe**: Journal of Materials Science Vol.24 (1989) pp3096-3100

118 **S.Li, R.J.Arsenault and P.Jena**: as ref.10. pp.33-37

119 **S.R.Nutt and R.W.Carpenter**: Materials Science and Engineering, Vol.75 (1985) 169-177

120 **L.D.Brown, B.Maruyama, Y.M.Cheong, L.K.Rabenberg and H.L.Marcus** in: 'Composite Interfaces', Proceedings of the 1st International Conference on Composite Interfaces (ICCI-1) held May 27-30, 1986 in Cleveland, Ohio, USA. edited by H.Ishida, and J.L.Koenig. Elsevier Science Publishing Co. 1986. pp. 27-35

121 **C.Marumo and J.A.Pask** : Journal of Materials Science Vol.12 (1977) 223-233

122 **L.M Dignard-Bailey, T.F.Malis, J.D.Boyd and J.D.Embury** : as ref. 106. pp 87 - 95.

123 **M.Nathan**: Journal of Materials Science Letters Vol.8 (1989) pp.311-314

124 **K.C.Russell, J.A.Cornie, and S-Y. Oh** : as ref .12, pp 61-91

125 **V.Laurent, D.Chatain, N.Eustaphopoulos**: Journal of Materials Science Vol.22, 1987 244-250

126 **J.A.Pask and A.P.Tomsia** in:' Surfaces and Interfaces in Ceramic and Ceramic-Metal Systems', Materials Science Research. Vol 14. Ed. J.Pask and A.Evans. Plenum Press 1981.pp411-419

127 **A.R.Kieffer, W.H.Wruss, A.F.Vendl and R.M.Hubatschek**: as ref.43, 'SiC 1973' pp. 375-385

128 **P.Wynblatt and R.C.McCune**: as ref.126, pp83-95

129 **V.Laurent, D.Chatain, N.Eustaphopoulos and X.Dumant**: as ref.10, pp27-31

130 **T.Choh, R.Kammel and T.Oki**: Z.Metallkde. Bd.78 (1987) H.4 pp286-290

131 **M.G.McKimpson and T.E.Scott**: Materials Science and Engineering A107, (1989) 93-106

132 **Z.Zhu** : as ref.10, pp93-99

133 **D.J.Lloyd and B.Chamberlain:** as ref.10, pp263-269

134 **M.A.Bayoumi and M.Suery:** as ref.18, ICCM6 - ECCM2 Vol.2 (1987) pp480-490

135 **T.Z.Kattamis and J.A.Cornie:** as ref.10, pp47-51

136 **M.A.Bayoumi and M.Suery:** as ref.10, pp167-172

137 **J.P.Rocher, J.M.Quenisset and R.Naslain:** Journal of Materials Science Vol.24 (1989) 2697-2703

138 **J.W.McCoy, F.E.Wawner:** as ref.10, pp237-242

139 **P.K.Rohatgi, F.M.Yarandi and Y.Liu:** as ref.10, pp249-255

140 **R.Sasikumar, T.R.Ramamohan and B.C.Pai:** Acta Metallurgica Vol.37 No.7 (1989) 2085-2091

141 **W.C.Moshier, J.S.Ahearn and D.C.Cooke:** Journal of Materials Science, Vol.22, 1987 pp115-122

142 **S.Das, S.V.Prasad, T.K.Dan and P.K.Rohatgi** : as ref.10, pp243-248

143 **R.W.Evans, A.G.Leatham, and R.G.Brooks:** Powder Metallurgy Vol28. No.2 (1985) 13-20

144 **T.C.Willis:** Metals and Materials, August 1988 485-488

145 **D.Apelian and G.Gillan:** Journal of Metals December 1986 p44

146 **P.Mathur, D.Apelian and A.Lawley:** Acta Metallurgica, Vol 37 No.2 (1989) 429-443

147 **'Woldmans' Engineering Alloys'**, 6th Edition, Ed. R.C.Gibbons, ASM,Metals Park, Ohio

148 **British Standard BS.1490** (with latest ammemdments) 1970

149 **ALCAN Enfield Alloys Ltd.:** laboratory test certificate dated 20 Jan 1986

150 **M.Almas** : PhD thesis, Imperial College, London 1989, p44 and p47

151 **B.Kujur, A.K.Ray, C.B.Raju and M.Patel:** Journal of Materials Science, Vol.22 (1987) 962-964

152 **A.Blazek:**' Thermal Analysis', Van Nostrand Reinhold Company Ltd.,1973, pp75-164

153 **P.B.Hirsch, A.Howie, R.B.Nicholson, D.W.Pashley and J.Whelan** :'Electron Microscopy of Thin Crystals', Butterworths. London 1965. pp160 - 161

154 **Alison Kent** : Part 2 Thesis, Oxford University, June1988. Unpublished.

156 **V.G.Rivlin and G.V.Raynor** : International Metals Reviews 1981, No.3 p140

157 **L.F.Mondolfo** : 'Aluminium : Structure and Properties', Butterworths, London, p534

158 **E.T.Turkdogan** :'Physical Chemistry of High Temperature Technology', Academic Press 1980

159 **R.Hultgren, P.D.Desai, D.T.Hawkins, M.Gleiser, K.K.Kelly and D.D.Wagman** : Selected Values of the Thermodynamic Properties of the Elements, ASM,1973 p467

160 **D.R.Gaskell** : 'Introduction to Metallurgical Thermodynamics', 2nd Edition, M^{C}Graw-Hill Book Company, 1981 pp411 - 413

161 **F.H.Hayes** :'Thermodynamic Basis and Principles of Phase Diagram Calculations' a paper presented at a one day meeting entitled ' Introduction to the Computer Calculation of Phase Diagrams' at The Institute of Metals, London, 10 December 1986

162 **R.F.Strickland-Constable** : 'Kinetics and Mechanism of Crystallization', Academic Press .1968 p110

163 **W.Kurz and D.J.Fischer** : 'Fundamentals of Solidification', Trans Tech Publications,1989, p129

164 **V.G.Rivlin and G.V.Raynor** : International Metals Reviews 1981, No.3 p149

165 **H.Jones** : 'Rapid Solidification of Metals and Alloys', Monograph 8, Inst. of Metals, London 1982 p42

166 **J.Burke** :'The Kinetics of Phase Transformations in Metals', Pergamon Press 1965

167 **J.G.Barlock and L.F.Mondolfo** : Z. Metallkde Bd 66 (1975) H.10 p605

168 **P.A.Kinzie** :'Thermocouple Temperature Measurement', Wiley-Interscience, John Wiley And Sons Inc. 1973 p149

169 **'Advanced Inorganic Chemistry'**: Eds. F.A.Cotton and G.Wilkinson, 5th Edition,1988,John Wiley and Sons. p266

170 **D.A.Porter and K.E.Easterling** : 'Phase Transformations in Metals and Alloys', Van Nostrand Reinhold Ltd. 1981 p81

171 **S.N.Omenyi and A.W.Neumann**, Journal of Applied Physics Vol.47 (1976) 3956

172 **W.K.Burton, N.Cabrera and F.C. Frank** : Philosophical Transactions of the Royal Society A, Vol.243 (1950-51) pp51

173 **D.Hull and D.J. Bacon** : 'Introduction to Dislocations', 3rd Edition Pergamon 1984 p162

174 **R.F.Strickland-Constable** : 'Kinetics and Mechanism of Crystallisation', Academic Press, 1968, p.14

175 **G.Lambert** , editor : 'Typical Microstructures of Cast Metals', The Institute of British Foundrymen, 1957, pp184-185

176 **R.Kowatschewa, R.Dafinowa, Z.Kamenowa and E.Momtschilov** : Praktishe Metallographie Vol.10 (1973) pp131-143

177 **G.V.Raynor and B.J.Ward** : Journal of the Institute of Metals Vol.86 (1957-58) p136

178 **L.F.Mondolfo**: 'Aluminium: Structure and Properties', Butterworths, London,1976, p655

179 **'CRC Handbook of Chemistry and Physics'**, 70th Edition, 1989-1990: edited by R.C.Weast et al. CRC Press, Florida, p B-68

180 **'Lange's Handbook of Chemistry'**, 13th Edition: edited by J.A.Dean. McGraw-Hill 1972

181 **W.H.Hunt Jr., O.Richmond, and R.D.Young**: as ref.18. ICCM6-ECCM2 (1987) Vol.2 pp209-223

182 **J.J.Lewandowski, C.Liu and W.H.Hunt Jr.**: Materials Science and Engineering A107 (1989) pp241-255

183 **M.Manoharan and J.J.Lewandowski**: Scripta Metallurgica Vol.23 (1989)301-304

184 **J.Pilling**: Scripta Metallurgica, Vol.23(1989)pp1375-1380

185 **W.S.Miller, L.A.Lenssen and F.J.Humphreys**: Proceedings of the 5th International Al-Li Conference, Williamsburg, Virginia, March 27-31, 1989. Eds. T.H.Sanders, Jr. and E.A.Starke, Jr., MCE Publications Ltd. Birmingham, UK ,1989. Vol.2, p.931

186 **F.Zok , J.D.Embury, M.F.Ashby and O.Richmond** in: 9th RISO International Symposium on Metallurgy and Materials Science: Mechanical and Physical Behaviour of Metallic and Ceramic Composites. 5-9 September 1988 pp517-526

187 **H.Nayeb-Hashemi and J.Seyyedi:** Metallurgical Transactions A, Vol.20A April 1989 pp 729-739

188 **J.J.Stephens, J.P.Lucas and F.M.Hosking**: Scripta Metallurgica, Vol.22 (1988) pp1307-1312

Acknowledgements

I would like to thank my departmental supervisors Dr.H.M.Flower and Professor D.R.F.West, and my supervisors at ALCAN International Ltd, Dr.J.White and Dr.I.R.Hughes, for their generally good humoured guidance and support during this project, and for a mixture of tactful, and tactless advice!

I am most grateful for the inestimable technical assistance freely given by Mr.G.W.Briers, the EM Group's oracle. Mr.N.Salpardoru, Mr.R.Sweeney, and Mr.K.Hortin are especially acknowledged for their generous technical support. Thanks are due to Dr.H.M.Flower for operating the HVEM, and to Mr.J.Woodal for maintaining the beast. The help given by Mr.L.Russell, and Mr.R.Baxter in the workshop was appreciated.

I am indebted to all the members of the Electron Microscopy Group who have over the past years provided company: in this respect I would like to mention Dr.S.K.Chang, Mr.T.Ahmed, Dr.P.N.Kalu, Dr.M.R.Djazeb, Dr.G.Cam, and the present members of the group.

The provision of laboratory facilities by Professor D.W.Pashley is acknowledged. The author was the recipient of a SERC CASE award and received financial support from the SERC and the collaborating body ALCAN International Ltd, Banbury, Oxen. which also supplied the materials. The author would like to thank Mr. S. Justice at ALCAN for his sound instruction on the metallographic preparation of the composites: samples shown in figures 4.1a,b,c,d and 4.5 c,d were both polished at ALCAN and badly photo-micrographed by the author.